FINITE ELEMENT ANALYSIS OF STRAIN LOCALIZATION IN GEOMATERIALS TAKING A STRONG DISCONTINUITY APPROACH

A DISSERTATION
SUBMITTED TO THE DEPARTMENT OF CIVIL AND ENVIRONMENTAL ENGINEERING
AND THE COMMITTEE ON GRADUATE STUDIES
OF STANFORD UNIVERSITY
IN PARTIAL FULFILLMENT OF THE REQUIREMENTS
FOR THE DEGREE OF
DOCTOR OF PHILOSOPHY

Richard Anderson Regueiro

August 1998

I certify that I have read this dissertation and that in my opinion it is fully adequate, in scope and quality, as a dissertation for the degree of Doctor of Philosophy.

Ronaldo I. Borja (Principal Advisor)
Associate Professor of Civil and Environmental Engineering
Associate Professor (By Courtesy) of Geological and Environmental Sciences

I certify that I have read this dissertation and that in my opinion it is fully adequate, in scope and quality, as a dissertation for the degree of Doctor of Philosophy.

Francisco Armero
Assistant Professor of Civil and Environmental Engineering
University of California, Berkeley

I certify that I have read this dissertation and that in my opinion it is fully adequate, in scope and quality, as a dissertation for the degree of Doctor of Philosophy.

Peter M. Pinsky
Professor of Mechanical Engineering
Professor (By Courtesy) of Civil and Environmental Engineering

I certify that I have read this dissertation and that in my opinion it is fully adequate, in scope and quality, as a dissertation for the degree of Doctor of Philosophy.

Sheri D. Sheppard
Associate Professor of Mechanical Engineering

Approved for the University Committee on Graduate Studies:

Abstract

Localized deformation in the form of slip surfaces and shear bands occurs naturally in geomaterials such as soil and rock. As a result, in order for the geotechnical engineer or engineering geologist to make informed analysis and design decisions for geomechanical structures in which localized deformation may develop, slip surfaces and shear bands should be represented numerically by a finite element model. The usefulness of a finite element model is realized when analyzing geomechanical structures with complex geometry and geomaterial behavior because for such problems an analytical limit equilibrium solution is unwieldy.

Concurrent with the appearance of localized deformation is the loss of overall strength of the geomaterial body. Thus, rate-independent, strain-softening plasticity models have typically been used to represent this 'softening behavior' in geomaterials. Rate-independent plasticity models, however, do not contain a material length scale needed to define the width of a localized deformation zone, thus rendering finite element solutions mesh-size dependent for softening plasticity problems. In addition, the mesh alignment of standard finite elements has been shown to affect the simulated localized deformation pattern. Therefore, a more sophisticated numerical tool to represent the formation of slip surfaces and shear bands in geomaterials in a mesh-independent manner is in order.

Many attempts have been made to numerically model localized deformation using rate-independent, strain-softening plasticity models, but, in the absence of a material 'length scale', adaptive remeshing, or other regularization technique, these attempts typically do not satisfy two necessary criteria for a finite element solution to be meaningful (i.e., mesh-independent): objectivity with respect to mesh refinement and insensitivity to mesh alignment. A previously-developed model which meets these two criteria without introducing a material length scale and without requiring special mesh alignment strategies represents localized deformation as a strong discontinuity (jump in displacement field). This model is adopted to formulate a non-associative, rate-independent, strain-softening Drucker-Prager plasticity model in the context of strong discontinuities and to implement this plasticity model along with an enhanced quadrilateral element within the framework of an assumed enhanced strain finite element method. The formulation and implementation are carried out for small deformations and rotations and for the drained condition, whereby the effect of pore-fluid is neglected.

Numerical simulations of the load-displacement behavior of soft rock under plane strain loading demonstrate the ability of the model to approximate, in a mesh-independent manner, the experimentally observed failure surface orientation, stress level at which onset of localization occurs, and post-localization overall ‘softening’ behavior. Numerical simulations of strain localization occurring in a slope and in an excavation demonstrate near mesh-independence of finite element solutions resulting from the strong discontinuity approach.

To My Parents

Acknowledgements

First and foremost, I thank my advisor, Ronnie Borja, for his guidance and support throughout my Ph.D. studies. His insight into problems and creative approaches to solving them will be an inspiration to me throughout my research career.

I acknowledge the members of my oral defense and reading committee: Professors Francisco Armero, Peter Pinsky, Sheri Sheppard, and chairman Atilla Aydin. I am extremely appreciative of their comments during the defense and the review of my thesis.

I am grateful to Dr. Krishna Garikipati for answering questions regarding the strong discontinuity approach.

I want to recognize my former advisors: Professor John Dugundji of the Massachusetts Institute of Technology, Dr. Rick Johansen of E.T. Techtonics, Dr. David Kang of the Charles Stark Draper Laboratory, Dr. John Lepore of the University of Pennsylvania, and Dr. Richard Sause of Lehigh University. I am thankful for their continuing advice.

One of the most rewarding aspects of working toward a Ph.D. is interacting with your colleagues with whom you share an office/computer lab. Thus, I acknowledge my geomechanics colleagues: Dr. Heng-Yih Chao, Tim Lai, Eric Lin, Dr. Francisco Montans, Dr. Claudio Tamagnini, and Dr. Jon Wren. They made the time spent in the office and computer lab much more rewarding and enjoyable.

Above all, I thank my family and Moira for their unwavering support. This would not have been possible without them.

The work presented in this thesis was supported by the G3S Division of the National Science Foundation through Grant No. CMS97-00426. This support is gratefully acknowledged.

Contents

List of Figures

List of Tables

Notation

$(\bullet)_e$	denotes association with element e
$(\bullet)^h$	denotes discretization with respect to finite elements of diameter h
$(\bullet)^s$	denotes symmetric part
$(\bullet)^T$	transpose of a matrix
$(\bullet)^{\mathrm{tr}}$	denotes trial value
$(\bullet)_{n+1}^{k+1}$	denotes current iteration $k+1$ at time step $n+1$
$\mathbf{1}$	second order identity tensor
A	cross-sectional area of plane strain experimental sample (m^2)
A_e	area of element e (m^2)
$\boldsymbol{A}$	second order acoustic tensor (Pa)
b	material dilation constant
b_e	residual expresssing equilibrium along discontinuity $\mathcal{S}_e$ associated with the jump displacment (N/m)
$\boldsymbol{B}_e$	strain-displacement matrix for element e
$\boldsymbol{b}$	body force vector (N/m^3)
c	wave speed (m/s^2)
$\bar{c}$	cohesion (Pa)
$\boldsymbol{c}^e$	fourth order elastic tangent modulus tensor (Pa)
$\boldsymbol{c}_e$	displacement variation vector of element e (m)

$\boldsymbol{c}_e^A$	displacement variation vector of node A of element e (m)
$\boldsymbol{C}$	general fourth order elastic tangent modulus tensor (Pa)
$\boldsymbol{C}^{ep}$	fourth order elastic-plastic tangent modulus tensor (Pa)
$\boldsymbol{d}_e$	displacement vector of element e (m)
$\boldsymbol{d}_e^A$	displacement vector of node A of element e (m)
D	material strain-rate sensitivity constant (Pa/s)
$\boldsymbol{D}^e$	elastic tangent matrix (Pa)
e	void ratio
e^p	measure of deviatoric plastic strain (%)
E	modulus of elasticity (Pa)
f^h	extra interpolation function used to construct $M_{\mathcal{S}}$
$\boldsymbol{F}_e$	enhanced strain matrix resulting from singular part
$\boldsymbol{g}$	prescribed displacement (m)
$\boldsymbol{G}_e$	enhanced strain matrix resulting from regular part
h	deviatoric stress ratio
h^{tol}	localization tolerance
H'	shear hardening/softening plastic modulus (Pa)
H_δ	coefficient of singular part of shear softening plastic modulus (Pa/m)
$H_{\mathcal{S}}$	Heaviside function at $\mathcal{S}$
$\boldsymbol{H}$	tangential plastic modulus matrix (Pa)
$\boldsymbol{H}_\delta$	coefficient of singular part of tangential plastic modulus matrix (Pa/m)
$\boldsymbol{I}$	fourth order identity tensor
K'	bulk hardening/softening plastic modulus (Pa)
K_δ	coefficient of singular part of bulk softening plastic modulus (Pa/m)
$\bar{K}$	bulk modulus of elasticity (Pa)

$\boldsymbol{K}^e_{dd}$	stiffness matrix associated with nodal displacements (N/m)
$\boldsymbol{K}^e_{d\zeta}$	stiffness matrix coupling nodal displacements to jump displacement (N/m)
$\boldsymbol{K}^e_{\zeta d}$	stiffness matrix coupling jump displacement to nodal displacements (N/m^2)
$\boldsymbol{K}^e_{d}$	stiffness matrix coupling jump displacement to nodal displacements for elastic unloading (N/m^2)
$K^e_{\zeta\zeta}$	stiffness matrix associated with jump displacement (N/m^2)
K^e_{ζ}	softening modulus along discontinuity $\mathcal{S}_e$ (N/m^2)
$\tilde{\boldsymbol{K}}^e_{dd}$	stiffness matrix for reduced system of equations as a result of condensing out the jump displacement (N/m)
$l_{\mathcal{S}_e}$	length of slip line within element e (m)
$\boldsymbol{m}$	unit vector denoting jump direction
$M_{\mathcal{S}}$	function used to reparameterize the displacement field
n_{dim}	number of dimensions
n_{nds}	number of nodes
n_{el}	number of elements
$n_{el,\mathrm{loc}}$	number of localized elements
$\boldsymbol{n}$	unit vector denoting slip-line orientation
$\hat{\boldsymbol{n}}$	normalized deviatoric Cauchy stress tensor
N^A	shape function at node A
$\boldsymbol{N}_e$	shape function matrix for element e
p	mean stress (Pa)
P	compressive load for plane strain experimental sample (N)
q	resolved deviatoric Cauchy stress along discontinuity $\mathcal{S}$ (Pa)
Q	combined Cauchy stress along discontinuity $\mathcal{S}$ (Pa)

r	stress difference (Pa)
r^{tol}	Newton-Raphson iteration convergence tolerance
$\boldsymbol{r}_e$	standard residual for equilibrium within element e associated with the nodal displacments (N)
$\tilde{\boldsymbol{r}}_e$	residual for reduced system of equations as a result of condensing out the jump displacement (N)
s	characteristic coordinate (m)
$\boldsymbol{s}$	deviatoric Cauchy stress tensor (Pa)
t	time (s)
$\boldsymbol{t}$	applied traction (Pa)
$\bar{\boldsymbol{t}}$	regular part of traction vector (Pa)
$\boldsymbol{t}_\delta$	coefficient of singular part of traction vector (Pa·m)
T	end of time period (s)
u	displacement (m)
$\boldsymbol{u}$	displacement vector (m)
$\delta\boldsymbol{u}$	variational displacement vector (m)
$\bar{\boldsymbol{u}}$	continuous part of displacement field vector (m)
v	velocity for 1D bar example (m/s^2)
v^p	volumetric plastic strain (%)
ΔV	change in volume (m^3)
V_0	initial volume (m^3)
V_v	volume of voids (m^3)
V_s	volume of solids (m^3)
x	coordinate for 1D bar example (m)
$\boldsymbol{x}$	coordinate vector (m)
α_1	volumetric stress-like plastic internal variable (Pa)

α_2	deviatoric stress-like plastic internal variable (Pa)
$\bar{\alpha}$	cohesion material parameter for Drucker-Prager yield function
$\boldsymbol{\alpha}$	stress-like vector of plastic internal variables (Pa)
β	friction material parameter for Drucker-Prager yield function
γ^p	plastic shear strain (%)
$\tilde{\boldsymbol{\gamma}}$	enhanced strain variation (%)
$\delta_{\mathcal{S}}$	Dirac-delta function at $\boldsymbol{\mathcal{S}}$
ϵ	infinitesimal strain (%)
ϵ_2	compressive strain for plane strain experiment (%)
ϵ^e	elastic strain (%)
ϵ^p	plastic strain (%)
ϵ^{vp}	viscoplastic strain (%)
ϵ_{vol}	volumetric strain (%)
$\boldsymbol{\epsilon}$	second order infinitesimal strain tensor (%)
$\boldsymbol{\epsilon}^e$	elastic part of second order infinitesimal strain tensor (%)
$\boldsymbol{\epsilon}^p$	plastic part of second order infinitesimal strain tensor (%)
$\delta\boldsymbol{\epsilon}$	variational second order infinitesimal strain tensor (%)
$\tilde{\boldsymbol{\epsilon}}$	enhanced strain tensor (%)
$\delta\tilde{\boldsymbol{\epsilon}}$	enhanced strain variation tensor (%)
ζ	magnitude of jump displacement (m)
$\boldsymbol{\eta}$	variational displacement (m)
$\bar{\boldsymbol{\eta}}$	regular part of variational displacement (m)
η	arbitrary angle (°)
θ	orientation of normal $\boldsymbol{n}$ to slip line from major principal stress axis σ_1 (°)
κ	scalar stress parameter for Drucker-Prager yield function (Pa)

λ	plastic consistency parameter (m/(m·s))
λ_δ	coefficient of singluar part of plastic consistency parameter ((m·m)/(m·s))
$\bar{\lambda}$	Lame parameter (Pa)
Λ	arbitrary scalar parameter
$\bar{\Lambda}$	modified Lame parameter for implementation of $\hat{\boldsymbol{D}}^e$ (Pa)
$\bar{\mu}$	Lame parameter, elastic shear modulus (Pa)
ν	Poisson's ratio
$\boldsymbol{\nu}$	unit normal vector
$\boldsymbol{\xi}$	strain-like vector of plastic internal variables (%)
Π	energy functional (J)
ρ	mass density (kg/m^3)
σ	Cauchy stress for 1D bar example (Pa)
σ_1	major principal stress (Pa)
σ_2	intermediate or minor principal stress (Pa)
σ_3	intermediate or minor principal stress (Pa)
σ_c	confining stress/pressure (Pa)
$\boldsymbol{\sigma}$	second order Cauchy stress tensor (Pa)
$\bar{\boldsymbol{\sigma}}$	regular part of second order Cauchy stress tensor (Pa)
$\boldsymbol{\sigma}_\delta$	coefficient of singular part of second order Cauchy stress tensor (Pa·m)
$\delta\boldsymbol{\sigma}$	variational second order Cauchy stress tensor (Pa)
τ	shear stress (Pa)
ϕ	yield function (Pa)
$\bar{\phi}$	friction angle (°)
φ	plastic potential function (Pa)

ψ	jump dilation angle (°)
$\bar{\psi}$	material dilation angle (°)
Ψ	stored energy density function (J/m^3)
Ω	open body (m^3)
Ω_-	region of body from which $\boldsymbol{n}$ extends (m^3)
Ω_+	region of body into which $\boldsymbol{n}$ extends (m^3)
$\bar{\Omega}$	closed body (m^3)
$\bar{\Omega}_e^h$	discretized region for element e (m^3)
$\bar{\Omega}_{\mathrm{loc},e}^h$	discretized region for localized element e (m^3)
$\partial\Omega$	boundary of body Ω (m^2)
$\partial_t\Omega$	surface upon which traction is applied (m^2)
$\partial_u\Omega$	surface upon which displacement is applied (m^2)
$\mathcal{D}$	dissipation function (W/m^3)
$\mathcal{D}_\delta$	coefficient of singular part of dissipation function (W·m/m^3)
$\mathcal{D}_\Omega$	total dissipation over region Ω (W)
$\mathcal{E}$	space of compatible strains
$\tilde{\mathcal{E}}$	space of enhanced strains
$\mathcal{H}$	hardening/softening modulus (Pa)
$\mathcal{H}_\delta$	coefficient of singular part of plastic softening modulus (Pa/m)
$\mathcal{S}$	discontinuity surface (m^2)
$\mathcal{U}$	space of admissible trial solutions
$\mathcal{V}$	space of admissible weighting functions
$\mathbb{R}$	real number line
$\mathbb{R}^{n_{dim}}$	space of real numbers of dimension n_{dim}
$\mathbb{S}$	space of symmetric second order tensors

Chapter 1

Introduction

1.1 Background and Motivation

The term ‘geomaterial’ refers to soil, rock, and concrete, but in this thesis only the modeling of localized deformation occurring in soil and rock will be considered. The motivation for this thesis will stem from background research material covering evidence of localized deformation in soil and rock, the implications of rate-independent strain softening plasticity, and numerical methods for modeling localized deformation.

Not all soil types will exhibit localized deformation. Consider the typical stress-strain behavior of soil as described by Atkinson [5] and shown in Figs. 1.1–1.3. As an exception to the continuum mechanics convention adopted throughout this thesis, compressive stress and strain are positive in Figs. 1.1–1.5.

The behavior of a soil at two different initial states is described. A ‘wet’ soil refers to loose sand and normally consolidated or lightly overconsolidated clay. A normally consolidated clay refers to a soil which is currently experiencing its greatest state of stress. An overconsolidated clay is a soil which has experienced its greatest state of stress in the past. For example, a clay would be overconsolidated if a building

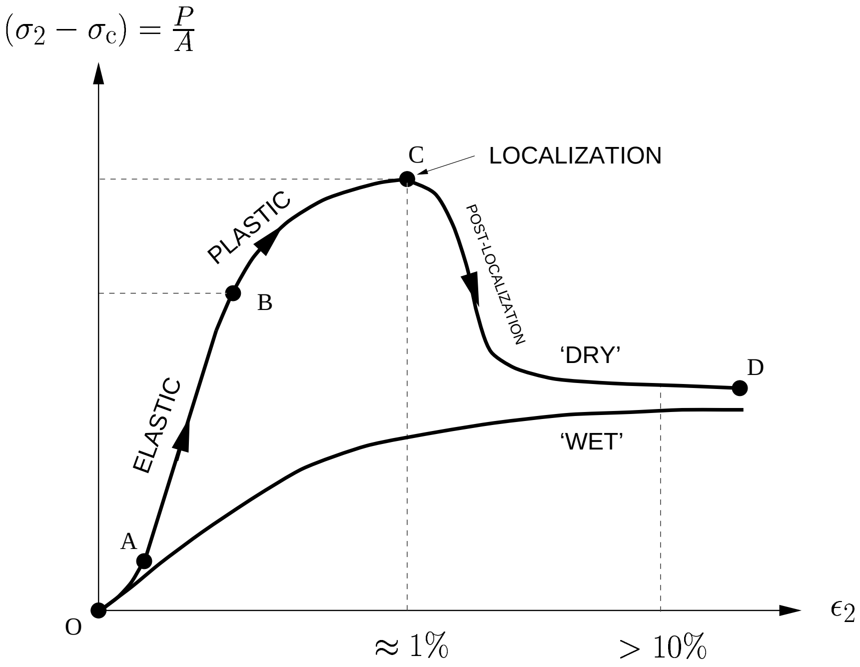

Figure 1.1. Typical stress-strain behavior for soil as described in [5].

which rested upon it was demolished, thus lowering the level of stress experienced by the clay. A 'wet' soil is defined relative to the critical state (i.e., the state of a soil at which further deformation produces no volume change) and is so named because when sheared it reduces in volume. In other words, fluid in the voids would be expelled. On the other hand, a 'dry' soil refers to dense sand and heavily overconsolidated clay. In this case, the soil is dry of critical state because after initial contraction, the soil dilates and will absorb fluid. The volumetric strain ϵ_{vol} and void ratio e (where V_v is the volume of voids and V_s is the volume of solids) behavior for these types of soils are shown in Figs. 1.2 and 1.3, respectively.

Clearly, it is of interest to model strain localization occurring in 'dry' soils, as evidenced by Fig. 1.1, which shows a plot of differential stress $(\sigma_2 - \sigma_c)$ versus axial strain ϵ_2 for typical soil behavior at the two different initial states. A 'dry' soil will deform elastically (i.e., insignificant irrecoverable deformations develop) from point A to point B, then dilate plastically (i.e., significant irrecoverable deformations are developing) from point B to point C, and at peak load at point C develop localized deformation which is followed by overall softening and a residual stress region as the soil approaches its critical state at point D. Localized deformation in soil may take the form of a slip surface or shear band. A "slip surface" is a zone of localized deformation with negligible width, and a "shear band" is a zone of localized deformation with finite width. A 'wet' soil will deform with monotonically increasing stress level as it approaches its critical state and not exhibit localized deformation.

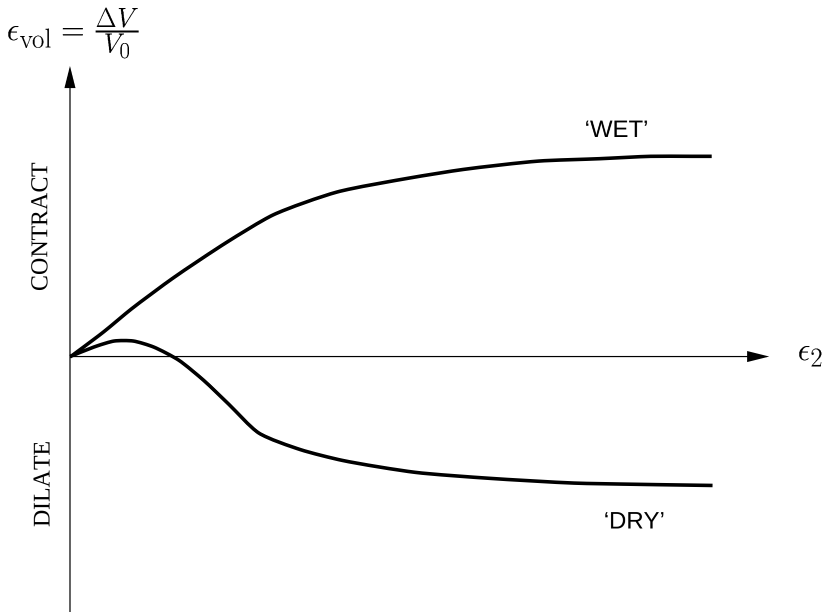

Figure 1.2. Typical volumetric strain vs. axial strain behavior for soil [5].

On the other hand, almost all rock types exhibit some form of localized deformation. Consider the typical stress-strain behavior of rock as described by JAEGER

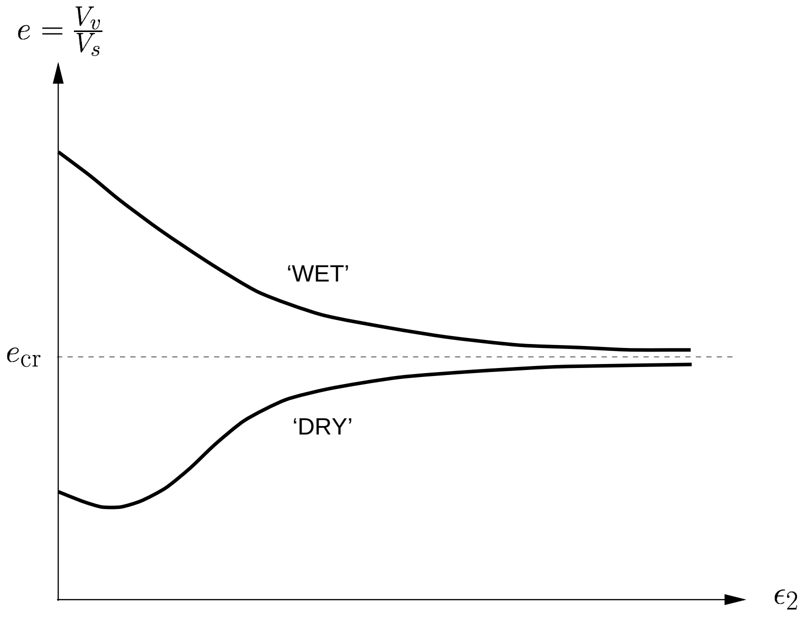

Figure 1.3. Typical void ratio vs. axial strain behavior for soil [5].

& Cook [37] and shown in Figs. 1.4 and 1.5.

Figure 1.4 is a plot of differential stress $(\sigma_2 - \sigma_{\rm c})$ versus axial strain ϵ_2 for typical rock behavior. The region from the origin O to the yield point B is considered elastic (i.e., no significant irrecoverable deformation develops) where from O to A the rock material reconstitutes itself as mircocracks close, and from A to B the rock material behaves elastically, although not necessarily linear. In the region from B to C significant irrecoverable deformations develop, and, as a result, this region may be called the 'plastic' region. At peak differential stress at C, localized deformation becomes prevalent. Thus, further loading from C to D (displacement driven) results in an overall 'softening' behavior of the material, which is called the 'post-localization' region of the stress-strain curve.

Figure 1.5 is a plot of differential stress versus volumetric strain, where the

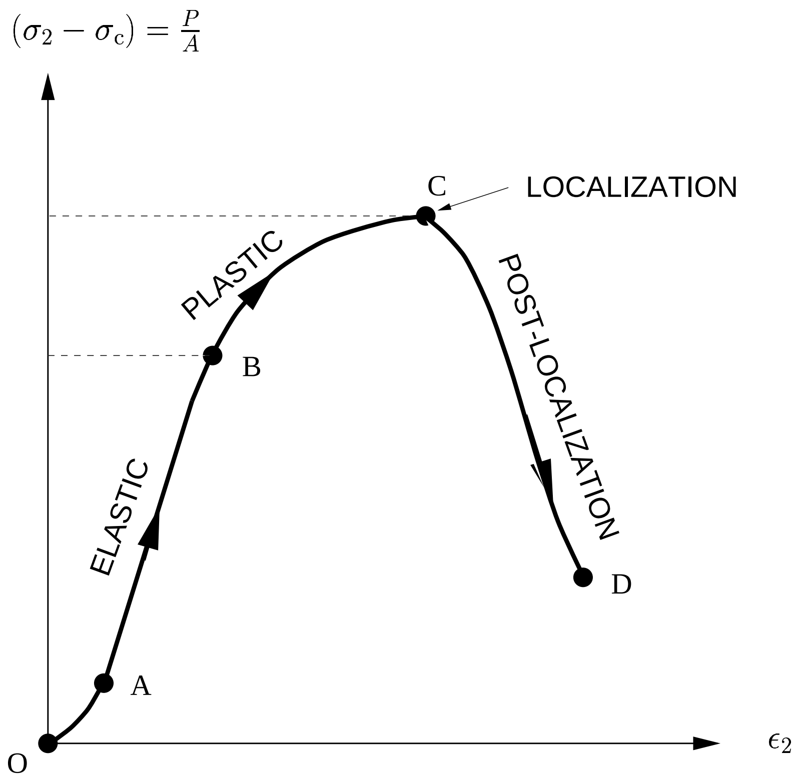

Figure 1.4. Typical stress-strain behavior for rock as described in [37].

same regions OA, AB, BC, and CD dilineated in Fig. 1.4 are also shown. From O to B the rock material contracts in accordance with linear elasticity ($\epsilon_{\text{vol}} = \frac{3(1-2\nu)}{E}\text{tr}(\boldsymbol{\sigma})$ if the elasticity is in fact linear). As the rock material is loaded into the plastic region from B to C, the rock material dilates with respect to the elastic contraction as a result of the formation and extension of open microcracks within the rock specimen. During post-localization from C to D, the rock material may continue to dilate and actually increase in volume with respect to its initial volume. This is in contrast to soil which will approach its critical state.

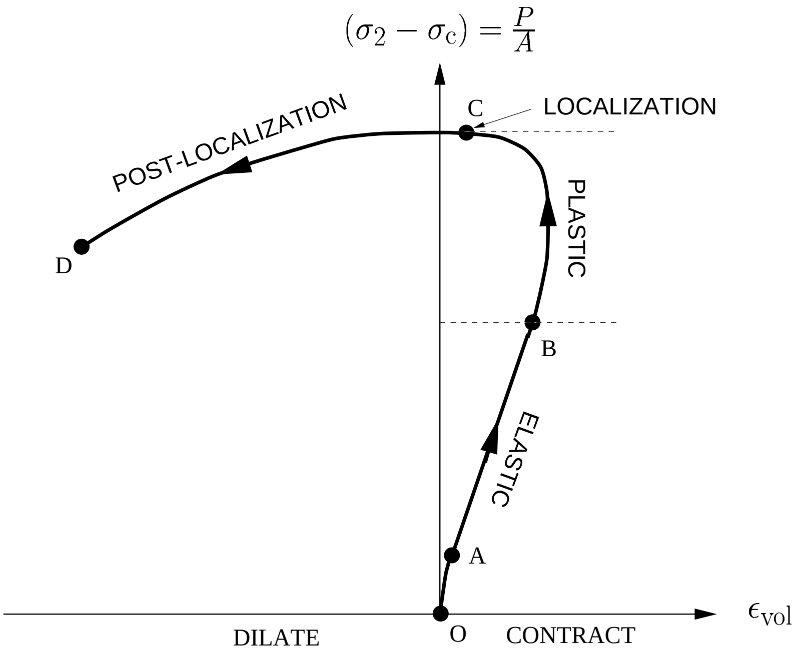

Figure 1.5. Typical volumetric behavior for rock as described in [37].

1.1.1 Evidence of Localized Deformation in Soil and Rock

There have been numerous experimental studies of the physical phenomenon of localized deformation in geomaterials such as soil and rock by Vardoulakis et al. [93], Vardoulakis & Goldschieder [94], Hallbauer et al. [31], Santarelli & Brown [77], Wawersik et al. [98], Ord et al. [56], Yumlu & Ozbay [101], and Labuz et al. [41], to name a few (see Read & Hegemier [66] for a review). Many of these studies have attempted to understand the connection between the microscopic actions (e.g., micro-cracking in brittle rock, mineral particle rolling and sliding in granular soil, and mineral particle rotation and translation in the cement matrix of soft rock) and the macroscopic behavior (e.g., formation of slip surfaces and shear bands and progressive loss of overall material body strength). A number of microscopic-based numerical models of localized deformation in granular materials have been considered to attempt to establish this connection numerically CUNDALL & STRACK [18], CUNDALL [19], BARDET & PROUBET [7], BORJA & WREN [11], and WREN & BORJA [99]. This thesis, on the other hand, discusses a macroscopic approach to modeling localized deformation via the finite element method.

READ & HEGEMIER [66] provide a solid argument—with supporting data provided by other researchers—that the strain softening observed in stress-strain or load-displacement curves of experimental compression tests on soil, rock, and concrete is not a material property of a homogeneously deforming material body, but rather a structural phenomenon in the form of inhomogeneous deformation. This argument is not consistent with the use of traditional local continuum constitutive models to represent strain softening behavior because these models assume homogeneous deformation and thus cannot adequately capture inhomogeneous deformation like strain localization at the local continuum level. In addition to this argument, rate-independent strain softening plasticity results in mesh-dependent finite element solutions as a result of the governing equilibrium equations being ill-posed; this will be elaborated upon in the next section.

Field evidence of localized deformation may take the form of faulting in rocks (see AYDIN & JOHNSON [6]) and slip surfaces and shear bands in geotechnical structures such as excavations (see CHAN & MORGENSTERN [13], FINNO et al. [25], and FINNO & NERBY [26]). As mentioned previously, a finite element method which is capable of modeling localized deformation in geomaterials in a mesh-independent manner is especially useful for simulating the behavior of actual field geomechanical structures such as these because an analytical limit equilibrium solution is unwieldy.

It is noteworthy that fracture mechanics also has been used to model localized deformation in soil (see PALMER & RICE [59] and RICE [68]) and rock (see COSTIN

[15]). This thesis, however, concentrates on the use of plasticity models to represent localized deformation.

1.1.2 Wave Propagation Analysis of Strain Softening Plasticity - Brief Review

Why consider approaches for modeling strain softening phenomena in solids other than the classical, rate-independent, continuum plasticity approach? Besides the experimental evidence allying against such an approach (as described in [66]), the answer lies with the analysis of wave propagation in a one-dimensional, rate-independent strain softening bar. The following analysis is taken from similar treatments by Read & Hegemier [66], Needleman [54], Loret & Prevost [46], and Sluys & de Borst [85].

1.1.2.1 Wave Propagation in 1D Rate-Independent, Strain Softening Bar

Equilibrium is expressed as

$$\sigma_{,x} = \rho\, v_{,t} \tag{1.1}$$

where σ is the Cauchy stress, x is the coordinate along the bar, ρ is the mass density of the material, v is the velocity ($= dx/dt$), t is time, and $(\bullet)_{,x} = \partial(\bullet)/\partial x$ denotes the partial differentiation of the quantity in $(\bullet)$ with respect to x. The rate-independent constitutive relation for strain softening is

$$\sigma = f(\epsilon^p)\,; \quad f'(\epsilon^p) = \frac{\partial f(\epsilon^p)}{\partial \epsilon^p} < 0 \tag{1.2}$$

where ϵ^p is the plastic strain. Assuming linear softening ($f'(\epsilon^p) = \mathcal{H} =$ constant), the constitutive relation in rate form becomes

$$\dot{\sigma} \;=\; \mathcal{H}\,\dot{\epsilon^p}\,; \quad \mathcal{H} \;<\; 0 \tag{1.3}$$

where $\mathcal{H}$ is the hardening/softening modulus ($\mathcal{H} > 0$ for hardening plasticty, $\mathcal{H} < 0$ for softening plasticity, and $\mathcal{H} = 0$ for perfect plasticity). The total strain rate is decomposed into elastic and plastic parts, with the elastic part expressed in terms of the stress rate $\dot{\sigma}$ via Hooke's Law as

$$\dot{\epsilon} \;=\; \dot{\epsilon}^e + \dot{\epsilon}^p\,; \quad \dot{\epsilon}^e \;=\; \frac{\dot{\sigma}}{E} \tag{1.4}$$

where E is the modulus of elasticity and $\dot{\epsilon} = v_{,x}$.

Substituting the expression for $\dot{\epsilon^p}$ from Eq. (1.4) into Eq. (1.3) and the equilibrium equation Eq. (1.1), the following partial differential equation (PDE) governing dynamic equilibrium results as

$$v_{,tt} \;-\; \frac{1}{\rho}\left(\frac{E\mathcal{H}}{E+\mathcal{H}}\right) v_{,xx} \;=\; 0\,. \tag{1.5}$$

The method of characteristics may be used to determine the character of the wave equation; refer to Achenbach [1] for a brief discussion of the method of characteristics, and to Courant & Hilbert [16] and Petrovskii [61] for more details. Take the derivatives of $v_{,t}$ and $v_{,x}$ with respect to a new coordinate s (which is a characteristic curve):

$$\begin{aligned} \frac{d}{ds}\left(\frac{\partial v}{\partial t}\right) &= \frac{\partial^2 v}{\partial t^2}\frac{dt}{ds} + \frac{\partial^2 v}{\partial t \partial x}\frac{dx}{ds} \\ \frac{d}{ds}\left(\frac{\partial v}{\partial x}\right) &= \frac{\partial^2 v}{\partial x \partial t}\frac{dt}{ds} + \frac{\partial^2 v}{\partial x^2}\frac{dx}{ds}\,. \end{aligned} \tag{1.6}$$

Thus, the characteristic determinant becomes:

$$\begin{vmatrix} 1 & 0 & -\frac{1}{\rho}\left(\frac{E\mathcal{H}}{E+\mathcal{H}}\right) \\ \frac{dt}{ds} & \frac{dx}{ds} & 0 \\ 0 & \frac{dt}{ds} & \frac{dx}{ds} \end{vmatrix} = \left(\frac{dx}{ds}\right)^2 - \frac{1}{\rho}\left(\frac{E\mathcal{H}}{E+\mathcal{H}}\right)\left(\frac{dt}{ds}\right)^2 \tag{1.7}$$

and the characteristics are

$$\frac{dx}{dt} = \pm\sqrt{\frac{1}{\rho}\left(\frac{E\mathcal{H}}{E+\mathcal{H}}\right)} \tag{1.8}$$

which are also the physical wave speeds. For strain softening the hardening/softening modulus is negative ($\mathcal{H} < 0$) which yields imaginary wave speeds and transforms the PDE from hyperbolic to elliptic (no longer do waves propagate; they are 'standing' waves [1]). Elliptic initial value problems are ill-posed because initial disturbances cannot propagate through the solid body. For perfect plasticity ($\mathcal{H} = 0$) the PDE becomes parabolic and is again not well-posed because initial disturbances cannot travel through the solid body (see WU & FRUEND [100] for a description of this wave phenomenon call 'deformation trapping').

1.1.2.2 Wave Propagation in 1D Rate-Dependent, Strain Softening Bar

One way to correct the ill-posedness of the PDE for a rate-independent, strain softening bar, is to introduce rate dependence:

$$\sigma = f(\epsilon^{vp}) + D\,\dot{\epsilon}^{vp} \tag{1.9}$$

where ϵ^{vp} is the viscoplastic strain ($\epsilon^{vp} = \epsilon - \epsilon^{e}$), such as that defined in the manner of PERZYNA [60], and D is a material constant representing the strain-rate sensitivity of the material. Assuming linear softening, the rate form of Eq. (1.9) becomes

$$\dot{\sigma} = \mathcal{H}\,\dot{\epsilon}^{vp} + D\,\ddot{\epsilon}^{vp} \tag{1.10}$$

where $\mathcal{H}$ is the softening modulus ($\mathcal{H} < 0$). Using the decomposition of strain ($\epsilon = \epsilon^e + \epsilon^{vp}$), equilibrium ($\sigma_{,x} = \rho\, v_{,t}$), and Hooke's Law ($\sigma = E\,\epsilon^e$), the governing PDE becomes

$$\rho\,\frac{D}{E}\,v_{,ttt} - D\,v_{,txx} - \mathcal{H}\,v_{,xx} + \rho\left(\frac{E+\mathcal{H}}{E}\right) v_{,tt} = 0\,. \tag{1.11}$$

Note that if $D \to 0$, the rate-independent PDE in Eq. (1.5) is recovered. Considering that the higher-order terms determine the character of the PDE [16], the derivatives of $v_{,tt}$ and $v_{,tx}$ with respect to the new coordinate s (which is a characteristic curve) are

$$\begin{aligned} \frac{d}{ds}\left(\frac{\partial^2 v}{\partial t^2}\right) &= \frac{\partial^3 v}{\partial t^3}\frac{dt}{ds} + \frac{\partial^3 v}{\partial t^2 \partial x}\frac{dx}{ds} \\ \frac{d}{ds}\left(\frac{\partial^2 v}{\partial t \partial x}\right) &= \frac{\partial^3 v}{\partial x \partial t^2}\frac{dt}{ds} + \frac{\partial^3 v}{\partial t \partial x^2}\frac{dx}{ds}\,. \end{aligned} \tag{1.12}$$

Thus, the characteristic determinant becomes:

$$\begin{vmatrix} \rho\frac{D}{E} & 0 & -D \\ \frac{dt}{ds} & \frac{dx}{ds} & 0 \\ 0 & \frac{dt}{ds} & \frac{dx}{ds} \end{vmatrix} = \rho\,\frac{D}{E}\left(\frac{dx}{ds}\right)^2 - D\left(\frac{dt}{ds}\right)^2 \tag{1.13}$$

and the characteristics are

$$\frac{dx}{dt} = \pm\sqrt{\frac{E}{\rho}} \tag{1.14}$$

which are the elastic wave speeds regardless of the choice of $\mathcal{H}$. Thus, the PDE is well-posed. In this case the characteristics do not represent the physical wave speed, except for the limiting case $D \to \infty$, whereby the second order terms drop out of Eq. (1.11), and then the physical wave speed will be the elastic wave speed.

Because of this result, rate-dependent strain softening has been considered as one approach to address the ill-posedness associated with the governing PDE for rate-independent strain softening, Sandler & Wright [76]. Because there is no loss of strong ellipticity (i.e., change of form of PDE, to be defined in the next section) to detect onset of localization, material inhomogeneities are needed to trigger a localization of deformation (see Needleman [54]). This approach to finite element analysis of strain localization is well documented by Loret & Prevost [46] and Prevost & Loret [64].

Rate-dependent plasticity is not considered for the following reasons: 1) the initial, boundary value problem is well-posed and thus does not need any special consideration; 2) rate-dependent plasticity has already been implemented with respect to modeling geomaterials [46], [64]; and 3) since, typically, a rate-independent geomaterial is of interest, the rate-independent limit of rate-dependent plasticity is used [46], [64].

1.1.3 Strong Ellipticity Condition

The strong ellipticity condition as probably first put forth by Hadamard [30] implies that elastic wave speeds are real and nonzero. Consider the strong ellipticity condition as stated by Marsden & Hughes [50]:

$$(\boldsymbol{m} \otimes \boldsymbol{n}) : \boldsymbol{C} : (\boldsymbol{m} \otimes \boldsymbol{n}) \; > \; \beta \, \|\boldsymbol{m}\| \, \|\boldsymbol{n}\| \, ; \quad \forall \, \beta > 0 \, , \tag{1.15}$$

where $(\boldsymbol{m} \otimes \boldsymbol{n}) : \boldsymbol{C} : (\boldsymbol{m} \otimes \boldsymbol{n}) = m_i n_j C_{ijkl} m_k n_l$, $\boldsymbol{C}$ is the general fourth order tangent modulus tensor constant in $\boldsymbol{x}$ (i.e., homogeneous), $\boldsymbol{m}$ and $\boldsymbol{n}$ are nonzero vectors ($\boldsymbol{m}, \boldsymbol{n} \in \mathbb{R}^{n_{dim}}$), and β is a real, nonzero number. The following three-dimensional wave propagation analysis proves that strong ellipticity implies real and nonzero elastic wave speeds.

Ignoring body forces, dynamic equilibrium is written as

$$\rho\,\ddot{\boldsymbol{u}} \;=\; \boldsymbol{\nabla}\cdot\boldsymbol{\sigma} \tag{1.16}$$

where ρ is the mass density, $\boldsymbol{u}$ is the displacement field, $\boldsymbol{\sigma}$ is the Cauchy stress, $(\ddot{\bullet}) = \partial^2(\bullet)/\partial t^2$, and $(\boldsymbol{\nabla}\cdot\boldsymbol{\sigma})_i = \sigma_{ij,j}$. The constitutive equation may be written in rate form as

$$\dot{\boldsymbol{\sigma}} \;=\; \boldsymbol{C} : \dot{\boldsymbol{\epsilon}}\,; \quad \dot{\boldsymbol{\epsilon}} \;=\; \boldsymbol{\nabla}^s\dot{\boldsymbol{u}} \tag{1.17}$$

where $(\bullet)^s$ denotes the symmetric part, and $(\boldsymbol{\nabla}^s\dot{\boldsymbol{u}})_{ij} = \frac{1}{2}(\dot{u}_{i,j} + \dot{u}_{j,i})$. Assume a plane traveling wave of the form

$$\boldsymbol{u}(\boldsymbol{x},t) \;=\; f(\boldsymbol{x}\cdot\boldsymbol{n} + c\,t)\,\boldsymbol{m} \tag{1.18}$$

where $\boldsymbol{n}$ is the propagation direction, $\boldsymbol{m}$ is the motion direction, and c is the wave speed (see ACHENBACH [1]). Note that if $\boldsymbol{n}\cdot\boldsymbol{m} = 0$ the wave is called a transverse or shear wave, and if $\boldsymbol{n} = \pm\,\boldsymbol{m}$ the wave is called a longitudinal or pressure wave. Dynamic equilibrium in Eq. (1.16) now takes the form

$$\rho\,c^2\boldsymbol{m} \;=\; \boldsymbol{A}\cdot\boldsymbol{m}\,; \quad \boldsymbol{A} \;=\; \boldsymbol{n}\cdot\boldsymbol{C}\cdot\boldsymbol{n} \tag{1.19}$$

where $\boldsymbol{A}$ is commonly known as the ‘acoustic tensor.’ Taking the dot product of both sides of Eq. (1.19) by $\boldsymbol{m}$, the wave speed may be calculated from the following:

$$c \;=\; \sqrt{\frac{\boldsymbol{m}\cdot\boldsymbol{A}\cdot\boldsymbol{m}}{\rho}} \;=\; \sqrt{\frac{(\boldsymbol{m}\otimes\boldsymbol{n}) : \boldsymbol{C} : (\boldsymbol{m}\otimes\boldsymbol{n})}{\rho}}\,. \tag{1.20}$$

Thus, if $\boldsymbol{m}\cdot\boldsymbol{A}\cdot\boldsymbol{m} > 0$, the wave speeds are real and nonzero. If $\boldsymbol{m}\cdot\boldsymbol{A}\cdot\boldsymbol{m} \leq 0$, the wave speeds are imaginary or zero, and the governing equations become ill-posed as discussed in the previous section concerning the 1D problem. If isotropic linear elasticity is assumed, the tangent modulus tensor becomes

$$\boldsymbol{C} \;:=\; \boldsymbol{c}^e \;=\; \bar{\lambda}\,\mathbf{1}\otimes\mathbf{1} \,+\, 2\bar{\mu}\,\boldsymbol{I} \tag{1.21}$$

where $\bar{\lambda}$ and $\bar{\mu}$ are the Lamé parameters. Strong ellipticity then implies real, nonzero elastic wave speeds. Note that strong ellipticity does not imply pointwise stability (i.e., positive definiteness) of $\boldsymbol{C}$ (see [50]).

Loss of strong ellipticity in the sense of Hadamard [30] (expounded upon by Hill [32]) refers to the formation of a 'stationary discontinuity' (or standing wave) detected via the condition

$$\det \boldsymbol{A} \;=\; 0\,. \tag{1.22}$$

Rice [69] called Eq. (1.22) the condition for onset of localization, using a discontinuous deformation gradient rate as a point of departure.

In this work, loss of strong ellipticity will occur when Eq. (1.15) is not satisfied, and will specifically be the zero condition

$$(\boldsymbol{m}\otimes\boldsymbol{n}) : \boldsymbol{C} : (\boldsymbol{m}\otimes\boldsymbol{n}) \;=\; 0 \tag{1.23}$$

or

$$\boldsymbol{m}\cdot\boldsymbol{A}\cdot\boldsymbol{m} \;=\; 0\,. \tag{1.24}$$

Equation (1.24) is called the localization condition and arises naturally from the equilibrium requirement that traction be continuous across a discontinuity surface $\mathcal{S}$ (see Section 2.5.4).

It is important to note that Eq. (1.24) is only a *necessary* condition for the appearance of strain localization and for the detection of the bifurcation point. It is *not sufficient* because the plasticity problem needs to be formulated with strain localization in order for the strain localization to appear.

1.2 Methods for Numerical Modeling of Strain Localization

The motivation for rate-dependent strain softening approaches to modeling strain localization in inelastic materials has been touched upon in the previous section, and their finite element implementations were cited ([54], [46], [64], and [85]). Here in this section, however, approaches based on rate-independent strain softening plasticity models are only considered for the reasons stated at the end of Section 1.1.2.2.

Concurrent with the appearance of localized deformation is the loss of overall strength of the geomaterial body. Typically, rate-independent strain-softening plasticity models have been used to represent this overall 'softening' behavior in geomaterials like soil and rock [63]. It is well-known, however, that rate-independent strain-softening plasticity models lead to mesh-dependent finite element solutions because such models do not contain a material length scale needed to define the width of a localized deformation zone and because the associated governing partial differential equation is ill-posed [76]. In addition, the mesh alignment of standard finite elements has been shown to affect the simulated localized deformation pattern. Therefore, a more sophisticated numerical tool to represent the formation of slip surfaces and shear bands in geomaterials like soil and rock in a mesh-independent manner is in order.

The phenomenon of localized deformation has been studied as a material instability leading to a bifurcation in solution of the initial boundary value problem by HADAMARD [30], THOMAS [92], HILL [32], MANDEL [49], and RICE [69]. These works laid the foundation for determining a localization condition which detects the bifurcation point of solution, a condition used by many numerical modelers to determine when to include enhancements to the finite element displacement or strain interpolations. In this thesis, a model which leads to a bifurcated solution is used. This model will be introduced after a brief discussion of other numerical models which have been developed to simulate localized deformation.

Many attempts have been made to numerically model localized deformation using rate-independent, strain-softening plasticity models, but, in the absence of a material 'length scale,' adaptive remeshing, or other regularization technique, these attempts typically do not satisfy two necessary criteria for a finite element solution to be meaningful (i.e., mesh-independent): objectivity with respect to mesh refinement and insensitivity to mesh alignment. The length-scale approach for modeling localized deformation in a manner independent of element size was considered by PIETRUSZCZAK & MRÓZ [62], BAŽANT & LIN [9], and OLIVER [55], among others. The basic idea of incorporating a material length scale within the constitutive model and/or at the finite element level is to fix the width of the localized deformation zone since rate-independent plasticity models do not provide this information. Essentially, the introduction of a material length scale precludes a causal *a priori*-defined length scale of the associated mesh-size pathology; this *a priori*-defined length scale takes the form of the finite element diameter. From a purely numerical perspective, the adaptive remeshing approach for modeling localized deformation was considered by ZIENKIEWICZ & HUANG [102] and ZIENKIEWICZ et al. [103], among others. This approach does not consider local material instability but addresses the phenomenon of localized deformation solely via adaptive mesh strategies. The difficulty with this approach is that one needs to refine the mesh to the 'fine scale' of the physical manifestation of localized deformation in order to adequately represent the phenomenon. It would thus be more attractive to incorporate this 'fine scale' into a 'coarse scale' like a finite element mesh through a multiscale approach [36], [28]. The length-scale approach is multiscale but requires the *ad hoc* introduction of a material length scale and also typically does not sharply capture the orientation of the localized deformation pattern, unless combined with an enhanced finite element method like that of ORTIZ et al. [57], BELYTSCHKO et al. [10], or LEROY & ORTIZ [45]. On the other hand, it has been shown that rate-dependent plasticity models contain an implicit length scale which regularizes the mesh pathology associated with the rate-independent limit [46], [53], [54], [64], [76], [85]. Here, though, it is of interest to consider the rate-independent case directly. Other models which contain an implicit length scale are the higher-order gradient plasticity models [2], [21] and the micropolar continuum models [14], [20], [52]. For a review of some numerical models of localized deformation, consult STEIN et al. [87].

A previously-developed model which falls under the rubric of 'multiscale approach' represents localized deformation as a strong discontinuity (jump in displacement field) and is called the *strong discontinuity approach* in this thesis. The strong discontinuity approach referred to in this thesis is that developed by SIMO and co-workers [3], [4], [27], [82], [83] and yields mesh-independent finite element solutions without introducing a material length scale and without requiring special mesh alignment strategies. There have been other strong discontinuity approaches by WAN et al. [96], LARSSON et al. [43], and LARSSON et al. [44] in the sense that displacement jumps are treated directly rather than smeared into weak discontinuities (jump in strain field; see [39]); in [96], however, the weak discontinuity formulation is adopted to arrive at a localization condition. The strong discontinuity approach by Simo and co-workers is adopted in this thesis to formulate a rate-independent, non-associated, strain-softening Drucker-Prager plasticity model in the context of strong discontinuities and to implement this plasticity model along with an enhanced quadrilateral element within the framework of an assumed enhanced strain finite element method. The formulation and implementation are carried out for small deformations and rotations, and under drained condition (whereby the effect of pore-fluid influence is neglected) and quasi-static loading.

A brief review of the expected results of the strong discontinuity approach appears in Fig. 1.6 which is taken from the seminal paper by SIMO et al. [82]. This

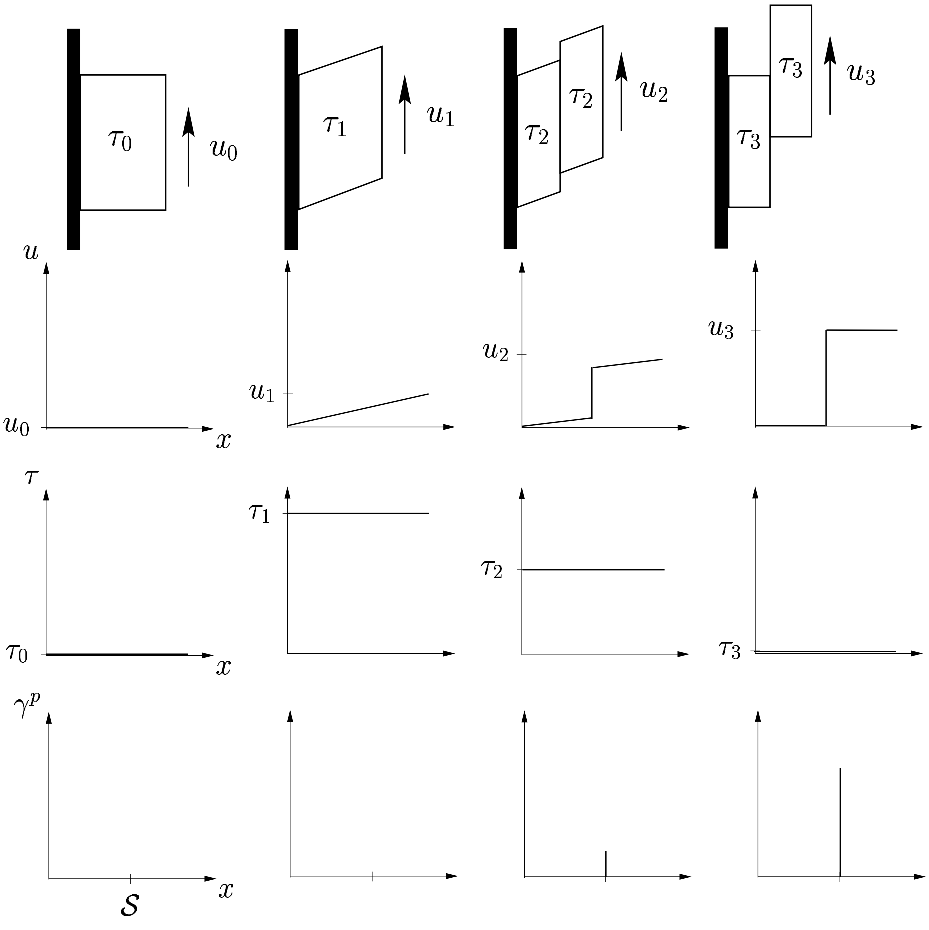

Figure 1.6. Results for 1D Problem taking Strong Discontinuity Approach (after SIMO et al. [82])

is a 1D shear problem showing the evolution of the jump in displacement u, the overall softening of the stress τ, and the localized plastic flow γ^p. Mesh-independence was observed. Note that the localized plastic flow in Fig. 1.6 is observable because in [82] the jump in displacement is regularized (i.e., continuous displacement and discontinuous strain over a 'small' width) as opposed to unregularized as in ARMERO & GARIKIPATI [3]. In this thesis, the unregularized formulation is adopted because it represents the actual jump in displacement and because it leads to a more robust numerical method [27].

1.3 Objectives

The objectives of this thesis are:

1. To formulate a non-associated, strain-softening Drucker-Prager plasticity model in the context of strong discontinuities in the manner of SIMO et al. [82] and ARMERO & GARIKIPATI [3] to be able to model, in a mesh-independent manner, geomaterials exhibiting localized deformation.

2. To implement the aforementioned plasticity model along with an enhanced quadrilateral element within the Assumed Enhanced Strain (AES) finite element method in the manner of SIMO & RIFAI [79] and ARMERO & GARIKIPATI [3].

3. To demonstrate mesh-independence for enhanced finite element solutions of softening plasticity, taking classical geotechnical problems under drained condition (i.e., pore fluid influence has no effect) like slope stability and top-down sequential excavation as numerical examples.

4. To simulate in a mesh-independent manner the occurence and effect of strain localization in actual experimental test specimens of soft rock.

5. To essentially espouse and extend the continuum plasticity and finite element framework developed in [3], [4], [27], [82], and [83] to be able to numerically simulate localized deformation in geomaterials in a mesh-independent manner, and to use this framework to incorporate the following capabilities in the future: modeling pore-fluid influence (see RUDNICKI [75] for background), modeling nonlinear geometric effects for Drucker-Prager plasticity with strong discontinuity, and modeling three-dimensional boundary value problems via implementation of an enhanced brick element.

Chapter 2

Non-associated, Infinitesimal, Rate-Independent Plasticity with Strong Discontinuity

2.1 Introduction

Geomaterials are predominantly frictional and dilatant in nature, with their friction and dilation angles typically not being equal, leading to non-associated plasticity models (see VERMEER & DE BORST [95]). Thus, in this chapter, a non-associated, rate-independent plasticity model is presented and formulated within the context of strong discontinuities in order to capture localized deformation at the local, material level. This general, non-associated plasticity model is specialized to a non-associated Drucker-Prager plasticity model.

2.2 Governing Equations with Discontinuity

Consider a closed body $\bar{\Omega} \subset \mathbb{R}^{n_{dim}}$ ($n_{dim} = 1,\ 2,\ \text{or}\ 3$) with smooth (i.e., C^1) internal discontinuity surface $\mathcal{S} \subset \mathbb{R}^{n_{dim}-1}$ as shown in Fig. 2.1. Let $\boldsymbol{x} \in \Omega$ denote the location of material particles $\boldsymbol{x}$ in Ω.

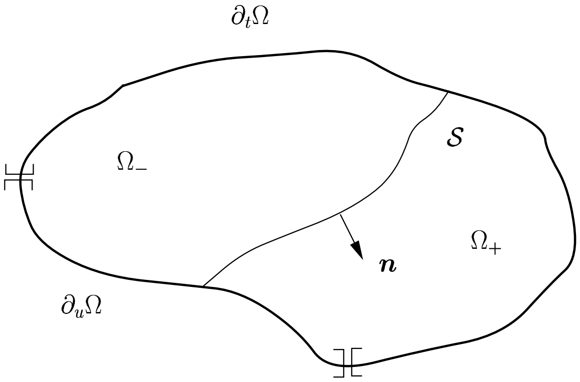

Figure 2.1. Body $\bar{\Omega}$ with discontinuity $\mathcal{S}$ ($\Omega = \Omega_+ \cup \Omega_-$, $\partial\Omega = \partial_t\Omega \cup \partial_u\Omega \cup \mathcal{S}$, $\bar{\Omega} = \Omega \cup \partial\Omega$).

The local (strong) form of the quasi-static, isothermal equilibrium equations may be expressed as follows [35]: Given $\boldsymbol{b} : \Omega \to \mathbb{R}^{n_{dim}}$, $\boldsymbol{t} : \partial_t\Omega \to \mathbb{R}^{n_{dim}}$, and $\boldsymbol{g} : \partial_u\Omega \to \mathbb{R}^{n_{dim}}$, find $\boldsymbol{u} : \bar{\Omega} \times [0,T] \to \mathbb{R}^{n_{dim}}$ (where $[0,T] \subset \mathbb{R}_+$ is the time interval of interest) such that

$$\begin{aligned} \boldsymbol{\nabla} \cdot \boldsymbol{\sigma} + \boldsymbol{b} &= \boldsymbol{0} \quad \text{in } \Omega \\ \boldsymbol{\sigma} \cdot \boldsymbol{\nu} &= \boldsymbol{t} \quad \text{on } \partial_t\Omega \\ \boldsymbol{u} &= \boldsymbol{g} \quad \text{on } \partial_u\Omega \\ [\![\boldsymbol{\sigma}]\!] \cdot \boldsymbol{n} = [\![\boldsymbol{t}_{\mathcal{S}}]\!] &= \boldsymbol{0} \quad \text{across } \mathcal{S} \end{aligned} \tag{2.1}$$

where $\boldsymbol{\sigma}$ is the Cauchy stress, $\boldsymbol{b}$ is the prescribed body force, $\boldsymbol{\nu}$ is the unit normal to $\partial_t\Omega$, $\boldsymbol{n}$ is the unit normal to $\mathcal{S}$, $\boldsymbol{t}$ is the prescribed traction, $\boldsymbol{g}$ is the prescribed displacement, and $[\![\bullet]\!]$ denotes the jump of a quantity across $\mathcal{S}$ (i.e., $[\![\boldsymbol{\sigma}]\!] = \boldsymbol{\sigma}^+ - \boldsymbol{\sigma}^-$). Refer to pg. 242 of MALVERN [48] for a brief discussion of discontinuity surfaces and their effect on the variational form of equilibrium. The expression "$\boldsymbol{b} : \Omega \rightarrow \mathbb{R}^{n_{dim}}$" states that for $\boldsymbol{x}$ in Ω, $\boldsymbol{b}(\boldsymbol{x})$ is in $\mathbb{R}^{n_{dim}}$ (the n_{dim} dimensional space of real numbers), where Ω is the domain of $\boldsymbol{b}$, and $\mathbb{R}^{n_{dim}}$ is its range. The fourth equation of Eq. (2.1) expresses the traction continuity across the discontinuity surface $\mathcal{S}$.

The variational (weak) form of the quasi-static equilibrium equations, using the strong form as a point of departure (or vice versa), may be expressed as follows [35]: Given $\boldsymbol{b} : \Omega \rightarrow \mathbb{R}^{n_{dim}}$, $\boldsymbol{t} : \partial_t\Omega \rightarrow \mathbb{R}^{n_{dim}}$, and $\boldsymbol{g} : \partial_u\Omega \rightarrow \mathbb{R}^{n_{dim}}$, find $\boldsymbol{u} \in \mathcal{U}$ such that for all $\boldsymbol{\eta} \in \mathcal{V}$,

$$\int_\Omega \boldsymbol{\nabla}^s\boldsymbol{\eta} : \boldsymbol{\sigma}\, d\Omega \;=\; \int_\Omega \boldsymbol{\eta}\cdot\boldsymbol{b}\, d\Omega \;+\; \int_{\partial_t\Omega} \boldsymbol{\eta}\cdot\boldsymbol{t}\, d\Gamma \;+\; \int_{\mathcal{S}} \boldsymbol{\eta}\cdot(\llbracket\boldsymbol{\sigma}\rrbracket\cdot\boldsymbol{n})\, d\Gamma \tag{2.2}$$

where $\boldsymbol{\eta}$ is the weighting function. The space of admissible weighting functions is

$$\mathcal{V} \;:=\; \{\boldsymbol{\eta} : \Omega \rightarrow \mathbb{R}^{n_{dim}}\;;\; \boldsymbol{\eta} = \boldsymbol{0} \text{ on } \partial_u\Omega\}\;, \tag{2.3}$$

and the space of admissible trial solutions is defined as

$$\mathcal{U} \;:=\; \left\{\boldsymbol{u} : \bar{\Omega} \rightarrow \mathbb{R}^{n_{dim}}\;;\; \boldsymbol{u} = \boldsymbol{g} \text{ on } \partial_u\Omega\right\}\;. \tag{2.4}$$

Notice that in Eq. (2.2) traction continuity across the discontinuity surface $\mathcal{S}$ is required for equilibrium to be satisfied.

2.3 Kinematics of Strong Discontinuities

It was proven for rate-independent, infinitesimal, perfect plasticity that discontinuous displacement fields are admissible solutions to the boundary value problem—as setup in Section 2.2—and are contained within the bounded deformation (BD) space (see Matthies et al. [51], Temam & Strang [91], Strang et al. [88], and Suquet [89]).

The infinitesimal strains are singular distributions, which are contained within the space of bounded measures because the integral of the Dirac-delta function is a finite measurable quantity. This work by [51], [91], [88], and [89] was the motivation for formulating the proper framework for softening plasticity with strong discontinuity in Simo et al. [82]. In Section 2.5.4, a localization condition is formulated which detects the inception of such discontinuous displacements.

Define the discontinuous displacement field as follows

$$\boldsymbol{u}(\boldsymbol{x},t) = \underbrace{\bar{\boldsymbol{u}}(\boldsymbol{x},t)}_{\text{continuous}} + \underbrace{[\![\boldsymbol{u}(t)]\!]\, H_{\mathcal{S}}(\boldsymbol{x})}_{\text{discontinuous}} \tag{2.5}$$

where $[\![\boldsymbol{u}]\!] = \boldsymbol{u}^{+} - \boldsymbol{u}^{-} = \zeta \boldsymbol{m}$ is the jump in displacement across the discontinuity surface $\mathcal{S}$ and is independent of $\boldsymbol{x}$, ζ is the jump magnitude, $\boldsymbol{m}$ is the unit vector designating the jump direction, and $H_{\mathcal{S}}(\boldsymbol{x})$ is the Heaviside function defined as

$$H_{\mathcal{S}}(\boldsymbol{x}) = \begin{cases} 1 & \text{if } \boldsymbol{x} \in \Omega_{+} \\ 0 & \text{if } \boldsymbol{x} \in \Omega_{-} \end{cases} \tag{2.6}$$

It is possible for $[\![\boldsymbol{u}]\!]$ to vary along the discontinuity $\mathcal{S}$, but here it is considered constant with respect to $\boldsymbol{x}$. Taking the symmetric gradient of the displacement field in Eq. (2.5) and treating the Dirac-delta function as a distribution (see Appendix B), the small strain tensor results

$$\boldsymbol{\epsilon} := \boldsymbol{\nabla}^{s}\boldsymbol{u} = \underbrace{\boldsymbol{\nabla}^{s}\bar{\boldsymbol{u}}}_{\text{regular}} + \underbrace{([\![\boldsymbol{u}]\!] \otimes \boldsymbol{n})^{s}\delta_{\mathcal{S}}}_{\text{singular}} \tag{2.7}$$

where $\boldsymbol{n}$ is the unit normal to the discontinuity surface $\mathcal{S}$ pointing into Ω_{+} (see Fig. 2.1), and $\delta_{\mathcal{S}}$ is the Dirac-delta function on $\mathcal{S}$. Essentially, Appendix B yields $\boldsymbol{\nabla} H_{\mathcal{S}} = \boldsymbol{n}\delta_{\mathcal{S}}$. It is important that the Dirac-delta function be treated in the distributional framework throughout the formulation of a plasticity model with strong discontinuity.

2.4 Standard Infinitesimal Non-associated Plasticity

Here, a standard non-associated plasticity model is formulated in the small strain regime. Refer to SIMO & HUGHES [80] for a detailed discussion of the formulation and numerical implementation of plasticity models.

Consider a convex elastic domain $\mathbb{E}$ defined by a smooth (i.e., C^1 continuous) yield surface $\phi : \mathbb{S} \times \mathbb{R}^m \to \mathbb{R}$ in the Cauchy stress space $\boldsymbol{\sigma} : \Omega \times [0,T] \to \mathbb{S}$ as

$$\mathbb{E} \ := \ \{(\boldsymbol{\sigma}, \boldsymbol{\alpha}) \in \mathbb{S} \times \mathbb{R}^m \mid \phi(\boldsymbol{\sigma}, \boldsymbol{\alpha}) \leq 0\} \tag{2.8}$$

where $[0,T]$ is the time increment of interest, $\mathbb{S}$ is the space of symmetric second order tensors, and $\boldsymbol{\alpha} : \Omega \times [0,T] \to \mathbb{R}^m$ is the stress-like vector of plastic internal variables of dimension m characterizing the hardening response of the material. The constitutive equation is expressed in terms of a stored energy density function $\Psi(\boldsymbol{\epsilon}^e, \boldsymbol{\xi}) : \mathbb{S} \times \mathbb{R}^m \to \mathbb{R}$, where $\boldsymbol{\epsilon}^e : \Omega \to \mathbb{S}$ is the elastic part of the infinitesimal strain tensor, and $\boldsymbol{\xi} : \Omega \times [0,T] \to \mathbb{R}^m$ is the strain-like vector of plastic internal variables, which is (energy) conjugate to $\boldsymbol{\alpha}$. The constitutive equations are then defined via consideration of the First and Second Laws of Thermodynamics in the manner of LUBLINER [47] as

$$\boldsymbol{\sigma} \ = \ \frac{\partial \Psi(\boldsymbol{\epsilon}^e, \boldsymbol{\xi})}{\partial \boldsymbol{\epsilon}^e} \, ; \quad \boldsymbol{\alpha} \ = \ -\frac{\partial \Psi(\boldsymbol{\epsilon}^e, \boldsymbol{\xi})}{\partial \boldsymbol{\xi}} \, . \tag{2.9}$$

For the linearized theory (i.e., infinitesimal strains) the strain tensor is additively decomposed into elastic and plastic parts:

$$\boldsymbol{\epsilon} \ = \ \boldsymbol{\epsilon}^e + \boldsymbol{\epsilon}^p \, . \tag{2.10}$$

The plastic strain rate $\dot{\boldsymbol{\epsilon}}^p : \Omega \times [0,T] \to \mathbb{S}$ is defined via the flow rule as

$$\dot{\boldsymbol{\epsilon}}^p = \lambda \frac{\partial \varphi(\boldsymbol{\sigma}, \boldsymbol{\alpha})}{\partial \boldsymbol{\sigma}} \tag{2.11}$$

where $\lambda : \Omega \times [0, T] \rightarrow \mathbb{R}$ is the plastic consistency parameter, and $\varphi(\boldsymbol{\sigma}, \boldsymbol{\alpha}) : \mathbb{S} \times \mathbb{R}^m \rightarrow \mathbb{R}$ is the plastic potential function, which is not necessarily equal to $\phi(\boldsymbol{\sigma}, \boldsymbol{\alpha})$. Associative plasticity results if $\partial_{\boldsymbol{\sigma}} \varphi = \partial_{\boldsymbol{\sigma}} \phi$ and associative hardening if $\partial_{\boldsymbol{\alpha}} \varphi = \partial_{\boldsymbol{\alpha}} \phi$. As mentioned previously, for frictional materials like soil and rock, plasticity models are non-associative because the dilation angle is experimentally observed to be less than the friction angle, making $\partial_{\boldsymbol{\sigma}} \varphi \neq \partial_{\boldsymbol{\sigma}} \phi$ (as will be demonstrated in Section 2.6.1). Non-associated plasticity models violate Drucker's stability postulate [22], but make physical sense with respect to a calculation of dissipation for a cohesionless, perfectly-plastic material [95]. The evolution equations for $\boldsymbol{\epsilon}^e$ and $\boldsymbol{\xi}$ are defined as

$$\dot{\boldsymbol{\epsilon}}^e = \dot{\boldsymbol{\epsilon}} - \lambda \frac{\partial \varphi}{\partial \boldsymbol{\sigma}}, \quad \dot{\boldsymbol{\xi}} = \lambda \frac{\partial \varphi}{\partial \boldsymbol{\alpha}}. \tag{2.12}$$

The classical Kuhn-Tucker complementary conditions for loading and unloading apply:

$$\lambda \geq 0; \quad \phi(\boldsymbol{\sigma}, \boldsymbol{\alpha}) \leq 0; \quad \lambda \phi(\boldsymbol{\sigma}, \boldsymbol{\alpha}) = 0 \tag{2.13}$$

as well as the consistency condition

$$\dot{\phi} = 0, \quad \lambda > 0 \tag{2.14}$$

which states that plastic flow must persist on the yield surface. Applying the chain rule to the consistency condition in Eq. (2.14), the following results

$$\dot{\phi} = \frac{\partial \phi}{\partial \boldsymbol{\sigma}} : \dot{\boldsymbol{\sigma}} + \frac{\partial \phi}{\partial \boldsymbol{\alpha}} \cdot \dot{\boldsymbol{\alpha}} = 0. \tag{2.15}$$

Recall the constitutive equations from Eq. (2.9) and express them in rate form as

$$\dot{\boldsymbol{\sigma}} \;=\; \boldsymbol{C} : \dot{\boldsymbol{\epsilon}}^e \,; \quad \dot{\boldsymbol{\alpha}} \;=\; -\boldsymbol{H} \cdot \dot{\boldsymbol{\xi}} \tag{2.16}$$

where

$$\boldsymbol{C} \;=\; \frac{\partial^2 \Psi(\boldsymbol{\epsilon}^e, \boldsymbol{\xi})}{\partial \boldsymbol{\epsilon}^e \partial \boldsymbol{\epsilon}^e} \,, \quad \boldsymbol{H} \;=\; \frac{\partial^2 \Psi(\boldsymbol{\epsilon}^e, \boldsymbol{\xi})}{\partial \boldsymbol{\xi} \partial \boldsymbol{\xi}} \tag{2.17}$$

are the symmetric Hessian tensors of $\Psi(\boldsymbol{\epsilon}^e, \boldsymbol{\xi})$ evaluated with respect to $\boldsymbol{\epsilon}^e$ and $\boldsymbol{\xi}$, respectively. The fourth order tensor $\boldsymbol{C}$ is the tangential elastic modulus tensor, and the second order tensor $\boldsymbol{H}$ is the tangential plastic modulus matrix. For linear elasticity and linear hardening, $\boldsymbol{C}$ and $\boldsymbol{H}$ would be constant. Substituting Eq. (2.12) into Eq. (2.16) and then Eq. (2.16) into Eq. (2.15) the plastic consistency parameter is solved for:

$$\lambda \;=\; \frac{\partial_{\boldsymbol{\sigma}} \phi : \boldsymbol{C} : \dot{\boldsymbol{\epsilon}}}{\partial_{\boldsymbol{\sigma}} \phi : \boldsymbol{C} : \partial_{\boldsymbol{\sigma}} \varphi \,+\, \mathcal{H}} \tag{2.18}$$

where

$$\mathcal{H} = \partial_{\boldsymbol{\alpha}} \phi \cdot \boldsymbol{H} \cdot \partial_{\boldsymbol{\alpha}} \varphi \,. \tag{2.19}$$

The continuum elastic-plastic tangent modulus tensor may then be derived as

$$\boldsymbol{C}^{ep} \;=\; \boldsymbol{C} \,-\, \frac{\boldsymbol{C} : \partial_{\boldsymbol{\sigma}} \varphi \otimes \partial_{\boldsymbol{\sigma}} \phi : \boldsymbol{C}}{\partial_{\boldsymbol{\sigma}} \phi : \boldsymbol{C} : \partial_{\boldsymbol{\sigma}} \varphi \,+\, \mathcal{H}} \,. \tag{2.20}$$

With the standard, non-associated plasticity model in place, the formulation of the plasticity model in the context of strong discontinuituies will proceed.

2.5 Non-associated Plasticity with Strong Discontinuity

In this section, plastic dissipation, a stress-displacement relation, and a localization condition will be formulated for a general, non-associated plasticity model with strong discontinuity in the infinitesimal strain regime. In the next section the model will be specialized for a Drucker-Prager plasticity model.

2.5.1 Localized Plastic Flow

For hardening, associative plasticity ($\mathcal{H} > 0$ from Eq. (2.19)) λ is regular, and the setting for standard plasticity as outlined in Section 2.4 holds. For softening or perfect plasticity ($\mathcal{H} \leq 0$), however, it is possible for displacements to be discontinuous and for λ to be *singular*, as described in Section 2.3; note that—although not rigorously proven in the manner of [51]—discontinuous displacements may be detected via the localization condition for non-associative hardening plasticity. When discontinuous displacements are present within a material body (detected via the localization condition; see Eq. (2.45)), the strains are singular at the discontinuity $\mathcal{S}$, plastic flow is localized to the discontinuity $\mathcal{S}$ [82], and the plastic consistency parameter λ is a singular distribution

$$\lambda = \lambda_\delta \, \delta_{\mathcal{S}} \, . \tag{2.21}$$

Equation (2.21) states that all further irrecoverable deformation occurs along the discontinuity $\mathcal{S}$ as the body outside the discontinuity unloads elastically. Equation (2.21) is the key to the remaining formulation of a non-associated plasticity model with strong discontinuity.

2.5.2 Plastic Dissipation

A derivation of plastic dissipation with strong discontinuity yields three important results: 1) the stress rate $\dot{\boldsymbol{\sigma}}$ must be regular, 2) the rate of the stress-like vector of plastic internal variables $\dot{\boldsymbol{\alpha}}$ must be regular, and 3) a finite element analysis will calculate mesh-independent dissipation for localized softening problems.

Recall the definition of plastic dissipation resulting from the Second Law of Thermodynamics in the form of the Clausius-Duhem inequality for an isothermal solid (Lubliner [47], Simo [84]):

$$\mathcal{D} \; := \; \boldsymbol{\sigma} : \dot{\boldsymbol{\epsilon}} \; - \; \dot{\Psi}(\boldsymbol{\epsilon}^e, \boldsymbol{\xi})\,. \tag{2.22}$$

See Appendix A for a discussion of plastic dissipation in one-dimension. The term $\boldsymbol{\sigma} : \dot{\boldsymbol{\epsilon}}$ is the stress power, and, for quasi-static problems, it is the total external power input into the system

$$\int_\Omega \boldsymbol{\sigma} : \dot{\boldsymbol{\epsilon}}\, d\Omega \; = \; \int_\Omega \boldsymbol{\sigma} : \boldsymbol{\nabla}^s \dot{\boldsymbol{u}}\, d\Omega \; = \; \int_\Omega \boldsymbol{b} \cdot \dot{\boldsymbol{u}}\, d\Omega \; + \; \int_{\partial_t \Omega} \boldsymbol{t} \cdot \dot{\boldsymbol{u}}\, d\Gamma\,. \tag{2.23}$$

From Eq. (2.7), the strain rate $\dot{\boldsymbol{\epsilon}}$ has a singular part. If $\dot{\boldsymbol{\sigma}}$ also has a singular part, the calculation of the stress power (and, in turn, the dissipation) would not be possible since the product of two Dirac-delta functions is undefineable. Thus, it is required that the stress rate be *regular* [82]. Decomposing the stress rate into its regular and singular parts yields

$$\dot{\boldsymbol{\sigma}} \; = \; \dot{\bar{\boldsymbol{\sigma}}} \; + \; \dot{\boldsymbol{\sigma}}_\delta \delta_{\mathcal{S}} \tag{2.24}$$

where

$$\dot{\bar{\boldsymbol{\sigma}}} \;\; = \;\; \boldsymbol{C} : \boldsymbol{\nabla}^s \dot{\bar{\boldsymbol{u}}}$$

$$\dot{\boldsymbol{\sigma}}_{\delta} \;=\; \boldsymbol{C} : ((\llbracket \dot{\boldsymbol{u}} \rrbracket \otimes \boldsymbol{n})^{s} \;-\; \lambda_{\delta}\partial_{\boldsymbol{\sigma}}\varphi) \;. \tag{2.25}$$

A regular stress rate requires $\dot{\boldsymbol{\sigma}}_{\delta} = \boldsymbol{0}$, which implies

$$\dot{\boldsymbol{\sigma}} \;=\; \dot{\bar{\boldsymbol{\sigma}}} \;=\; \boldsymbol{C} : \boldsymbol{\nabla}^{s}\dot{\bar{\boldsymbol{u}}} \tag{2.26}$$

and

$$(\llbracket \dot{\boldsymbol{u}} \rrbracket \otimes \boldsymbol{n})^{s} \;=\; \lambda_{\delta}\partial_{\boldsymbol{\sigma}}\varphi \,. \tag{2.27}$$

Continuing with the calculation of plastic dissipation, the stored energy rate is expressed as follows

$$\dot{\Psi}(\boldsymbol{\epsilon}^{e}, \boldsymbol{\xi}) \;=\; \boldsymbol{\sigma} : \dot{\boldsymbol{\epsilon}} \;-\; \lambda(\boldsymbol{\sigma} : \partial_{\boldsymbol{\sigma}}\varphi \;+\; \boldsymbol{\alpha}\cdot\partial_{\boldsymbol{\alpha}}\varphi) \,. \tag{2.28}$$

Thus, the rate of dissipation is

$$\mathcal{D} \;=\; \lambda(\boldsymbol{\sigma} : \partial_{\boldsymbol{\sigma}}\varphi \;+\; \boldsymbol{\alpha}\cdot\partial_{\boldsymbol{\alpha}}\varphi) \;=\; \mathcal{D}_{\delta}\,\delta_{\mathcal{S}} \tag{2.29}$$

since $\lambda = \lambda_{\delta}\delta_{\mathcal{S}}$. The rate of dissipation is a density quantity, and, as a result, the total rate of dissipation over a region Ω is calculated as

$$\mathcal{D}_{\Omega} \;=\; \int_{\Omega} \mathcal{D}\, d\Omega \;=\; \int_{\mathcal{S}} \lambda_{\delta}(\boldsymbol{\sigma} : \partial_{\boldsymbol{\sigma}}\varphi \;+\; \boldsymbol{\alpha}\cdot\partial_{\boldsymbol{\alpha}}\varphi)\, d\Gamma \,. \tag{2.30}$$

Notice that the total rate of dissipation is calculated over a set of zero measure, the discontinuity surface $\mathcal{S}$.

Using a similar argument as that used for regularity of the stress $\boldsymbol{\sigma}$ from Eq. (2.24), in order for a calculation of dissipation in Eq. (2.29) to make sense, the stress-like vector of plastic internal variables $\boldsymbol{\alpha}$ must also be regular. From Eq. (2.16) and Eq. (2.21), $\dot{\boldsymbol{\alpha}}$ may be written as

$$\dot{\boldsymbol{\alpha}} \;=\; -\boldsymbol{H}\cdot\dot{\boldsymbol{\xi}} \;=\; -\lambda_{\delta}\boldsymbol{H}\cdot\partial_{\boldsymbol{\alpha}}\varphi\delta_{\mathcal{S}} \tag{2.31}$$

or

$$\boldsymbol{H}^{-1} \cdot \dot{\boldsymbol{\alpha}} = -\lambda_\delta \partial_{\boldsymbol{\alpha}} \varphi \delta_{\mathcal{S}} \,. \tag{2.32}$$

A significant observation made in Simo et al. [82] states that since $\dot{\boldsymbol{\alpha}}$ must be regular, the inverse of the softening moduli matrix must itself be a singular distribution

$$\boldsymbol{H}^{-1} = \boldsymbol{H}_\delta^{-1} \delta_{\mathcal{S}} \tag{2.33}$$

which states that softening is localized to the discontinuity $\mathcal{S}$. As a result of Eq. (2.33), the following results

$$\dot{\boldsymbol{\alpha}} = -\lambda_\delta \boldsymbol{H}_\delta \cdot \partial_{\boldsymbol{\alpha}} \varphi \,. \tag{2.34}$$

Thus, as a result of $\lambda = \lambda_\delta \delta_{\mathcal{S}}$, the evolution of the internal variables is localized to the discontinuity $\mathcal{S}$. This result of the strong discontinuity approach could be viewed as a rather 'strong' approximation for some materials (i.e., those which exhibit shear bands of finite width), in the sense that irrecoverable deformation is most likely not completely localized to a surface (except possibly for brittle rock, in which a clear rupture surface is present [98]).

A finite element model which draws its constitutive behavior from a plasticity model with strong discontinuity will calculate mesh-independent dissipation because the total rate of dissipation is calculated over a set of zero measure and not over any *a priori* defined element size.

2.5.3 Consistency Condition and Stress-Displacement Relation

The consistency condition $\dot{\phi} = 0$ must be satisfied pointwise, thus any singularities which arise in $\dot{\phi}$ must be eliminated. Recall Eq. (2.15)

$$\dot{\phi} \;=\; \partial_{\boldsymbol{\sigma}}\phi : \dot{\boldsymbol{\sigma}} \;+\; \partial_{\boldsymbol{\alpha}}\phi \cdot \dot{\boldsymbol{\alpha}} \;=\; 0\,. \tag{2.35}$$

From Section 2.5.2 on plastic dissipation, note that $\dot{\boldsymbol{\sigma}}$ and $\dot{\boldsymbol{\alpha}}$ are regular distributions in order for a calculation of plastic dissipation to be possible, which here also implies that the consistency condition Eq. (2.15) is satisfied pointwise (i.e., contains no singularities). Substituting the regular expressions for $\dot{\boldsymbol{\sigma}}$ and $\dot{\boldsymbol{\alpha}}$ into Eq. (2.35), λ_δ is solved as

$$\lambda_\delta \;=\; \mathcal{H}_\delta^{-1}\partial_{\boldsymbol{\sigma}}\phi : \boldsymbol{C} : \boldsymbol{\nabla}^s\dot{\bar{\boldsymbol{u}}} \tag{2.36}$$

where $\mathcal{H}_\delta = \partial_{\boldsymbol{\alpha}}\phi \cdot \boldsymbol{H}_\delta \cdot \partial_{\boldsymbol{\alpha}}\varphi$. Premultiply Eq. (2.27) by $\partial_{\boldsymbol{\sigma}}\phi : \boldsymbol{C}$ to find an equivalent expression for λ_δ:

$$\lambda_\delta \;=\; \dot{\zeta}\,\frac{\partial_{\boldsymbol{\sigma}}\phi : \boldsymbol{C} : (\boldsymbol{m}\otimes\boldsymbol{n})^s}{\partial_{\boldsymbol{\sigma}}\phi : \boldsymbol{C} : \partial_{\boldsymbol{\sigma}}\varphi} \tag{2.37}$$

where $[\![\dot{\boldsymbol{u}}]\!] = \dot{\zeta}\boldsymbol{m}$. Equating Eq. (2.36) and Eq. (2.37) gives an expression for the magnitude of the jump displacement rate:

$$\dot{\zeta} \;=\; \frac{(\partial_{\boldsymbol{\sigma}}\phi : \boldsymbol{C} : \partial_{\boldsymbol{\sigma}}\varphi)(\partial_{\boldsymbol{\sigma}}\phi : \boldsymbol{C} : \boldsymbol{\nabla}^s\dot{\bar{\boldsymbol{u}}})}{\mathcal{H}_\delta(\partial_{\boldsymbol{\sigma}}\phi : \boldsymbol{C} : (\boldsymbol{m}\otimes\boldsymbol{n})^s)} \tag{2.38}$$

Equation (2.38) may be simplified using results from the localization condition.

2.5.4 Localization Condition

Here, a condition which detects the presence of discontinuous displacements is derived and called the localization condition. Equation (2.2) showed that for equilibrium to be satisfied, the traction must be continuous across the discontinuity surface $\mathcal{S}$:

$$[\![\dot{\boldsymbol{\sigma}}]\!] \cdot \boldsymbol{n} \;=\; \left[\left[\dot{\boldsymbol{t}}_{\mathcal{S}}\right]\right] \;=\; \boldsymbol{0}\,. \tag{2.39}$$

The discussion in Section 2.5.2 showed that the stress rate must be regular. Either of these two conditions (the traction must be continuous, and the stress rate is regular) require that the traction rate be regular. Write the traction rate as follows

$$\dot{\boldsymbol{t}} \;=\; \dot{\boldsymbol{\sigma}} \cdot \boldsymbol{n} \;=\; \boldsymbol{C} : (\dot{\boldsymbol{\epsilon}} - \lambda \partial_{\boldsymbol{\sigma}} \varphi) \cdot \boldsymbol{n} \;=\; \dot{\bar{\boldsymbol{t}}} + \dot{\boldsymbol{t}}_\delta \delta_{\mathcal{S}} \tag{2.40}$$

where

$$\dot{\bar{\boldsymbol{t}}} \;=\; \boldsymbol{C} : \boldsymbol{\nabla}^s \dot{\bar{\boldsymbol{u}}} \cdot \boldsymbol{n} \tag{2.41}$$

is the regular part, and

$$\dot{\boldsymbol{t}}_\delta \;=\; \dot{\zeta} \boldsymbol{C}^{ep} : (\boldsymbol{m} \otimes \boldsymbol{n})^s \cdot \boldsymbol{n} \tag{2.42}$$

is the singular part (using λ_δ from Eq. (2.37)), with

$$\boldsymbol{C}^{ep} \;=\; \boldsymbol{C} - \frac{\boldsymbol{C} : \partial_{\boldsymbol{\sigma}} \varphi \otimes \partial_{\boldsymbol{\sigma}} \phi : \boldsymbol{C}}{\partial_{\boldsymbol{\sigma}} \phi : \boldsymbol{C} : \partial_{\boldsymbol{\sigma}} \varphi} \tag{2.43}$$

representing the elastic perfectly-plastic tangent modulus tensor. For the traction rate to be regular

$$\dot{\boldsymbol{t}}_\delta \;=\; \boldsymbol{0} \tag{2.44}$$

which leads to the localization condition

$$\boldsymbol{A} \cdot \boldsymbol{m} \;=\; \boldsymbol{0}\,; \quad \boldsymbol{A} \;=\; \boldsymbol{n} \cdot \boldsymbol{C}^{ep} \cdot \boldsymbol{n} \tag{2.45}$$

where $\boldsymbol{A}$ is the second order elastic perfectly-plastic acoustic tensor. The localization condition requires that $\boldsymbol{m}$ lies in the nullspace of $\boldsymbol{A}$, and likewise that $\boldsymbol{m} \otimes \boldsymbol{n}$ lies in the nullspace of $\boldsymbol{C}^{ep}$. Recall from Eq. (2.27) that

$$(\boldsymbol{m} \otimes \boldsymbol{n})^s \;=\; \Lambda \partial_{\boldsymbol{\sigma}} \varphi \tag{2.46}$$

where $\Lambda = \lambda_\delta / \dot{\zeta}$; Λ for this analysis can be any real number. It is straightforward to show that $\partial_{\boldsymbol{\sigma}}\varphi$ lies in the nullspace of $\boldsymbol{C}^{ep}$:

$$\boldsymbol{C}^{ep} : \partial_{\boldsymbol{\sigma}}\varphi \;=\; \boldsymbol{C} : \partial_{\boldsymbol{\sigma}}\varphi \;-\; \boldsymbol{C} : \partial_{\boldsymbol{\sigma}}\varphi \frac{\partial_{\boldsymbol{\sigma}}\phi : \boldsymbol{C} : \partial_{\boldsymbol{\sigma}}\varphi}{\partial_{\boldsymbol{\sigma}}\phi : \boldsymbol{C} : \partial_{\boldsymbol{\sigma}}\varphi} \;=\; \boldsymbol{0}\,. \tag{2.47}$$

Note that $\boldsymbol{C}^{ep}$ is the elastic *perfectly-plastic* tangent modulus tensor, and thus a derivation of a critical hardening modulus $\mathcal{H}_{\mathrm{cr}}$ similar to that derived by RUDNICKI & RICE [73] is not possible. Also note that the trace of Eq. (2.46) leads to an expression for the angle made by the jump rate vector $[\![\dot{\boldsymbol{u}}]\!] = \dot{\zeta}\boldsymbol{m}$ and the tangent to the slip line $\mathcal{S}$ (see Fig. 2.2), called the jump dilation angle ψ:

$$\sin\psi \;:=\; \boldsymbol{m}\cdot\boldsymbol{n} \;=\; \Lambda \mathrm{tr}(\partial_{\boldsymbol{\sigma}}\varphi)\,. \tag{2.48}$$

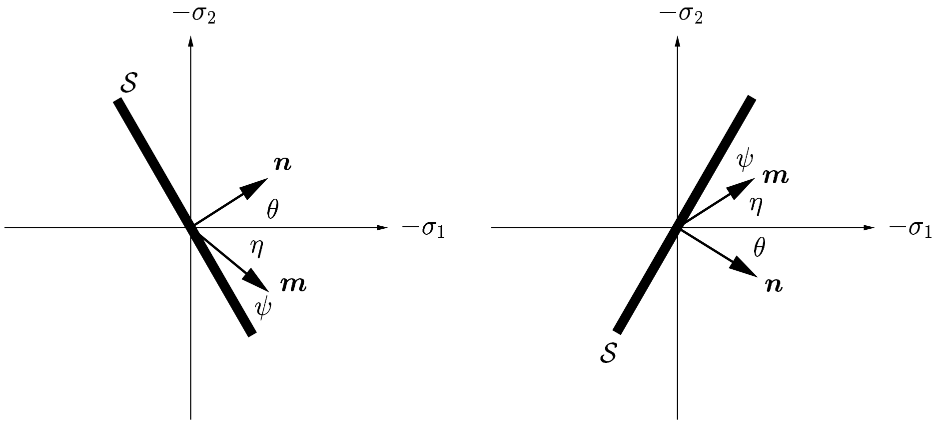

Figure 2.2. Slip line orientation with respect to major principal stress axis for $\pm\theta$.

Equation (2.48) will be used to determine the orientation of $\boldsymbol{m}$ when the plastic potential function φ is specified for a particular plasticity model; this will be done for a Drucker-Prager plasticity model in Section 2.6. Thus, another way of writing Eq. (2.38) for $\dot{\zeta}$, using Eq. (2.36) for λ_δ and Eq. (2.48) to find $\dot{\zeta}$, is as follows

$$\dot{\zeta} \;=\; \frac{\mathrm{tr}(\partial_{\boldsymbol{\sigma}}\varphi)}{\mathcal{H}_\delta \boldsymbol{m}\cdot\boldsymbol{n}} \partial_{\boldsymbol{\sigma}}\phi : \dot{\boldsymbol{\sigma}}\,. \tag{2.49}$$

Equation (2.49) will be used to derive the stress-displacement relation for a Drucker-Prager plasticity model in Section 2.6.2.2.

2.6 Drucker-Prager Plasticity with Strong Discontinuity

The formulation of the preceding section is now specialized for a non-associated Drucker-Prager plasticity model. First, the standard Drucker-Prager plasticity model is described.

2.6.1 Standard Drucker-Prager Plasticity

A quadratic stored energy function $\Psi(\boldsymbol{\epsilon}^e, \boldsymbol{\xi})$, which results in linear elasticity and linear hardening, is defined as

$$\Psi(\boldsymbol{\epsilon}^e, \boldsymbol{\xi}) \; := \; \frac{1}{2}\boldsymbol{\epsilon}^e : \boldsymbol{c}^e : \boldsymbol{\epsilon}^e \, + \, \frac{1}{2}\boldsymbol{\xi} \cdot \boldsymbol{H} \cdot \boldsymbol{\xi} \tag{2.50}$$

where $\boldsymbol{c}^e$ and $\boldsymbol{H}$ are constant modulus tensors. Note that $\Psi(\boldsymbol{\epsilon}^e, \boldsymbol{\xi})$ could be defined such that nonlinear elasticity and/or hardening would result. The fourth order tensor $\boldsymbol{c}^e$ is the isotropic elastic tangent modulus tensor defined as

$$\boldsymbol{c}^e \; = \; \bar{K}\, \mathbf{1} \otimes \mathbf{1} \, + \, 2\bar{\mu}\, (\boldsymbol{I} - \frac{1}{3}\mathbf{1} \otimes \mathbf{1}) \tag{2.51}$$

where $\bar{K} = \bar{\lambda} + \frac{2}{3}\bar{\mu}$ is the elastic bulk modulus, $\bar{\lambda}$ and $\bar{\mu}$ are the Lamé parameters, $(\mathbf{1})_{ij} = \delta_{ij}$ is the Kronecker delta, and $(\boldsymbol{I})_{ijkl} = (\delta_{ik}\delta_{jl} + \delta_{il}\delta_{jk})/2$ is the fourth order identity tensor.

Let the strain-like vector of plastic internal variables $\boldsymbol{\xi} : \Omega \times [0, T] \rightarrow \mathbb{R}^2$ have a volumetric component and deviatoric component:

$$\boldsymbol{\xi} := \left\{ \begin{array}{c} v^p \\ e^p \end{array} \right\} \tag{2.52}$$

where

$$\dot{v}^p = \mathrm{tr}(\dot{\boldsymbol{\epsilon}}^p)\,; \quad \dot{e}^p = \sqrt{\frac{2}{3}}\|\dot{\boldsymbol{e}}^p\|\,; \quad \dot{\boldsymbol{e}}^p = \dot{\boldsymbol{\epsilon}}^p - (\dot{v}^p/3)\mathbf{1} \tag{2.53}$$

and

$$v^p = \int_0^T \dot{v}^p\,dt\,; \quad e^p = \int_0^T \dot{e}^p\,dt\,. \tag{2.54}$$

The hardening/softening modulus matrix $\boldsymbol{H}$ is defined as

$$\boldsymbol{H} := \left[\begin{array}{cc} K' & 0 \\ 0 & H' \end{array} \right] \tag{2.55}$$

where K' and H' are the bulk and shear hardening/softening moduli, respectively. The stress-like vector of plastic internal variables $\boldsymbol{\alpha}$ is defined as

$$\boldsymbol{\alpha} := \left\{ \begin{array}{c} \alpha_1 \\ \alpha_2 \end{array} \right\} = -\boldsymbol{H}\cdot\boldsymbol{\xi}\,. \tag{2.56}$$

Note that the sign on $\boldsymbol{\alpha}$ implies that, when added to the yield function $\phi(\boldsymbol{\sigma}, \boldsymbol{\alpha})$, $\boldsymbol{\alpha}$ with hardening plasticity ($K' > 0$, $H' > 0$) causes the yield surface to expand in stress space.

A Drucker-Prager yield function [23] takes the form

$$\phi(\boldsymbol{\sigma}, \boldsymbol{\alpha}) = \sqrt{\frac{3}{2}}\|\boldsymbol{s}\| + \sqrt{3}(\kappa + \beta p) = 0 \tag{2.57}$$

with derivatives

$$\frac{\partial \phi}{\partial \boldsymbol{\sigma}} = \sqrt{\frac{3}{2}}\hat{\boldsymbol{n}} + \frac{1}{\sqrt{3}}\beta \mathbf{1}\,, \quad \frac{\partial \phi}{\partial \boldsymbol{\alpha}} = \left\{ \begin{array}{c} \sqrt{3}b \\ 1 \end{array} \right\} \tag{2.58}$$

where

$$p = \frac{1}{3}\mathrm{tr}(\boldsymbol{\sigma})\,, \quad \boldsymbol{s} = \boldsymbol{\sigma} - p\mathbf{1}\,, \quad \hat{\boldsymbol{n}} = \boldsymbol{s}/\|\boldsymbol{s}\| \tag{2.59}$$

and

$$\kappa := -\bar{\alpha} + b\alpha_1 + \frac{1}{\sqrt{3}}\alpha_2 \tag{2.60}$$

where $\|\boldsymbol{s}\| = \sqrt{s_{ij}s_{ij}}$. Note that for the continuum mechanics convention used throughout this work, compression implies $p < 0$. The material constants $\bar{\alpha}$ and β may be defined in terms of the cohesion $\bar{c}$ and friction angle $\bar{\phi}$ used to describe a Mohr-Coulomb material [58]

$$\bar{\alpha} = \frac{6\bar{c}\cos\bar{\phi}}{\sqrt{3}(3 + A\sin\bar{\phi})}\,; \quad \beta = \frac{6\sin\bar{\phi}}{\sqrt{3}(3 + A\sin\bar{\phi})}\,; \quad -1 \leq A \leq 1\,. \tag{2.61}$$

The value $A = -1$ coincides with a cone that circumscribes the Mohr-Coulomb envelope—passing through its outer apexes—in three-dimensional stress space, and $A = 1$ coincides with a cone that passes through the inner apexes of the Mohr-Coulomb envelope. Because of the form of κ in Eq. (2.60), standard bulk and shear hardening/softening through α_1 and α_2 cause the size of the yield cone to change, and not its shape. Incorporating additional hardening/softening through β would allow frictional hardening/softening which is appropriate for modeling a cohesionless granular material like sand, and thus the change of slope of the yield cone would be possible.

A plastic potential function $\varphi(\boldsymbol{\sigma}, \boldsymbol{\alpha})$ is defined similarly to the yield function

$\phi(\boldsymbol{\sigma}, \boldsymbol{\alpha})$ [65] as

$$\varphi(\boldsymbol{\sigma}, \boldsymbol{\alpha}) = \sqrt{\frac{3}{2}}\|\boldsymbol{s}\| + \sqrt{3}(\kappa + bp) \tag{2.62}$$

with derivatives

$$\frac{\partial \varphi}{\partial \boldsymbol{\sigma}} = \sqrt{\frac{3}{2}}\hat{\boldsymbol{n}} + \frac{1}{\sqrt{3}}b\mathbf{1}\,, \quad \frac{\partial \varphi}{\partial \boldsymbol{\alpha}} = \left\{ \begin{array}{c} \sqrt{3}b \\ 1 \end{array} \right\} \tag{2.63}$$

where b is the material dilation constant. Refer to Appendix C for a derivation of the material constants $\bar{\alpha}$ and β in Eq. (2.61) and for a description of the material dilation angle $\bar{\psi}$ for the plane strain condition (refer also to [5] for a discussion of dilation, a concept probably first formally reported by REYNOLDS [67]). Notice that associated plasticity results if $\beta = b$, but typically for soil and rock this is not the case. Usually, $\beta > b$ with $b > 0$ for a dilatant material and $b < 0$ for a contractant material. By setting $\beta = b = 0$, the J2 flow (von Mises) plasticity model is recovered, which is useful for modeling the undrained condition in a cohesive soil.

With the plastic potential function $\varphi(\boldsymbol{\sigma}, \boldsymbol{\alpha})$ defined in Eq. (2.62), the evolution of $\boldsymbol{\xi}$ then becomes

$$\dot{\boldsymbol{\xi}} = \lambda \frac{\partial \varphi}{\partial \boldsymbol{\alpha}} = \lambda \left\{ \begin{array}{c} \sqrt{3}b \\ 1 \end{array} \right\} . \tag{2.64}$$

Note that the constants in front of α_1 and α_2 in Eq. (2.60) are chosen so that

$$\lambda \frac{\partial \varphi}{\partial \boldsymbol{\alpha}} = \left\{ \begin{array}{c} \dot{v}^p \\ \dot{e}^p \end{array} \right\} \tag{2.65}$$

where $\dot{v}^p$ and $\dot{e}^p$ are defined in Eq. (2.53). Note that b now takes the form

$$b = \frac{\dot{v}^p}{\sqrt{3}\dot{e}^p} \tag{2.66}$$

which is analogous to the dilatancy factor used by RUDNICKI & RICE [73] and RUDNICKI [74].

Refer to Appendix D for numerical integration of $\dot{\boldsymbol{\sigma}}$—defined from Eqs. (2.9), $(2.12)_1$, and (2.50)—and the form of the algorithmic (consistent) tangent operator (see [80] for a more detailed discussion).

2.6.2 Drucker-Prager Plasticity with Strong Discontinuity

Here, the standard non-associated Drucker-Prager plasticity model presented in Section 2.6.1 is placed within the framework of Section 2.5. In particular, the two model-specific features which need to be derived are the localization condition and stress-displacement relation.

2.6.2.1 Localization Condition

Recall from Section 2.5.4 the localization condition, which detects the presence of discontinuous displacements

$$\boldsymbol{A} \cdot \boldsymbol{m} \;=\; \boldsymbol{0}\,; \quad \boldsymbol{A} \;=\; \boldsymbol{n} \cdot \boldsymbol{C}^{ep} \cdot \boldsymbol{n} \tag{2.67}$$

where for Drucker-Prager plasticity the elastic-perfectly-plastic tangent modulus tensor is

$$\begin{aligned}\boldsymbol{C}^{ep} \;=\; & \left(\bar{K} - \frac{2\bar{\mu}}{3} - \frac{3\beta b\bar{K}^2}{\chi}\right) \mathbf{1}\otimes\mathbf{1} \;+\; 2\bar{\mu}\boldsymbol{I} \\ & - \frac{6\bar{\mu}^2}{\chi}\hat{\boldsymbol{n}}\otimes\hat{\boldsymbol{n}} \;-\; \frac{3\sqrt{2}\bar{\mu}\bar{K}}{\chi}\left(\beta\hat{\boldsymbol{n}}\otimes\mathbf{1} \;+\; b\mathbf{1}\otimes\hat{\boldsymbol{n}}\right)\end{aligned} \tag{2.68}$$

where $\chi = 3(\bar{\mu} + \beta b\bar{K})$. Note that $\boldsymbol{C}^{ep}$ is the same as the continuum elastic-plastic tangent modulus tensor $\boldsymbol{c}^{ep}$ if $\mathcal{H}$ from Eq. (2.19) is added to χ in Eq. (2.68), where $\mathcal{H} = 3b^2K' + H'$. The corresponding perfectly-plastic acoustic tensor is

$$\begin{aligned}\boldsymbol{A} \;=\; \boldsymbol{n}\cdot\boldsymbol{C}^{ep}\cdot\boldsymbol{n} \;&=\; \left(\bar{K} + \frac{\bar{\mu}}{3} - \frac{3\beta b\bar{K}^2}{\chi}\right)\boldsymbol{n}\otimes\boldsymbol{n} \;+\; \bar{\mu}\mathbf{1} \\ &\quad - \frac{6\bar{\mu}^2}{\chi}\boldsymbol{N}\otimes\boldsymbol{N} \;-\; \frac{3\sqrt{2}\bar{\mu}\bar{K}}{\chi}\left(\beta\boldsymbol{N}\otimes\boldsymbol{n} \;+\; b\boldsymbol{n}\otimes\boldsymbol{N}\right)\end{aligned} \tag{2.69}$$

where $\boldsymbol{N} = \hat{\boldsymbol{n}}\cdot\boldsymbol{n} = \boldsymbol{n}\cdot\hat{\boldsymbol{n}}$. Note that neither $\boldsymbol{C}^{ep}$ nor $\boldsymbol{A}$ has major symmetry unless $\beta = b$.

The localization condition $\boldsymbol{A}\cdot\boldsymbol{m} = \mathbf{0}$ naturally yields the following form of the localization condition:

$$\boldsymbol{m}\cdot\boldsymbol{A}\cdot\boldsymbol{m} \;=\; 0 \tag{2.70}$$

which may be viewed as a loss of strong ellipticity of $\boldsymbol{C}^{ep}$ from Eq. (1.24). Recall Eq. (2.46), which for Drucker-Prager plasticity yields

$$(\boldsymbol{m}\otimes\boldsymbol{n})^s \;=\; \Lambda\left(\sqrt{\frac{3}{2}}\hat{\boldsymbol{n}} \;+\; \frac{1}{\sqrt{3}}b\mathbf{1}\right) \tag{2.71}$$

and

$$\boldsymbol{m}\cdot\boldsymbol{n} \;=\; \Lambda\sqrt{3}b\,. \tag{2.72}$$

Expand out $\boldsymbol{m}\cdot\boldsymbol{A}\cdot\boldsymbol{m} = 0$ as

$$\begin{aligned}&\left(\bar{K} \,+\, \tfrac{\bar{\mu}}{3} \,-\, \tfrac{3\beta b\bar{K}^2}{\chi}\right)(\boldsymbol{m}\cdot\boldsymbol{n})^2 \;+\; \bar{\mu} - \tfrac{6\bar{\mu}^2}{\chi}\left(\hat{\boldsymbol{n}} : (\boldsymbol{m}\otimes\boldsymbol{n})^s\right)^2 \\ &\quad - \tfrac{3\sqrt{2}\bar{\mu}\bar{K}}{\chi}(\beta + b)(\boldsymbol{m}\cdot\boldsymbol{n})\left(\hat{\boldsymbol{n}} : (\boldsymbol{m}\otimes\boldsymbol{n})^s\right) \;=\; 0\,.\end{aligned} \tag{2.73}$$

Substituting Eq. (2.71) and Eq. (2.72) into Eq. (2.73) yields a solution for Λ:

$$\Lambda \;=\; \pm\frac{1}{\sqrt{3 - b^2}}\,. \tag{2.74}$$

Recall that $\Lambda = \lambda_\delta / \dot{\zeta}$ where $\lambda_\delta > 0$, $\dot{\zeta} > 0$. Thus, the solution of interest is

$$\Lambda \;=\; \frac{1}{\sqrt{3-b^2}}\,. \tag{2.75}$$

As a result of Eq. (2.75), the jump dilation angle ψ may be determined from the following equation:

$$\sin\psi \;=\; \boldsymbol{m}\cdot\boldsymbol{n} \;=\; \frac{\sqrt{3}b}{\sqrt{3-b^2}} \tag{2.76}$$

where b is determined from Eq. (2.66).

Consider a plane strain stress condition and calculate the localization condition and slip line orientation. Refer to Appendix E for a general formulation in three-dimensional stress space. It turns out that the localization condition is the same for the plane strain and three-dimensional cases because the slip plane is found to be perpendicular to the major-minor principal stress plane, as shown in Appendix E, which results because the yield function and plastic potential function are isotropic functions of stress, i.e. composed of stress invariants. Therefore, without loss of generality the analysis is carried out in the principal stress space, where σ_2 is the minor principal stress (major *compressive* principal stress), σ_1 is the major principal stress, and σ_3 is the intermediate principal stress, such that $0 \geq \sigma_1 \geq \sigma_3 \geq \sigma_2$ and $|\sigma_1| \leq |\sigma_3| \leq |\sigma_2|$; refer to the Mohr's circles in Fig. 2.3 (this ordering corresponds to a plane strain stress condition in terms of aligning the principal stresses with the coordinate axes, but is still general).

Refer to Fig. 2.2 to construct the unit vectors

$$\boldsymbol{n} \;=\; \left\{ \begin{array}{c} \cos\theta \\ \sin\theta \\ 0 \end{array} \right\} \; ; \quad \boldsymbol{m} \;=\; \left\{ \begin{array}{c} \cos\eta \\ -\sin\eta \\ 0 \end{array} \right\} \; ; \quad \eta \;=\; 90^\circ - \theta - \psi\,. \tag{2.77}$$

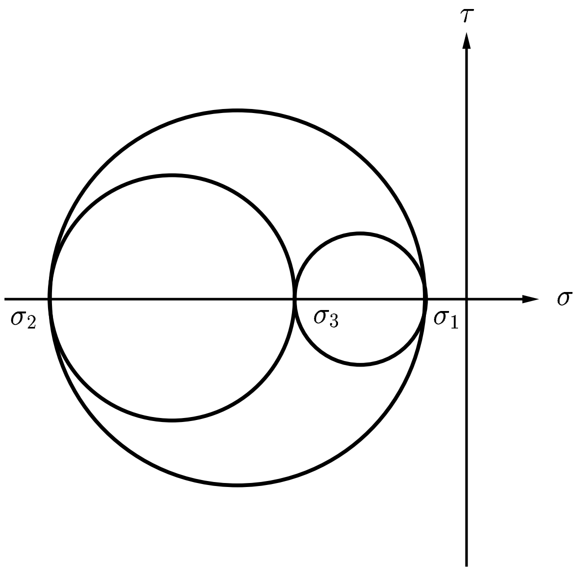

Figure 2.3. Mohr's circles for localization condition stress analysis in plane strain.

Recall from Eq. (2.71) the expression for the symmetric tensor product of $\boldsymbol{m}$ and $\boldsymbol{n}$, written now explicitly as

$$\begin{bmatrix} \cos\eta\cos\theta & \cos\eta\sin\theta & 0 \\ -\sin\eta\cos\theta & -\sin\eta\sin\theta & 0 \\ 0 & 0 & 0 \end{bmatrix}^s$$

$$= \frac{1}{\sqrt{3-b^2}} \begin{bmatrix} \sqrt{\frac{3}{2}}\hat{n}_1 + \frac{1}{\sqrt{3}}b & 0 & 0 \\ 0 & \sqrt{\frac{3}{2}}\hat{n}_2 + \frac{1}{\sqrt{3}}b & 0 \\ 0 & 0 & \sqrt{\frac{3}{2}}\hat{n}_3 + \frac{1}{\sqrt{3}}b \end{bmatrix} . \tag{2.78}$$

For $(\boldsymbol{m} \otimes \boldsymbol{n})^s$ to diagonalize, the following must hold

$$\cos\eta\sin\theta - \sin\eta\cos\theta = \sin(\theta-\eta) = 0 \tag{2.79}$$

or

$$\theta - \eta = 2\theta - 90^\circ + \psi = 0 \tag{2.80}$$

which implies

$$\boxed{\theta \;=\; \pm(45^\circ \;-\; \psi/2)} \tag{2.81}$$

where the ± comes from Fig. 2.2. Which angle is chosen is determined in Appendix F. Thus, Eq. (2.81) is the orientation of the normal to the slip line with respect to the major principal stress axis (see Fig. 2.2). This result has also been reached by Roscoe (pg. 166) [71] and Atkinson (pg. 217) [5] and refuted by Vardoulakis et al. [93]. For deviatoric plastic flow, $b = 0 \;\Rightarrow\; \psi = 0$, the orientation $\theta = 45^\circ$ is recovered. Note that from Eq. (2.78), localized plastic flow $\dot{\boldsymbol{\epsilon}}^p_\delta = \lambda_\delta \partial_{\boldsymbol{\sigma}} \varphi = \dot{\zeta}(\boldsymbol{m} \otimes \boldsymbol{n})^s$ (where $\dot{\boldsymbol{\epsilon}}^p = \dot{\boldsymbol{\epsilon}}^p_\delta \delta_{\mathcal{S}}$) for the plane strain condition does not have an out-of-plane component, whereby the standard plastic strain rate would have an out-of-plane component.

To obtain a condition on the stress state at which localization is detected, take the difference between the (1,1) and (2,2) components of Eq. (2.78), which yields

$$\cos\eta\cos\theta \;+\; \sin\eta\sin\theta \;=\; \sqrt{\frac{3}{3-b^2}}\,\frac{(s_1 - s_2)/\sqrt{2}}{\|\boldsymbol{s}\|} \tag{2.82}$$

where

$$\cos\eta\cos\theta \;+\; \sin\eta\sin\theta \;=\; \cos^2\theta \;+\; \sin^2\theta \;=\; 1\,. \tag{2.83}$$

Thus, the localization condition may be expressed in terms of a deviator stress ratio h defined as

$$\boxed{h \;:=\; \frac{\|\boldsymbol{s}\|}{\sqrt{2}r} \;=\; \sqrt{\frac{3}{3-b^2}}} \tag{2.84}$$

where $r = (s_1 - s_2)/2 = (\sigma_1 - \sigma_2)/2$.

The following analysis will determine the range of h, taking the principal stress convention as shown in Fig. 2.3. Write out the second deviator stress invariant in principal stress space as

$$(\sigma_1 - \sigma_2)^2 + (\sigma_1 - \sigma_3)^2 + (\sigma_3 - \sigma_2)^2 = 3\boldsymbol{s} : \boldsymbol{s} \tag{2.85}$$

or

$$u^2 + v^2 + w^2 = \frac{3}{2} \tag{2.86}$$

where

$$u = \frac{\sigma_1 - \sigma_2}{\sqrt{2}\|\boldsymbol{s}\|}, \quad v = \frac{\sigma_1 - \sigma_3}{\sqrt{2}\|\boldsymbol{s}\|}, \quad w = \frac{\sigma_3 - \sigma_2}{\sqrt{2}\|\boldsymbol{s}\|}. \tag{2.87}$$

Since $u = v + w$ rewrite Eq. (2.86) as

$$f(u, v) = u^2 + v^2 + (u - v)^2 - \frac{3}{2} = 0 \tag{2.88}$$

Maximizing u with respect to v (i.e., $\partial u/\partial v = 0$ and $\partial^2 u/\partial v^2 < 0$), the critical value v_{cr} and maximum value $u_{\max}$ result as

$$v_{\mathrm{cr}} = \frac{u}{2} \quad \Rightarrow \quad u_{\max} = 1\,. \tag{2.89}$$

Note also that $w_{\mathrm{cr}} = u/2$. As a result, u is maximized when $\sigma_3 = (\sigma_1 + \sigma_2)/2$, which states that the intermediate principal stress is the average of the major and minor principal stresses. Furthermore, by definition, the bound on v is $0 \leq v \leq u$ (as σ_3 approaches either σ_1 or σ_2), which yields the minimum for u as $u_{\min} = \sqrt{3}/2$. Thus, the minimum of u corresponds to the biaxial stress condition: $\sigma_3 = \sigma_1$ or $\sigma_3 = \sigma_2$. As a result, u is bounded by

$$\frac{\sqrt{3}}{2} \leq u \leq 1 \tag{2.90}$$

or, since $h = 1/u$,

$$\boxed{1 \leq h \leq \frac{2}{\sqrt{3}}} \tag{2.91}$$

which defines the range of the deviator stress ratio h in the localization condition

Eq. (2.84). Note that Eq. (2.91) is consistent with the range of b. First, rewrite b from Eq. (2.76) as

$$b \;=\; \sqrt{\frac{3\sin^2\psi}{3+\sin^2\psi}} \tag{2.92}$$

where, since $0 \leq \sin^2\psi \leq 1$, the range on b is

$$0 \;\leq\; b \;\leq\; \frac{\sqrt{3}}{2}\,. \tag{2.93}$$

Substituting the bounds of b from Eq. (2.93) into the localization condition Eq. (2.84) yields Eq. (2.91). For $\sin^2\psi = 1$, the jump dilation angle is $\psi = 90°$, which corresponds to $\boldsymbol{m}\|\boldsymbol{n}$ and a normal splitting of the material, a case not of interest when analyzing soil and rock.

It is expected that localization cannot occur in the (σ_1, σ_3) or (σ_2, σ_3) planes, which may be verified by the following analysis. Recall the bound on v

$$0 \;\leq\; v \;\leq\; u \tag{2.94}$$

or

$$\frac{1}{u} \;\leq\; \frac{1}{v} \;<\; \infty\,. \tag{2.95}$$

The lower bound on $1/v$ corresponds to the biaxial stress condition $\sigma_3 = \sigma_2$, and thus

$$\frac{2}{\sqrt{3}} \;\leq\; \frac{1}{v} \;<\; \infty\,. \tag{2.96}$$

Thus, if $\boldsymbol{m}$ and $\boldsymbol{n}$ were placed in the (x_1, x_3) plane for the plane strain condition considered here, the resulting localization condition $\frac{\|\boldsymbol{s}\|}{\sqrt{2}(\sigma_1-\sigma_3)/2} = \sqrt{\frac{3}{3-b^2}}$ would never be met, except for the extreme case of normal splitting, which is not of interest for modeling frictional materials like soil and rock. This analysis likewise dictates that localization would not occur in the (σ_2, σ_3) plane.

Thus, together with the result of Appendix E this analysis predicts that a slip plane is perpendicular to the major-minor principal stress plane for a general three-dimensional stress condition.

2.6.2.2 Stress-Displacement Relation

The stress-displacement relation governs the evolution of plastic softening localized to the discontinuity $\mathcal{S}$. Upon the detection of discontinuous displacement fields via the localization condition, plastic flow is localized to the discontinuity via $\lambda = \lambda_\delta \delta_{\mathcal{S}}$; likewise, softening is localized to the discontinuity via $\boldsymbol{H}^{-1} = \boldsymbol{H}_\delta^{-1} \delta_{\mathcal{S}}$. Thus, the stress-displacement relation becomes the constitutive equation for post-localization plasticity. The standard plasticity equations no longer apply, except to provide the framework in which the strong discontinuity is incorporated to produce the bifurcated solution.

Recall the general form for the stress displacement relation from Eq. (2.49)

$$\dot{\zeta} = \frac{\mathrm{tr}(\partial_{\boldsymbol{\sigma}} \varphi)}{\mathcal{H}_\delta \boldsymbol{m} \cdot \boldsymbol{n}} \partial_{\boldsymbol{\sigma}} \phi : \dot{\boldsymbol{\sigma}} = \frac{1}{\mathcal{H}_\delta \Lambda} \partial_{\boldsymbol{\sigma}} \phi : \dot{\boldsymbol{\sigma}} \tag{2.97}$$

where $\mathcal{H}_\delta = 3b^2 K_\delta + H_\delta$,

$$\boldsymbol{H}_\delta = \begin{bmatrix} K_\delta & 0 \\ 0 & H_\delta \end{bmatrix} \tag{2.98}$$

and $\Lambda = (3 - b^2)^{-\frac{1}{2}}$. From Eq. (2.58), the following results

$$\partial_{\boldsymbol{\sigma}} \phi : \dot{\boldsymbol{\sigma}} = \sqrt{\frac{3}{2}} \frac{\boldsymbol{s} : \dot{\boldsymbol{s}}}{\|\boldsymbol{s}\|} + \sqrt{3} \beta \dot{p} \tag{2.99}$$

where it can be shown that

$$\boldsymbol{s} : \dot{\boldsymbol{s}} = \frac{1}{2} \frac{\mathrm{d}}{\mathrm{dt}} \left(\|\boldsymbol{s}\|^2 \right) . \tag{2.100}$$

Define q to be the resolved deviatoric stress on the discontinuity $\mathcal{S}$ as

$$q \;:=\; \boldsymbol{m}\cdot\boldsymbol{s}\cdot\boldsymbol{n} \;=\; \boldsymbol{s} : (\boldsymbol{m}\otimes\boldsymbol{n})^{s} \;=\; \sqrt{\frac{3}{2}}\Lambda\|\boldsymbol{s}\|\,. \tag{2.101}$$

Solving for $\|\boldsymbol{s}\|^2$ from Eq. (2.101) gives

$$\|\boldsymbol{s}\|^2 \;=\; \frac{2}{3}\left(\frac{q}{\Lambda}\right)^2 \;=\; \frac{2}{3}(3-b^2)q^2 \tag{2.102}$$

and

$$\frac{\mathrm{d}}{\mathrm{dt}}\left(\|\boldsymbol{s}\|^2\right) \;=\; \frac{4}{3}(3-b^2)q\dot{q} \;=\; \frac{4}{3}\sqrt{\frac{3}{2}}\sqrt{3-b^2}\|\boldsymbol{s}\|\dot{q}\,. \tag{2.103}$$

Therefore, Eq. (2.99) takes the scalar form

$$\partial_{\boldsymbol{\sigma}}\phi : \dot{\boldsymbol{\sigma}} \;=\; \sqrt{3-b^2}\dot{q} \;+\; \sqrt{3}\beta\dot{p} \tag{2.104}$$

which when substituted into Eq. (2.97) produces the rate form of the stress-displacement relation

$$\dot{q} \;+\; \frac{\sqrt{3}\beta}{\sqrt{3-b^2}}\dot{p} \;=\; \frac{\mathcal{H}_\delta}{3-b^2}\dot{\zeta}\,. \tag{2.105}$$

Integrate Eq. (2.105) to yield the combined stress at time instant t, $Q(t)$, as

$$\begin{aligned} Q(t) \;&:=\; q(t) \;+\; \frac{\sqrt{3}\beta}{\sqrt{3-b^2}}p(t) \\ &=\; q(0) \;+\; \frac{\sqrt{3}\beta}{\sqrt{3-b^2}}p(0) \;+\; \frac{\mathcal{H}_\delta}{3-b^2}\zeta(t) \end{aligned} \tag{2.106}$$

where $t = 0$ corresponds to the onset of localization and $\zeta(0) = 0$, (i.e., there is no jump displacement yet developed at the instant of localization). Here, $\mathcal{H}_\delta$ is constant for linear softening, thus Eq. (2.105) is easily integrated. Otherwise, for nonlinear softening, the integration of Eq. (2.105) would depend on the form of $\mathcal{H}_\delta(\zeta)$; designating the localized softening modulus $\mathcal{H}_\delta$ to depend on the jump displacement

ζ is a reasonable assumption (see [3]).

2.7 Summary

This chapter presented the formulation of a non-associated, rate-independent, strain-softening plasticity model in the context of strong discontinuities and its specialization to a non-associated, strain-softening Drucker-Prager plasticity model. Some noteworthy results of the analysis are that plastic dissipation is calculated over a set of zero measure (i.e., slip surface in three dimensions and slip line in two dimensions) and thus is independent of finite element size, a stress-displacement relation along the discontinuity governs post-localization behavior, and the localization condition and discontinuity orientation are both explicitly determined (i.e., not numerically calculated). A finite element implementation of this Drucker-Prager plasticity model with strong discontinuity will now proceed.

Chapter 3

Finite Element Implementation

3.1 Introduction

The finite element implementation of the strong discontinuity approach has previously been conducted within the Assumed Enhanced Strain (AES) method formalized by Simo & Rifai [79]; refer to Armero & Garikipati [3] for the implementation of a J2 flow plasticity model and damage model based on the unregularized formulation. To begin, the functions which motivate the form of the enhanced strains are developed (the shape functions themselves are not enhanced—only the strains—because it is an assumed *enhanced strain* method). The modified variational (weak) form of the quasi-static, isothermal equilibrium equations which results from introducing an assumed strain field into the standard variational equations is described. The nonlinear matrix finite element equations along with the solution algorithm for a Newton-Raphson method are then outlined.

3.2 Variational Form of Assumed Enhanced Strain Method

The AES method is a logical choice as a framework for implementing the strong discontinuity approach because it satisfies the two conditions necessary and sufficient for convergence for a numerical method: 1) stability, and 2) consistency (i.e., the patch test); these two conditions will be described later.

The AES method for the linearized theory stems from an additive decomposition of the infinitesimal strain tensor into compatible and enhanced parts:

$$\boldsymbol{\epsilon} = \underbrace{\boldsymbol{\nabla}^s \boldsymbol{u}}_{\text{compatible}} + \underbrace{\tilde{\boldsymbol{\epsilon}}}_{\text{enhanced}} \tag{3.1}$$

where the enhanced strain field may be derived from incompatible displacement fields across element sides. The standard three-field variational equations emanating from the Hu-Washizu principle for non-linear elasticity (see Chapter 13 of [97]) may be written as

$$\begin{aligned}
\int_\Omega \delta\boldsymbol{u} \cdot (\boldsymbol{\nabla} \cdot \boldsymbol{\sigma} + \boldsymbol{b})\, d\Omega &= 0 \\
\int_\Omega \delta\boldsymbol{\sigma} : (\boldsymbol{\nabla}^s \boldsymbol{u} - \boldsymbol{\epsilon})\, d\Omega &= 0 \\
\int_\Omega \delta\boldsymbol{\epsilon} : (-\boldsymbol{\sigma} + \partial_{\boldsymbol{\epsilon}} \Psi)\, d\Omega &= 0
\end{aligned} \tag{3.2}$$

where $\boldsymbol{u}, \boldsymbol{\sigma}$, and $\boldsymbol{\epsilon}$ are treated as independent variables, and $\delta\boldsymbol{u}, \delta\boldsymbol{\sigma}$, and $\delta\boldsymbol{\epsilon}$ are their variations. Localizing the integrals of Eq. (3.2) (see pg. 38 of [29]) yields the governing equations as expressed in Section 2.2. The equations in Eq. (3.2) result from the stationary condition (i.e., at equilibrium, $\delta\Pi = 0$) on the energy functional:

$$\Pi(\boldsymbol{u}, \boldsymbol{\sigma}, \boldsymbol{\epsilon}) := \int_\Omega [\Psi(\boldsymbol{x}, \boldsymbol{\epsilon}) - \boldsymbol{b} \cdot \boldsymbol{u} + \boldsymbol{\sigma} : (\boldsymbol{\nabla}^s \boldsymbol{u} - \boldsymbol{\epsilon})]\, d\Omega - \int_{\partial_t \Omega} \boldsymbol{t} \cdot \boldsymbol{u}\, d\Gamma\,. \tag{3.3}$$

Introducing the newly defined strain field Eq. (3.1) into the energy functional Eq. (3.3) and applying the stationary condition ($\delta\Pi = 0$) yields the modified three-field variational form:

$$\int_\Omega \boldsymbol{\nabla}^s(\delta\boldsymbol{u}) : \boldsymbol{\sigma}\, d\Omega \;=\; \int_\Omega \delta\boldsymbol{u}\cdot\boldsymbol{b}\, d\Omega + \int_{\partial_t\Omega} \delta\boldsymbol{u}\cdot\boldsymbol{t}\, d\Gamma \tag{3.4}$$

$$\int_\Omega \delta\boldsymbol{\sigma} : \tilde{\boldsymbol{\epsilon}}\, d\Omega \;=\; 0 \tag{3.5}$$

$$\int_\Omega \delta\tilde{\boldsymbol{\epsilon}} : (-\boldsymbol{\sigma} + \partial_{\boldsymbol{\epsilon}}\Psi)\, d\Omega \;=\; 0\,. \tag{3.6}$$

Because of the orthogonality condition on the stress and enhanced strain spaces in Eq. (3.5), the stress field is eliminated from the variational equations and Eq. (3.6) drops out.

Since the purpose of the enhanced strain field is to 'enhance' the compatible strain field, it makes sense that their spaces have null intersection:

$$\tilde{\mathcal{E}} \cap \mathcal{E} \;=\; \emptyset \tag{3.7}$$

where the space for the compatible strains is

$$\mathcal{E} \;=\; \{\boldsymbol{\epsilon} : \Omega \to \mathbb{S};\; \boldsymbol{\epsilon} = \boldsymbol{\nabla}^s\boldsymbol{u}\} \tag{3.8}$$

and the space for the enhanced strains is

$$\tilde{\mathcal{E}} \;=\; \{\tilde{\boldsymbol{\epsilon}} : \Omega \to \mathbb{S};\; \tilde{\boldsymbol{\epsilon}} \text{ is assumed}\}\;. \tag{3.9}$$

It has been shown for the discrete problem that Eq. (3.7) leads to stability of the AES method [79].

For the patch test to be satisfied—as revisited in TAYLOR et al. [90]—piecewise constant stress functions must be admissible (i.e., as $h \to 0$, where h is the element diameter, the stress at a continuum point should be recovered). This condition will directly affect the choice of the discrete enhanced strain variation $\delta\tilde{\boldsymbol{\epsilon}}^h$. Rewrite Eq. (3.5) as

$$\int_\Omega \boldsymbol{\sigma} : \delta\tilde{\boldsymbol{\epsilon}}\, d\Omega \;=\; 0 \tag{3.10}$$

because the *spaces* are orthogonal. Thus, piecewise constant stress functions $\boldsymbol{\sigma}_0$ will require

$$\int_\Omega \delta\tilde{\boldsymbol{\epsilon}}\, d\Omega \;=\; \mathbf{0} \tag{3.11}$$

which will be described in particular for singular enhanced strains in Section 3.4.

3.3 Reparameterization of the Displacement Field

The need for a reparameterized displacement field for adequately approximating the jump displacement was recognized in Simo et al. [82] for the 1D problem. In similar fashion, the need for a reparameterized displacement field is motivated here from the 1D problem.

Consider the approximations of an actual discontinuous displacement field as shown in Fig. 3.1. The deficiency associated with the approximation by an unaltered discretized displacement field $u^h(x)$ is that the nodal displacements are the *total* displacements, which already include the enhancement. Figure 3.1 clearly shows the inadequacy of this approximation. Thus, the approach outlined by Simo et al. [82] is to contain the enhancement within the element boundaries. The resulting reparameterized displacement field is clearly a better approximation as shown in Fig. 3.1. The restrictions on this newly defined function $M_{\mathcal{S}}(\boldsymbol{x}) : \bar{\Omega}^e_{\text{loc}} \rightarrow \mathbb{R}$ are

1. compact support in $\bar{\Omega}^h$; i.e. $M_{\mathcal{S}}(\boldsymbol{x}) = 0$ for $\boldsymbol{x}$ outside of $\bar{\Omega}^h$ and $\boldsymbol{x} \in \partial\Omega^h$, where $\bar{\Omega}^h = \Omega^h \cup \partial\Omega^h$

2. $[\![M_{\mathcal{S}}]\!] = 1$ at $\mathcal{S}$.

Thus, the construction of $M_{\mathcal{S}}(\boldsymbol{x})$ is as follows:

$$M_{\mathcal{S}}(\boldsymbol{x}) \;=\; H_{\mathcal{S}}(\boldsymbol{x}) \;-\; f^h(\boldsymbol{x}) \tag{3.12}$$

where

$$f^h(\boldsymbol{x}) \;=\; \begin{cases} 1 & \text{at node A} \in \; \partial\Omega^h_+ \\ 0 & \text{at node A} \in \; \partial\Omega^h_- \end{cases} . \tag{3.13}$$

Recall that the unit normal $\boldsymbol{n}$ to the discontinuity $\mathcal{S}$ points into Ω^h_+. The reparameterized displacement field then becomes

$$\boldsymbol{u}^h(\boldsymbol{x}, t) \;=\; \bar{\boldsymbol{u}}^h(\boldsymbol{x}, t) \;+\; [\![\boldsymbol{u}^h(t)]\!] \, M_{\mathcal{S}}(\boldsymbol{x}) \,. \tag{3.14}$$

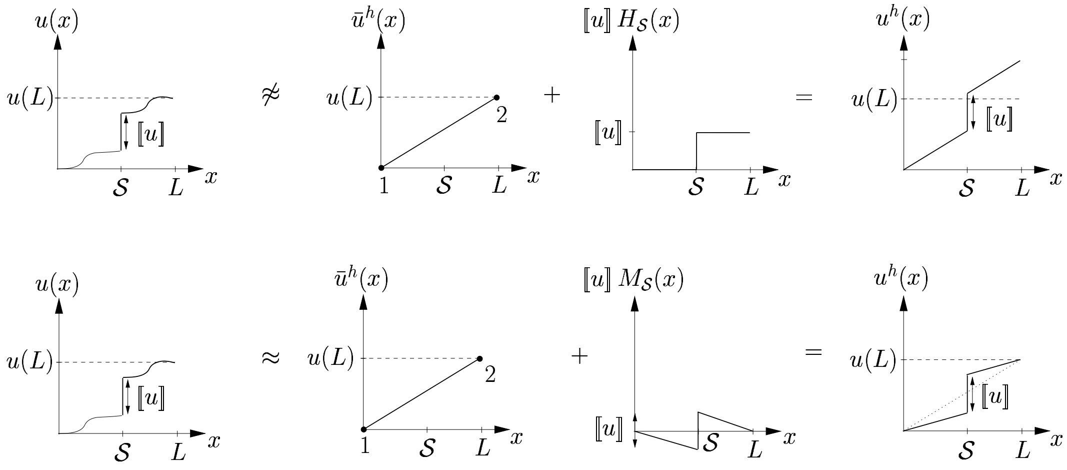

Figure 3.1. 1D motivation for the construction of $M_{\mathcal{S}}$. $\bar{u}^h(x)$ linearly interpolates the displacement between nodes 1 and 2. Actual localized displacement field $u(x)$ and incorrect finite element interpolation, $u(x) \not\approx \bar{u}^h(x) + [\![u]\!]\, H_{\mathcal{S}}(x)$. Reparameterization of the displacement field is then needed: $u(x) \approx \bar{u}^h(x) + [\![u]\!]\, M_{\mathcal{S}}(x)$.

Applying this same methodology to the two-dimensional problem, it is possible to formulate these functions $M_{\mathcal{S}}$ for the two slip line cases for a quadrilateral element as shown in Fig. 3.2. The functions which result via the above construction are shown in Fig. 3.3. The function f^h for slip line type 1 in Fig. 3.3 is the shape function at that node (node 4 in Fig. 3.3), and f^h for type 2 is the sum of the shape functions at node 1 and node 4. It is then straightforward to see how one would construct f^h for the four slip line types of a brick element (although more difficult to visualize). Note that the functions in Fig. 3.3 appear similar to those in WAN et al. [96]. The main difference between the quadrilateral element presented in this thesis and that presented in [96] is that when a corner node is cut by the slip line, the quadrilateral element is retained, rather than split into triangular elements such as that done in [96]. It is noted that this enhanced quadrilateral element was formulated independently from [96], with motivation coming from the work by Simo and co-workers.

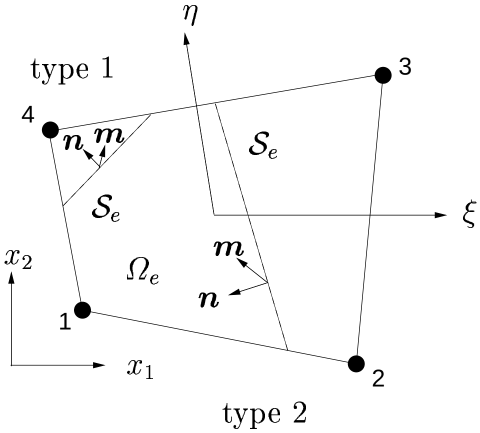

Figure 3.2. Two slip line types in a quadrilateral element.

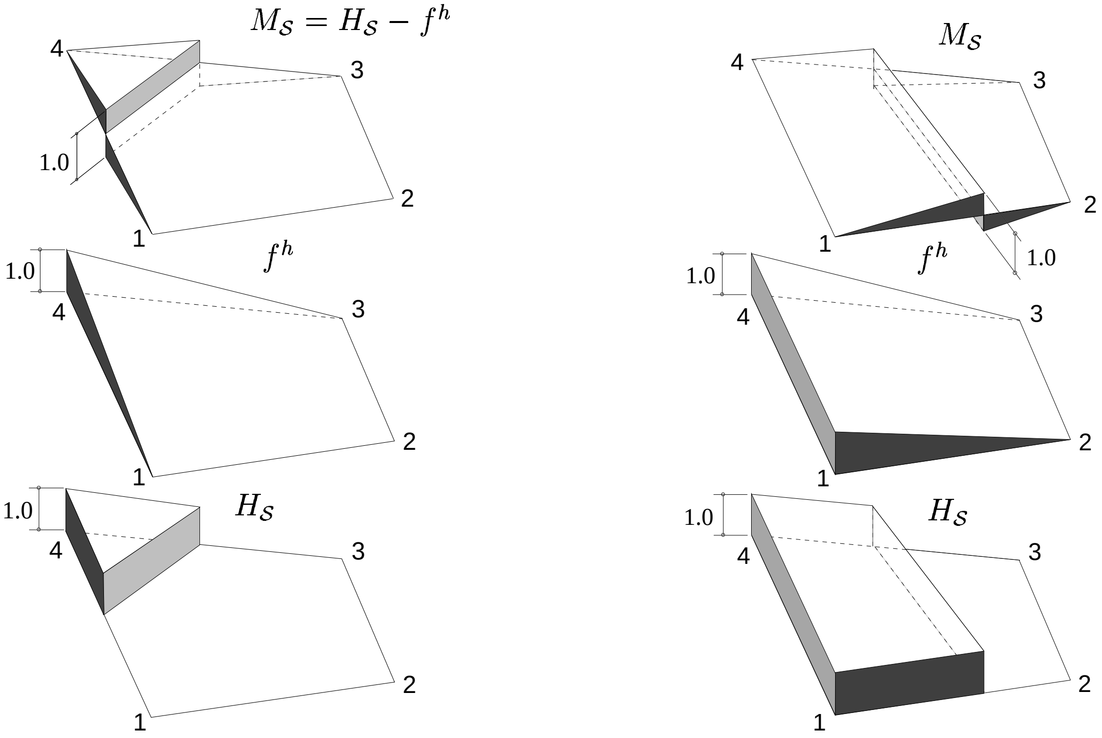

Figure 3.3. Slip line types 1 and 2. Motivation for enhanced strain interpolations via $M_{\mathcal{S}}$.

3.4 Finite Element Equations for Strong Discontinuity Approach

With the displacement field now reparameterized as in Section 3.3, and the variational form of the AES method in place from Section 3.2, it is possible to proceed with formulating the nonlinear matrix finite element equations. A thorough analysis of the weak form with strong discontinuity has been presented by Simo & Oliver [83] for the regularized formulation and by Armero & Garikipati [3] for the unregularized formulation. The framework of the unregularized formulation in [3] is adopted here and modified to account for dilative plastic flow.

3.4.1 Variational Equations

Let $\bar{\Omega}^h = \cup_{e=1}^{n_{el}} \bar{\Omega}_e^h$ be the finite element discretization of a closed region $\bar{\Omega}$, and $\bar{\Omega}_{\text{loc}}^h = \cup_{e=1}^{n_{el,\text{loc}}} \bar{\Omega}_{\text{loc},e}^h$ be the finite element discretization of the localized region, where $\bar{\Omega}_{\text{loc}}^h \subset \bar{\Omega}^h$, n_{el} is the number of elements, and $n_{el,\text{loc}}$ is the number of localized elements which is *not* a priori known. The resulting discretized weak form results as follows

$$
\begin{aligned}
\int_{\Omega^h} \boldsymbol{\nabla}^s \bar{\boldsymbol{\eta}}^h : \boldsymbol{\sigma}^h \, d\Omega \;&=\; \int_{\Omega^h} \bar{\boldsymbol{\eta}}^h \cdot \boldsymbol{b}^h \, d\Omega + \int_{\partial_t \Omega^h} \bar{\boldsymbol{\eta}}^h \cdot \boldsymbol{t}^h \, d\Gamma \\
\int_{\Omega_{\text{loc},e}^h} \tilde{\boldsymbol{\gamma}}^h : \boldsymbol{\sigma}^h \, d\Omega \;&=\; 0
\end{aligned}
\tag{3.15}
$$

where $\bar{\boldsymbol{\eta}} = \delta \bar{\boldsymbol{u}}$ and $\tilde{\boldsymbol{\gamma}} = \delta \tilde{\boldsymbol{\epsilon}}$.

The rest of this presentation will concentrate on the formulation for an element e with strong discontinuity. Recall the reparameterized displacement field written for element e as

$$
\boldsymbol{u}_e^h \;=\; \bar{\boldsymbol{u}}_e^h + [[\boldsymbol{u}_e^h]]\, M_{\mathcal{S}_e}^h \,, \quad [[\boldsymbol{u}_e^h]] \;=\; \zeta_e^h \boldsymbol{m}_e \,, \tag{3.16}
$$

where now

$$\boldsymbol{\eta}_e^h \;=\; \delta \boldsymbol{u}_e^h \;=\; \bar{\boldsymbol{\eta}}_e^h \,+\, [\![\boldsymbol{\eta}_e^h]\!]\, M_{\mathcal{S}_e}^h\,, \;\; [\![\boldsymbol{\eta}_e^h]\!] \;=\; \eta_e^h \boldsymbol{m}_e\,, \tag{3.17}$$

and

$$M_{\mathcal{S}_e}^h \;=\; H_{\mathcal{S}_e} \,-\, f_e^h \tag{3.18}$$

with f_e^h defined in Fig. 3.3. Thus, the strain and strain variation become

$$\boldsymbol{\epsilon}_e^h \;:=\; \boldsymbol{\nabla}^s \boldsymbol{u}_e^h \;=\; \boldsymbol{\nabla}^s \bar{\boldsymbol{u}}_e^h \,+\, \tilde{\boldsymbol{\epsilon}}_e^h \tag{3.19}$$

where

$$\tilde{\boldsymbol{\epsilon}}_e^h \;=\; -\zeta_e^h \left(\boldsymbol{m}_e \otimes \boldsymbol{\nabla} f_e^h\right)^s \,+\, \zeta_e^h \left(\boldsymbol{m}_e \otimes \boldsymbol{n}_e\right)^s \delta_{\mathcal{S}_e} \tag{3.20}$$

and

$$\boldsymbol{\gamma}_e^h \;:=\; \boldsymbol{\nabla}^s \boldsymbol{\eta}_e^h \;=\; \boldsymbol{\nabla}^s \bar{\boldsymbol{\eta}}_e^h \,+\, \tilde{\boldsymbol{\gamma}}_e^h\,. \tag{3.21}$$

Recall that the choice of $\tilde{\boldsymbol{\gamma}}_e^h$ is made such that Eq.$(3.15)_2$ is satisfied for piecewise constant stress fields $\boldsymbol{\sigma}_0^h$, or

$$\int_{\Omega_{\mathrm{loc},e}^h} \tilde{\boldsymbol{\gamma}}_e^h \, d\Omega \;=\; \mathbf{0}\,. \tag{3.22}$$

Equation (3.22) may be written independently from other localized elements because the enhanced strains are discontinuous between elements (which is also a property of the standard C^0 finite element theory, that strains are typically discontinuous between elements; the C^0 theory, however, requires continuous displacements, which is not a requirement of the functions which motivate the enhanced strains used in the AES method). Considering Eq. (3.22), choose $\tilde{\boldsymbol{\gamma}}_e^h$ to have the following form:

$$\tilde{\boldsymbol{\gamma}}_e^h \;=\; -\eta_e^h c_e \left(\boldsymbol{m}_e \otimes \boldsymbol{n}_e\right)^s \,+\, \eta_e^h \left(\boldsymbol{m}_e \otimes \boldsymbol{n}_e\right)^s \delta_{\mathcal{S}_e}\,; \quad c_e \in \mathbb{R}\,. \tag{3.23}$$

Now, use Eq. (3.22) to solve for the constant c_e:

$$\begin{aligned}\int_{\Omega^h_{\mathrm{loc},e}} \tilde{\gamma}^h_e \, d\Omega &= \eta^h_e \, (\boldsymbol{m}_e \otimes \boldsymbol{n}_e)^s \int_{\Omega^h_{\mathrm{loc},e}} (-c_e + \delta_{\mathcal{S}_e}) \, d\Omega \\ &= \eta^h_e \, (\boldsymbol{m}_e \otimes \boldsymbol{n}_e)^s \left(- \int_{\Omega^h_{\mathrm{loc},e}} c_e \, d\Omega + \int_{\mathcal{S}_e} d\Gamma \right) \;=\; \boldsymbol{0} \end{aligned} \tag{3.24}$$

where

$$c_e \;=\; \frac{l_{\mathcal{S}_e}}{A_e} \tag{3.25}$$

and $l_{\mathcal{S}_e}$ is the length of the slip line within element e, and A_e is the area of element e. Thus, satisfaction of the patch test is ensured.

3.4.2 Matrix Finite Element Equations

The standard finite element interpolations in isoparametric coordinates $\boldsymbol{\xi}$ are as follows

$$\bar{\boldsymbol{u}}^h_e(\boldsymbol{\xi}) \;=\; \sum_{A=1}^{n_{nds}} N^A(\boldsymbol{\xi}) \boldsymbol{d}^A_e \, ; \quad \bar{\boldsymbol{\eta}}^h_e \;=\; \sum_{A=1}^{n_{nds}} N^A(\boldsymbol{\xi}) \boldsymbol{c}^A_e \tag{3.26}$$

where n_{nds} is the number of nodes of an element e, $N^A(\boldsymbol{\xi})$ is the shape function at node A, and $\boldsymbol{d}^A_e$ and $\boldsymbol{c}^A_e$ are the displacement vector and displacement variation vector, respectively, at node A. It is convenient to write the expressions in Eq. (3.26) in the following matrix form

$$\bar{\boldsymbol{u}}^h_e(\boldsymbol{\xi}) \;=\; \boldsymbol{N}_e(\boldsymbol{\xi}) \cdot \boldsymbol{d}_e \, ; \quad \bar{\boldsymbol{\eta}}^h_e \;=\; \boldsymbol{N}_e(\boldsymbol{\xi}) \cdot \boldsymbol{c}_e \tag{3.27}$$

where $\boldsymbol{N}_e(\boldsymbol{\xi})$ is the element shape function matrix, and $\boldsymbol{d}_e$ and $\boldsymbol{c}_e$ are the displacement vector and displacement variation vector, respectively, for element e. Taking the symmetric gradient of the expressions in Eq. (3.27) yields

$$\boldsymbol{\nabla}^s \bar{\boldsymbol{u}}^h_e(\boldsymbol{\xi}) \;=\; \boldsymbol{B}_e(\boldsymbol{\xi}) \cdot \boldsymbol{d}_e \, ; \quad \boldsymbol{\nabla}^s \bar{\boldsymbol{\eta}}^h_e \;=\; \boldsymbol{B}_e(\boldsymbol{\xi}) \cdot \boldsymbol{c}_e \tag{3.28}$$

where $\boldsymbol{B}_e(\boldsymbol{\xi})$ is the element strain-displacement matrix. Likewise, write $\tilde{\boldsymbol{\epsilon}}^h_e$ and $\tilde{\boldsymbol{\gamma}}^h_e$ in matrix form as

$$\tilde{\boldsymbol{\epsilon}}^h_e = -\boldsymbol{G}_e\zeta^h_e + \boldsymbol{F}_e\zeta^h_e\delta_{\mathcal{S}_e}\,; \quad \boldsymbol{G}_e = \left[(\boldsymbol{m}_e \otimes \boldsymbol{\nabla} f^h_e)^s\right] \tag{3.29}$$

and

$$\tilde{\boldsymbol{\gamma}}^h_e = -\frac{l_{\mathcal{S}_e}}{A_e}\boldsymbol{F}_e\eta^h_e + \boldsymbol{F}_e\eta^h_e\delta_{\mathcal{S}_e}\,; \quad \boldsymbol{F}_e = [(\boldsymbol{m}_e \otimes \boldsymbol{n}_e)^s] \tag{3.30}$$

where $[\bullet]$ denotes matrix form of the tensor. Substituting the matrix expressions for $\bar{\boldsymbol{\eta}}^h_e$ from Eq. (3.27), $\boldsymbol{\nabla}^s\bar{\boldsymbol{\eta}}^h_e$ from Eq. (3.28), and $\tilde{\boldsymbol{\gamma}}^h_e$ from Eq. (3.30) into Eq. (3.15), and assuming arbitrary values of $\boldsymbol{c}_e$ and η^h_e, the nonlinear finite element equations expressed in residual form result as

$$\begin{aligned} \boldsymbol{r}_e &:= \int_{\Omega^h_e} \boldsymbol{B}^T_e\boldsymbol{\sigma}^h\,d\Omega - \int_{\Omega^h_e} \boldsymbol{N}^T_e\boldsymbol{b}^h\,d\Omega - \int_{\partial_t\Omega^h_e} \boldsymbol{N}^T_e\boldsymbol{t}^h\,d\Gamma = \boldsymbol{0} \\ b_e &:= \frac{1}{A_e}\int_{\Omega^h_{\text{loc},e}} \boldsymbol{F}^T_e\boldsymbol{\sigma}^h\,d\Omega - \left(q^h_{\mathcal{S}_e} + \boldsymbol{n}\cdot\boldsymbol{m}p^h_{\mathcal{S}_e}\right) = 0 \end{aligned} \tag{3.31}$$

where $\boldsymbol{r}_e$ is the standard residual for equilibrium within an element e associated with the nodal degrees of freedom, b_e is the residual expressing equilibrium along the discontinuity $\mathcal{S}_e$ associated with the jump displacement, $\boldsymbol{\sigma}^h$ is in vector form, and $\boldsymbol{n}\cdot\boldsymbol{m} = \sqrt{3}b/\sqrt{3-b^2}$. Note that Eq. $(3.31)_2$ imposes the following conditions

$$q^h_{\mathcal{S}_e} = \frac{1}{A_e}\int_{\Omega^h_{\text{loc},e}} \boldsymbol{m}_e\cdot\boldsymbol{s}^h\cdot\boldsymbol{n}_e\,d\Omega \tag{3.32}$$

and

$$p^h_{\mathcal{S}_e} = \frac{1}{3A_e}\int_{\Omega^h_{\text{loc},e}} \operatorname{tr}(\boldsymbol{\sigma}^h)\,d\Omega \tag{3.33}$$

for the resolved stress values along the discontinuity $\mathcal{S}_e$. The next step is to linearize the equations in Eq. (3.31) for solution by the Newton-Raphson method, but first consider Eq. $(3.31)_2$ more closely and then the numerical integration of the stress tensor.

Recall the integrated form of the stress-displacement relation from Eq. (2.106):

$$q^h_{\mathcal{S}_e} + \frac{\sqrt{3}\beta}{\sqrt{3-b^2}} p^h_{\mathcal{S}_e} = q^h_{\mathcal{S}_e,\mathrm{loc}} + \frac{\sqrt{3}\beta}{\sqrt{3-b^2}} p^h_{\mathcal{S}_e,\mathrm{loc}} + \frac{\mathcal{H}_\delta}{3-b^2}\zeta^h_e \tag{3.34}$$

where the subscript $(\bullet)_{,\mathrm{loc}}$ designates the resolved stress value at onset of localization. Rewrite Eq. (3.34) for $q^h_{\mathcal{S}_e}$ as

$$q^h_{\mathcal{S}_e} = -\frac{\sqrt{3}\beta}{\sqrt{3-b^2}} p^h_{\mathcal{S}_e} + q^h_{\mathcal{S}_e,\mathrm{loc}} + \frac{\sqrt{3}\beta}{\sqrt{3-b^2}} p^h_{\mathcal{S}_e,\mathrm{loc}} + \frac{\mathcal{H}_\delta}{3-b^2}\zeta^h_e\,. \tag{3.35}$$

Substituting Eq. (3.35) into Eq. $(3.31)_2$ and using Eq. (3.33) yields

$$b_e = \frac{1}{A_e}\int_{\Omega^h_{\mathrm{loc},e}} \boldsymbol{F}^T_e \hat{\boldsymbol{\sigma}}^h \, d\Omega - \left(q^h_{\mathcal{S}_e,\mathrm{loc}} + \frac{\sqrt{3}\beta}{\sqrt{3-b^2}} p^h_{\mathcal{S}_e,\mathrm{loc}} + \frac{\mathcal{H}_\delta}{3-b^2}\zeta^h_e \right) = 0 \tag{3.36}$$

where

$$\hat{\boldsymbol{\sigma}}^h = \boldsymbol{s}^h + \frac{\beta}{3b}\mathrm{tr}(\boldsymbol{\sigma}^h)\{\mathbf{1}\}\,, \tag{3.37}$$

and $\{\mathbf{1}\}$ is the vector form of $\mathbf{1}$. Thus, when linearizing the residual b_e, this new form in Eq. (3.36) must be used.

Recall that the stress $\boldsymbol{\sigma}^h$ is regular, but with a reparameterization of the displacement field in Eq. (3.16), the stress rate becomes

$$\dot{\boldsymbol{\sigma}}^h = \boldsymbol{D}^e \cdot \left[\dot{\bar{\boldsymbol{\epsilon}}}^h_e - \boldsymbol{G}_e\dot{\zeta}^h_e\right] \quad \text{in} \quad \Omega^h_{\mathrm{loc},e}/\mathcal{S}_e \tag{3.38}$$

where $\boldsymbol{D}^e$ is the matrix form of $\boldsymbol{c}^e$ and $\dot{\bar{\boldsymbol{\epsilon}}}^h_e = \boldsymbol{\nabla}^s\dot{\bar{\boldsymbol{u}}}^h_e$. For subsequent derivations, the discretization flag h is left off for certain terms for ease of presentation. Integrating Eq. (3.38) yields

$$\boldsymbol{\sigma}_{n+1} = \boldsymbol{\sigma}^{\mathrm{tr}}_{n+1} - \boldsymbol{D}^e \cdot \boldsymbol{G}_e\Delta\zeta_e \quad \text{in} \quad \Omega^h_{\mathrm{loc},e}/\mathcal{S}_e \tag{3.39}$$

where $\boldsymbol{\sigma}^{\mathrm{tr}}_{n+1} = \boldsymbol{\sigma}_n + \boldsymbol{D}^e \cdot \Delta\bar{\boldsymbol{\epsilon}}_e$, $\Delta\bar{\boldsymbol{\epsilon}}_e = \bar{\boldsymbol{\epsilon}}_{e,n+1} - \bar{\boldsymbol{\epsilon}}_{e,n}$, $\Delta\zeta_e = \zeta_{e,n+1} - \zeta_{e,n}$, and $n+1$ is the current time step. Integrating the stress-displacement relation in Eq. (2.105) yields

$$|q_{\mathcal{S}_e,n+1}| + \frac{\sqrt{3}\beta}{\sqrt{3-b^2}} p_{\mathcal{S}_e,n+1} = |q_{\mathcal{S}_e,\mathrm{loc}}| + \frac{\sqrt{3}\beta}{\sqrt{3-b^2}} p_{\mathcal{S}_e,\mathrm{loc}} + \frac{\mathcal{H}_\delta}{3-b^2}|\zeta_{e,n+1}| \quad \text{on } \mathcal{S}_e \tag{3.40}$$

where $\mathcal{H}_\delta < 0$, and $\mathcal{H}_\delta$ is constant for linear softening along the discontinuity. Note that if one were to change the sign convention from continuum mechanics convention ($\epsilon > 0$ and $\sigma > 0$ in tension for 1D) to soil mechanics convention ($\epsilon > 0$ and $\sigma > 0$ in compression), Eq. (3.40) would still be valid taking account of the appropriate change in sign before the pressure term in the yield function in Eq. (2.57). Thus, the stress update for a localized element e is fully defined by Eqs. (3.39) and (3.40).

3.4.3 Newton-Raphson Iterative Solution Algorithm

A linearization of the (generally) nonlinear finite element equations in Eq. (3.31) for solution by the Newton-Raphson method will now proceed; refer to [80]. Express the residuals as

$$\begin{aligned} \boldsymbol{r}_e(\boldsymbol{d}_e^*, \zeta_e^*) &= \boldsymbol{0} \\ b_e(\boldsymbol{d}_e^*, \zeta_e^*) &= 0 \end{aligned} \tag{3.41}$$

where $\boldsymbol{d}_e^*$ and ζ_e^* exactly satisfy equilibrium. Approximate the displacements as

$$\begin{aligned} \boldsymbol{d}_e^* &\approx \boldsymbol{d}_{e,n+1}^{k+1} = \boldsymbol{d}_{e,n+1}^{k} + \Delta \boldsymbol{d}_e \\ \zeta_e^* &\approx \zeta_{e,n+1}^{k+1} = \zeta_{e,n+1}^{k} + \Delta \zeta_e \end{aligned} \tag{3.42}$$

where $k+1$ is the current iteration, the current iteration increment is $\Delta(\bullet) = (\bullet)_{e,n+1}^{k+1} - (\bullet)_{e,n+1}^{k}$, and $n+1$ is the current time step. Thus, the residuals are expressed as

$$\boldsymbol{r}_e(\boldsymbol{d}_{e,n+1}^{k+1}, \zeta_{e,n+1}^{k+1}) = \boldsymbol{0}$$

$$b_e(\boldsymbol{d}^{k+1}_{e,n+1}, \zeta^{k+1}_{e,n+1}) \;=\; 0\,. \tag{3.43}$$

Linearizing the residuals about the state $(\bullet)^k_{n+1}$ and ignoring higher order terms yields

$$\begin{aligned} -\boldsymbol{r}^k_{e,n+1} &= \boldsymbol{K}^e_{dd}\cdot\Delta\boldsymbol{d}_e \,+\, \boldsymbol{K}^e_{d\zeta}\Delta\zeta_e \\ -b^k_{e,n+1} &= (\boldsymbol{K}^e_{\zeta d}+\boldsymbol{K}^e_{d})\cdot\Delta\boldsymbol{d}_e \,+\, (K^e_{\zeta\zeta}+K^e_{\zeta})\Delta\zeta_e \end{aligned} \tag{3.44}$$

where

$$\begin{aligned} \boldsymbol{K}^e_{dd} &= \int_{\Omega^h_e} \boldsymbol{B}^T_e \frac{\partial\boldsymbol{\sigma}^k_{n+1}}{\partial\boldsymbol{\epsilon}^k_{n+1}}\boldsymbol{B}_e\, d\Omega \\ \boldsymbol{K}^e_{d\zeta} &= -\int_{\Omega^h_e} \boldsymbol{B}^T_e \frac{\partial\boldsymbol{\sigma}^k_{n+1}}{\partial\boldsymbol{\epsilon}^k_{n+1}}\boldsymbol{G}_e\, d\Omega \\ \boldsymbol{K}^e_{\zeta d} &= \frac{1}{A_e}\int_{\Omega^h_{e,\mathrm{loc}}} \boldsymbol{F}^T_e \frac{\partial\hat{\boldsymbol{\sigma}}^k_{n+1}}{\partial\boldsymbol{\epsilon}^k_{n+1}}\boldsymbol{B}_e\, d\Omega \\ \boldsymbol{K}^e_{d} &= -\boldsymbol{K}^e_{\zeta d} \quad \text{(for elastic unloading)} \\ K^e_{\zeta\zeta} &= -\frac{1}{A_e}\int_{\Omega^h_{e,\mathrm{loc}}} \boldsymbol{F}^T_e \frac{\partial\hat{\boldsymbol{\sigma}}^k_{n+1}}{\partial\boldsymbol{\epsilon}^k_{n+1}}\boldsymbol{G}_e\, d\Omega \\ K^e_{\zeta} &= -\frac{\mathcal{H}_\delta}{3-b^2}\,. \end{aligned} \tag{3.45}$$

Since the strain due to the jump displacement is treated as an enhanced strain (see Eq. (3.20)), the jump displacement ζ_e is discontinuous between elements and thus may be condensed out of the equations at the element level to form the reduced system

$$\begin{aligned} -\tilde{\boldsymbol{r}}^k_{e,n+1} &= \tilde{\boldsymbol{K}}^e_{dd}\cdot\Delta\boldsymbol{d}_e \\ \tilde{\boldsymbol{r}}^k_{e,n+1} &= \boldsymbol{r}^k_{e,n+1} \,-\, \boldsymbol{K}^e_{d\zeta}(K^e_{\zeta\zeta}+K^e_{\zeta})^{-1}b^k_{e,n+1} \\ \tilde{\boldsymbol{K}}^e_{dd} &= \boldsymbol{K}^e_{dd} \,-\, \boldsymbol{K}^e_{d\zeta}(K^e_{\zeta\zeta}+K^e_{\zeta})^{-1}(\boldsymbol{K}^e_{\zeta d}+\boldsymbol{K}^e_{d})\,. \end{aligned} \tag{3.46}$$

From Eq. (3.39) and Eq. (3.37) it is possible derive the tangential moduli tensors as

$$\frac{\partial\boldsymbol{\sigma}^k_{n+1}}{\partial\boldsymbol{\epsilon}^k_{n+1}} = \boldsymbol{D}^e\,; \quad \frac{\partial\hat{\boldsymbol{\sigma}}^k_{n+1}}{\partial\boldsymbol{\epsilon}^k_{n+1}} = \hat{\boldsymbol{D}}^e \tag{3.47}$$

where $\boldsymbol{D}^e$ and $\hat{\boldsymbol{D}}^e$ are the matrix forms of $\boldsymbol{c}^e$ and $\hat{\boldsymbol{c}}^e$, respectively:

$$\begin{aligned} \boldsymbol{c}^e &= \bar{K}\,\mathbf{1}\otimes\mathbf{1} + 2\bar{\mu}\,(\boldsymbol{I} - \frac{1}{3}\mathbf{1}\otimes\mathbf{1}) \\ \hat{\boldsymbol{c}}^e &= \frac{\beta}{b}\bar{K}\,\mathbf{1}\otimes\mathbf{1} + 2\bar{\mu}\,(\boldsymbol{I} - \frac{1}{3}\mathbf{1}\otimes\mathbf{1})\,. \end{aligned} \tag{3.48}$$

The elastic tangent $\hat{\boldsymbol{D}}^e$ is not implemented in this fashion because if $b = 0$ for the deviatoric case, $\hat{\boldsymbol{D}}^e$ is undefined. First, write out $\hat{\boldsymbol{D}}^e$ as

$$\hat{\boldsymbol{D}}^e = \begin{bmatrix} \bar{\Lambda} + 2\bar{\mu} & \bar{\Lambda} & 0 \\ \bar{\Lambda} & \bar{\Lambda} + 2\bar{\mu} & 0 \\ 0 & 0 & \bar{\mu} \end{bmatrix} \tag{3.49}$$

where $\bar{\Lambda} = \frac{\beta}{b}(\bar{\lambda} + \frac{2}{3}\bar{\mu}) - \frac{2}{3}\bar{\mu}$. In vector form, $\boldsymbol{F}_e$ from Eq. (3.30) and used in Eq. (3.45) is as follows

$$\boldsymbol{F}_e = \begin{bmatrix} m_1 n_1 \\ m_2 n_2 \\ \frac{1}{2}(m_1 n_2 + m_2 n_1) \end{bmatrix}. \tag{3.50}$$

Taking the matrix product $\boldsymbol{F}_e^T \cdot \hat{\boldsymbol{D}}^e$ yields

$$\boldsymbol{F}_e^T \cdot \hat{\boldsymbol{D}}^e = \begin{bmatrix} (\bar{\Lambda} + 2\bar{\mu}) m_1 n_1 + \bar{\Lambda} m_2 n_2 \\ \bar{\Lambda} m_1 n_1 + (\bar{\Lambda} + 2\bar{\mu}) m_2 n_2 \\ \frac{1}{2}\bar{\mu}(m_1 n_2 + m_2 n_1) \end{bmatrix}. \tag{3.51}$$

Using $\boldsymbol{m}\cdot\boldsymbol{n} = \sqrt{3}b/\sqrt{3-b^2}$, the matrix product becomes

$$\boldsymbol{F}_e^T \cdot \hat{\boldsymbol{D}}^e = \begin{bmatrix} \bar{\Lambda}^{\beta b} + 2\bar{\mu} m_1 n_1 \\ \bar{\Lambda}^{\beta b} + 2\bar{\mu} m_2 n_2 \\ \frac{1}{2}\bar{\mu}(m_1 n_2 + m_2 n_1) \end{bmatrix}. \tag{3.52}$$

where

$$\bar{\Lambda}^{\beta b} = \frac{\sqrt{3}\beta}{\sqrt{3-b^2}}\bar{K} - \frac{2}{3}\bar{\mu}\frac{\sqrt{3}b}{\sqrt{3-b^2}} . \tag{3.53}$$

Thus, the deviatoric case $b = 0$ is clearly defined. For monotonic plastic loading,

$$\boldsymbol{K}_d^e = \boldsymbol{0} , \quad K_\zeta^e = -\frac{\mathcal{H}_\delta}{3-b^2} \tag{3.54}$$

else for elastic unloading,

$$\begin{aligned} \boldsymbol{K}_d^e &= -\boldsymbol{K}_{\zeta d}^e \\ K_\zeta^e &= 0 \\ \tilde{\boldsymbol{K}}_{dd}^e &= \boldsymbol{K}_{dd}^e . \end{aligned} \tag{3.55}$$

The stress integration algorithm along the discontinuity in a localized element with linear softening is summarized as follows:

1) compute the trial state by freezing localized plastic flow (i.e., use $\zeta_{e,n}$) and incrementing the total strain:

$$\begin{aligned} \boldsymbol{\sigma}_{n+1}^{\mathrm{tr},(k+1)} &= \boldsymbol{\sigma}_n + \boldsymbol{c}^e : (\bar{\boldsymbol{\epsilon}}_{n+1}^{k+1} - \bar{\boldsymbol{\epsilon}}_n) \\ p_{n+1}^{\mathrm{tr},(k+1)} &= \frac{1}{3}\mathrm{tr}\left(\boldsymbol{\sigma}_{n+1}^{\mathrm{tr},(k+1)}\right) \\ \boldsymbol{s}_{n+1}^{\mathrm{tr},(k+1)} &= \boldsymbol{\sigma}_{n+1}^{\mathrm{tr},(k+1)} - p_{n+1}^{\mathrm{tr},(k+1)}\boldsymbol{1} \\ q_{\mathcal{S}_e,n+1}^{\mathrm{tr},(k+1)} &= \frac{1}{A_e}\int_{\Omega_{\mathrm{loc},e}^h} \boldsymbol{m}_e \cdot \boldsymbol{s}_{n+1}^{\mathrm{tr},(k+1)} \cdot \boldsymbol{n}_e \, d\Omega \\ p_{\mathcal{S}_e,n+1}^{\mathrm{tr},(k+1)} &= \frac{1}{3A_e}\int_{\Omega_{\mathrm{loc},e}^h} \mathrm{tr}(\boldsymbol{\sigma}_{n+1}^{\mathrm{tr},(k+1)})\, d\Omega \\ Q_{\mathcal{S}_e}^{\mathrm{tr}} &= \left(\left|q_{\mathcal{S}_e,n+1}^{\mathrm{tr},(k+1)}\right| + \frac{\sqrt{3}\beta}{\sqrt{3-b^2}} p_{\mathcal{S}_e,n+1}^{\mathrm{tr},(k+1)}\right) \\ &\quad - \left(|q_{\mathcal{S}_e,\mathrm{loc}}| + \frac{\sqrt{3}\beta}{\sqrt{3-b^2}} p_{\mathcal{S}_e,\mathrm{loc}} + \frac{\mathcal{H}_\delta}{3-b^2}\,|\zeta_{e,n}|\right) \end{aligned} \tag{3.56}$$

2) check for yielding along the discontinuity $\mathcal{S}_e$, and if yielding is detected, update stress:

```
IF ($Q^{\mathrm{tr}}_{\mathcal{S}_e} > 0$)[†] THEN
    $\left|q^{k+1}_{\mathcal{S}_e,n+1}\right| + \frac{\sqrt{3}\beta}{\sqrt{3-b^2}} p^{k+1}_{\mathcal{S}_e,n+1} = |q_{\mathcal{S}_e,\mathrm{loc}}| + \frac{\sqrt{3}\beta}{\sqrt{3-b^2}} p_{\mathcal{S}_e,\mathrm{loc}} + \frac{\mathcal{H}_\delta}{3-b^2}\left|\zeta^{k+1}_{e,n+1}\right|$
    $\boldsymbol{K}^e_d = \boldsymbol{0}$
    $K^e_\zeta = -\mathrm{sign}(q^{\mathrm{tr},(k+1)}_{\mathcal{S}_e,n+1})\mathrm{sign}(\zeta^{k+1}_{e,n+1})\frac{\mathcal{H}_\delta}{3-b^2}$
ELSE
    $q^{k+1}_{\mathcal{S}_e,n+1} = q^{\mathrm{tr},(k+1)}_{\mathcal{S}_e,n+1}$
    $p^{k+1}_{\mathcal{S}_e,n+1} = p^{\mathrm{tr},(k+1)}_{\mathcal{S}_e,n+1}$
    $\zeta^{k+1}_{e,n+1} = \zeta_{e,n}$
    $\boldsymbol{K}^e_d = -\boldsymbol{K}^e_{\zeta d}$
    $K^e_\zeta = 0$
ENDIF
```

[†] Even for monotonic plastic loading, sometimes during an iteration sequence this check for yielding on the discontinuity is not passed, although softening along the discontinuity should occur. Thus, another check like $|q^{\mathrm{tr},(k+1)}_{\mathcal{S}_e,n+1}| > |q_{\mathcal{S}_e,n}|$ is necessary. What should be observed is that $|q|$ and $|p|$ are decreasing for softening along the discontinuity.

The following outlines the iterative Newton-Raphson algorithm:

1) initialize displacements ($k = 0$):

$$\begin{aligned} \boldsymbol{d}^k_{e,n+1} &= \boldsymbol{d}_{e,n} + \delta \boldsymbol{d}_e \\ \zeta^k_{e,n+1} &= \zeta_{e,n} \end{aligned}$$

where $\delta \boldsymbol{d}_e$ is the prescribed displacement increment for a strain-driven problem.

2) form residual and tangent:

$$\begin{aligned} \tilde{\boldsymbol{r}}^k_{n+1} &= \mathop{\mathsf{A}}_{e=1}^{n_{el}} \tilde{\boldsymbol{r}}^k_{e,n+1} \\ \tilde{\boldsymbol{K}}_{dd} &= \mathop{\mathsf{A}}_{e=1}^{n_{el}} \tilde{\boldsymbol{K}}^e_{dd} \end{aligned}$$

3) then solve for $\Delta \boldsymbol{d}$:

$$-\tilde{\boldsymbol{r}}^k_{n+1} = \tilde{\boldsymbol{K}}_{dd} \cdot \Delta \boldsymbol{d}$$

4) reform displacements for each element:

$$\begin{aligned} \boldsymbol{d}^{k+1}_{e,n+1} &= \boldsymbol{d}^k_{e,n+1} + \Delta \boldsymbol{d}_e \\ \zeta^{k+1}_{e,n+1} &= \zeta^k_{e,n+1} + \Delta \zeta_e \end{aligned}$$

where

$$\Delta \zeta_e = \frac{-1}{K^e_{\zeta\zeta} + K^e_{\zeta}} \left(b^k_{e,n+1} + (\boldsymbol{K}^e_{\zeta d} + \boldsymbol{K}^e_{d}) \cdot \Delta \boldsymbol{d}_e \right)$$

5) reform residual and check for convergence:

`IF` $\|\tilde{\boldsymbol{r}}^{k+1}_{n+1}\| < r^{\mathrm{tol}}$ `THEN` converged, and `GOTO` step 6

`ELSE` $k = k + 1$ and iterate, `GOTO` step 2

6) update displacements and continue with next load step:

$$
\begin{aligned}
\boldsymbol{d}_{e,n+1} &= \boldsymbol{d}_{e,n+1}^{k+1} \\
\zeta_{e,n+1} &= \zeta_{e,n+1}^{k+1}
\end{aligned}
$$

For the numerical simulations in Chapter 4, $r^{\mathrm{tol}} = 1 \times 10^{-10}$.

3.5 Summary

In this chapter, a Drucker-Prager plasticity model with strong discontinuity was implemented—along with an enhanced quadrilateral element—within the AES method, which ensures that enhanced finite element solutions are convergent. The nonlinear matrix finite element equations were formed, and a Newton-Raphson iterative solution scheme was outlined. The numerical integration of the stress at a Gauss point and the resolved stress along the discontinuity (within a localized element) were delineated.

Chapter 4

Numerical Simulations

4.1 Introduction

Numerical simulations conducted in plane strain are presented to demonstrate objectivity with respect to mesh refinement and insensitivity to mesh alignment of finite element solutions employing a Drucker-Prager plasticity model with strong discontinuity. Objectivity with respect to mesh refinement is shown by the load-displacement curves having similar slopes during softening for the enhanced finite element solutions; the standard finite element solutions show different slopes during softening (i.e., dissipation due to plastic softening varies with a varying softening slope; see Appendix A). Insensitivity to mesh alignment is evident by slip lines orienting sharply in the mesh without element sides being aligned with the expected slip line orientation and by the slip lines having similar orientation and location for each mesh refinement. All meshes (except the first example, simple shear) shown here are unstructured in the sense that no attempt is made to align element sides with an expected slip line orientation.

All analyses are drained analyses, for which either the water table is deeper than the problem geometry considered, or enough time has passed such that excess hydrostatic pore pressures have dissipated (thus, the effect of fluid flow is neglected). All analyses are run using a modified version of the finite element code `SPIN2D` written by Borja [12]. The modified version is called `SPIN2D-LOC` and contains the localization element and material subroutines written by the author.

The standard elements used are linear or quadratic quadrilateral elements with standard numerical integration (i.e., 2×2 for linear quad and 3×3 for quadratic quad) for dilative plastic flow and the $\bar{B}$-method [33] for deviatoric plastic flow to address the problem of mesh locking for incompressible plasticity in the infinitesimal strain regime.

The numerical implementation of the localization condition in Eq. (2.84), checked at each Gauss point, is as follows:

$$\begin{array}{lll} \texttt{IF} & \left| \dfrac{\|\boldsymbol{s}_{n+1}\|}{\sqrt{2}r_{n+1}} - \sqrt{\dfrac{3}{3-b^2}} \right| \leq h^{\mathrm{tol}} & \text{at a Gauss point,} \\ \texttt{THEN} & \text{the element has localized} & \end{array} \tag{4.1}$$

where $h^{\mathrm{tol}} = 1 \times 10^{-5}$ unless otherwise noted.

A note on post-processing for deformed meshes for enhanced solutions (i.e., with localized elements). Because the strong discontinuity approach is implemented within the assumed enhanced strain method, the strains within the localized finite elements are enhanced accordingly, and not the shape functions themselves. Thus, localized elements are shaded, as opposed to tracing the actual slip line through the meshes (which is what determines, by the way, which enhanced strain function to choose; refer again to Figs. 3.2 and 3.3).

4.2 Simple Examples

First, some simple numerical examples are presented to demonstrate the attributes of the strong discontinuity approach. The value $h^{\mathrm{tol}} = 1 \times 10^{-5}$ is used along with linear quadrilateral elements.

4.2.1 Simple Shear: von Mises Plasticity

Material properties are displayed in Table 4.1, and boundary conditions are shown in Fig. 4.1. The yield stress σ_Y in an element at the middle of each mesh is lowered by 25% to clearly define the initiation of the slip line and to cause localization of deformation for the standard finite element solution. The yield stress in the middle element could be lowered less than 25% (i.e., 1%; see section on Gosford sandstone).

E	20 MPa
ν	0.4
σ_Y	40 kPa
H'	–100 kPa
H_δ	–200 kPa/m

Table 4.1. Material parameters for simple shear example.

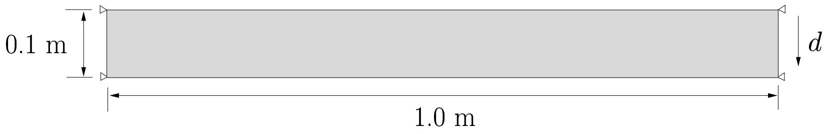

Figure 4.1. Plane strain simple shear. Boundary conditions and dimensions.

Note that the element sides are aligned with the expected slip line orientation and that, as a result, the standard finite element meshes are able to accurately capture the expected localized mode (see Fig. 4.2). This is a result of the standard C^0 theory of continuum finite element analysis: displacement fields are continuous across element boundaries while strain fields are not (refer to HUGHES [35]). Viewing the load-displacement plots in Fig. 4.3, however, mesh-dependence is observed in the form of decreasing plastic dissipation (considering dissipated energy as the area beneath the curve or that considered in Appendix A) due to softening plastic flow being localized to an element of smaller and smaller area as the mesh is refined. For the enhanced solution curves, mesh-independence is observed by the slopes of the softening portions of the curves being the same. In fact, because of the problem's simple geometry and nearly uniform stress state (which results in an overall linear slip line through the mesh; refer to the slope stability problem in Section 4.6 and excavation problem in Section 4.7 below for curved slip lines) the enhanced solution curves lie one on top of the other.

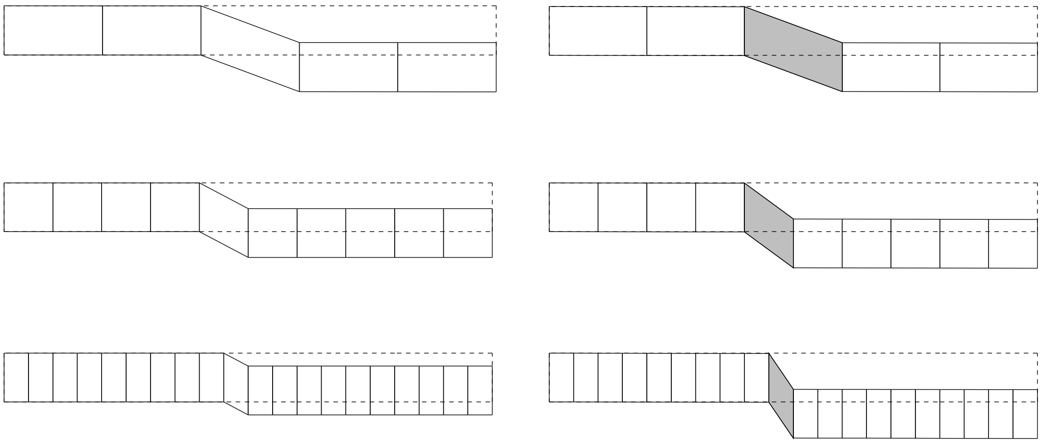

Figure 4.2. Plane strain simple shear. Deformed meshes.

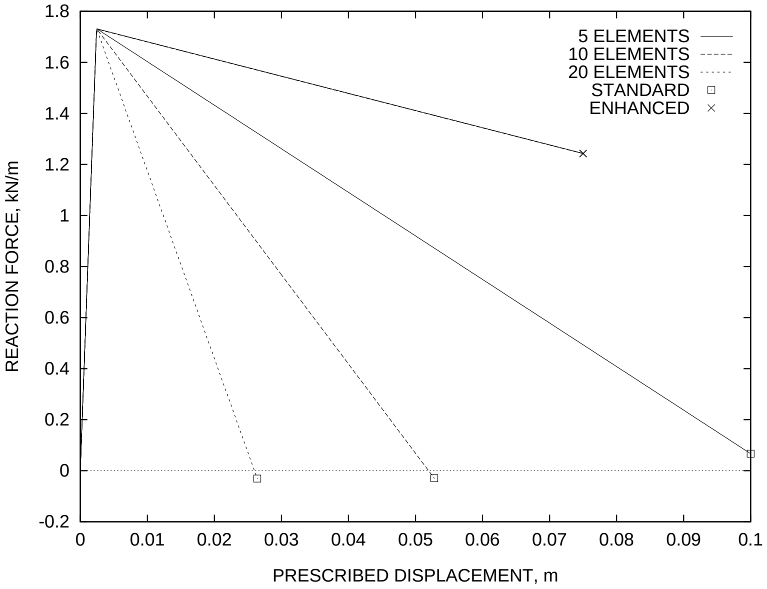

Figure 4.3. Plane strain simple shear. Load-displacement curves.

4.2.2 Compression: Drucker-Prager

Material properties are displayed in Table 4.2, and boundary conditions are shown in Fig. 4.4. The cohesion $\bar{c}$ in an element at the middle of each mesh is lowered by 25% to clearly define the initiation of the slip line.

E	20 MPa
ν	0.4
$\bar{c}$	20 kPa
$\bar{\phi}$	30°
b	0.49487, 0.0
H', K'	–50 kPa
H_δ, K_δ	–200 kPa/m

Table 4.2. Material parameters for one-element-wide compression example.

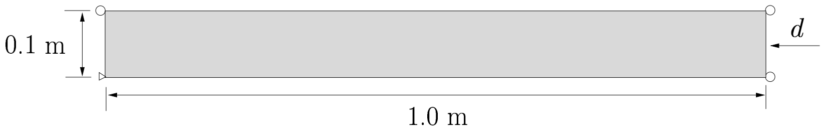

Figure 4.4. Plane strain one-element-wide compression example. Boundary conditions and dimensions.

Note that the element sides are not aligned with the expected slip line orientation and that, as a result, the standard finite element meshes are not able to accurately capture the expected localized mode (see Figs. 4.5 and 4.7). In Fig. 4.5, the 5-element mesh is too stiff and essentially represents a homogeneous deformation pattern, while the 10-element mesh represents a squashing deformation pattern, and the 20-element mesh a barreling deformation pattern. In Fig. 4.7, each mesh attempts to represent a barreling deformation pattern diffusely.

Viewing the load-displacement plots in Figs. 4.6, 4.8, and 4.9, mesh-dependence is again observed in the form of decreasing plastic dissipation due to softening plastic flow being localized to elements of smaller and smaller total area as the mesh is refined. For the enhanced solution curves, mesh-independence is observed by the slopes of the softening portions of the curves being similar. For associative, dilative plastic flow ($\beta = b = 0.49487$) in Fig. 4.6, the slope of the enhanced solution curve for the 20-element mesh eventually reaches that of the curves for the 5 and 10-element meshes, but the curve itself does not lie on top of the others as is the case for simple shear in Fig. 4.3. This result will be elucidated in the section describing the unconfined compression example, and essentially results from not all plastic flow being localized to the discontinuity as dilation in the localized elements is causing adjacent non-localized elements to develop continuing plastic deformation instead of unloading elastically (this will be discussed in more detail in Section 4.3). Contour plots for the unconfined compression example make this point clear. For non-associative, deviatoric plastic flow ($\beta = 0.49487$, $b = 0.0$) in Figs. 4.8 and 4.10, the enhanced solution curves have similar slopes during the softening regime.

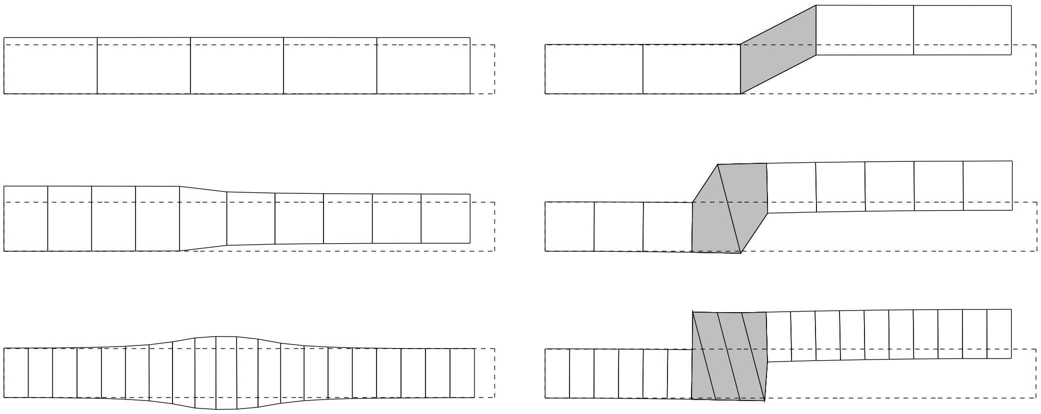

Figure 4.5. Plane strain one-element-wide compression. Deformed meshes. Associative, dilative plastic flow ($\beta = b = 0.49487$).

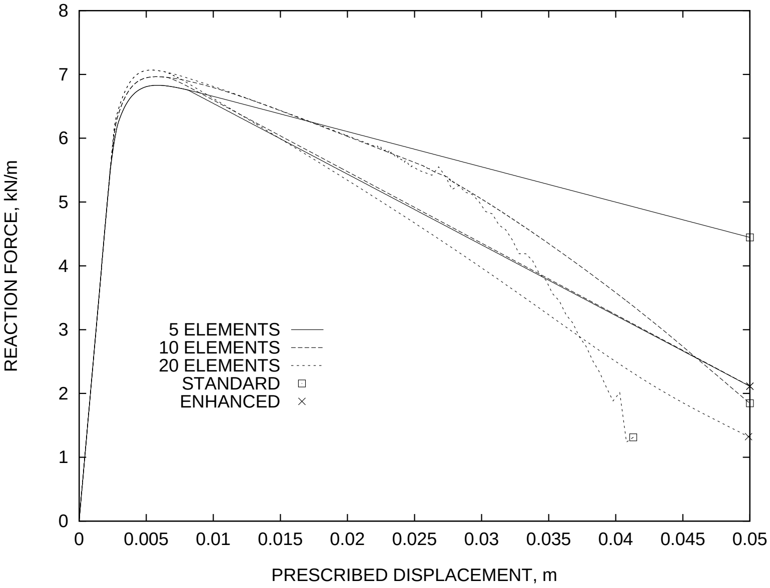

Figure 4.6. Plane strain one-element-wide compression. Load-displacement curves. Associative, dilative plastic flow ($\beta = b = 0.49487$).

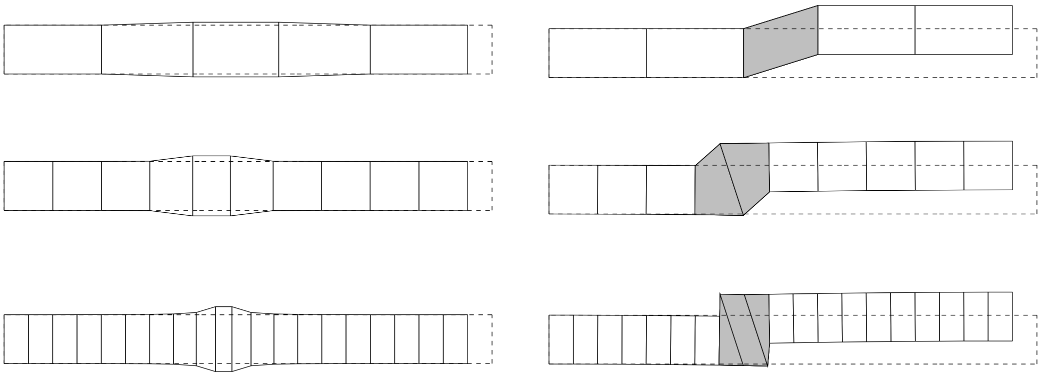

Figure 4.7. Plane strain one-element-wide compression. Deformed meshes. Non-associative, deviatoric plastic flow ($\beta = 0.49487\,,\ b = 0.0$).

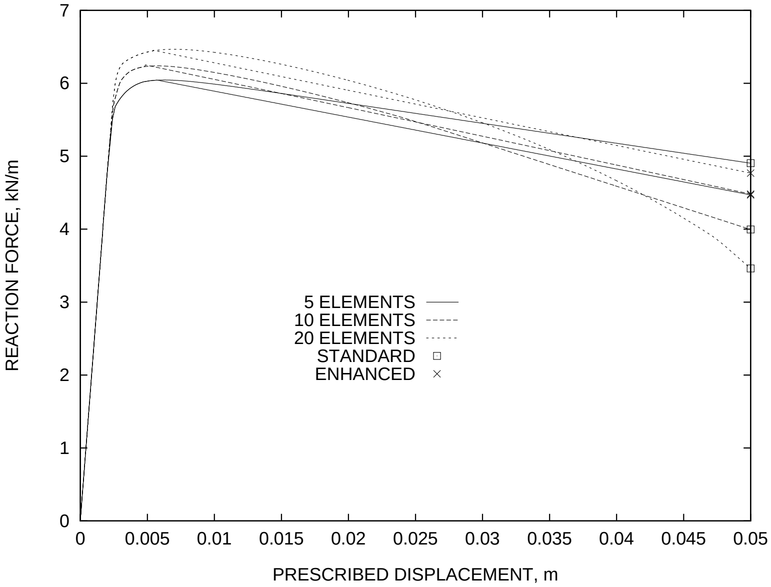

Figure 4.8. Plane strain one-element-wide compression. Load-displacement curves. Non-associative, deviatoric plastic flow ($\beta = 0.49487\,,\ b = 0.0$).

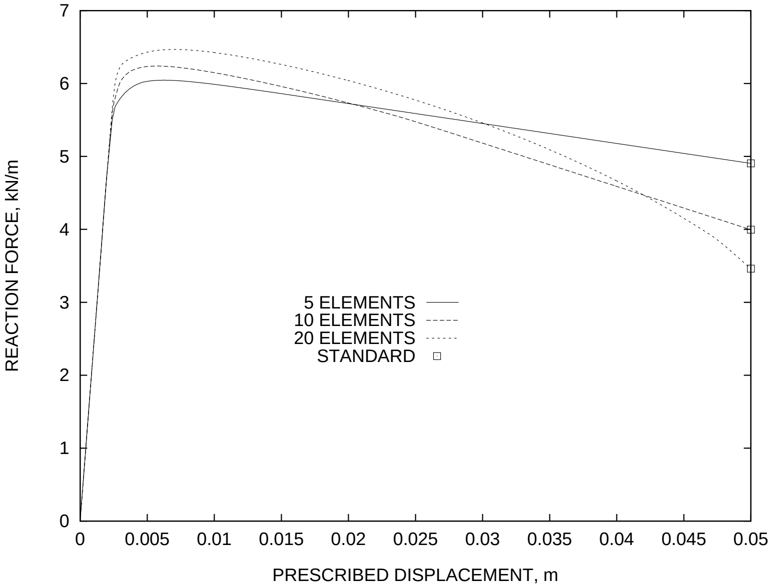

Figure 4.9. Plane strain one-element-wide compression. Load-displacement curves for standard solution. Non-associative, deviatoric plastic flow ($\beta = 0.49487\,,\ b = 0.0$).

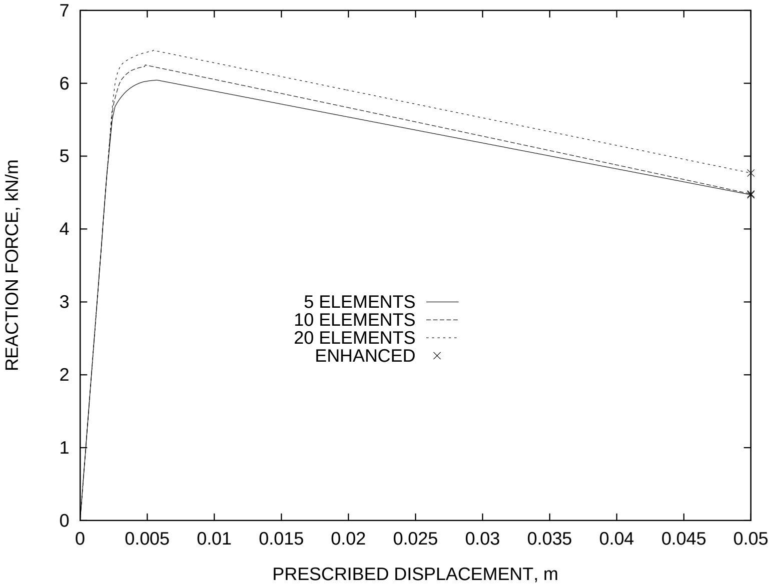

Figure 4.10. Plane strain one-element-wide compression. Load-displacement curves for enhanced solution. Non-associative, deviatoric plastic flow ($\beta = 0.49487\,,\ b = 0.0$).

4.3 Plane Strain Unconfined Compression Problem

Consider a strain-driven unconfined compression problem as shown in Figure 4.11. Three levels of mesh refinement are used to analyze the problem: 75-element mesh, 300-element mesh, and 1200-element mesh. Material properties are as summarized in Table 4.3. Three cases are considered: $b = \beta = 0.49487$ (associative, dilative plastic flow), $b = 0.3$ (non-associative, dilative plastic flow), and $b = 0$ (non-associative, deviatoric plastic flow). The $\bar{B}$-method [33] is employed to alleviate mesh locking for incompressible plastic flow ($b = 0$). The geometry and boundary conditions are shown in Fig. 4.11.

E	20 MPa
ν	0.4
$\bar{c}$	20 kPa
$\bar{\phi}$	30°
b	0.49487, 0.3, 0.0
H', K'	–50 kPa
H_δ, K_δ	–2 MPa/m

Table 4.3. Material parameters for unconfined compression problem.

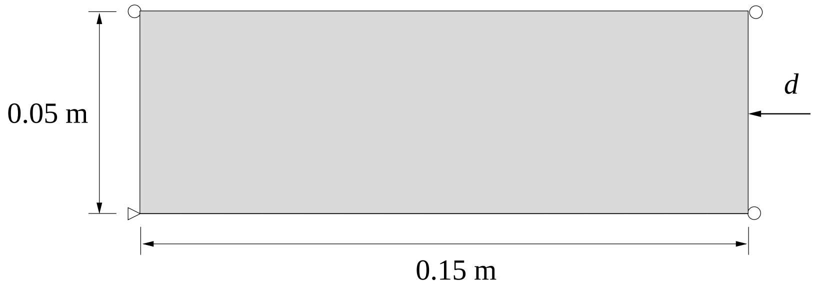

Figure 4.11. Plane strain unconfined compression problem with prescribed displacement, d.

In order to define the initiation of the slip line (i.e., first element to localize), the uniform stress state is perturbed by lowering the cohesion in one side element (see Fig. 4.12 for location of the weakened element for each mesh). A value of cohesion, $\bar{c}_{\text{weak}} = 15\,\text{kPa}$, is arbitrarily chosen, which corresponds to a 25% imperfection.

Results are shown in Figs. 4.13 to 4.26, with Figs. 4.13 to 4.20 showing results using an enhanced four-noded linear quadrilateral element for the three cases with varying b, and Figs. 4.27 and 4.26 showing results using an enhanced nine-noded quadratic quadrilateral element for the associative case. Note that the functions displayed in Fig. 3.3 are applicable to any quadrilateral element, quadratic or linear.

Figures 4.12 and 4.13 show results for the associative case with $\bar{\phi} = 30°, b = \beta = 0.49487$. Figure 4.13 is a plot of reaction force at the left-hand end of the mesh versus the prescribed displacement at the right-hand end. Objectivity with respect to mesh refinement is demonstrated by the eventual similar slopes of the enhanced solution curves during softening; the slopes of the standard solution curves during softening are different. Figure 4.12 demonstrates the bulging, diffuse deformation of the standard solutions and the sharp slip line orientation through unstructured meshes for the enhanced solutions. Figures 4.18 and 4.19 show results for non-associative, dilative plastic flow ($b = 0.3$). The same comments made for the associative case apply for this case as well. Figures 4.20 and 4.21 show results for non-associative, deviatoric plastic flow ($b = 0$). For this case the slopes of the enhanced solution curves during softening are similar earlier in the softening phase than for the two previous cases, and the slopes of the standard solution curves are more variable.

To address the dissimilar initial slopes of the enhanced solution curves upon softening as shown in Figs. 4.13 and 4.19, three different approaches were attempted. At first, it was speculated that since the area of weak material varied between the three meshes as a result of only one element in each mesh being weakened at the same location, possibly having equal areas of weak material for each mesh would alleviate these dissimilar initial slopes (i.e., one element for the 75-element mesh, four for the 300-element mesh, and sixteen for the 1200-element mesh). Upon applying this idea to the associative case, it was discovered that this approach did not address the problem of dissimilar initial slopes. Actually, it was found that elements in this weak area for the finer meshes, which had not been traced by the slip line and thus did not include strain enhancement, continued to plastify even though the slip line had fully propagated through the mesh, which signals that all plastic flow should be localized to the discontinuity. Second, it was considered that maybe the perturbation was too great (originally chosen at 25%). The material was weakened by 1% instead ($c_{\text{weak}} = 19.8\,\text{kPa}$) for the associative case, but it was found that this did not make the initial slopes of the enhanced solutions any more similar than that shown in Fig. 4.13. This result was expected because by weakening the one side element less, it is expected that the element's Gauss points will only plastify later and thus also localize later in the load history, as was observed. Finally, a p-type (higher order interpolation polynomial) refinement as opposed to an h-type (more of the same order elements) for the associative case was considered. This appeared to address the problem somewhat, as shown by the curves in Fig. 4.27 (deformed meshes are shown in Fig. 4.26), but still exhibited dissimilar initial slopes of the enhanced solution curves upon softening for the non-associative, dilative case ($b = 0.3$) and for the non-associative, deviatoric case ($b = 0$). The apparent oscillations in the latter portion of the enhanced solution curves in Fig. 4.27 may be explained by the increasing tension stresses at some Gauss points within certain localized elements because before these oscillations occured the tension stresses were minimal or nonexistent in these elements.

Contours of effective plastic strain ($\dot{\bar{\epsilon}}^p = \sqrt{\frac{2}{3}\dot{\boldsymbol{\epsilon}}^p : \dot{\boldsymbol{\epsilon}}^p}$) help to explain the different initial slopes of the enhanced solution curves shown in Fig. 4.12 for the associative, dilative plastic flow case. Contours of effective plastic strain for standard and enhanced solutions are shown in Figs. 4.14 and 4.15. Figure 4.14 shows the varying amounts of plastic strain which have accumulated in each mesh for the standard solution, which verifies the mesh-dependence of the standard solution for softening plasticity. Contours in Fig. 4.15 show plastic strain accumulating in elements adjacent to the localized elements along the slip line, which contradicts the expected result that all plastic flow be localized to the discontinuity. This non-localized plastic flow is most likely due to the dilation of the localized elements because for the deviatoric case in Fig. 4.23, less non-localized plastic flow is observed, and the slopes of the enhanced solution curves are similar throughout the loading history. Continuing with the associative, dilative plastic flow case, varying amounts of non-localized plastic flow are observed for each mesh which explains the different initial slopes of the enhanced solution curves in Fig. 4.13. The slopes eventually become the same as the accumulated non-localized plastic flow becomes constant, and the localized plastic flow governs the overall softening. The apparent valleys in Fig. 4.15 are a result of plastic flow being localized to the discontinuity within the localized elements. As a result, the effective plastic strain at the Gauss points in the localized elements is that which had accumulated before the localized elements had localized. Contours of octahedral shear strain ($\gamma_{\text{oct}} = \frac{1}{3}\sqrt{(\epsilon_1 - \epsilon_2)^2 + \epsilon_1^2 + \epsilon_2^2}$ for plane strain) for standard and enhanced solutions are shown in Figs. 4.16 and 4.17 to illustrate the effect of the enhanced strain due to the displacment jump.

For the non-associative, deviatoric plastic flow case, contour plots of effective plastic strain for the standard and enhanced solutions are shown in Figs. 4.22 and 4.23. The slopes of the enhanced solution curves are the same in Fig. 4.21 because the amount of non-localized plastic flow shown in Fig. 4.23 appears to be insignificant. Contours of octahedral shear strain for standard and enhanced solutions are shown in

Figs. 4.24 and 4.25 to illustrate the effect of the enhanced strain due to the displacment jump.

For the associative, dilative plastic flow case with quadratic quadrilateral elements, contour plots of effective plastic strain for the standard and enhanced solutions are shown in Figs. 4.28 and 4.29. In this case, non-localized plastic flow is significant for the enhanced solution as shown in Fig. 4.29 but appears to occur in similar amounts between the two meshes, which leads to similar slopes of the enhanced solution curves in Fig. 4.27. Thus, the choice of base element interpolation—linear or quadratic—affects the performance of the enhanced solution. Contours of octahedral shear strain for standard and enhanced solutions are shown in Figs. 4.30 and 4.31 to illustrate the effect of the enhanced strain due to the displacment jump.

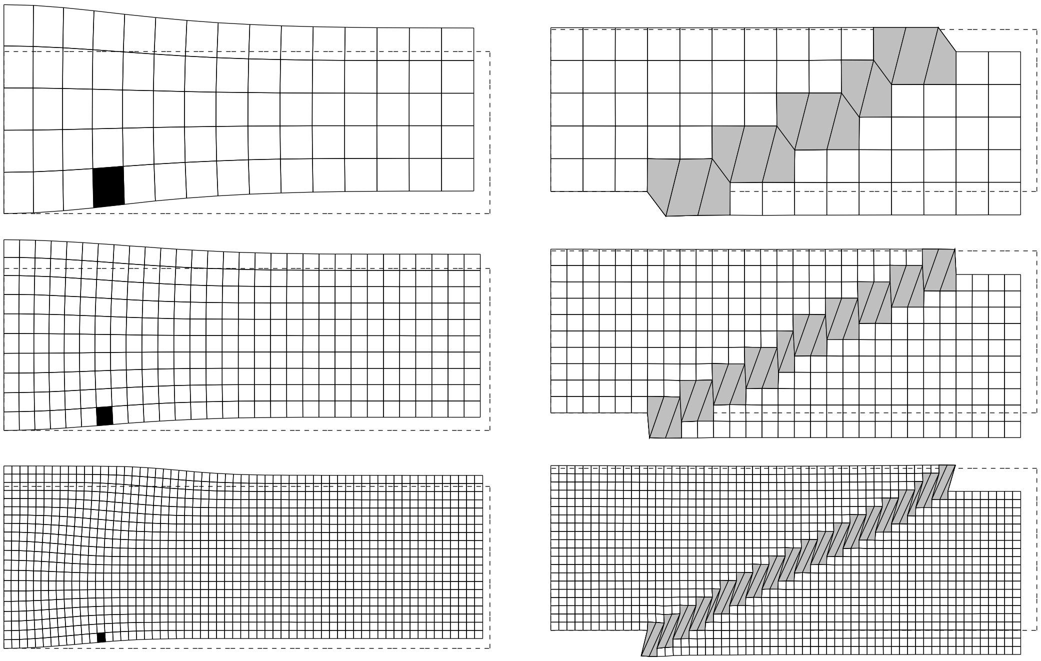

Figure 4.12. Plane strain compression problem: Associative, dilative plastic flow ($\beta = b = 0.49487$). Seventy-five, 300, and 1200 linear quadrilateral elements. Location of weakened element indicated by black squares on the deformed meshes resulting from the standard finite element solution. Localized elements are shaded. Slip lines trace sharply through unstructured meshes for enhanced solution, while standard solution meshes exhibit diffuse deformation.

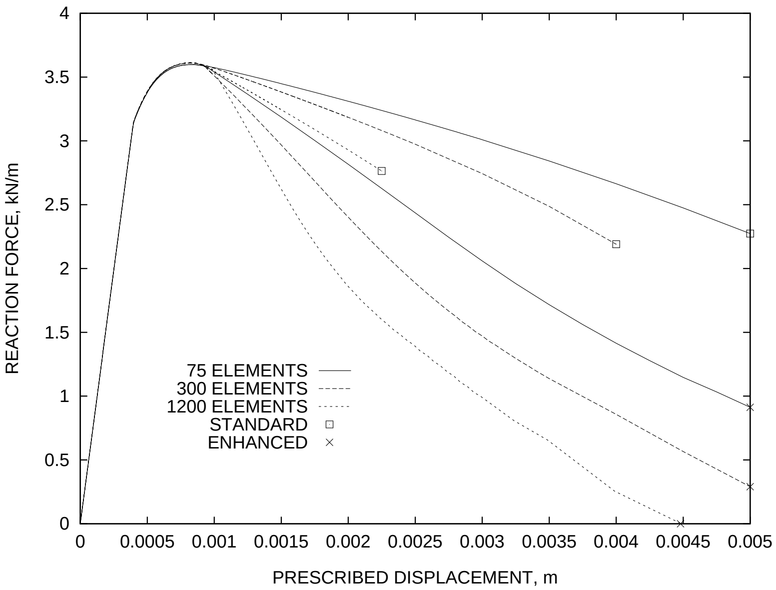

Figure 4.13. Plane strain compression problem: associative, dilative plastic flow ($\beta = b = 0.49487$). $h^{\text{tol}} = 0.005$. Eventual similar slopes of enhanced solution curves demonstrate objectivity with respect to mesh refinement.

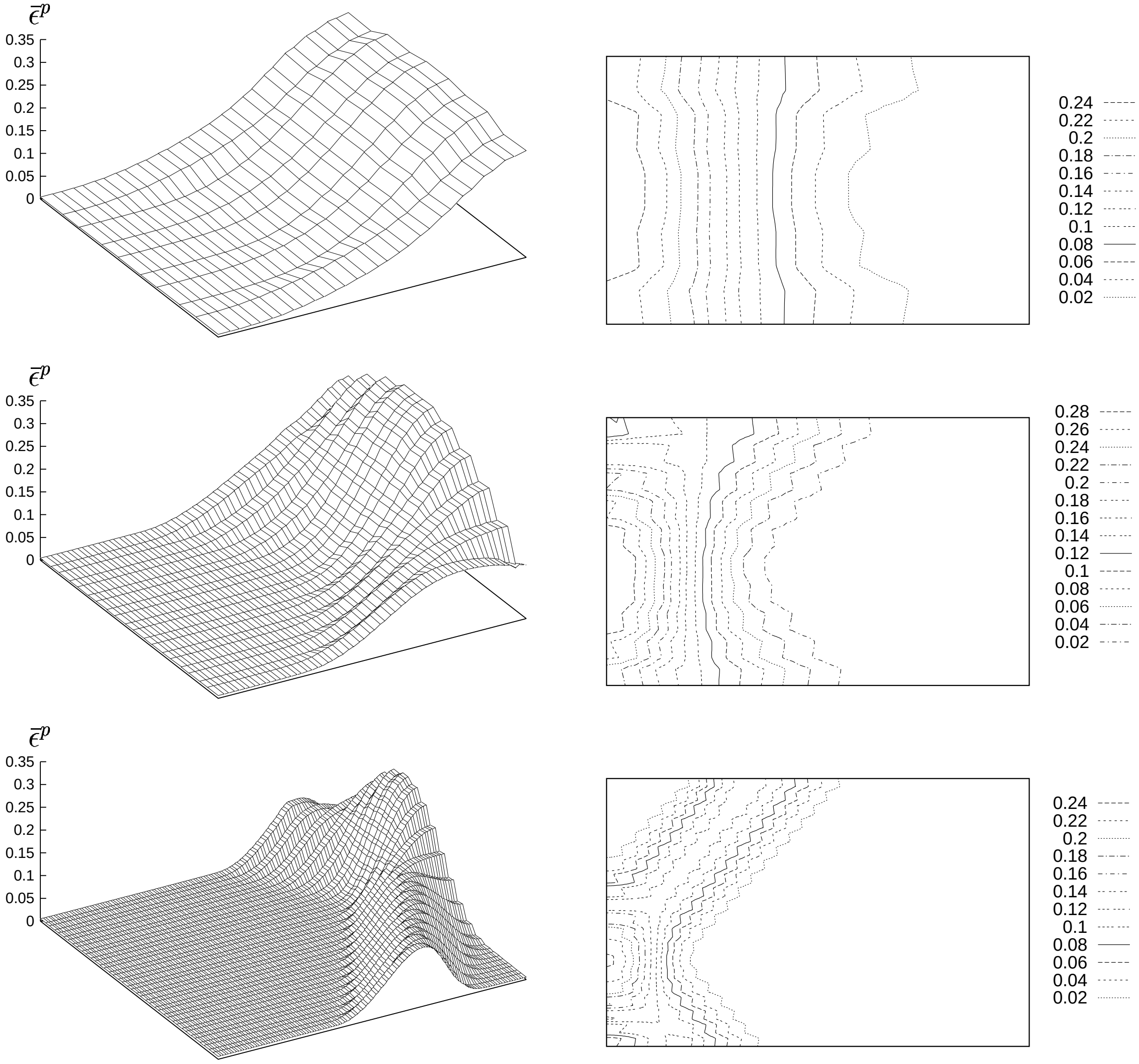

Figure 4.14. Contour plots of effective plastic strain $\bar{\epsilon}^p$ (× 100 %) for standard solution at end of loading: 75, 300, and 1200 linear quadrilateral elements. ($\beta = b = 0.49487$).

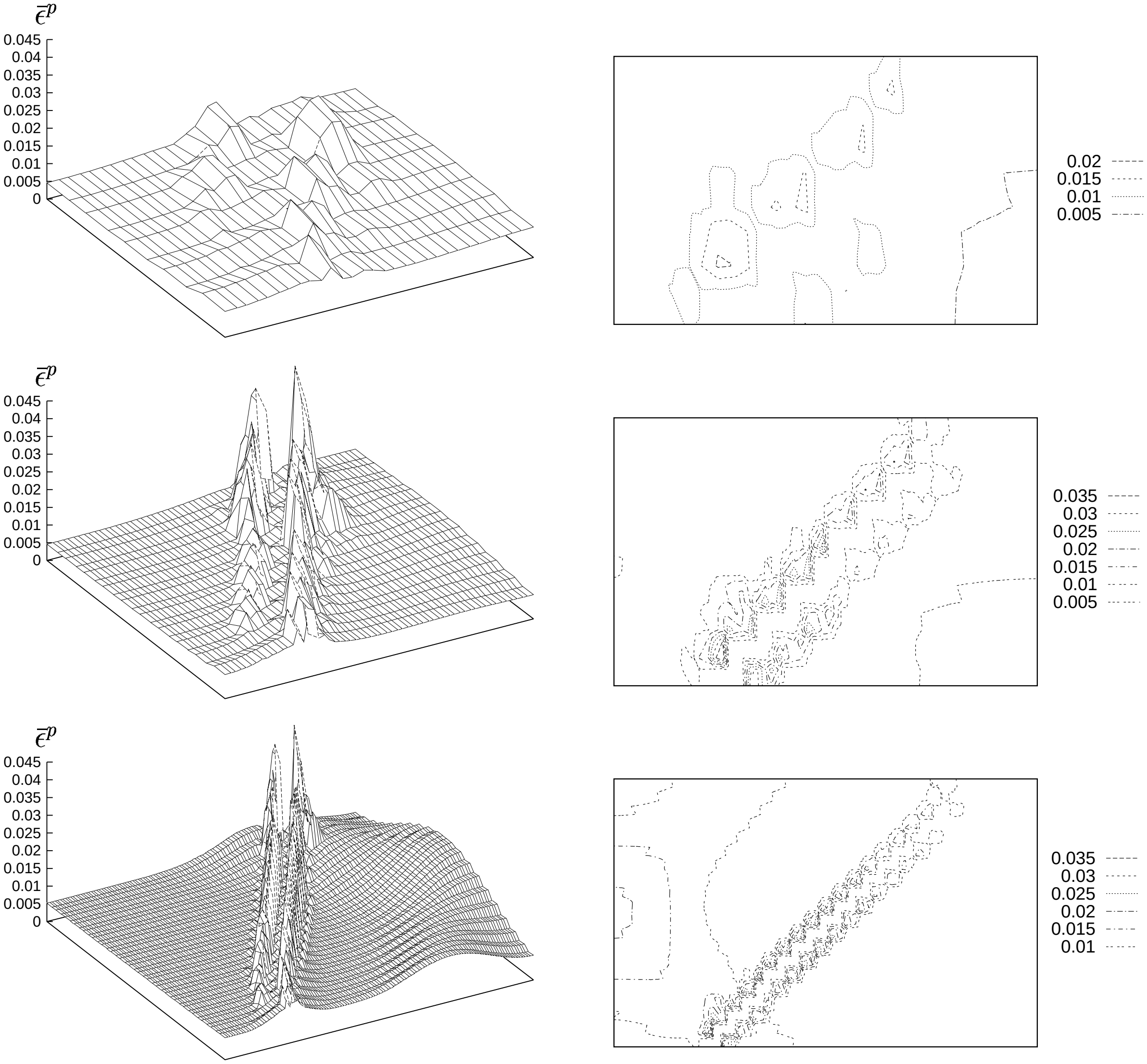

Figure 4.15. Contour plots of effective plastic strain $\bar{\epsilon}^p$ (× 100 %) for enhanced solution at end of loading: 75, 300, and 1200 linear quadrilateral elements. ($\beta = b = 0.49487$).

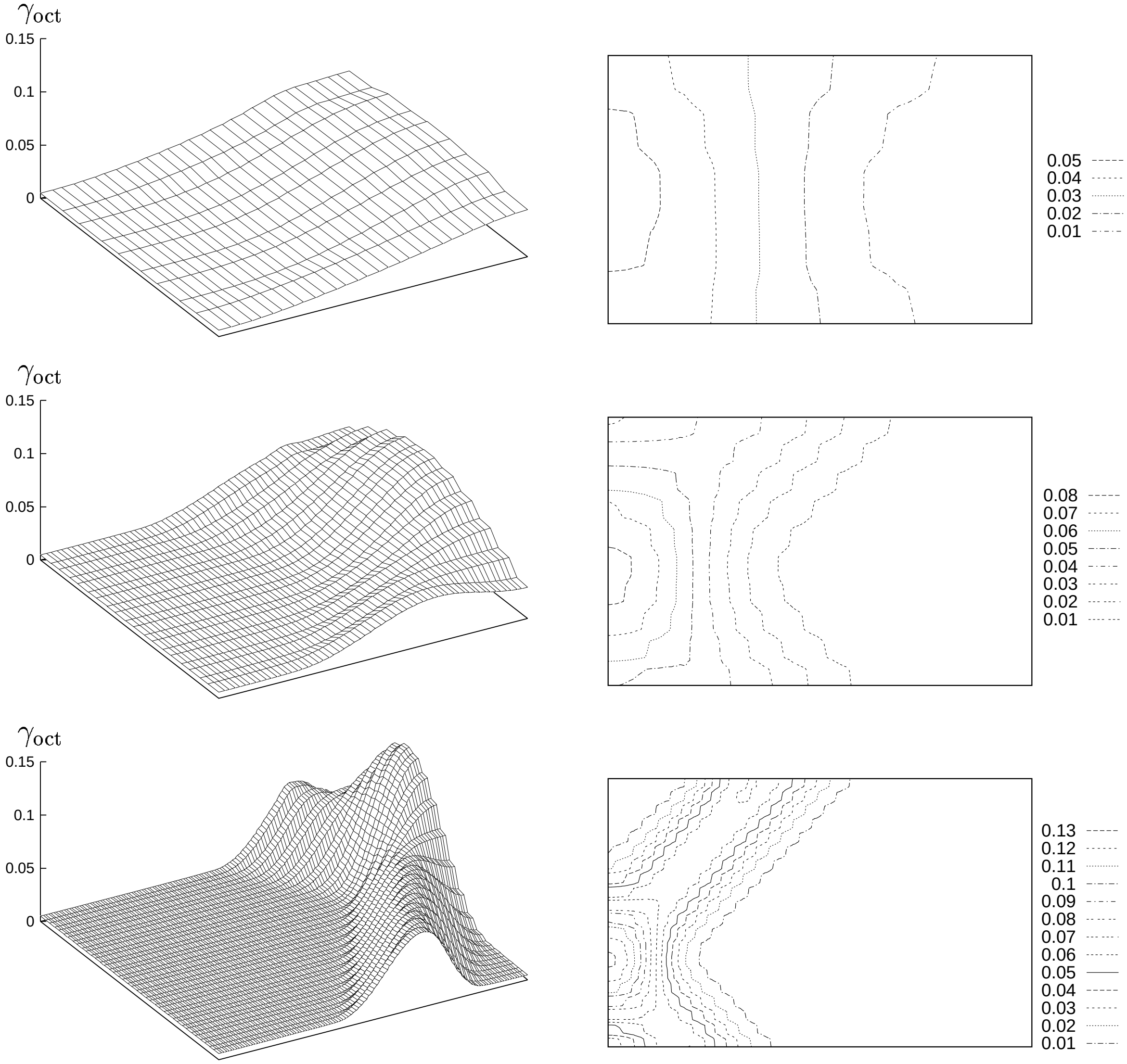

Figure 4.16. Contour plots of octahedral shear strain γ_{oct} (× 100 %) for standard solution at end of loading: 75, 300, and 1200 linear quadrilateral elements. ($\beta = b = 0.49487$).

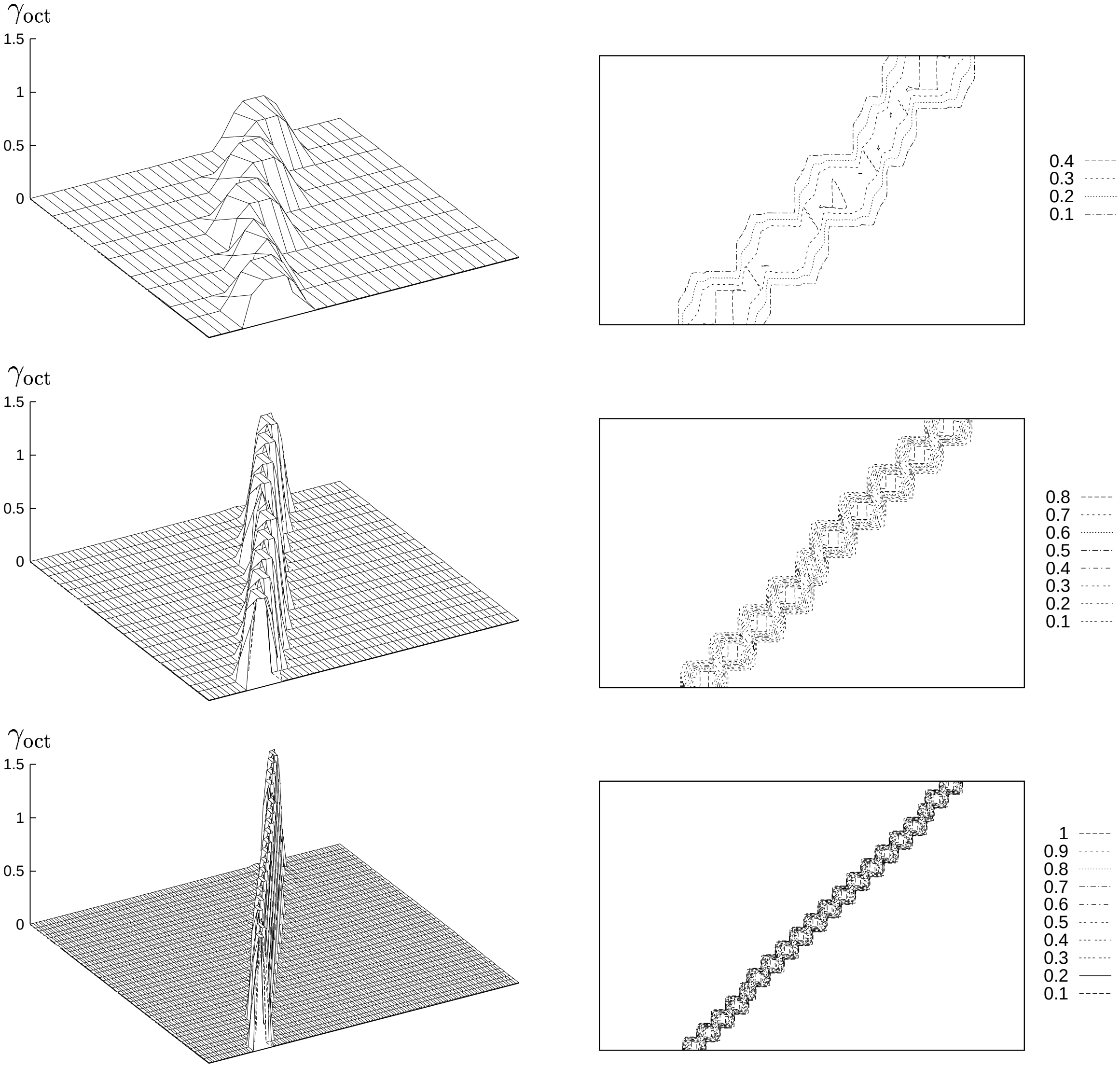

Figure 4.17. Contour plots of octahedral shear strain $\gamma_{\rm oct}$ (× 100 %) for enhanced solution at end of loading: 75, 300, and 1200 linear quadrilateral elements. ($\beta = b = 0.49487$).

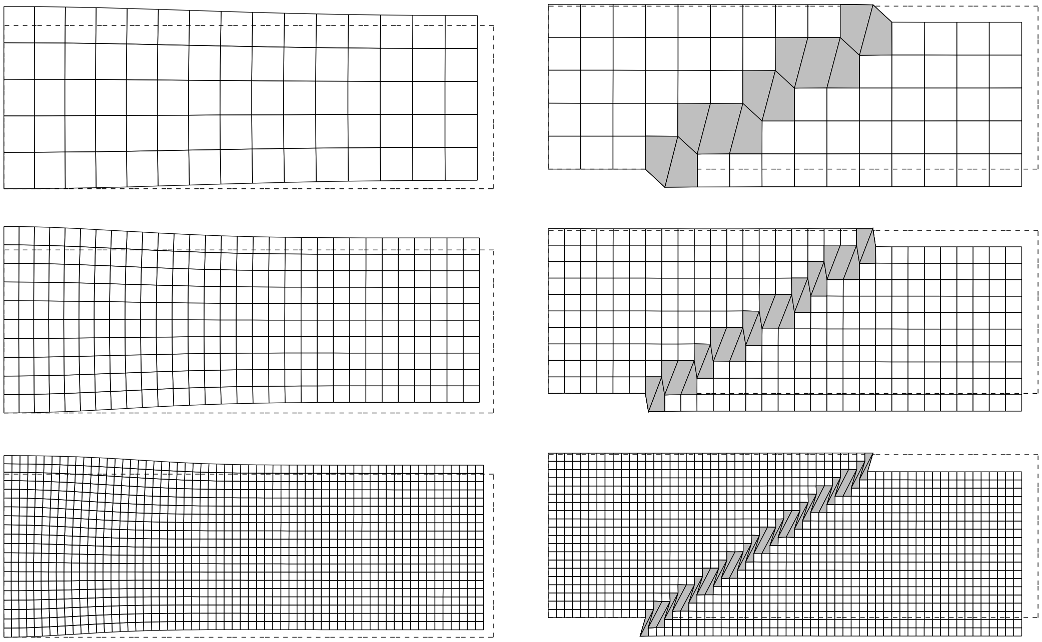

Figure 4.18. Plane strain compression problem: non-associative, dilative plastic flow ($\bar{\phi} = 30^\circ, b = 0.3$). Seventy-five, 300, and 1200 linear quadrilateral elements. Localized elements are shaded. Slip lines trace sharply through unstructured meshes for enhanced solution, while standard solution meshes exhibit diffuse deformation.

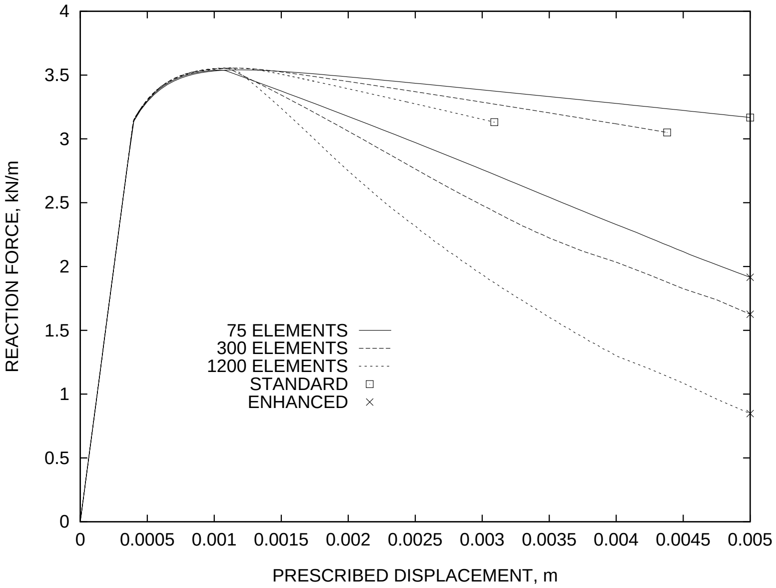

Figure 4.19. Plane strain compression problem: non-associative, dilative plastic flow ($\bar{\phi} = 30^\circ, b = 0.3, h^{\mathrm{tol}} = 0.002$). Linear quadrilateral elements. Eventual similar slopes of enhanced solution curves demonstrate objectivity with respect to mesh refinement.

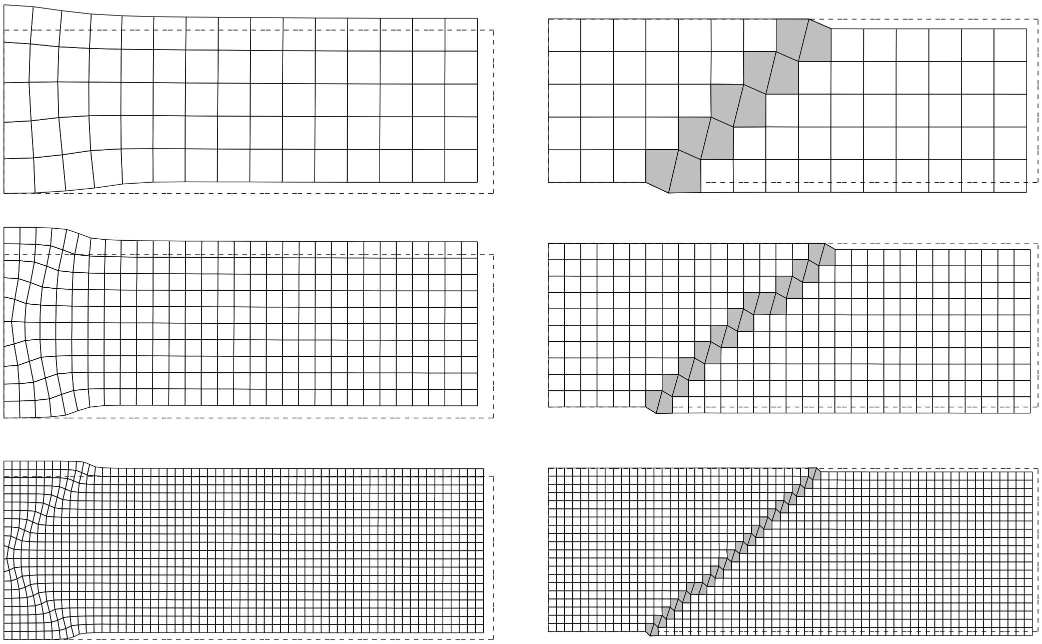

Figure 4.20. Plane strain compression problem: non-associative, deviatoric plastic flow ($\beta = 0.49487, b = 0.0$). Seventy-five, 300, and 1200 linear quadrilateral elements with $\bar{B}$. Localized elements are shaded. Slip lines trace sharply through unstructured meshes for enhanced solution, while standard solution meshes exhibit diffuse deformation.

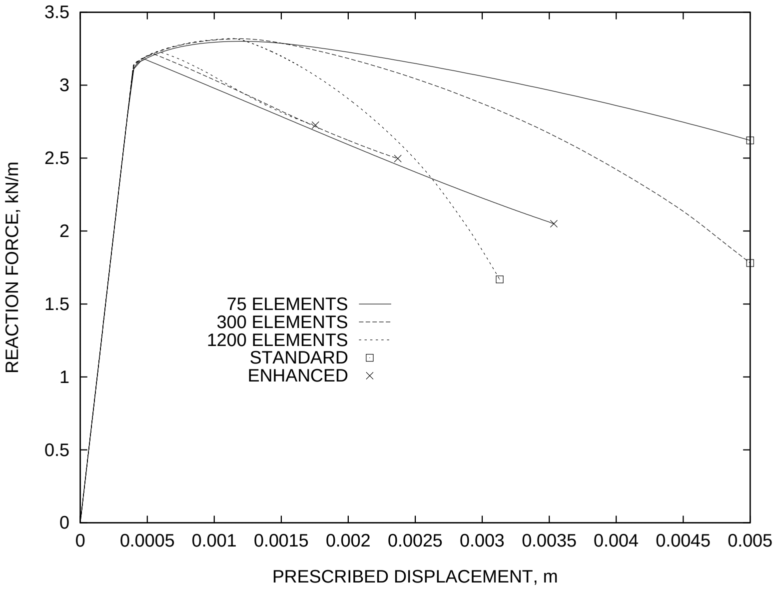

Figure 4.21. Plane strain compression problem: non-associative, deviatoric plastic flow ($\beta = 0.49487, b = 0.0$). $h^{\text{tol}} = 0.001$. Linear quadrilaterals with $\bar{B}$. Similar slopes of enhanced solution curves demonstrate objectivity with respect to mesh refinement.

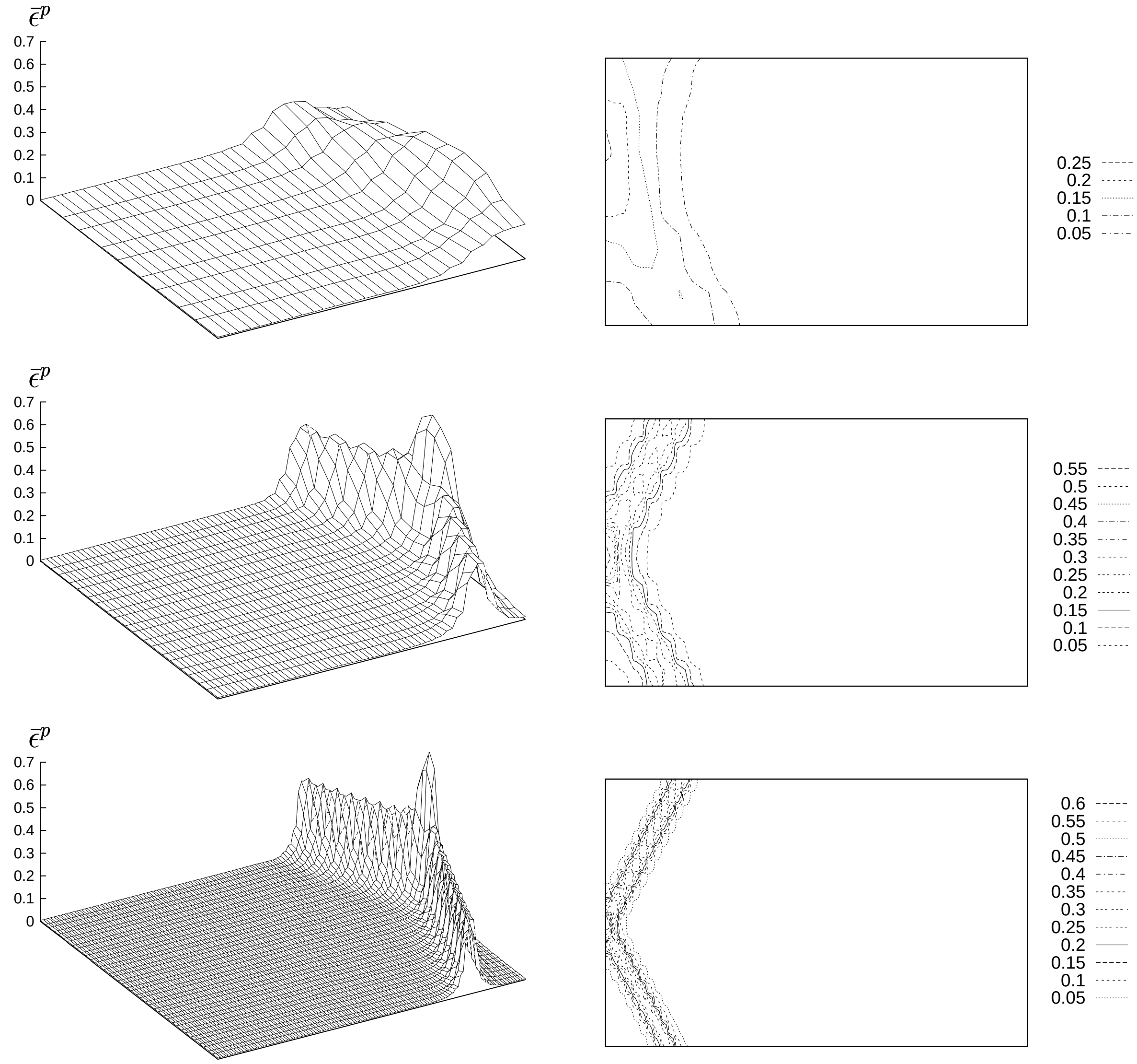

Figure 4.22. Contour plots of effective plastic strain $\bar{\epsilon}^p$ (× 100 %) for standard solution at end of loading: 75, 300, and 1200 linear quadrilateral elements. ($\beta = 0.49487, b = 0.0$).

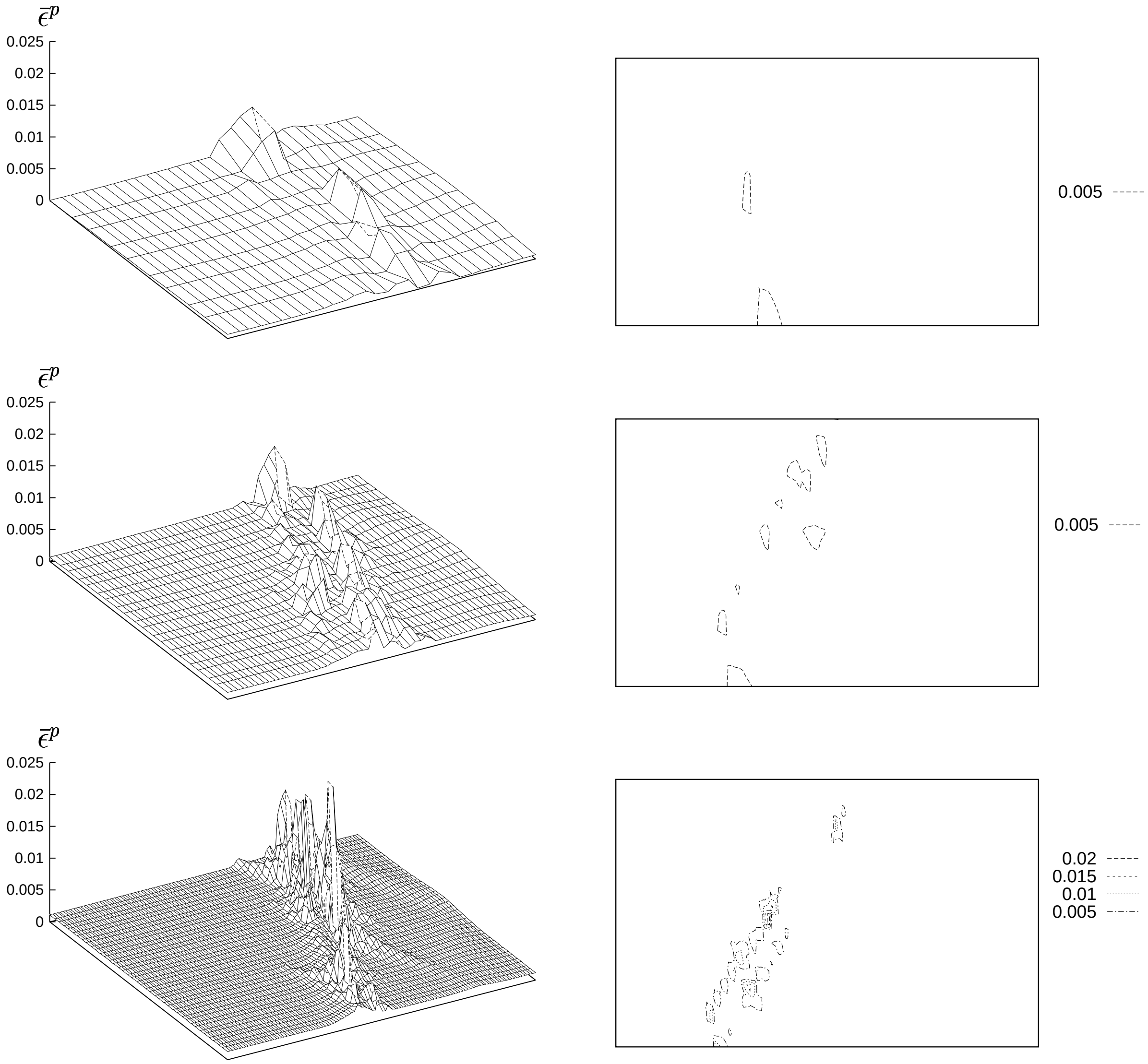

Figure 4.23. Contour plots of effective plastic strain $\bar{\epsilon}^p$ (× 100 %) for enhanced solution at end of loading: 75, 300, and 1200 linear quadrilateral elements. ($\beta = 0.49487, b = 0.0$).

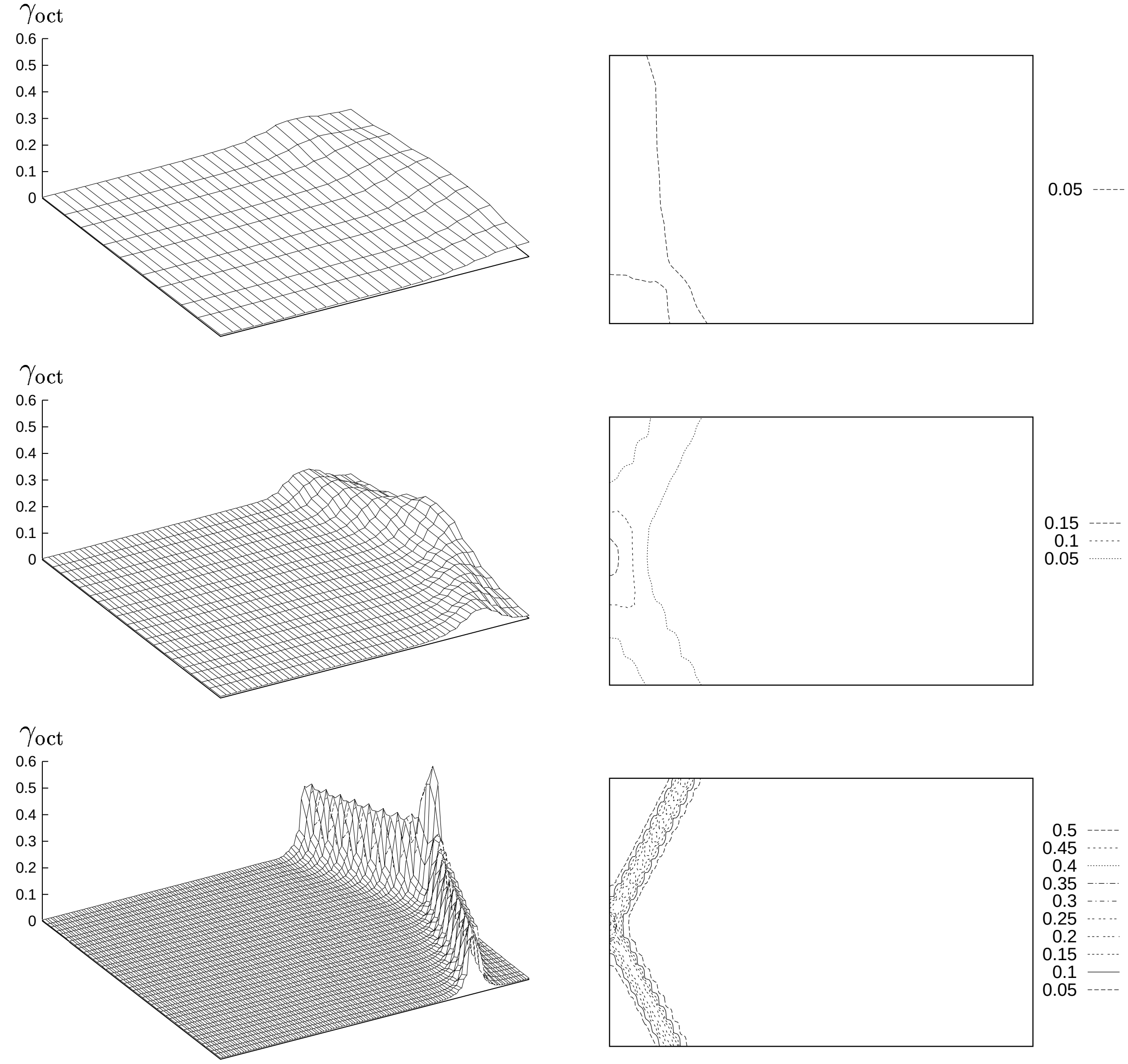

Figure 4.24. Contour plots of octahedral shear strain $\gamma_{\rm oct}$ (×100%) for standard solution at end of loading: 75, 300, and 1200 linear quadrilateral elements. ($\beta = 0.49487, b = 0.0$).

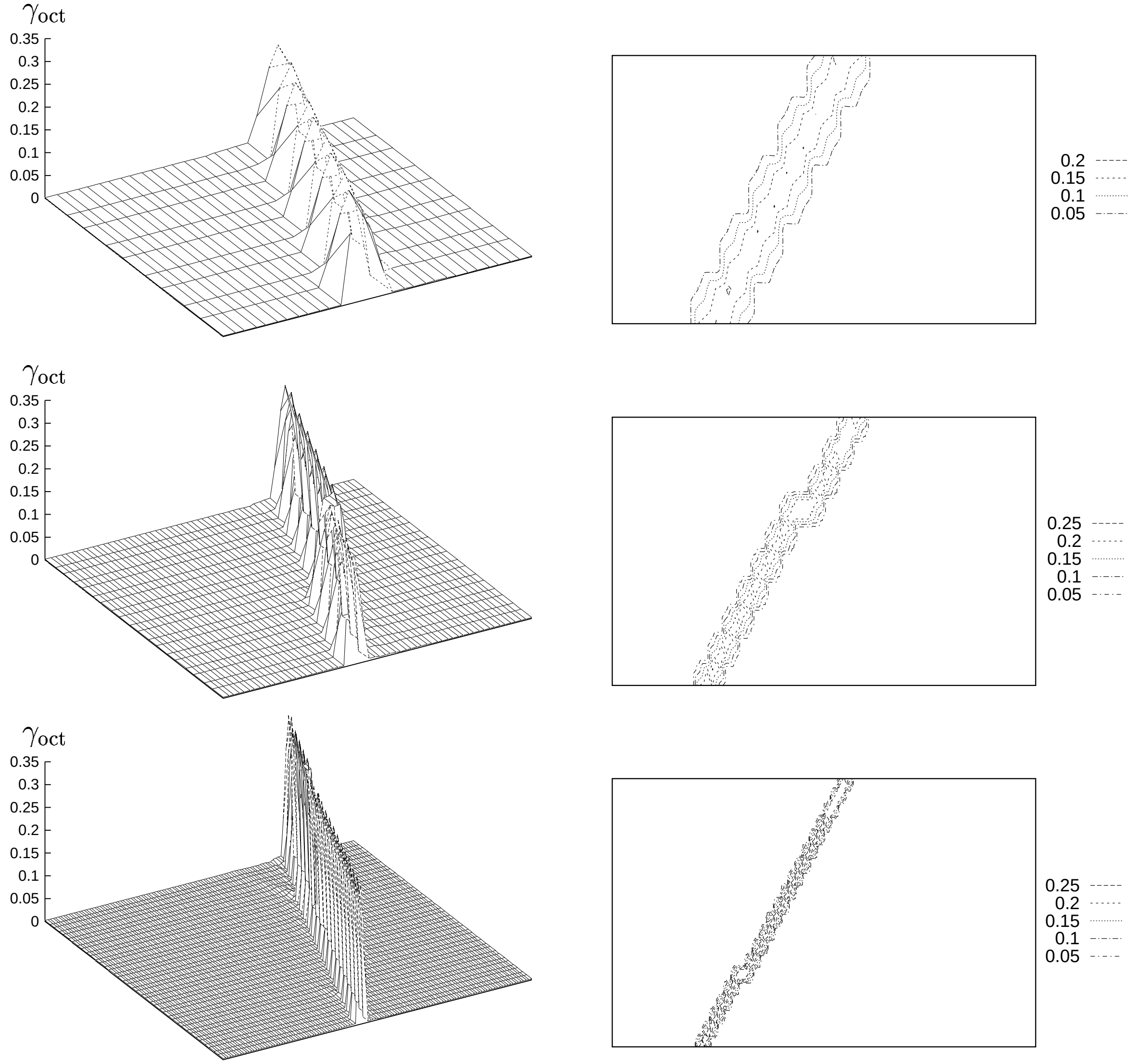

Figure 4.25. Contour plots of octahedral shear strain $\gamma_{\rm oct}$ (×100%) for enhanced solution at end of loading: 75, 300, and 1200 linear quadrilateral elements. ($\beta = 0.49487, b = 0.0$).

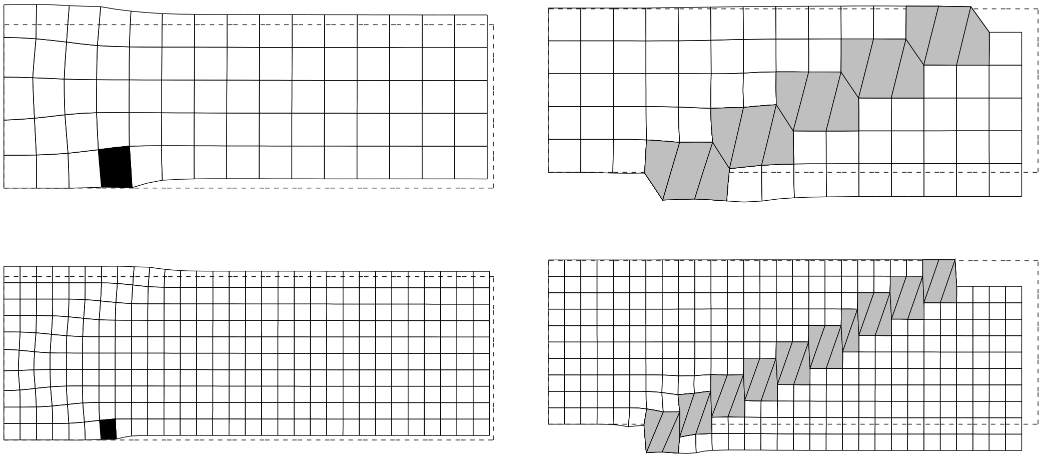

Figure 4.26. Plane strain compression problem: associative, dilative plastic flow ($\beta = b = 0.49487$). Seventy-five and 300 quadratic quadrilateral elements. Location of weakened element indicated by black squares on the deformed meshes resulting from the standard finite element solution. Localized elements are shaded. Slip lines trace sharply through unstructured meshes for enhanced solution, while standard solution meshes exhibit diffuse deformation.

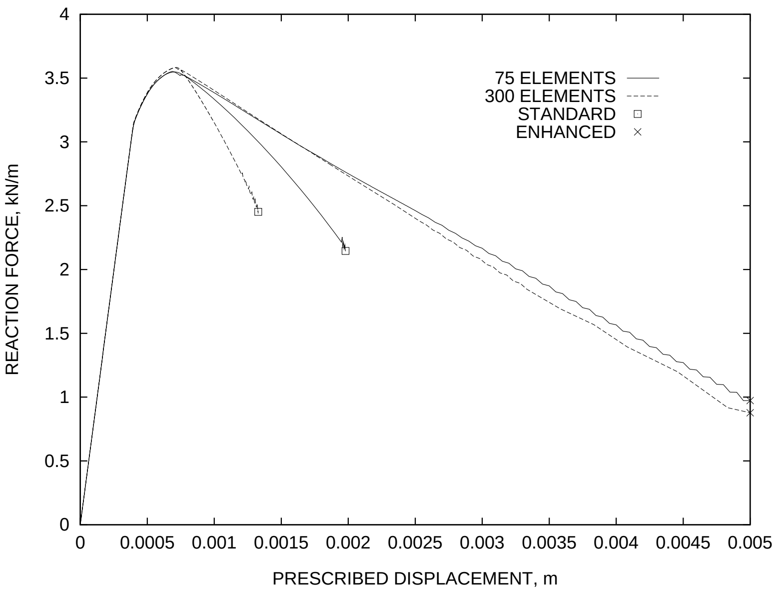

Figure 4.27. Plane strain compression problem: associative, dilative plastic flow ($\beta = b = 0.49487$). $h^{\mathrm{tol}} = 0.005$. Quadratic quadrilaterals. Slopes of enhanced curves, as well as the curves themselves, are similar.

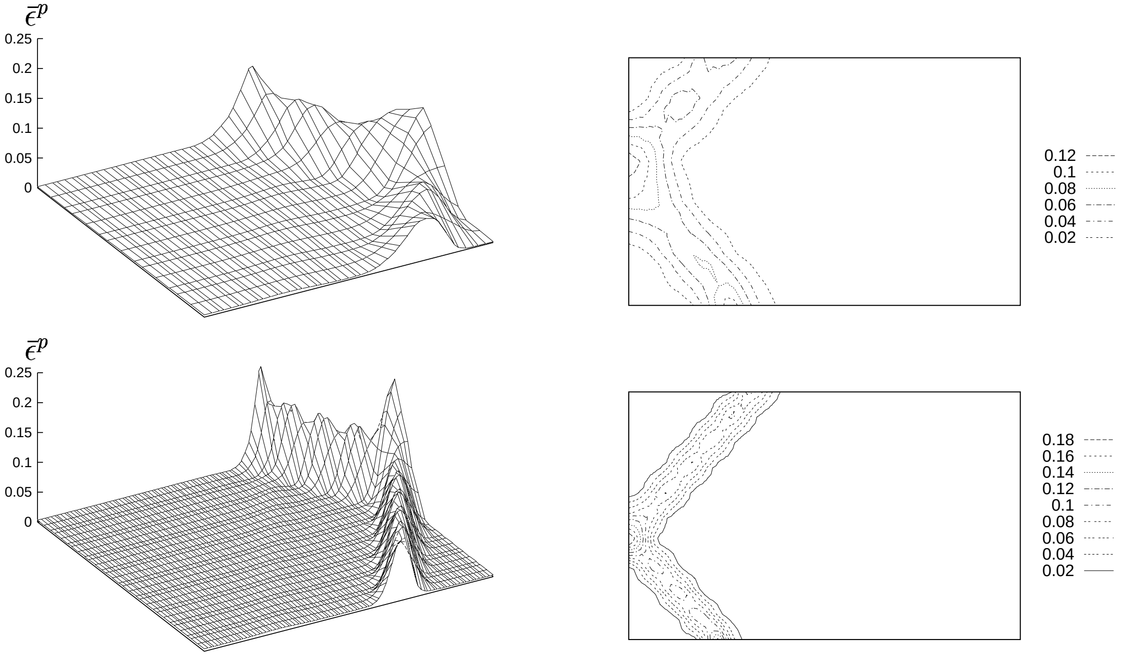

Figure 4.28. Contour plots of effective plastic strain $\bar{\epsilon}^p$ (× 100 %) for standard solution at end of loading: 75 and 300 quadratic quadrilateral elements. ($\beta = b = 0.49487$).

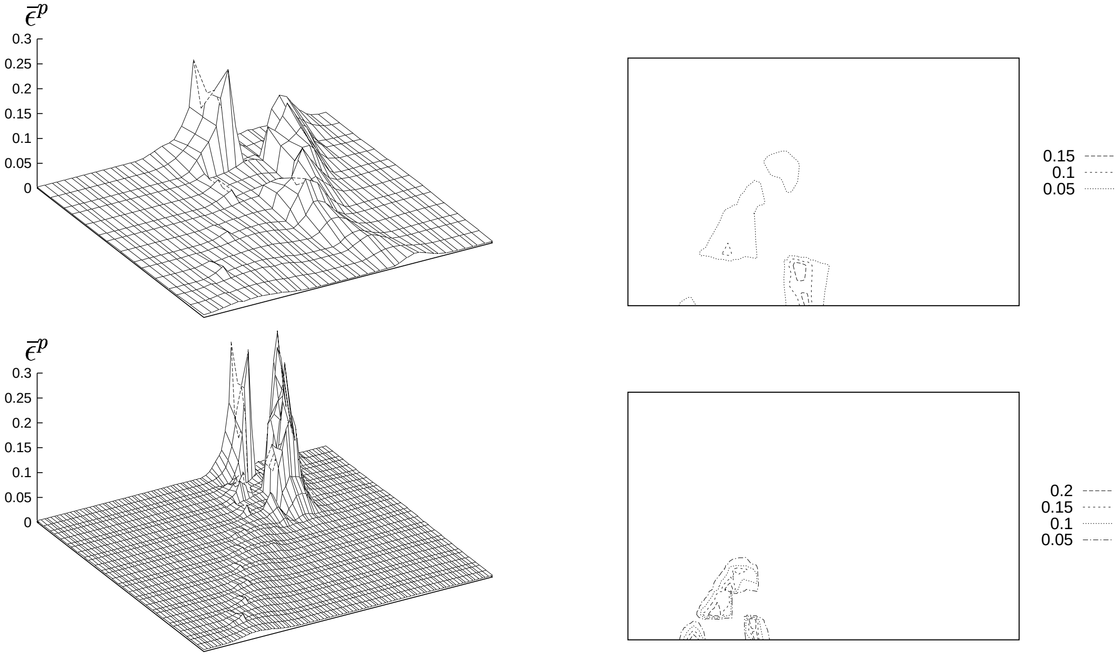

Figure 4.29. Contour plots of effective plastic strain $\bar{\epsilon}^p$ (× 100 %) for enhanced solution at end of loading: 75 and 300 quadratic quadrilateral elements. ($\beta = b = 0.49487$).

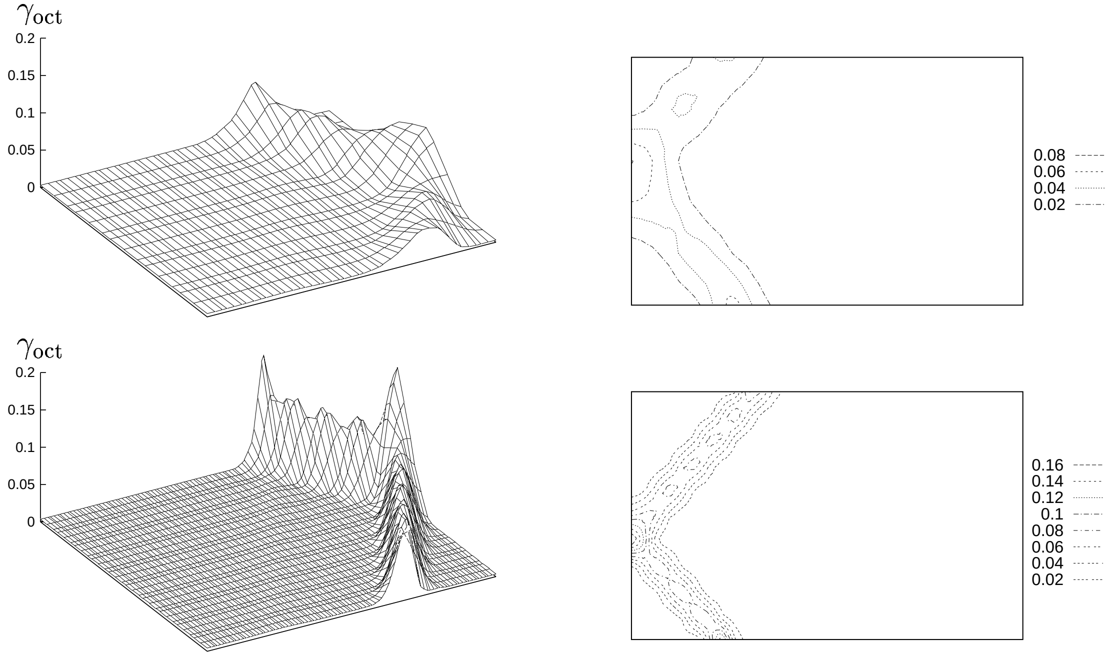

Figure 4.30. Contour plots of octahedral shear strain γ_{oct} (×100%) for standard solution at end of loading: 75 and 300 quadratic quadrilateral elements. ($\beta = b = 0.49487$).

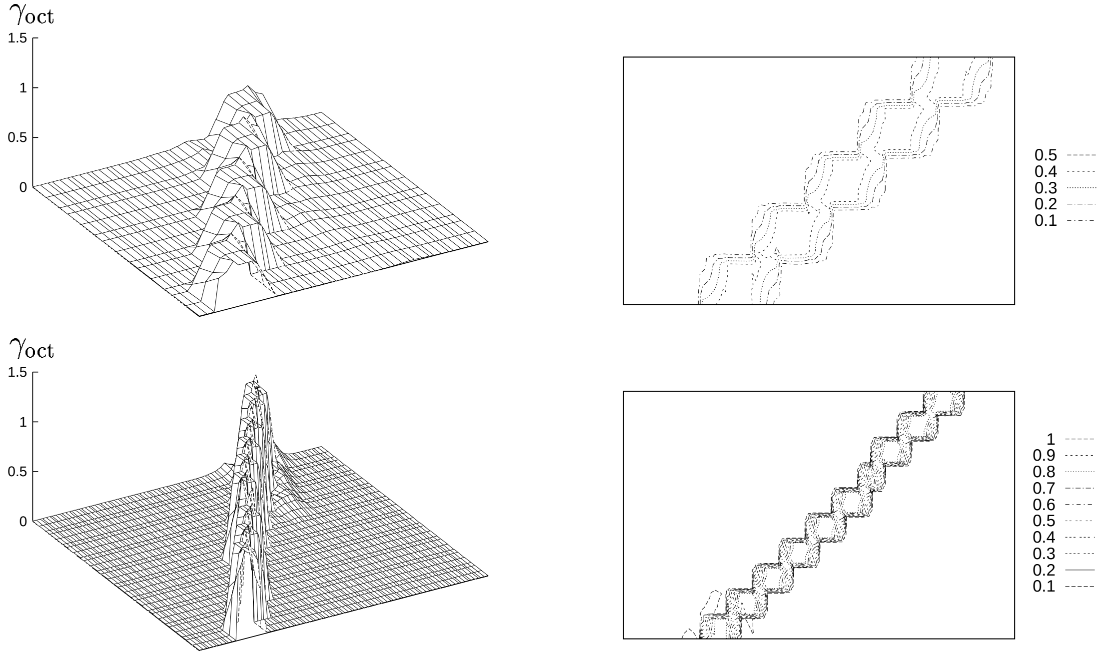

Figure 4.31. Contour plots of octahedral shear strain $\gamma_{\rm oct}$ (×100%) for enhanced solution at end of loading: 75 and 300 quadratic quadrilateral elements. ($\beta = b = 0.49487$).

4.4 Plane Strain Compression Experiment on Gosford Sandstone

Here, the model is used to attempt to simulate the behavior of Gosford sandstone under plane strain compression loading while demonstrating mesh independent finite element solutions. The experimental setup and results for plane strain compression experiments on Gosford sandstone are delineated by Ord et al. [56]. Refer to Fig. 4.32 for dimensions and boundary conditions of the experimental specimens. In particular, consider the experiments labeled RAO624, RAO629, RAO627, RAO640, and RAO636 for confining pressures of 5, 7.5, 10, 15, and 20 MPa, respectively.

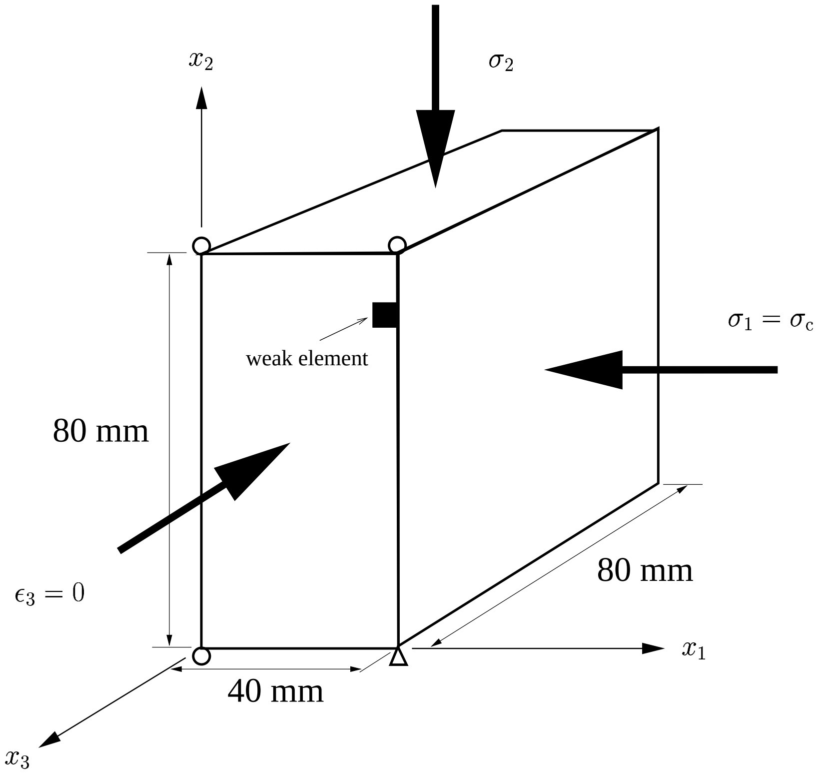

Figure 4.32. Finite element model boundary conditions and dimensions for plane strain compression of Gosford sandstone. Confining pressures are $\sigma_c = 5$, 7.5, 10, 15, and 20 MPa. Prescribed displacement of top loading platen results in load P, from which σ_2 may be calculated. Location of weakened element shaded black.

A plane strain stress condition was achieved in the experimental setup by preventing deformation from occurring in the out-of-plane direction via a stiff, passive constraint. In addition, the lower platen was supported by steel rollers, thus allowing lateral movement of the sample and development of shear bands. Further details of the experimental setup can be found in [56].

E	$\geq 11.6, \leq 16.9$ GPa
ν	0.25
$\bar{\alpha}$	10.2 MPa
β	0.46
b	0.35
H'	$\geq 8, \leq 15$ GPa
K'	0 GPa
H_δ	$\geq -100, \leq -50$ GPa/m
K_δ	0 GPa/m

Table 4.4. Material parameters for Gosford sandstone simulation.

It was found that the values of modulus of elasticity E reported in [56] were low and inconsistent with the initial tangent moduli of the stress-strain curves, and thus E is calculated directly from the reported stress-strain curve assuming homogeneous, linear elastic, plane strain behavior up until the yield point:

$$\frac{\Delta(\sigma_{22} - \sigma_{11})}{\Delta\epsilon_{22}} = \frac{2\mu}{1 - \nu} \tag{4.2}$$

where $\Delta(\bullet)$ implies increment of a quantity, $\bar{\mu} = E/(2(1+\nu))$, subscript 2 is the direction of compressive loading, and subscript 1 is the direction of confining pressure. Using a value for Poisson's ratio $\nu = 0.25$ (which is in the range of values reported by ORD et al. [56]) in Eq. (4.2), the following values were found: $E = 13.2$, 16.3, 11.6, 16.9, and 15.2 GPa for confining pressures of 5, 7.5, 10, 15, and 20 MPa, respectively. which fall near and within the range of 12.1 GPa to 18.3 GPa reported by ORD et al. [56]. The confining pressure is applied to the sample's sides as shown in Fig. 4.32.

Other material parameters are reported in Table 4.4. The parameters $\bar{\alpha}$ =10.2 MPa and $\beta = 0.46$ are calculated from a linear regression of the observed experimental yield points which are taken as the points on the experimental stress-strain curves where the curves begin to deviate from a line drawn through the initial linear portion. The material dilation constant b =0.35 was calculated from a reported average dilation angle of $\bar{\psi} = 20°$. The standard shear hardening/softening modulus (H') is chosen to best represent the experimental deviatoric load-displacement curve up until localization is detected, while the localized shear hardening/softening modulus (H_δ) is chosen to best represent the slope of the experimental deviatoric load-displacement curve after failure surface formation at peak stress level (written per meter because the Dirac-delta function has an implicit dimension of 1/length). See Table 4.5 for a summary of these parameters.

σ_1 (MPa)	E (GPa)	H' (GPa)	H_δ (GPa/m)
5	13.2	15.0	-80.0
7.5	16.3	12.0	-100.0
10	11.6	8.0	-75.0
15	16.9	12.0	-100.0
20	15.2	9.0	-50.0

Table 4.5. Summary of moduli for Gosford sandstone simulation.

The sample measures $40 \times 80 \times 80$mm (80 mm being the height of the sample and also the out-of-plane thickness, with 40 mm as the width) and is discretized by 128, 512, and 2048 linear quadrilateral elements in order to demonstrate objectivity with respect to mesh refinement. Frictionless boundaries are assumed (see Fig. 4.32), and the top boundary is displaced downward at given increments, while measuring the reaction forces at the bottom boundary to be able to plot load-displacement curves. Load-displacement curves are plotted as opposed to stress-strain curves because upon the development of localized deformation, stress and strain are nominal quantites and not those of a homogeneously deforming body. The cohesion parameter $\bar{\alpha}$ of one side element of each mesh is lowered by 1% to perturb the uniform stress state and to clearly define where the slip line initiates; see Fig. 4.32 for location. Another approach would be to include friction at the loading platens via contact elements to simulate an inhomogeneity in the loading which would trigger a non-uniform stress state, where the value of friction at the loading platens would be chosen arbitrarily since such values were not provided in [56]. Another way to introduce an inhomogeneity to produce a non-uniform stress field is to taper the mesh slightly at the midsection (see Simo & Armero [81]).

Deformed meshes are shown in Fig. 4.33 for a confining pressure of 20 MPa (since b is constant for each confining pressure, the slip line orientation will be the same for varying confining pressure) with corresponding deviatoric load-displacement curves shown in Figs. 4.34–4.38. Mesh independence is observed as the slip line propagates across elements without having element sides aligned with the expected slip line orientation (elements through which the slip line has propagated are shaded gray), and by the deviatoric load-displacement curves lying one on top of the other.

The linear elastic portion of the load-displacement curves proceeds up until yielding, a plastic region follows up until peak load at which time localization is detected, and then the slip line propagates through the mesh at peak load resulting in subsequent linear softening along the discontinuity (i.e., the slip line). Note that the slip line would propagate through the mesh over a wider range of displacement prior to peak load if the stress state was more non-uniform (see the slope stability problem and excavation problem presented in this chapter).

It is noteworthy that by solely choosing the moduli E, H', and H_δ to create a trilinear best fit of the experimental load-displacement curve, the stress levels at which localization is detected are proximate to the experimentally observed values for each confining pressure case. In addition, the experimentally observed failure surface orientation is closely represented by the simulation, as well as the post-localization overall softening behavior.

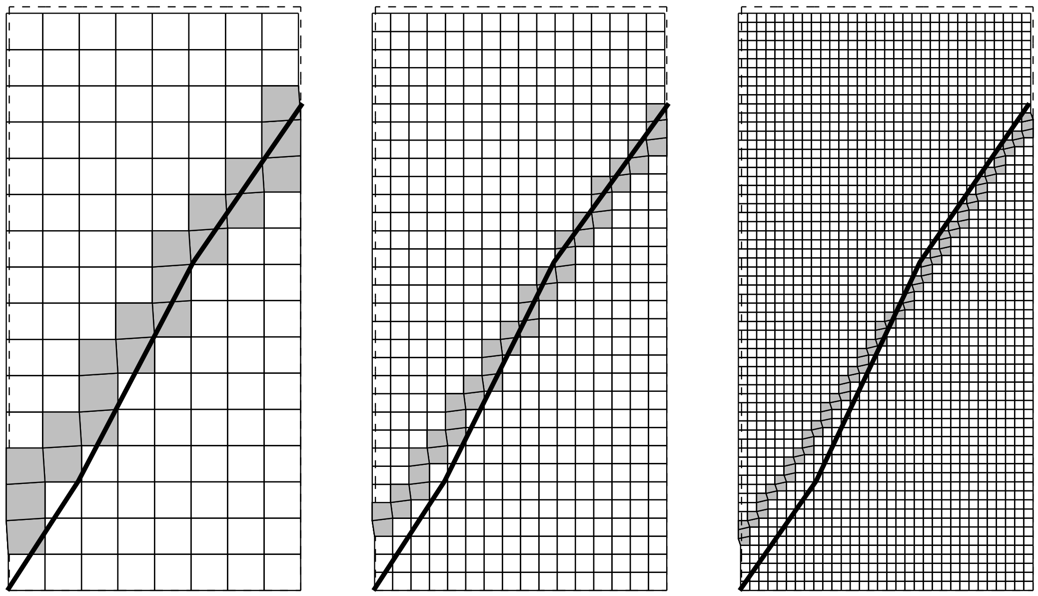

Figure 4.33. Deformed meshes for enhanced finite element solutions with 128, 512, 2048 linear quadrilateral elements at confining pressure of $\sigma_1 = 20$ MPa. Localized elements are shaded. Insensitivity to mesh alignment demonstrated by the slip line tracing across element sides. Actual failure surface orientation drawn as a solid line on the meshes.

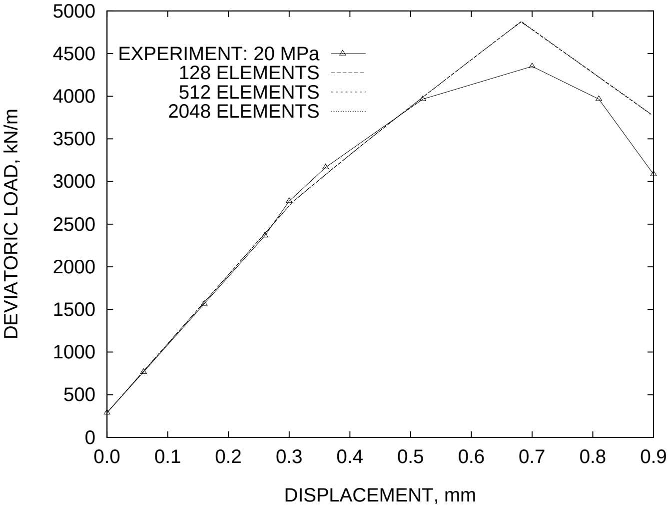

Figure 4.34. Enhanced finite element solutions with 128, 512, and 2048 linear quadrilateral elements at confining pressure of $\sigma_1 = 20$ MPa. Curves are one on top of the other, demonstrating objectivity with respect to mesh refinement.

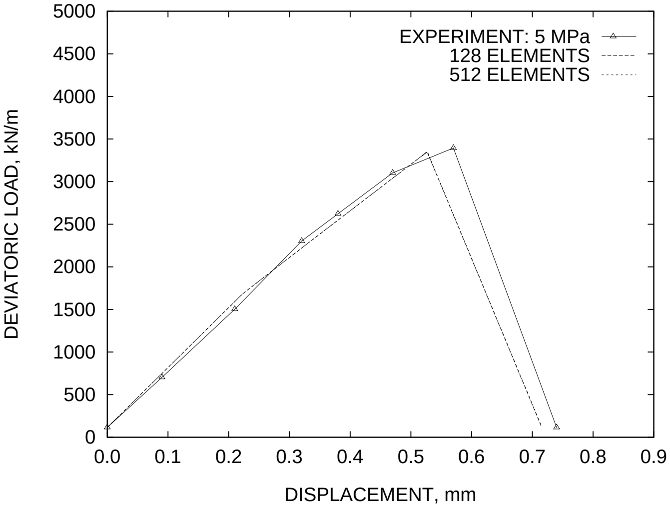

Figure 4.35. Enhanced finite element solutions with 128 and 512 linear quadrilateral elements at confining pressure of $\sigma_1 = 5$ MPa. Curves are one on top of the other, demonstrating objectivity with respect to mesh refinement.

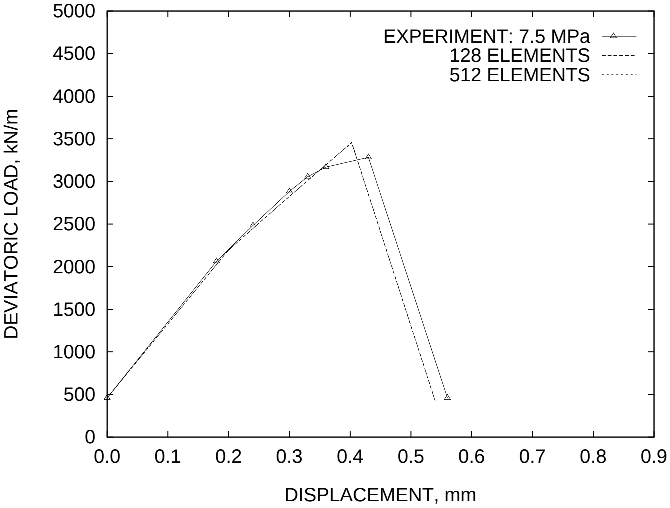

Figure 4.36. Enhanced finite element solutions with 128 and 512 linear quadrilateral elements at confining pressure of $\sigma_1 = 7.5$ MPa. Curves are one on top of the other, demonstrating objectivity with respect to mesh refinement.

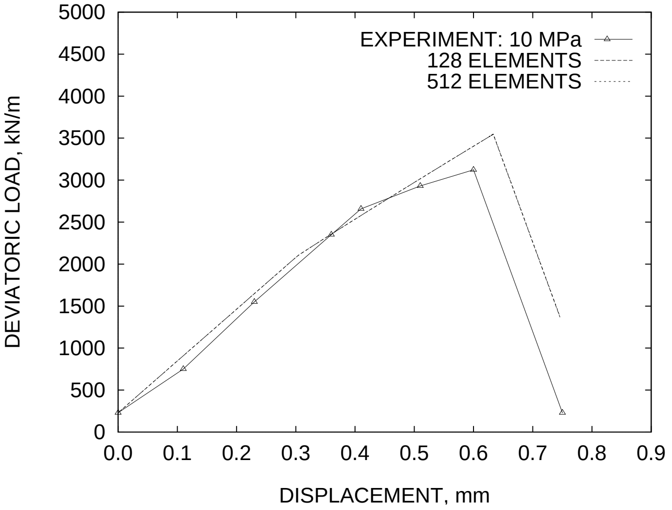

Figure 4.37. Enhanced finite element solutions with 128 and 512 linear quadrilateral elements at confining pressure of $\sigma_1 = 10$ MPa. Curves are one on top of the other, demonstrating objectivity with respect to mesh refinement.

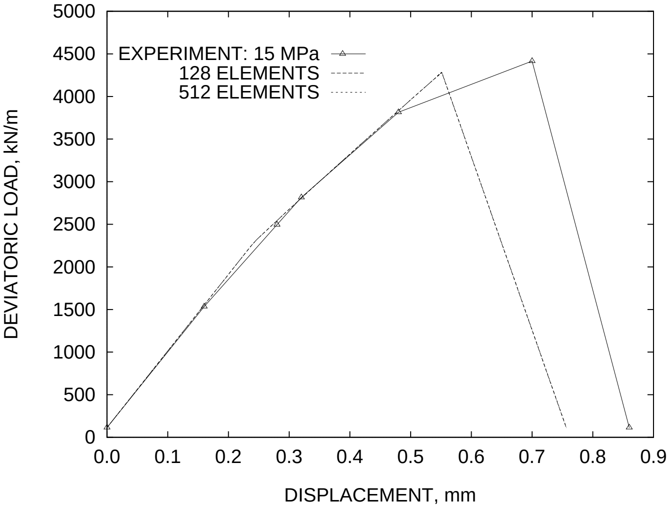

Figure 4.38. Enhanced finite element solutions with 128 and 512 linear quadrilateral elements at confining pressure of $\sigma_1 = 15$ MPa. Curves are one on top of the other, demonstrating objectivity with respect to mesh refinement.

4.5 Plane Strain Compression Experiment on Coal

Here, the model is used to attempt to simulate the behavior of coal under plane strain compression loading while demonstrating mesh independent finite element solutions. The experimental setup and results for plane strain compression experiments on the coal specimens are outlined in Yumlu & Ozbay [101]. Refer to Fig. 4.39 for dimensions and boundary conditions of the experimental specimens. Four experiments were conducted at confining pressures of 0, 3, 5, and 8 MPa.

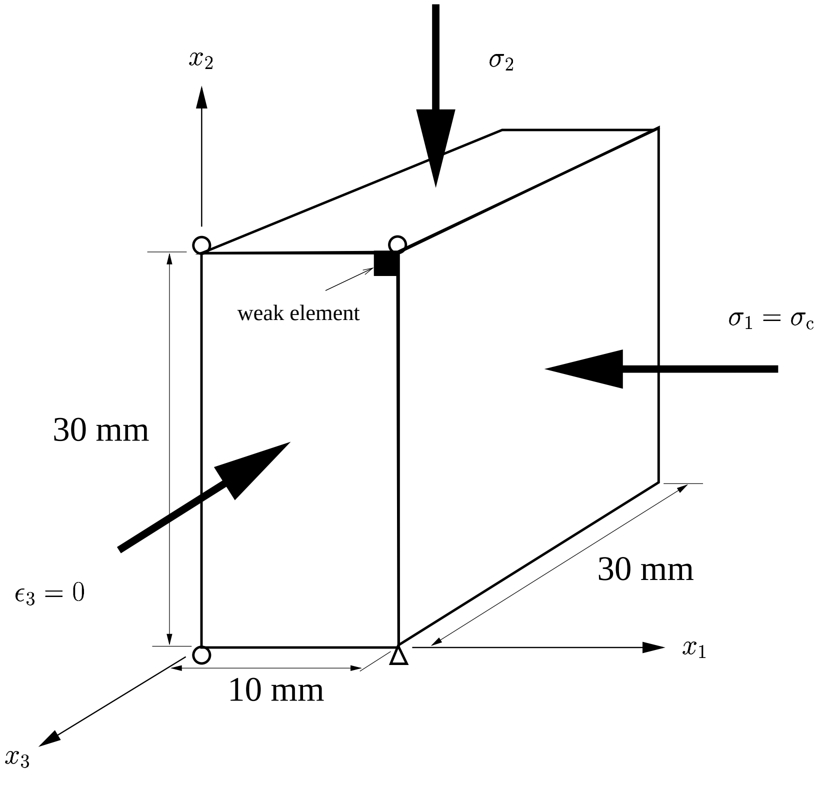

Figure 4.39. Finite element model boundary conditions for plane strain compression of coal. Confining pressures are σ_c = 0, 3, 5, and 8 MPa. Prescribed displacement of top loading platen results in load P, from which σ_2 may be calculated. Location of weakened element shaded black.

A plane strain condition was achieved in the experimental setup by preventing deformation from occurring in the out-of-plane direction via a stiff, passive constraint.

E	$\geq 4, \leq 4.75$ GPa
ν	0.19
$\bar{\alpha}$	20.2 MPa
β	0.39
b	0.5
H'	$\geq 0, \leq 3$ GPa
K'	0 GPa
H_δ	$\geq -50, \leq -35$ GPa/m
K_δ	0 GPa/m

Table 4.6. Material parameters for coal simulation.

Using a value for Poisson's ratio $\nu = 0.19$ reported by YUMLU & OZBAY [101] in Eq. (4.2), the following values for modulus of elasticity E were found: 4.0, 4.0, 4.4, and 4.75 GPa for confining pressures of 0, 3, 5, and 8 MPa, respectively, which are close the value of $E = 4.2$ GPa reported by YUMLU & OZBAY [101]. The confining pressure is applied to the sample's sides as shown in Fig. 4.39. Other material parameters are reported in Table 4.6. The parameters $\bar{\alpha}$ =20.2 MPa and $\beta = 0.39$ are calculated from a linear regression of the observed experimental yield points which are taken as the points on the experimental stress-strain curves where the curves begin to deviate from a line drawn through the initial linear portion. The material dilation constant b =0.5 was calculated from an average shear band orientation of the four specimens ($\bar{\psi} = 32°$) via Eq. (2.92). The standard shear hardening/softening modulus (H') is chosen to best represent the experimental deviatoric load-displacement curve up until localization is detected, while the localized shear hardening/softening modulus (H_δ) is chosen to best represent the slope of the experimental deviatoric load-displacement curve after failure surface formation at peak stress level (written per meter because the Dirac-delta function has an implicit dimension of 1/length). See Table 4.7 for a summary of these parameters.

The sample measures $10 \times 30 \times 30$mm (30 mm being the height of the sample

σ_1 (MPa)	E (GPa)	H' (GPa)	H_δ (GPa/m)
0	4.0	0.0	-50.0
3	4.0	0.0	-35.0
5	4.4	3.0	-40.0
8	4.75	3.0	-45.0

Table 4.7. Summary of moduli for coal simulation.

and also the out-of-plane thickness, with 10 mm as the width) and is discretized by 75, 300, and 1200 linear quadrilateral elements in order to demonstrate objectivity with respect to mesh refinement. Frictionless boundaries are assumed (see Fig. 4.39), and the top boundary is displaced downward at given increments, while measuring the reaction forces at the bottom boundary to be able to plot load-displacement curves. Load-displacement curves are plotted as opposed to stress-strain curves because upon the development of localized deformation, stress and strain are nominal quantities and not those of a homogeneously deforming body. The cohesion parameter $\bar{\alpha}$ of one side element of each mesh is lowered by 1% to perturb the uniform stress state and to clearly define where the slip line initiates; see Fig. 4.39 for location.

Deformed meshes are shown in Fig. 4.40 for a confining pressure of 3 MPa (since b is constant for each confining pressure, the slip line orientation will be the same for varying confining pressure) with corresponding deviatoric load-displacement curves shown in Figs. 4.41–4.44. Mesh independence is observed as the slip line propagates across elements without having element sides aligned with the expected slip line orientation (elements through which the slip line has propagated are shaded gray), and by the deviatoric load-displacement curves lying one on top of the other.

The linear elastic portion of the load-displacement curves proceeds up until yielding, a plastic region follows up until peak load at which time localization is detected, and then the slip line propagates through the mesh at peak load resulting in subsequent linear softening along the discontinuity (i.e., the slip line). Note that the slip line would propagate through the mesh over a wider range of displacement prior to peak load if the stress state was more non-uniform (see the slope stability problem and excavation problem presented in this chapter).

As for the Gosford sandstone example of the previous section, it is noteworthy that by solely choosing the moduli E, H', and H_δ to create a trilinear best fit of the experimental load-displacement curve, the stress levels at which localization is detected are proximate to the experimentally observed values for each confining pressure case. In addition, the experimentally observed failure surface orientation is closely represented by the simulation for the 5 MPa case, as well as the post-localization overall softening behavior.

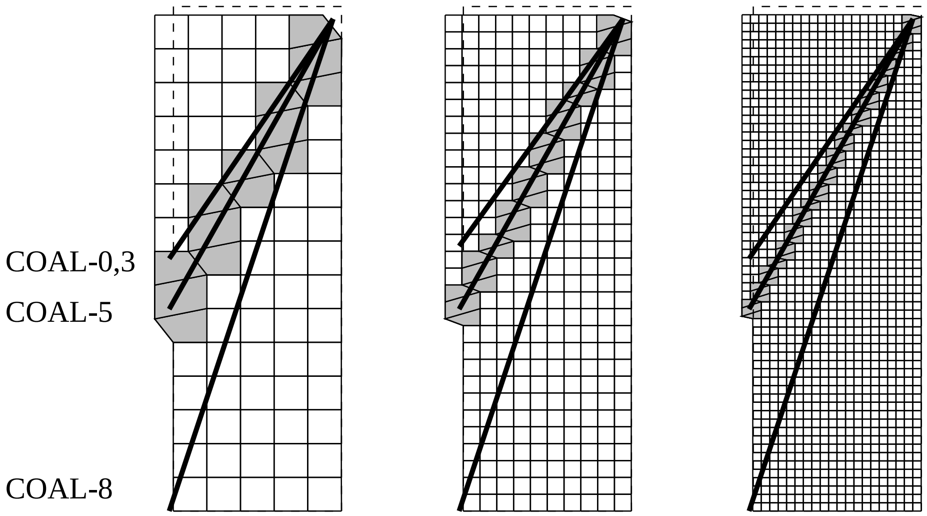

Figure 4.40. Deformed meshes for enhanced finite element solutions with 75, 300, 1200 linear quadrilateral elements at confining pressure of $\sigma_1 = 3$ MPa. Localized elements are shaded. Insensitivity to mesh alignment demonstrated by the slip line tracing across element sides. Actual failure surface orientations for four confining pressures drawn as a solid line on the meshes.

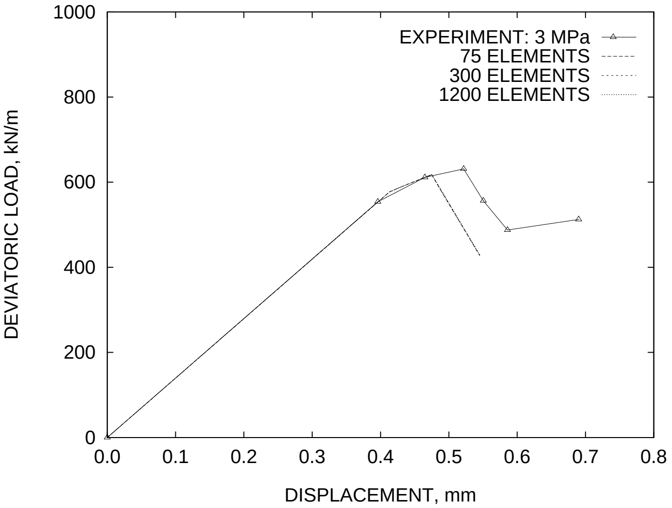

Figure 4.41. Enhanced finite element solutions with 75, 300, and 1200 linear quadrilateral elements at confining pressure of $\sigma_1 = 3$ MPa. Curves are one on top of the other, demonstrating objectivity with respect to mesh refinement.

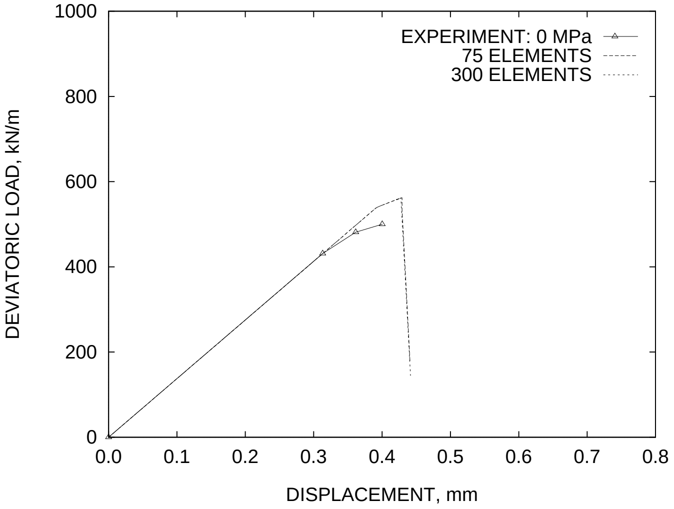

Figure 4.42. Enhanced finite element solutions with 75 and 300 linear quadrilateral elements at confining pressure of $\sigma_1 = 0$ MPa. Curves are one on top of the other, demonstrating objectivity with respect to mesh refinement.

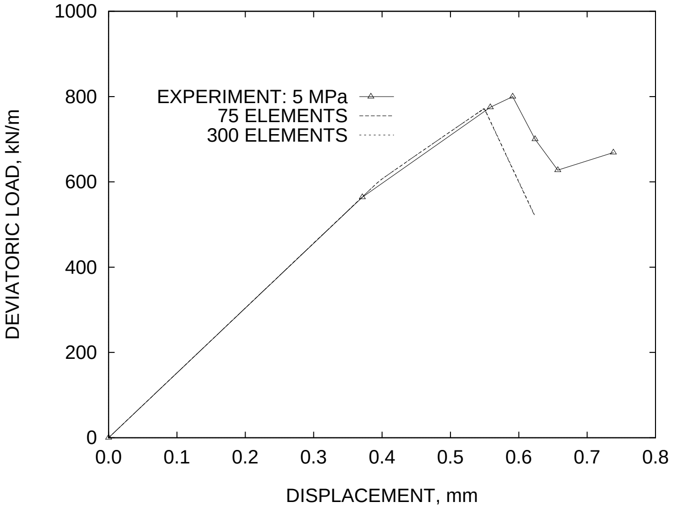

Figure 4.43. Enhanced finite element solutions with 75 and 300 linear quadrilateral elements at confining pressure of $\sigma_1 = 5$ MPa. Curves are one on top of the other, demonstrating objectivity with respect to mesh refinement.

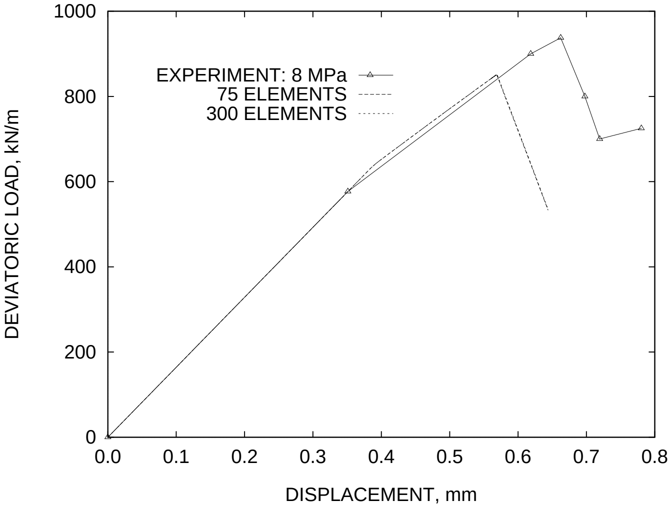

Figure 4.44. Enhanced finite element solutions with 75 and 300 linear quadrilateral elements at confining pressure of $\sigma_1 = 8$ MPa. Curves are one on top of the other, demonstrating objectivity with respect to mesh refinement.

4.6 Slope Stability Problem

A slope stability problem is now presented to demonstrate the capability of the model to represent strain localization in a classic geotechnical structure, an embankment (or slope). Material parameters are shown in Table 4.8 for three cases: associative deviatoric plastic flow (J2 flow, or von Mises plasticity), non-associative deviatoric plastic flow, and non-associative dilative plastic flow. A gravity load is first applied, the displacements are reset to zero, and a downward displacement is prescribed at the middle of a rigid footing resting at the crest of the slope. The downward displacement may represent the settlement due to a structure placed at the crest of the slope. It is desirable to run a strain-driven problem like this one because otherwise an arc-length method [70], [17] would be needed to advance the solution into and within the softening regime.

E	10 MPa
ν	0.4
$\bar{c}$	50, 20, 20 kPa
$\bar{\phi}$	0°, 30°, 30°
b	0.0, 0.0, 0.1895
H', K'	0
H_δ, K_δ	−200 kPa/m
γ	20 kN/m^3

Table 4.8. Material parameters for slope stability problem.

The dimensions and boundary conditions of the problem are designated in Fig. 4.45. Like the excavation problem presented in the next section, this is a fictitious example and not an attempt to model the behavior of an actual soil embankment, although material parameters are chosen to approximate those of a real soil. Two meshes with 400 and 1600 linear quadrilateral elements are used to analyze the problem.

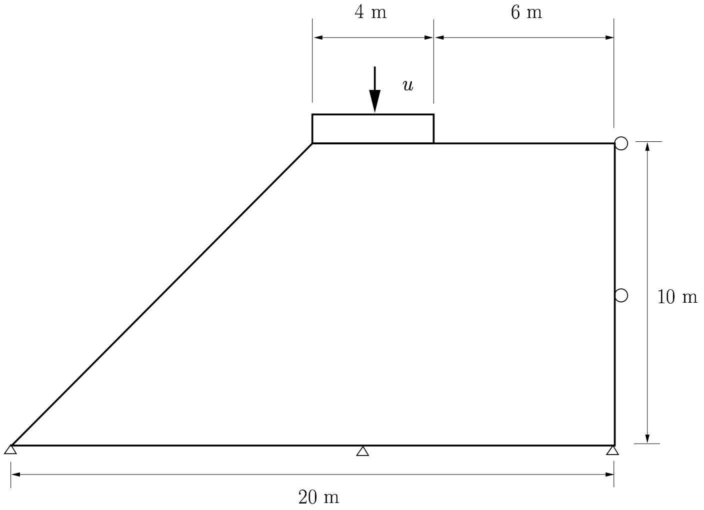

Figure 4.45. Slope stability problem. Gravity load applied before footing displacement u is prescribed.

Figure 4.46 shows deformed meshes at end of loading for the standard and enhanced solutions for associative, deviatoric plastic flow. Note the diffuse deformation patterns for the standard solutions and the sharp localized deformation for the enhanced solutions. Shaded elements are those through which the slip line has traced. Insensitivity to mesh alignment is demonstrated by the slip line tracing across elements without element sides being aligned with the slip line orientation and by slip lines having same orientation for the 400 and 1600-element meshes. The slip line initiates in the element just to the right of the rigid footing corresponding with the load at which the standard and enhanced solution curves begin to deviate from one another as seen in Figs. 4.47, 4.49, and 4.51. The load at which the enhanced solution curve begins to soften corresponds with the load at which the slip line has fully propagated through the mesh.

Load-displacement plots for associative, deviatoric plastic flow are shown in Fig. 4.47. Similar slopes of the enhanced solution curves demonstrate near-objectivity with respect to mesh refinement. The standard solution curves demonstrate the well-known mesh-dependence for perfect plasticity. Associative, deviatoric plastic flow may be used to simulate the behavior of a saturated cohesive soil in undrained condition (i.e., imcompressible for immediate loading).

Figure 4.48 shows deformed meshes at end of loading for the standard and enhanced solutions for non-associative, deviatoric platic flow. Again, note the diffuse deformation patterns for the standard solutions and the sharp localized deformation for the enhanced solutions. Load-displacement plots for non-associative, deviatoric plastic flow are shown in Fig. 4.49. Similar slopes of the enhanced solution curves demonstrate near-objectivity with respect to mesh refinement. The standard solution curves demonstrate the well-known mesh-dependence for perfect plasticity.

Figure 4.50 shows deformed meshes at end of loading for the standard and enhanced solutions for non-associative, dilative plastic flow. Again, note the diffuse deformation patterns for the standard solutions and the sharp localized deformation for the enhanced solutions. Also note the different slip lines in Figs. 4.48 and 4.50. The slip lines in Fig. 4.50 have a larger radius of curvature than the slip lines in Fig. 4.48. This is due to the different dilation constants used in each case. Load-displacement plots for non-associative, dilative plastic flow are shown in Fig. 4.51. Similar slopes of the enhanced solution curves demonstrate near-objectivity with respect to mesh refinement. The standard solution curves demonstrate the well-known mesh-dependence for perfect plasticity.

The effect of varying h^{tol} is now considered. The material parameters used to produce results shown in Figs. 4.50 and 4.51 are the same while now the results for $h^{\mathrm{tol}} = 1 \times 10^{-3}$ are compared with those already presented in Figs. 4.51 and 4.50 for $h^{\mathrm{tol}} = 5 \times 10^{-5}$. Results are shown in Figs. 4.52 and 4.53. Figure 4.53 compares the load-displacement curves. They each have similar slopes in the softening regime demonstrating that, although the choice of h^{tol} should be kept as small as possible, it is not essential that h^{tol} be kept especially small. To use a very small value like $h^{\text{tol}} = 1 \times 10^{-8}$, it is just a matter of refining the load steps to capture the bifurcation point to that accuracy. Comparing Figs. 4.50 and 4.52 show that for different values of h^{tol} the orientation of the slip line is essentially the same. The enhanced solution curves in Fig. 4.53 for $h^{\text{tol}} = 1 \times 10^{-3}$ appear to demonstrate near-objectivity with respect to mesh refinement better than for $h^{\text{tol}} = 5 \times 10^{-5}$, but this is a result of a larger 'drop' in the enhanced solution curve for the 400-element mesh for $h^{\text{tol}} = 1 \times 10^{-3}$ at peak load where the slip line has fully propagated through the mesh.

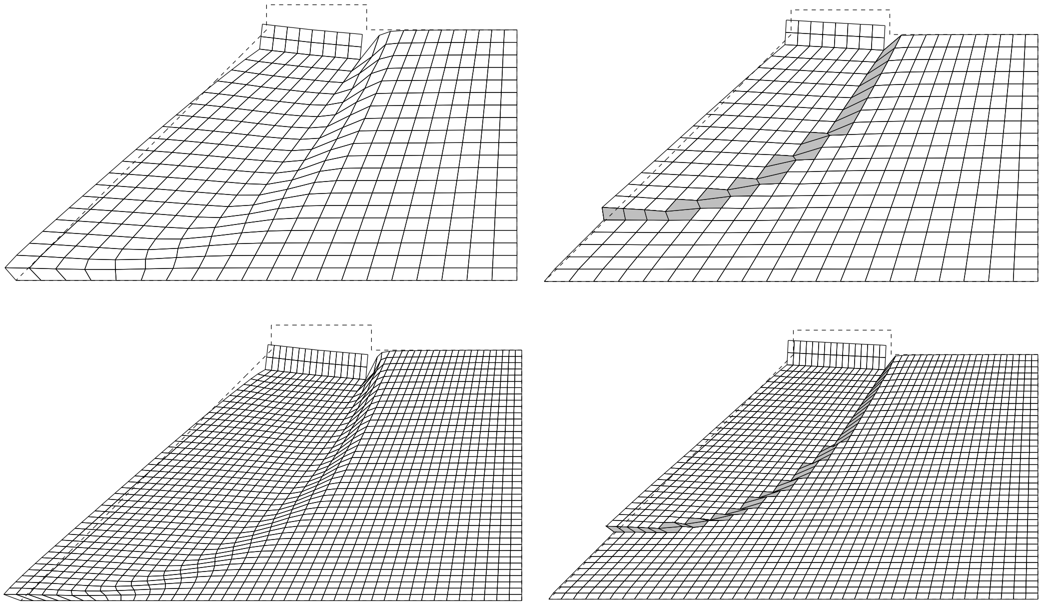

Figure 4.46. Slope stability problem. Deformed meshes for standard and enhanced solutions with associative, deviatoric plastic flow: $\beta = b = 0.0$; 400 and 1600 linear quad elements with $\bar{B}$. Localized elements are shaded.

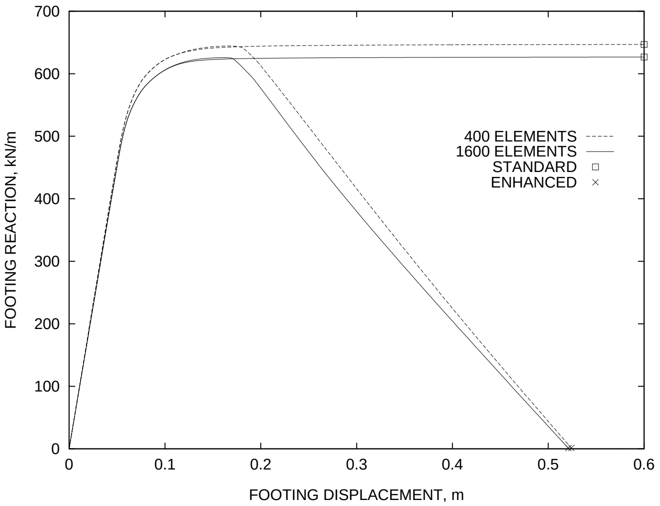

Figure 4.47. Slope stability problem. Load-displacement plots for associative, deviatoric plastic flow: $\beta = b = 0.0$. $h^{\mathrm{tol}} = 1 \times 10^{-5}$. Similar softening slopes of enhanced solution curves demonstrate near-objectivity with respect to mesh refinement.

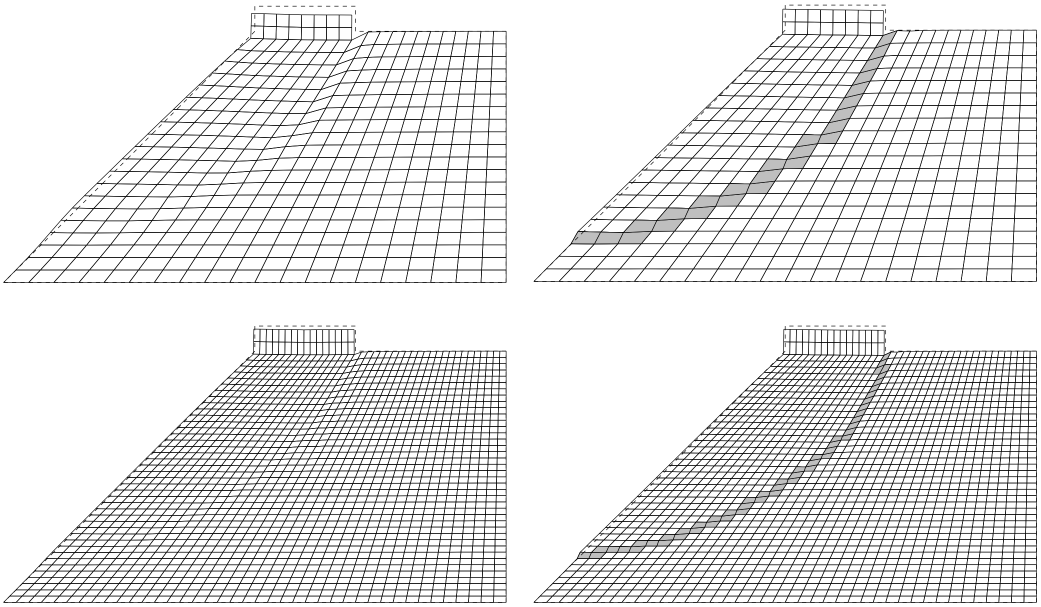

Figure 4.48. Slope stability problem. Deformed meshes for standard and enhanced solutions with non-associative, deviatoric plastic flow: $\beta = 0.49487, b = 0.0$; 400 and 1600 linear quad elements with $\bar{B}$. Localized elements are shaded.

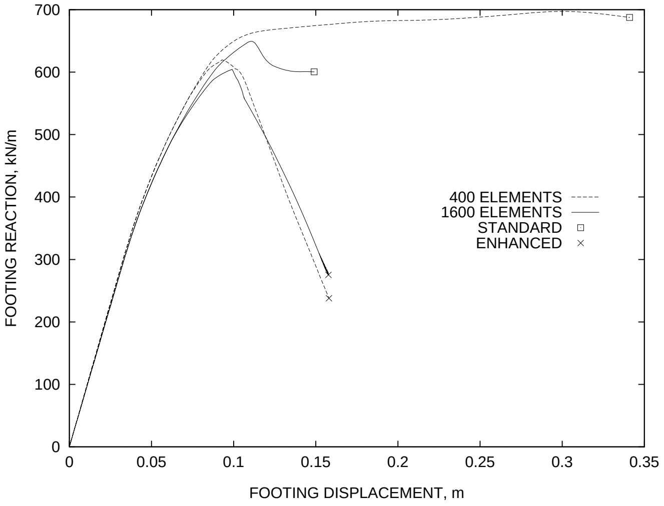

Figure 4.49. Slope stability problem. Load-displacement plots for non-associative, deviatoric plastic flow: $\beta = 0.49487, b = 0.0$. $h^{\mathrm{tol}} = 5 \times 10^{-5}$. Similar softening slopes of enhanced solution curves demonstrate near-objectivity with respect to mesh refinement.

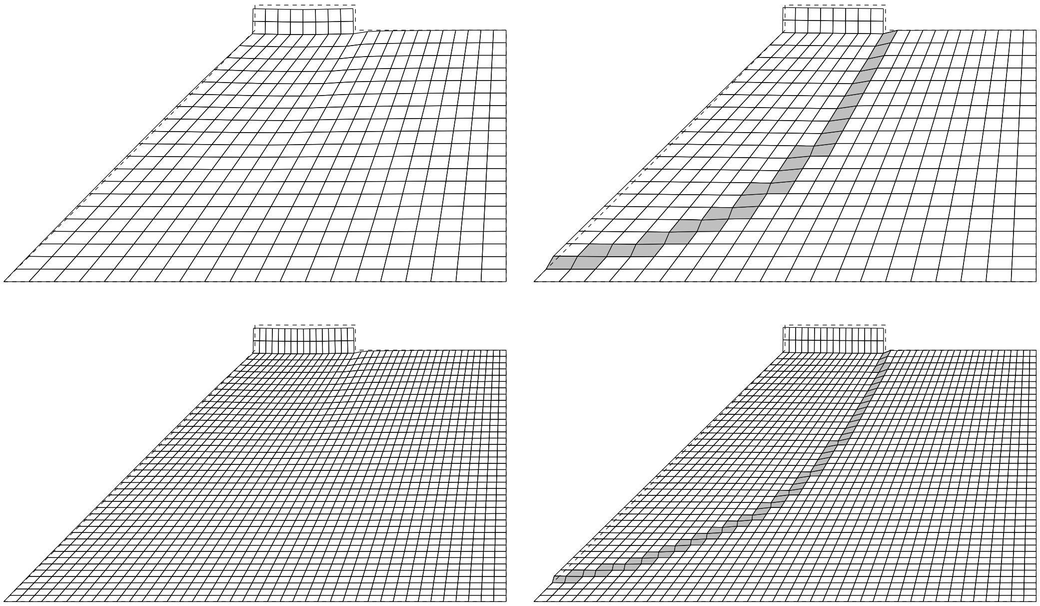

Figure 4.50. Slope stability problem. Deformed meshes for standard and enhanced solutions with non-associative, dilative plastic flow: $\beta = 0.49487, b = 0.1895$; 400 and 1600 linear quad elements. Localized elements are shaded.

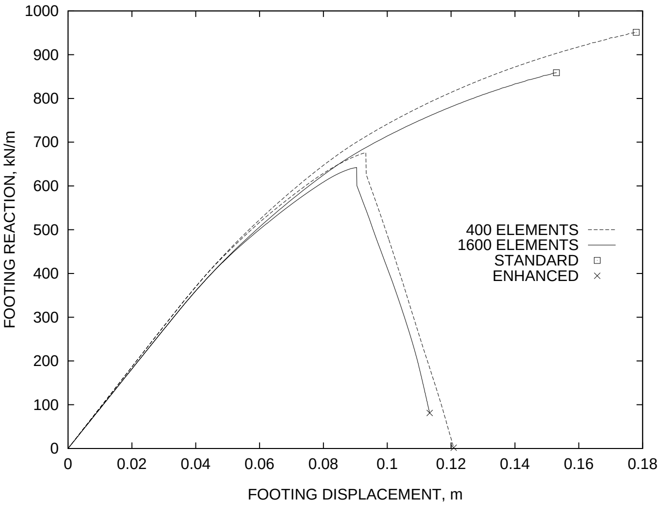

Figure 4.51. Slope stability problem. Load-displacement plots for non-associative, dilative plastic flow: $\beta = 0.49487, b = 0.1895$. $h^{\mathrm{tol}} = 5 \times 10^{-5}$. Similar softening slopes of enhanced solution curves demonstrate near-objectivity with respect to mesh refinement.

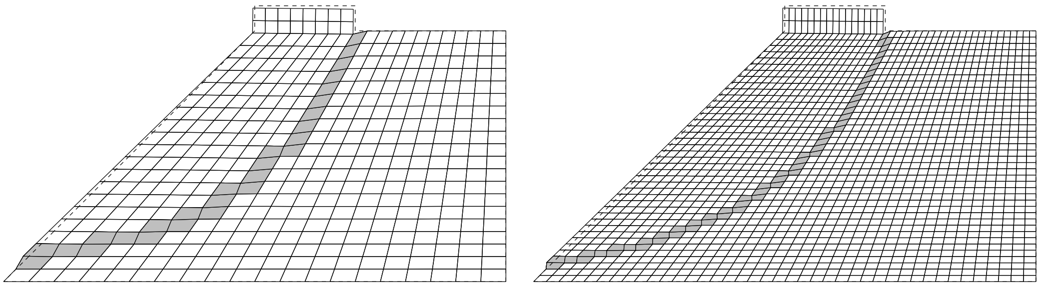

Figure 4.52. Slope stability problem. Deformed meshes for enhanced solutions with non-associative, dilative plastic flow: $\beta = 0.49487, b = 0.1895, h^{\mathrm{tol}} = 1 \times 10^{-3}$; 400 and 1600 linear quad elements. Localized elements are shaded.

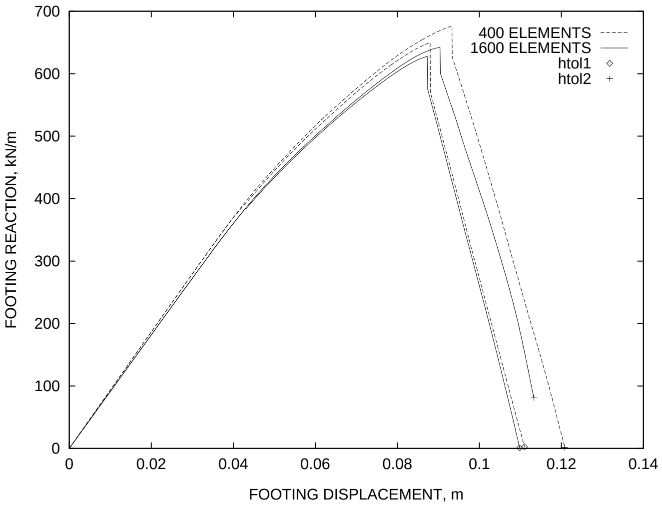

Figure 4.53. Slope stability problem. Load-displacement plots for non-associative, dilative plastic flow: $\beta = 0.49487, b = 0.1895$. Comparison of enhanced solutions for different h^{tol}: htol1 $= 1 \times 10^{-3}$, htol2 $= 5 \times 10^{-5}$.

4.7 Excavation Problem

An excavation problem shown in Fig. 4.54 will be analyzed to demonstrate the ability of the model to sharply capture slip line orientation in an unstructured mesh and to represent increasing strut loads when strain localization is present. Fig. 4.54 (a) shows a 2.5m deep layer of plastic soil atop a 1.5m deep layer of elastic rock. Fig. 4.54 (b) shows the excavation of five soil layers down to the rock layer and the placement of a rigid wall which allows the excavation of the fifth soil layer to converge. Removing soil layers is a load-driven problem. Thus, without an arc-length method to advance the solution, excavation of the fifth soil layer will not converge without the rigid wall in place. A simple limit equilibrium analysis (see ATKINSON [5] and Fig. 7-4 of [24] which is borrowed from Fig. 3-1 of JANBU [38])[†] shows that an unsupported vertical slope with the following material parameters will be unstable for a height of 2.5m. The depth from the ground surface to the top of the rock layer is chosen such that the soil may be excavated to a depth of 2.5m with the aid of the rigid wall while avoiding basal heaving during wall movement leftward, which simulates bracing system collapse.

Four levels of mesh refinement are used to analyze the problem: 80-element mesh, 320-element mesh, 1280-element mesh, and 5120-element mesh. Linear quadrilaterals were employed. Material properties are listed in Table 4.9. Different values of β and b were chosen to obtain three cases (associative dilative plastic flow, non-associative dilative plastic flow, and non-associative deviatoric plastic flow), to ensure that the five layers of soil can be excavated for each mesh (i.e., soil not too weak; recall

---

[†] Such an analysis assumes a circular failure surface and also does not account for the effect of dilatancy. Thus, it is used here only to provide an approximate analytical verification of the observed numerical result (i.e., that the load-driven problem will not converge for the removal of the fifth soil layer without the rigid wall in place, assuming no special load-stepping procedure like an arc-length method is used (see RIKS [70] and CRISFIELD [17])).

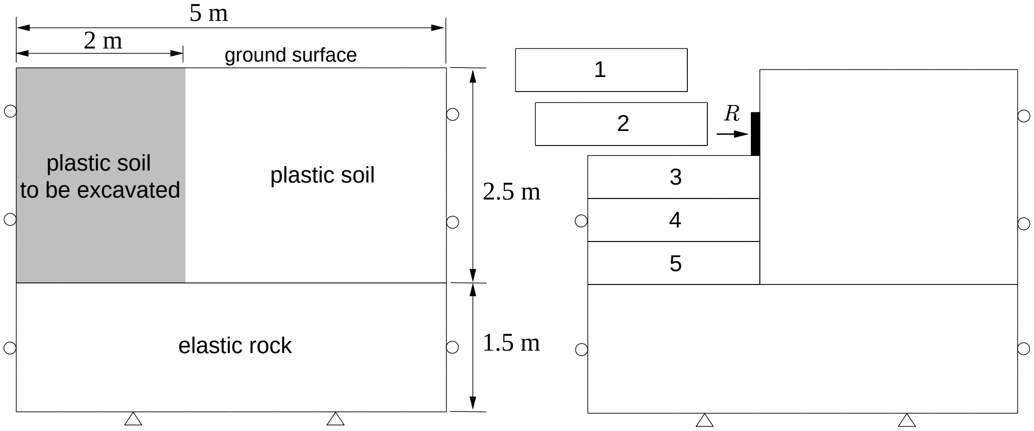

(a) Initial Soil Condition

(b) Excavation Sequence and Placement of Rigid Wall

Figure 4.54. Plane strain excavation problem: (a) Initial soil condition showing portion of soil to be excavated. (b) Excavation sequence and placement of rigid wall showing wall reaction, R. After five layers of soil have been excavated, rigid wall is moved leftward to simulate bracing system collapse.

Soil	
E	1 MPa
ν	0.4
$\bar{c}$	7.5 kPa
$\bar{\phi}$	$5°, 10°$, $15°$
b	0.0978, 0.0978, 0.0
H', K'	0
H_δ, K_δ	-10 kPa/m
γ	20 kN/m^3
Rock	
E	100 MPa
ν	0.1
γ	30 kN/m^3

Table 4.9. Material parameters for excavation problem.

that the excavation sequence is a load-driven problem), that slip lines may develop during the excavation sequence (i.e., soil not too strong), and that calculated wall reactions for the enhanced solutions remain positive (i.e., wall should not be allowed to pull the soil). The choice of material parameters is made only to demonstrate the abilities of the model and not to attempt a strain localization finite element analysis of an actual excavation field case study. The $\bar{B}$-method is again used for the non-associative, deviatoric case to preclude mesh locking for incompressble plasticity.

The finite element analysis proceeds as follows: the gravity load is applied, and the displacements are reset to zero; the five soil layers are removed sequentially as numbered in Fig. 4.54 (b), with a rigid wall placed simultaneously as the second soil layer is excavated. After the fifth soil layer is excavated, the rigid wall is moved leftward to simulate bracing system collapse, which is motivated by the observance of elements at the excavation base localizing during the fifth excavation step. To simulate the rigid wall, adjacent nodes to the wall shown in Fig. 4.54 (b) have prescribed horizontal displacement while their vertical displacment is left free (i.e., roller supports). The relative vertical displacements between the nodes on the wall were observed to be negligible, thus justifying using roller supports to simulate a rigid wall. Rigid elements were also used to simulate a rigid wall, but demonstrated almost no difference in solution to that obtained with roller supports.

The choice of the localization tolerance, $h^{\mathrm{tol}} = 0.001$, is made to allow the element at the base of the excavation to localize during the excavation of the fifth soil layer. It is possible for the deviator stress ratio h for dilative plastic flow in Eq. (4.1) to jump over the localization condition $(\sqrt{3/(3-b^2)})$, in which case the load steps (time steps for the quasi-static problem) must be refined in order to capture the point of bifurcation accurately (as is done for all other numerical examples presented in this chapter, which are strain-driven problems). For the excavation problem, however, it is not possible to refine the load steps without altering the sequence of excavation (during excavation, each load step corresponds to one soil layer being removed). Thus, it is noticed that the localization condition in Eq. (4.1) is jumped over for the element at the base of the excavation during the excavation of the fifth soil layer, as well as other elements at the base, for dilative plastic flow. For deviatoric plastic flow ($b = 0.0$) the deviator stress ratio in Eq. (4.1) approaches the localization condition at a minimum.

Upper slip lines may form during the excavation sequence. It is found that the upper slip lines do not always fully propagate to the ground surface while the lower slip line beginning at the excavation base does fully propagate to the ground surface when it is the only slip line. The consequences of these upper slip lines forming are that either they do not allow the lower slip line to fully propagate and thus do not allow the solution to converge further, or that they do allow the lower slip line to fully propagate but do not significantly alter the solution obtained if they had not existed in the first place (i.e., if they had been restricted from forming). More importantly, in order to produce comparisons between the different mesh refinement solutions (different upper slip lines may form for different mesh refinements), only one slip line is restricted to initiate at the excavation base for this example. Of course, while simulating an actual field excavation the simulation would be allowed to run unfettered. Furthermore, reports have shown that slip surfaces and/or shear bands typically form due to material inhomogeneities (CHAN & MORGENSTERN [13], FINNO et al. [25], and FINNO & NERBY [26]). This example, however, assumes a homogeneous material, but because of the geometry which results as soil layers are excavated, the stress field is non-uniform throughout the meshes (allowing certain elements to localize earlier than others). With material inhomogeneities represented throughout a mesh for an actual field excavation, the inception of slip surfaces and shear bands would be clear.

Results for associative, dilative plastic flow ($\beta = b = 0.0978$) are shown in Figs. 4.55 to 4.58. Observe the similar initial slopes of the enhanced solution curves and the dramatic ramp up for the 1280-element mesh. This case will be examined in more detail employing contour plots to attempt to understand the ramping-up behavior for the enhanced solution curve of the 1280-element mesh shown in Fig. 4.55. First, the slip lines for each mesh are compared in Fig. 4.59. As the mesh is refined, the slip line develops a smaller radius of curvature and becomes more S-shaped. The slip lines for each mesh at the end of excavation sequence and at full formation are shown in Figs. 4.60, 4.61, and 4.62. Contour plots of mean stress p, octahedral shear stress τ_{oct}, octahedral shear strain γ_{oct}, and effective plastic strain $\bar{\epsilon}^p$ at end of excavation sequence for standard solutions are shown in Figs. 4.63, 4.66, 4.69, and 4.72, respectively. The standard and enhanced solutions are the same at the end of excavation sequence because it takes one load step after elements have localized and traced in order for displacement jumps to develop along the slip line within the localized elements. Contour plots for standard solutions at end of loading are shown in Figs. 4.64, 4.67, 4.70, and 4.73, respectively. Contour plots for enhanced solutions are shown in Figs. 4.65, 4.68, 4.71, and 4.74, respectively. Note in Fig. 4.65 the tension that is occurring in the localized elements and in the elements at the ground surface away from the excavated soil portion. It is possible that the slip line becomes more S-shaped as the mesh is refined because more tension is observed at the ground surface. To test this hypothesis the simulation was run for each mesh just up until the slip lines had fully formed. The slip lines for each mesh at mid simulation—just before the upper portion of the slip line forms beyond its inflection point—are shown in Figs. 4.75, 4.76, and 4.77. Contour plots of mean stress p, octahedral shear stress τ_{oct}, octahedral shear strain γ_{oct}, and effective plastic strain $\bar{\epsilon}^p$ at mid simulation for enhanced solutions are shown in Figs. 4.78, 4.79, 4.80, and 4.81, respectively. Note in Fig. 4.78 the tension that is occurring in the elements at the ground surface just before the slip line has fully traced through each mesh. More tension is observed in the ground surface elements as the mesh is refined. It is not clear, though, whether this tension is causing the ramping-up behavior for the enhanced solution curve of the 1280-element mesh shown in Fig. 4.55 because a 'similar' amount of tension is also observed for the 320-element mesh, which does not demonstrate ramping-up behavior for its enhanced solution curve.

Results for non-associative, dilative plastic flow ($\beta = 0.1895, b = 0.0978$) are shown in Figs. 4.82 to 4.86. For the 5120-element mesh, the enhanced solution curve ramps up dramatically.

Results for non-associative, deviatoric plastic flow ($\beta = 0.275, b = 0.0$) are shown in Figs. 4.87 to 4.91. For the 5120-element mesh, the enhanced solution curve ramps up dramatically.

For each case the enhanced solutions are clearly insensitive to mesh alignment as seen by the slip line sharply tracing through unstructured meshes (i.e., element sides not aligned with the slip line orientation).

From the perspective of the practicing geotechnical engineer, the fact that the strut loads predicted by the enhanced finite element solution are greater than those predicted by the standard finite element solution (see Figs. 4.55, 4.82, and 4.87) indicates that the standard finite element solution underestimates the expected strut loads and thus could produce an unsafe design for the bracing system when strain localization is present.

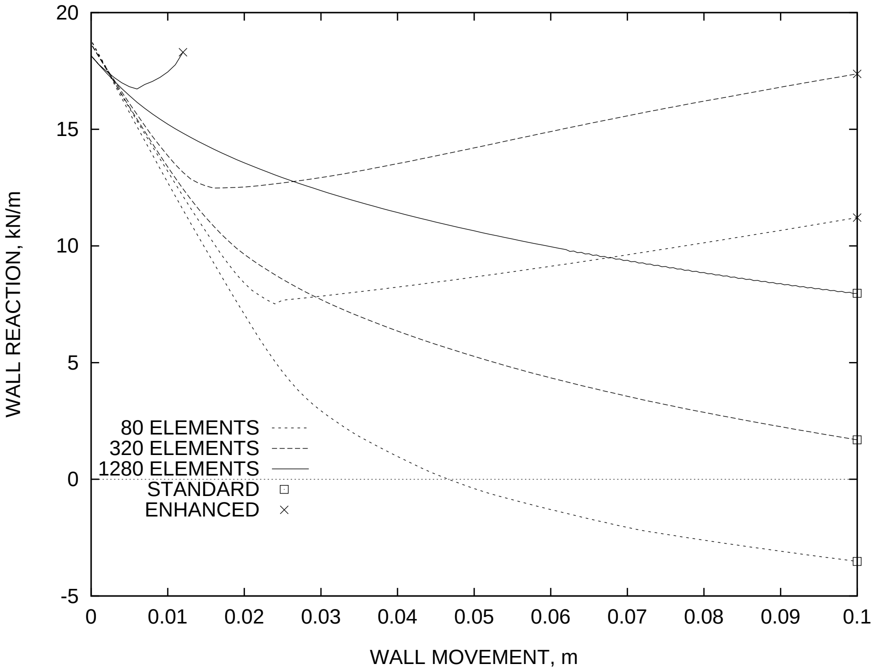

Figure 4.55. Plane strain excavation problem. Load-displacement plots for associative, dilative plastic flow: $\beta = b = 0.0978$. $h^{\mathrm{tol}} = 0.0015$. Enhanced solution curve for 1280-element mesh (shown in Fig. 4.58) ramps up dramatically.

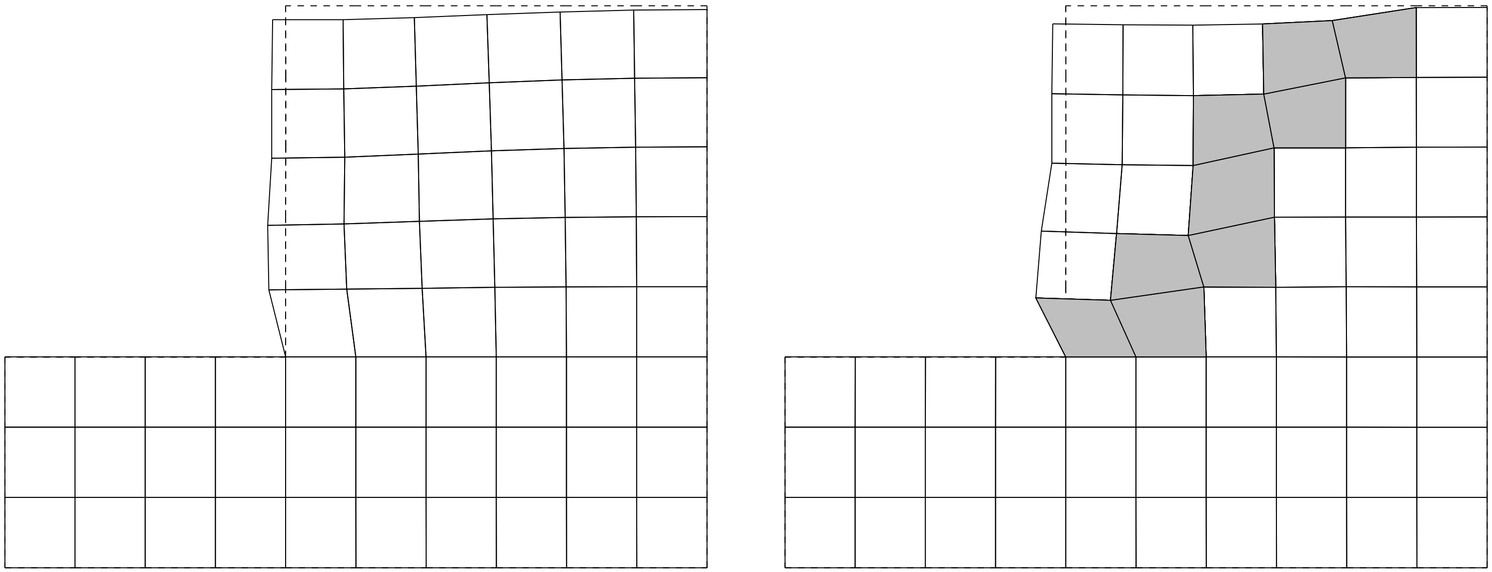

Figure 4.56. Plane strain excavation problem. Deformed meshes for standard and enhanced solutions with associative, dilative plastic flow: $\beta = b = 0.0978$. 80 linear quadrilateral elements. Localized elements are shaded.

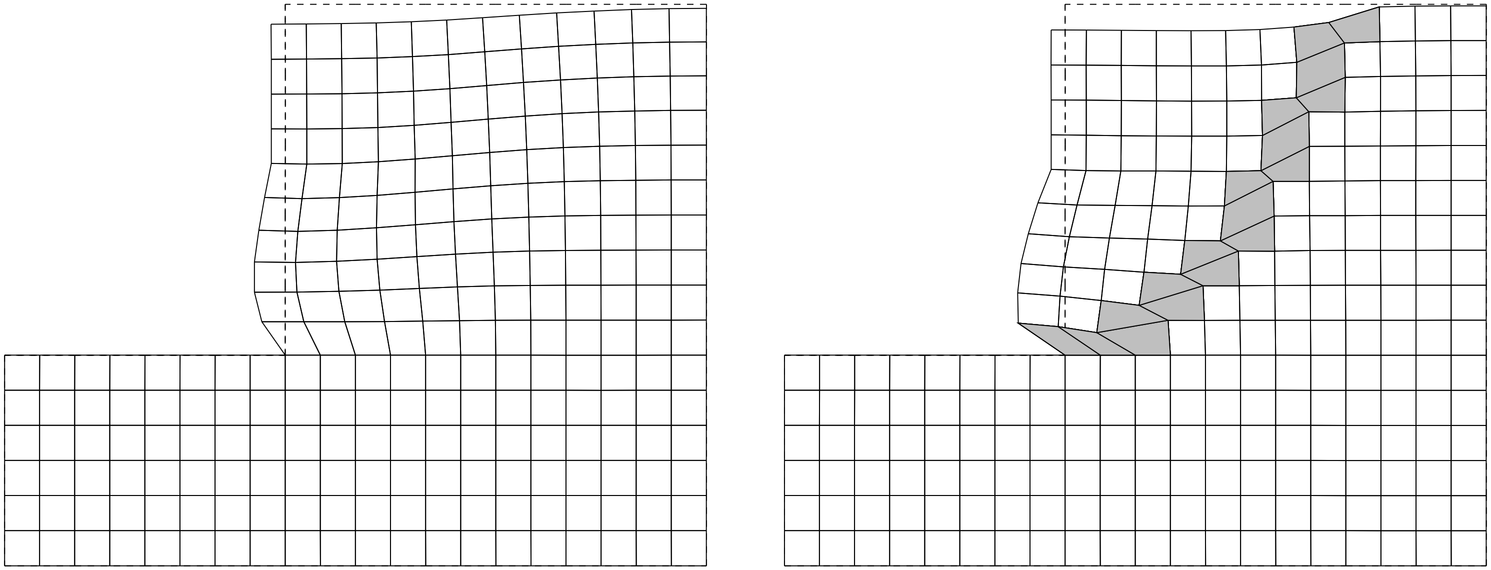

Figure 4.57. Plane strain excavation problem. Deformed meshes for standard and enhanced solutions with associative, dilative plastic flow: $\beta = b = 0.0978$. 320 linear quadrilateral elements. Localized elements are shaded.

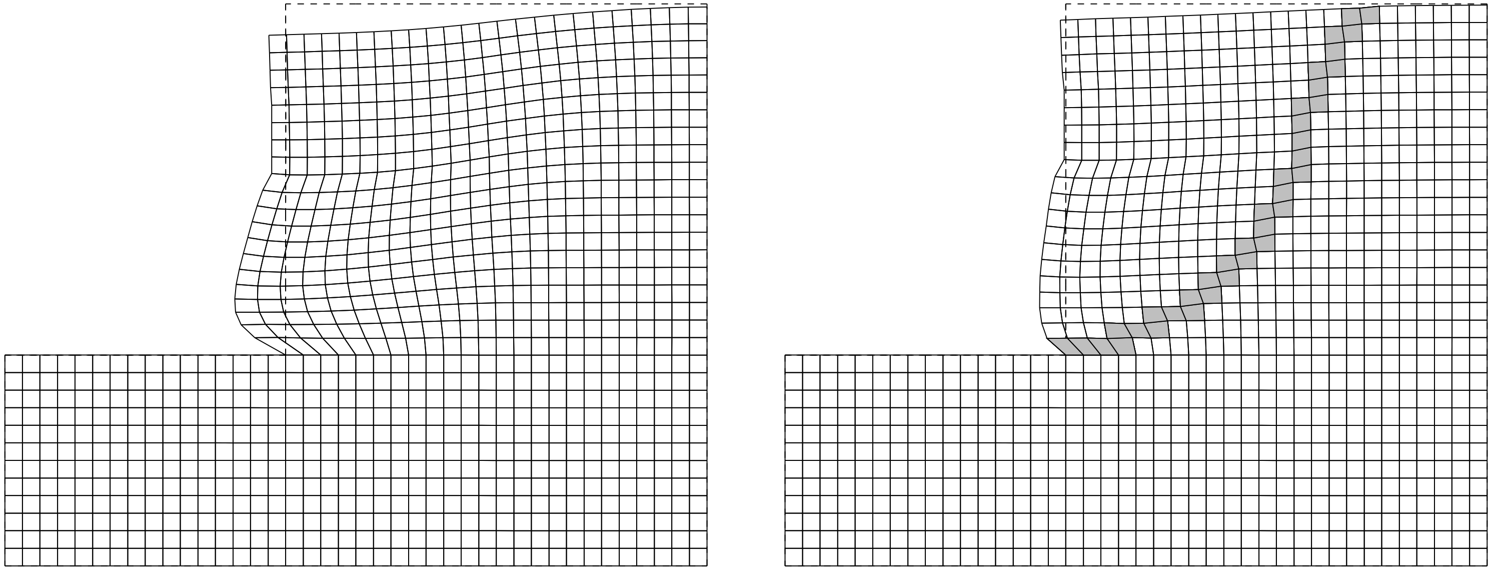

Figure 4.58. Plane strain excavation problem. Deformed meshes for standard and enhanced solutions with associative, dilative plastic flow: $\beta = b = 0.0978$. 1280 linear quadrilateral elements. Localized elements are shaded.

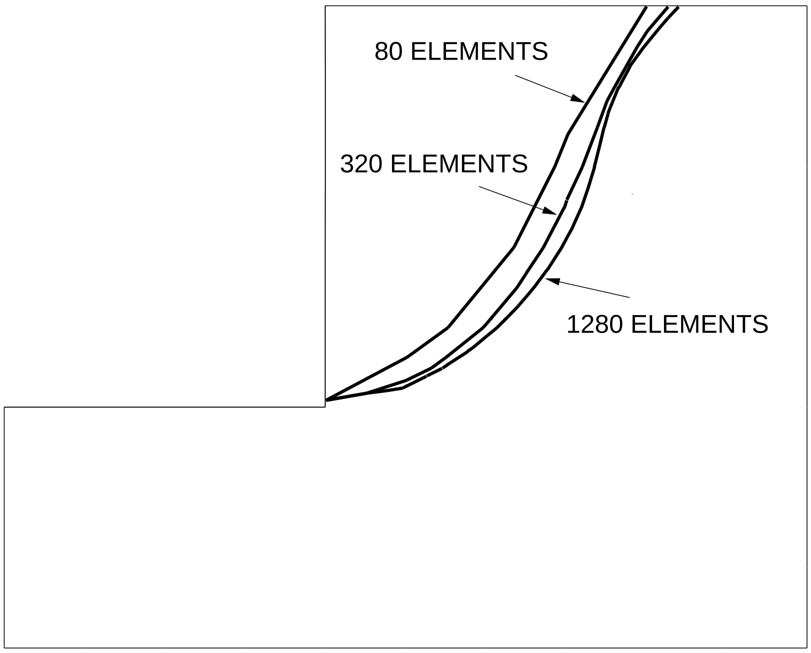

Figure 4.59. Plane strain excavation problem. Slip lines for three meshes for enhanced solutions with associative, dilative plastic flow: $\beta = b = 0.0978$.

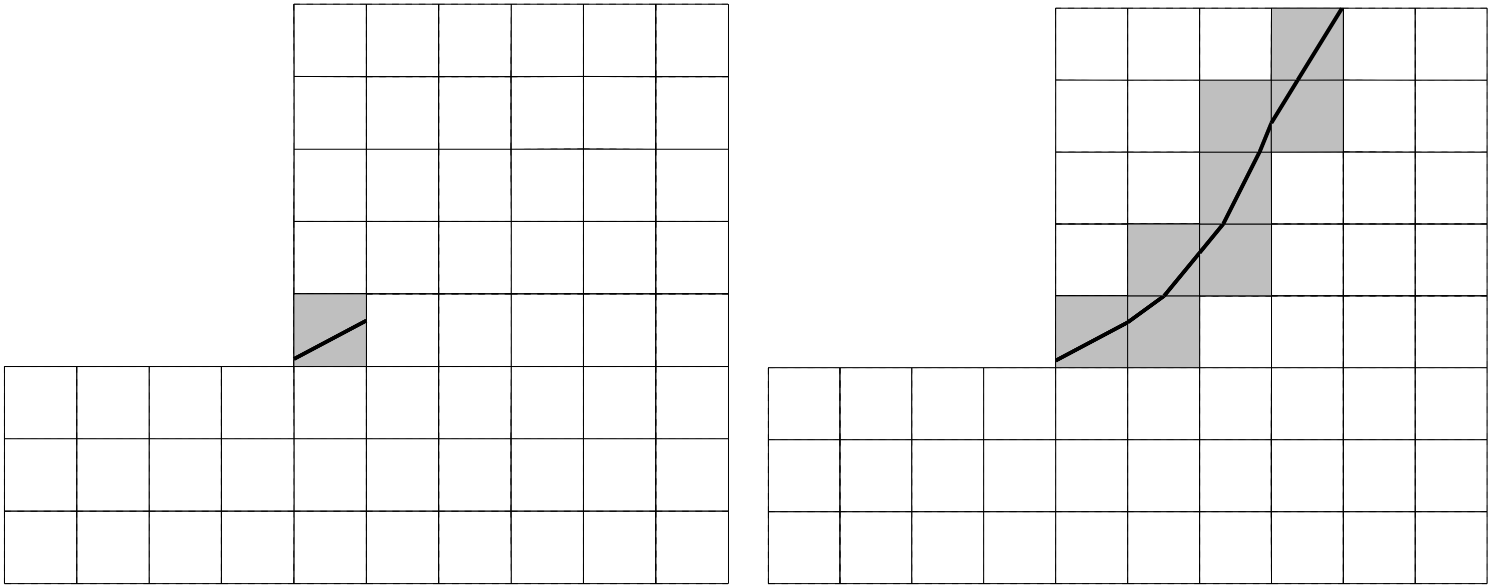

Figure 4.60. Plane strain excavation problem. Slip lines at end of excavation sequence and full formation of slip line for 80-element mesh enhanced solution with associative, dilative plastic flow: $\beta = b = 0.0978$. Localized elements are shaded. Slip lines drawn through localized elements.

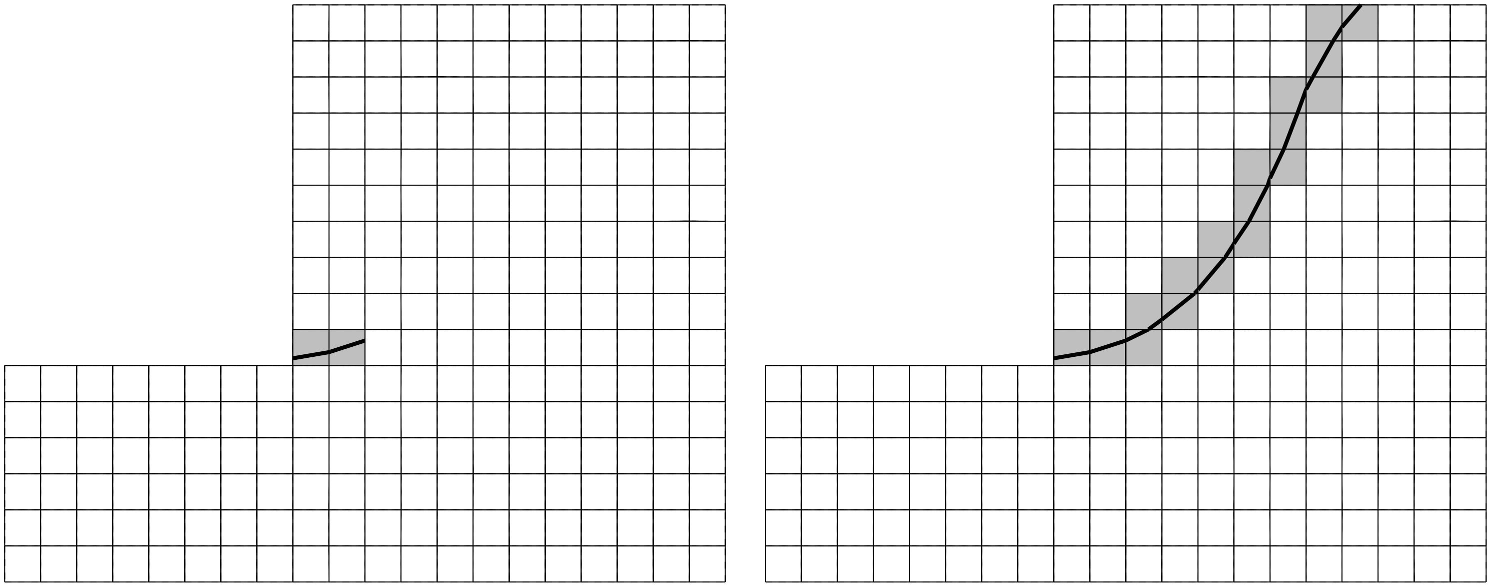

Figure 4.61. Plane strain excavation problem. Slip lines at end of excavation sequence and full formation of slip line for 320-element mesh enhanced solution with associative, dilative plastic flow: $\beta = b = 0.0978$. Localized elements are shaded. Slip lines drawn through localized elements.

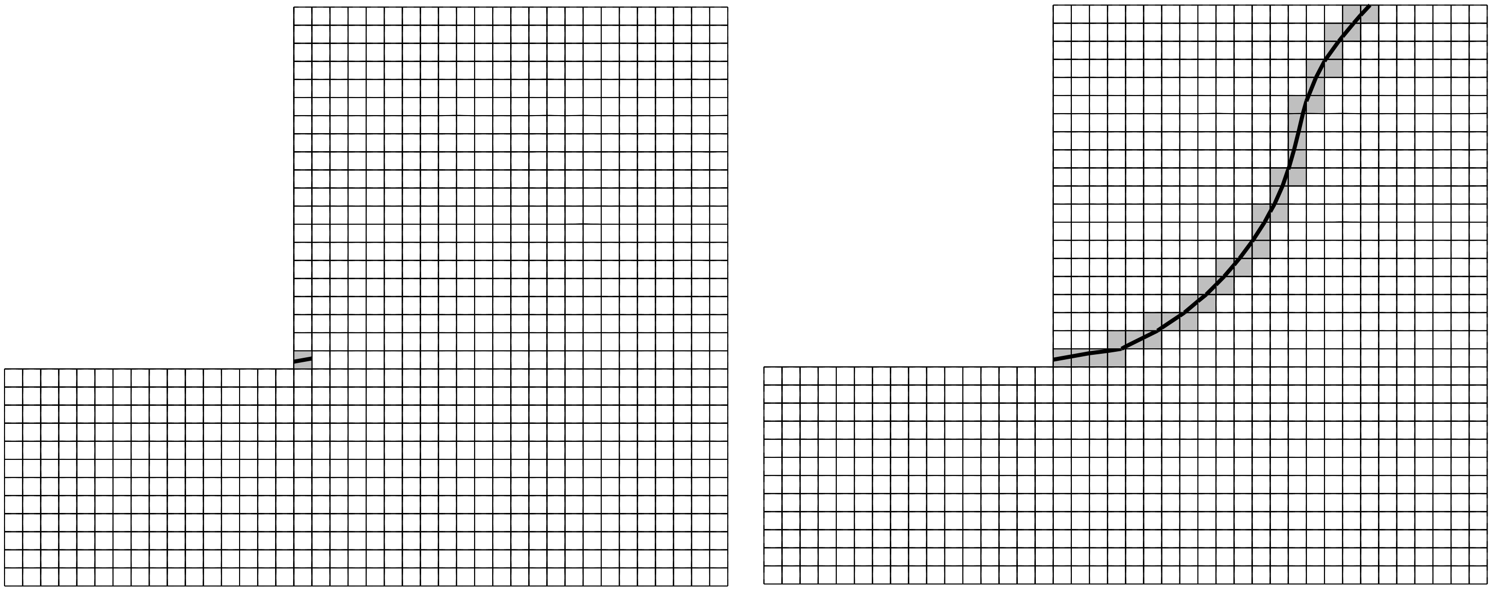

Figure 4.62. Plane strain excavation problem. Slip lines at end of excavation sequence and full formation of slip line for 1280-element mesh enhanced solution with associative, dilative plastic flow: $\beta = b = 0.0978$. Localized elements are shaded. Slip lines drawn through localized elements.

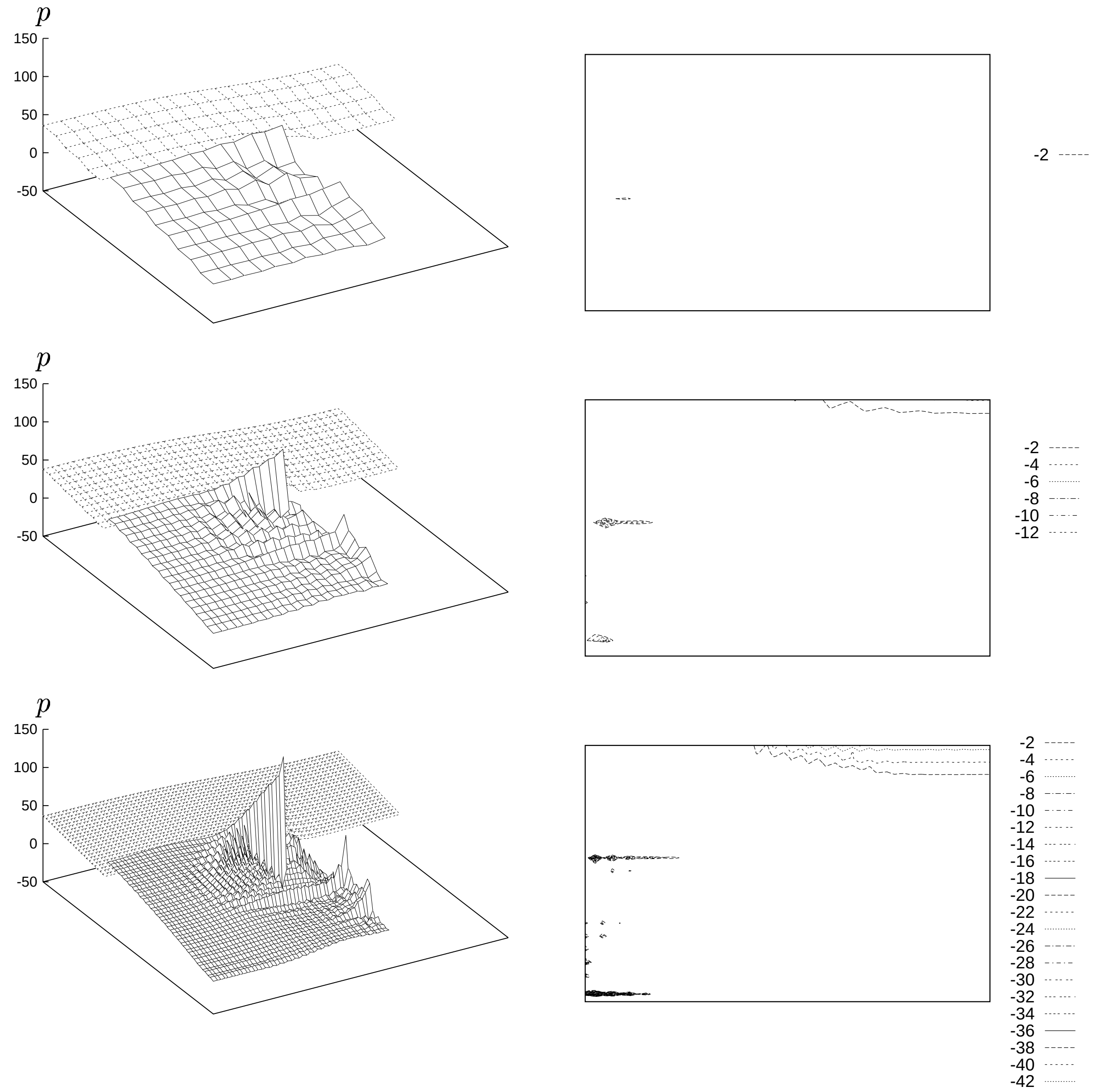

Figure 4.63. Contour plots of mean stress p (kPa) for standard solution at end of excavation sequence ($\beta = b = 0.0978$). Base contour plots on the right are of soil portion only (i.e., rock base is ignored) and of tension part only ($p < 0$ in these plots).

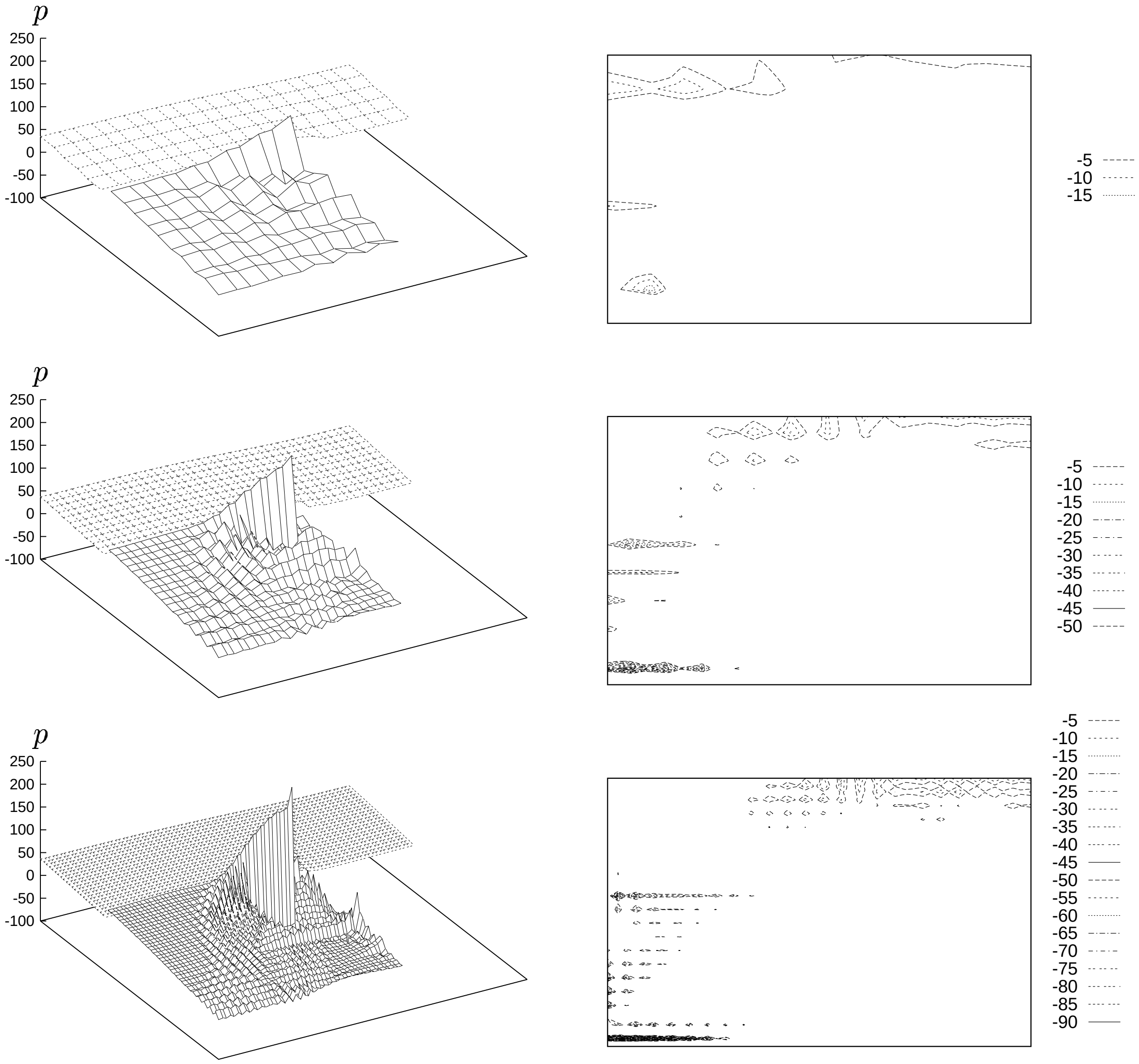

Figure 4.64. Contour plots of mean stress p (kPa) for standard solution at end of simulation ($\beta = b = 0.0978$). Base contour plots on the right are of soil portion only (i.e., rock base is ignored) and of tension part only ($p < 0$ in these plots).

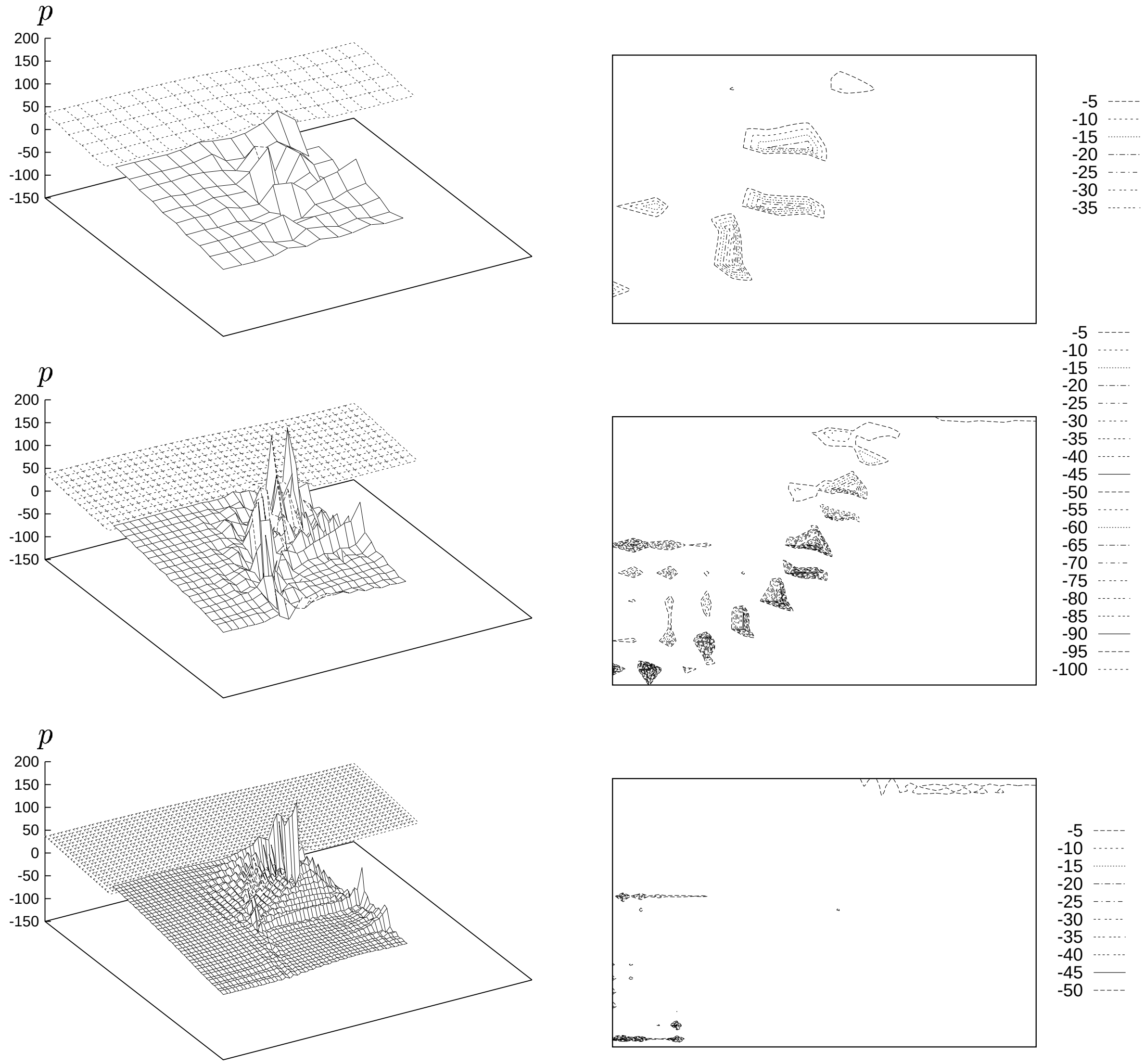

Figure 4.65. Contour plots of mean stress p (kPa) for enhanced solution at end of simulation ($\beta = b = 0.0978$). Base contour plots on the right are of soil portion only (i.e., rock base is ignored) and of tension part only ($p < 0$ in these plots).

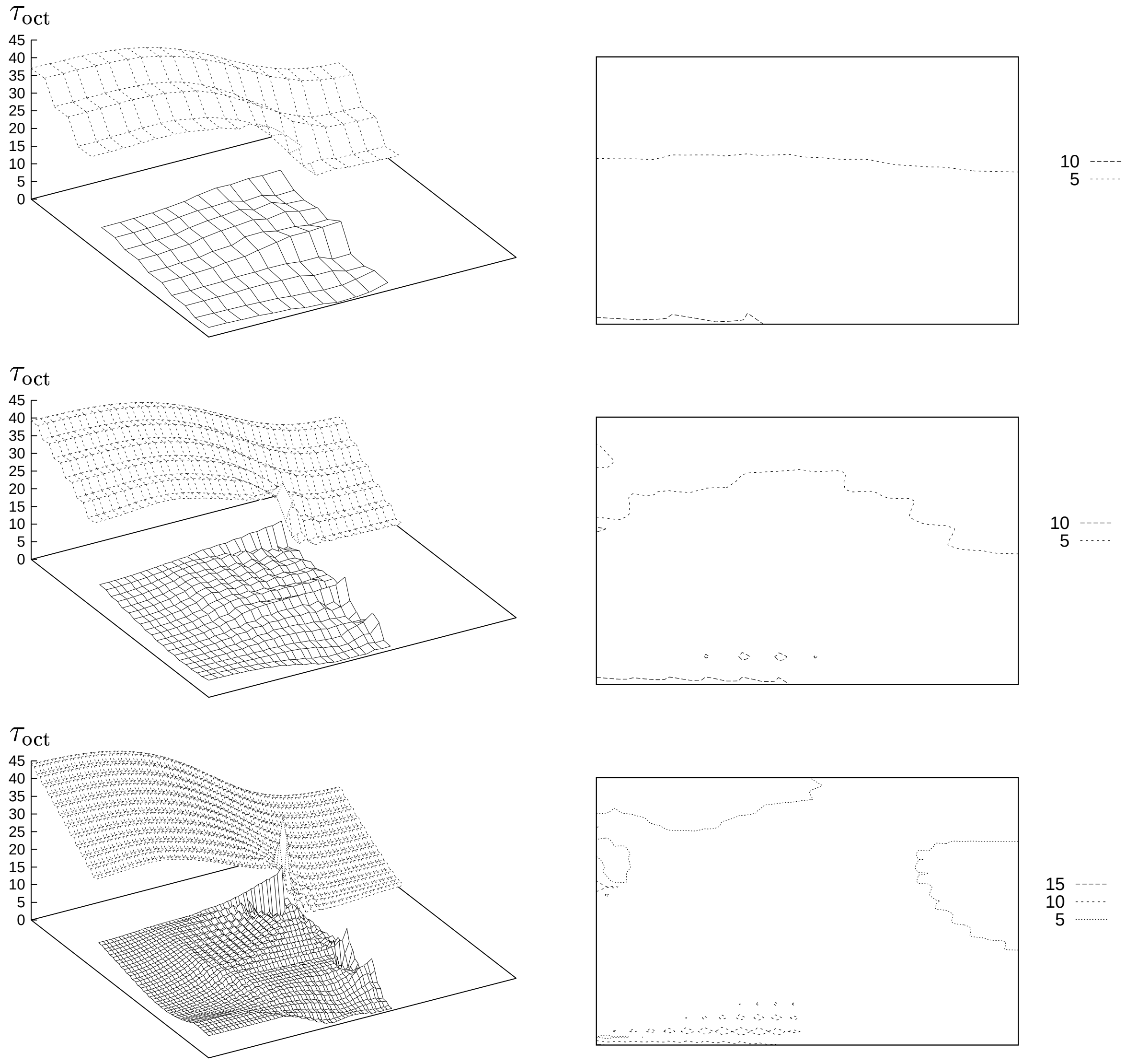

Figure 4.66. Contour plots of octahedral shear stress τ_{oct} (kPa) for standard solution at end of excavation sequence ($\beta = b = 0.0978$). Base contour plots on the right are of soil portion only (i.e., rock base is ignored).

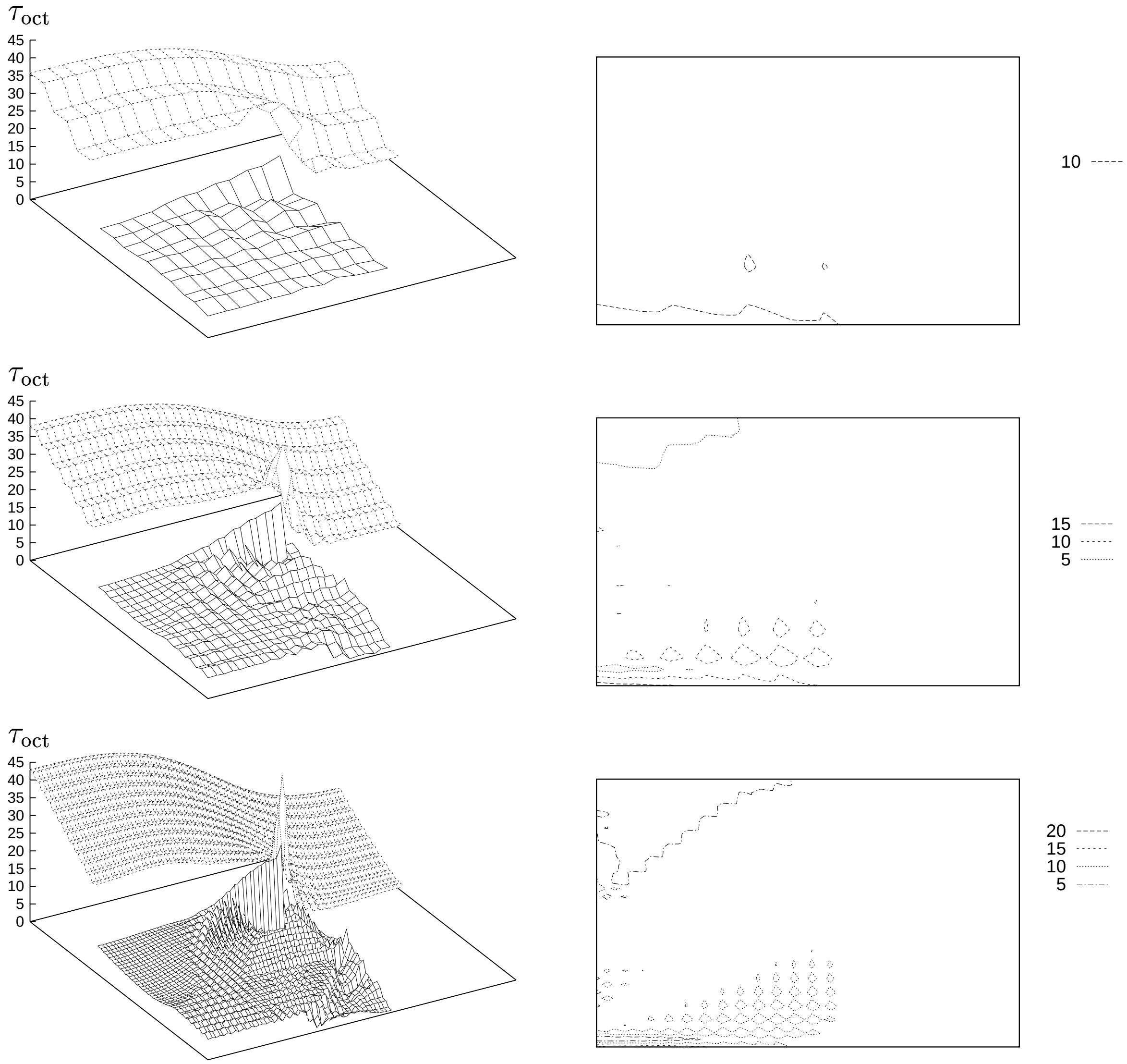

Figure 4.67. Contour plots of octahedral shear stress τ_{oct} (kPa) for standard solution at end of simulation ($\beta = b = 0.0978$). Base contour plots on the right are of soil portion only (i.e., rock base is ignored).

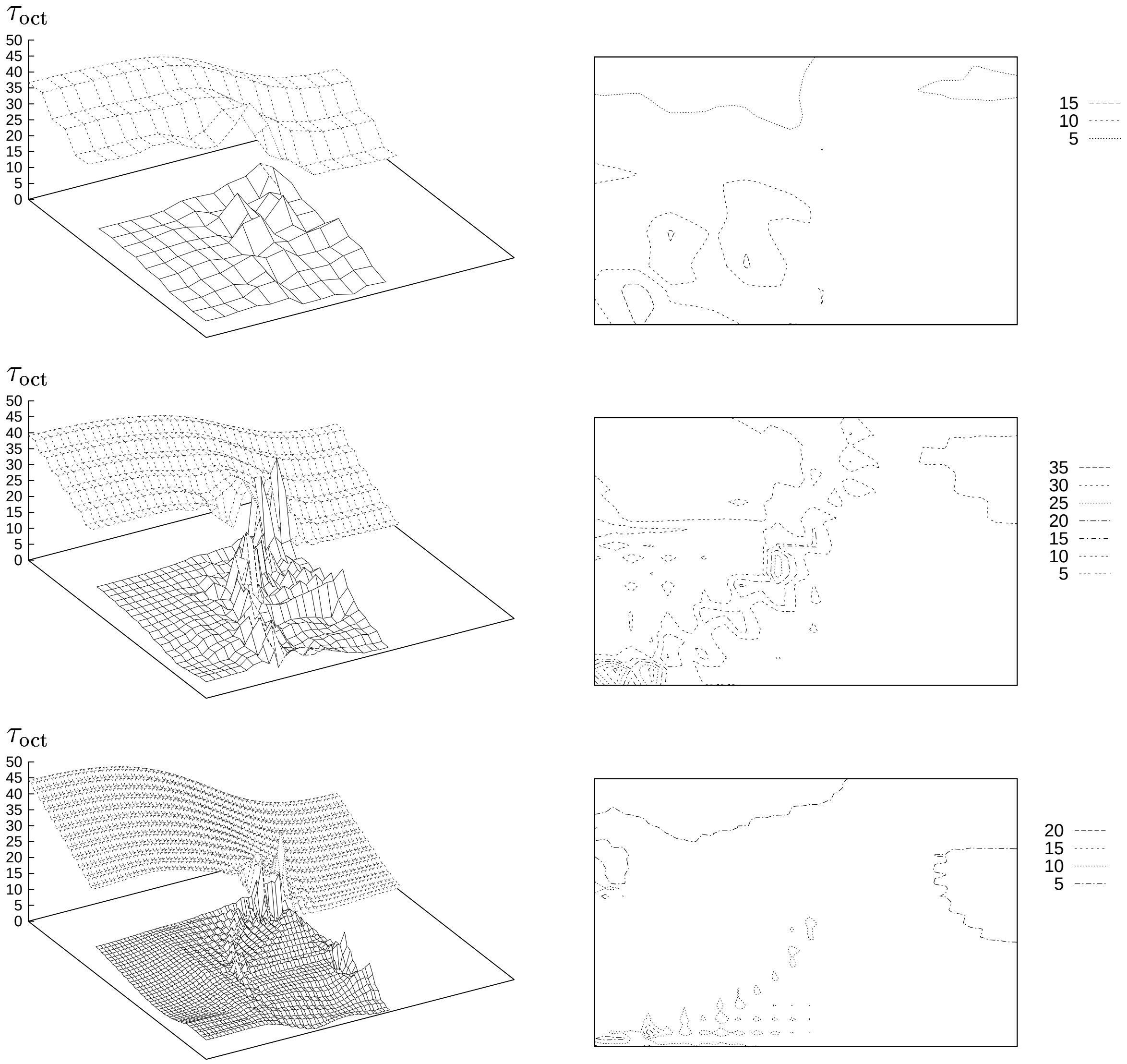

Figure 4.68. Contour plots of octahedral shear stress τ_{oct} (kPa) for enhanced solution at end of simulation ($\beta = b = 0.0978$). Base contour plots on the right are of soil portion only (i.e., rock base is ignored).

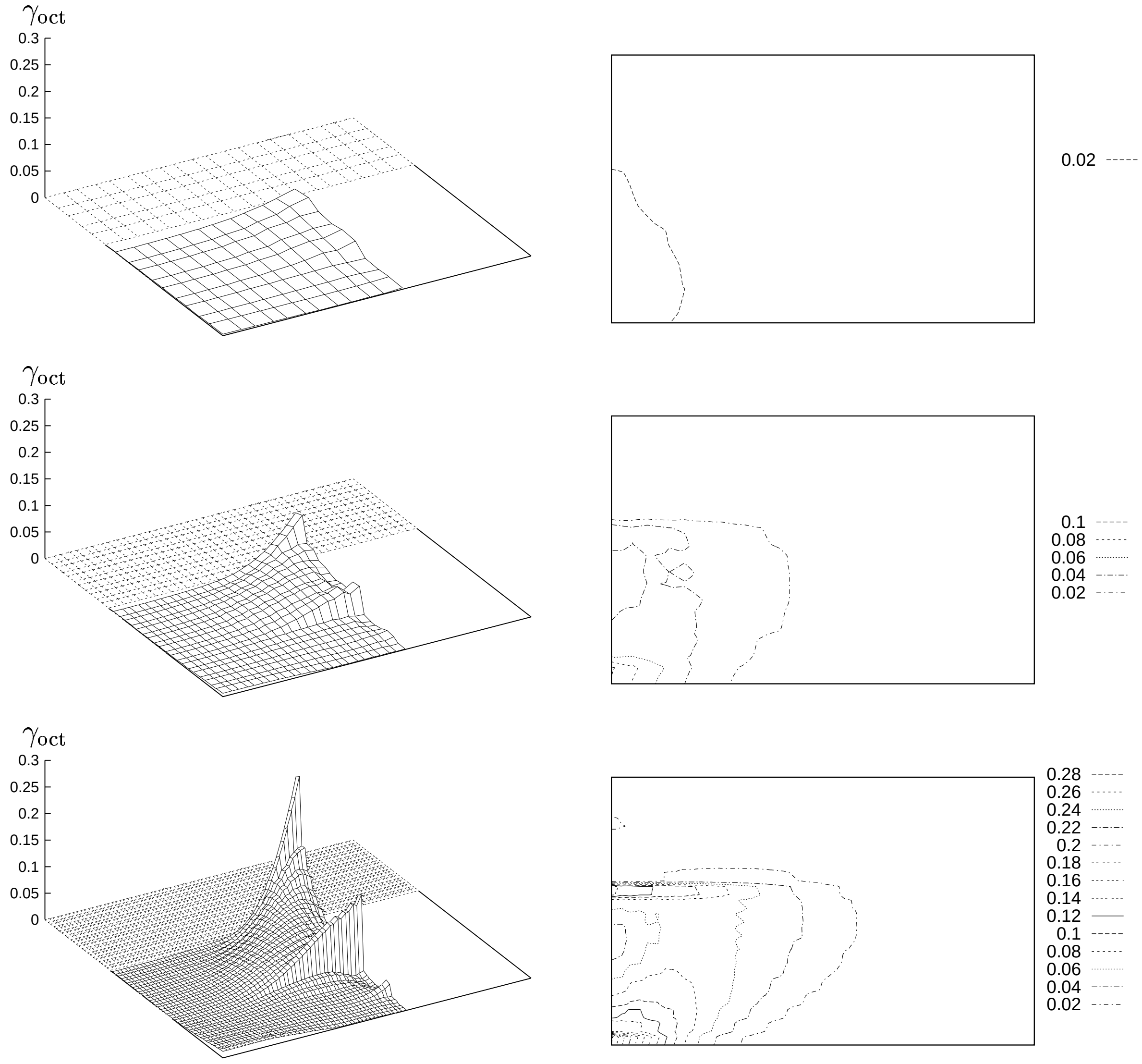

Figure 4.69. Contour plots of octahedral shear strain γ_{oct} (×100%) for standard solution at end of excavation sequence ($\beta = b = 0.0978$). Base contour plots on the right are of soil portion only (i.e., rock base is ignored).

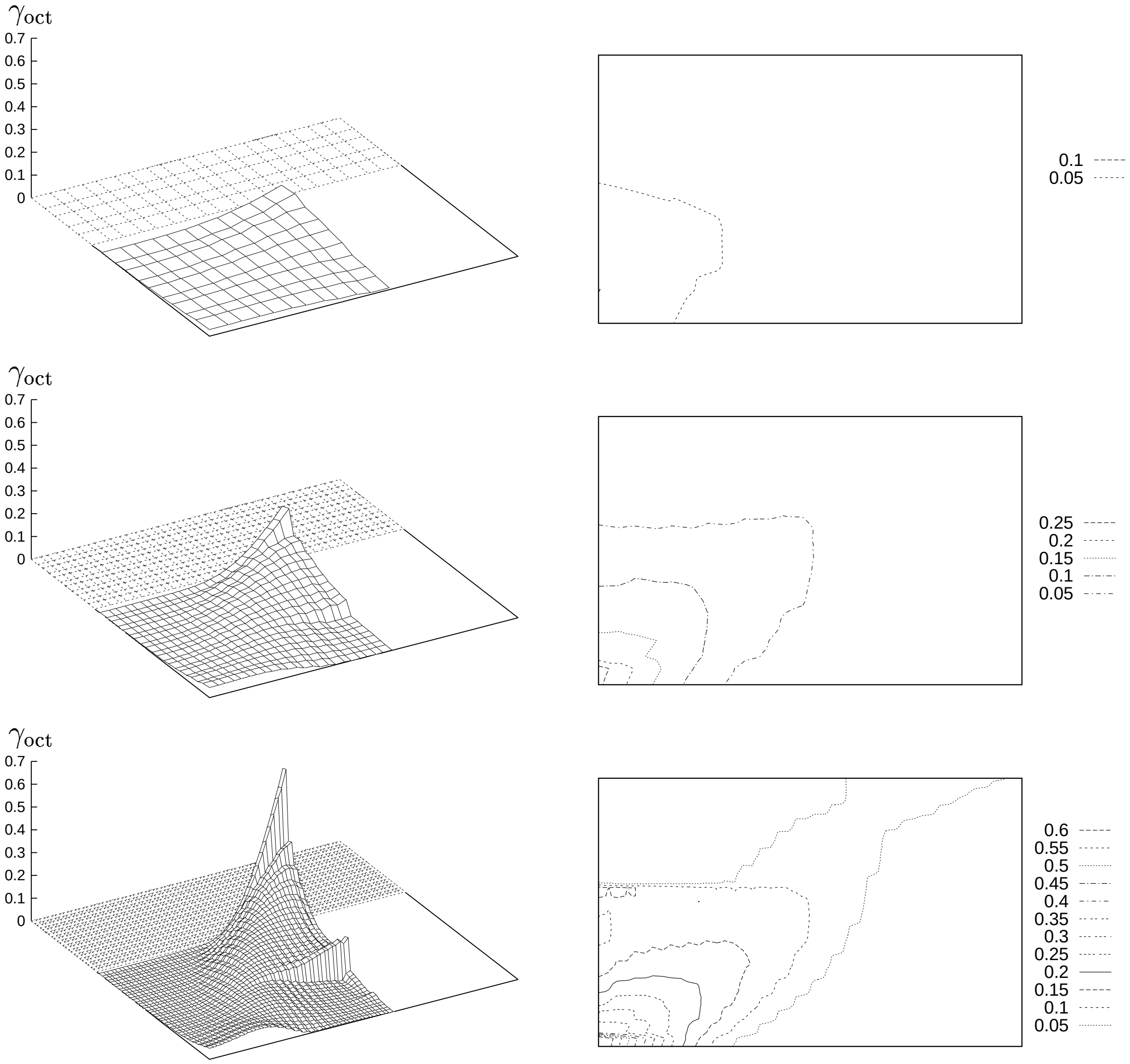

Figure 4.70. Contour plots of octahedral shear strain γ_{oct} (×100%) for standard solution at end of simulation ($\beta = b = 0.0978$). Base contour plots on the right are of soil portion only (i.e., rock base is ignored).

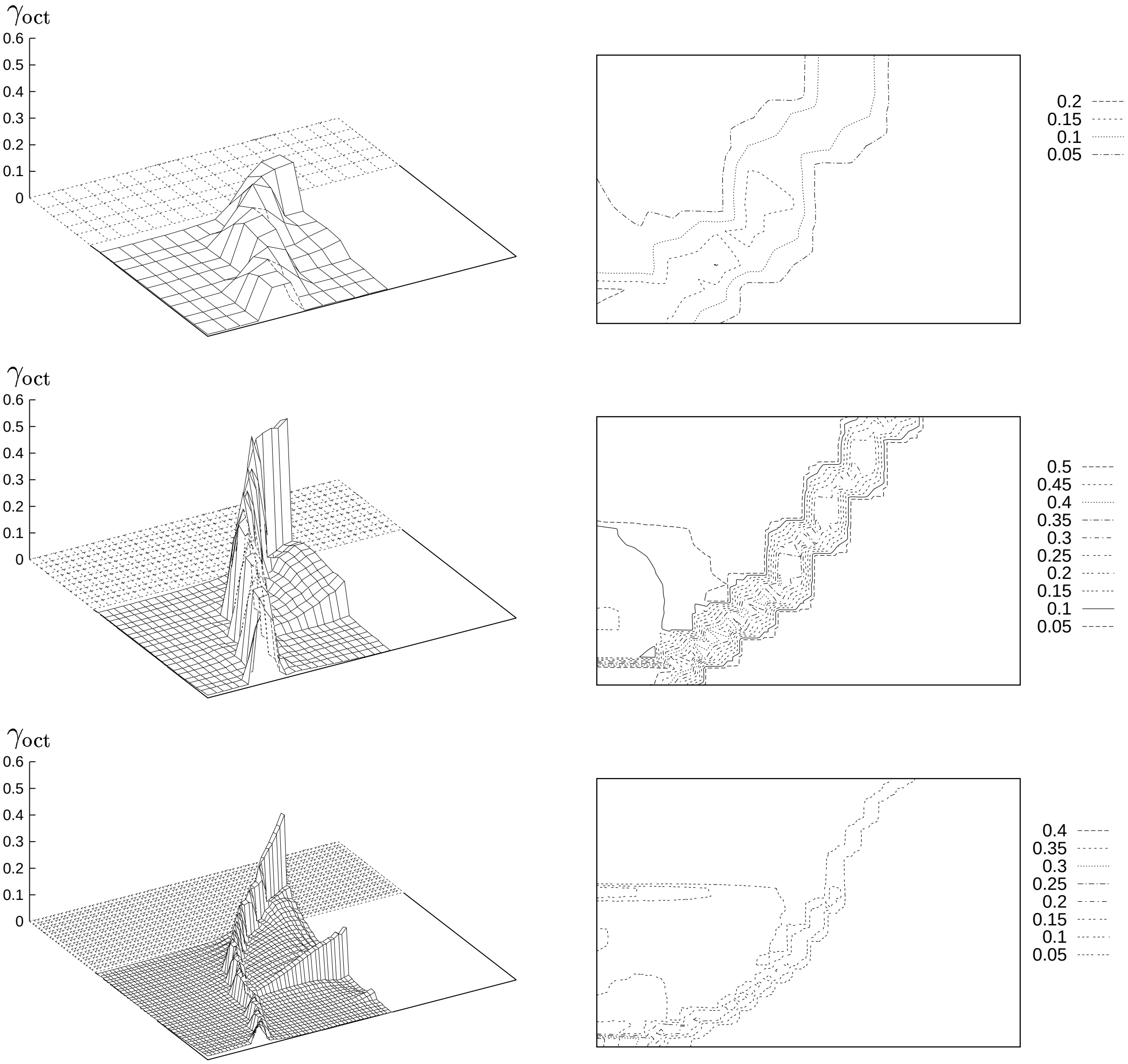

Figure 4.71. Contour plots of octahedral shear strain γ_{oct} (×100%) for enhanced solution at end of simulation ($\beta = b = 0.0978$). Base contour plots on the right are of soil portion only (i.e., rock base is ignored).

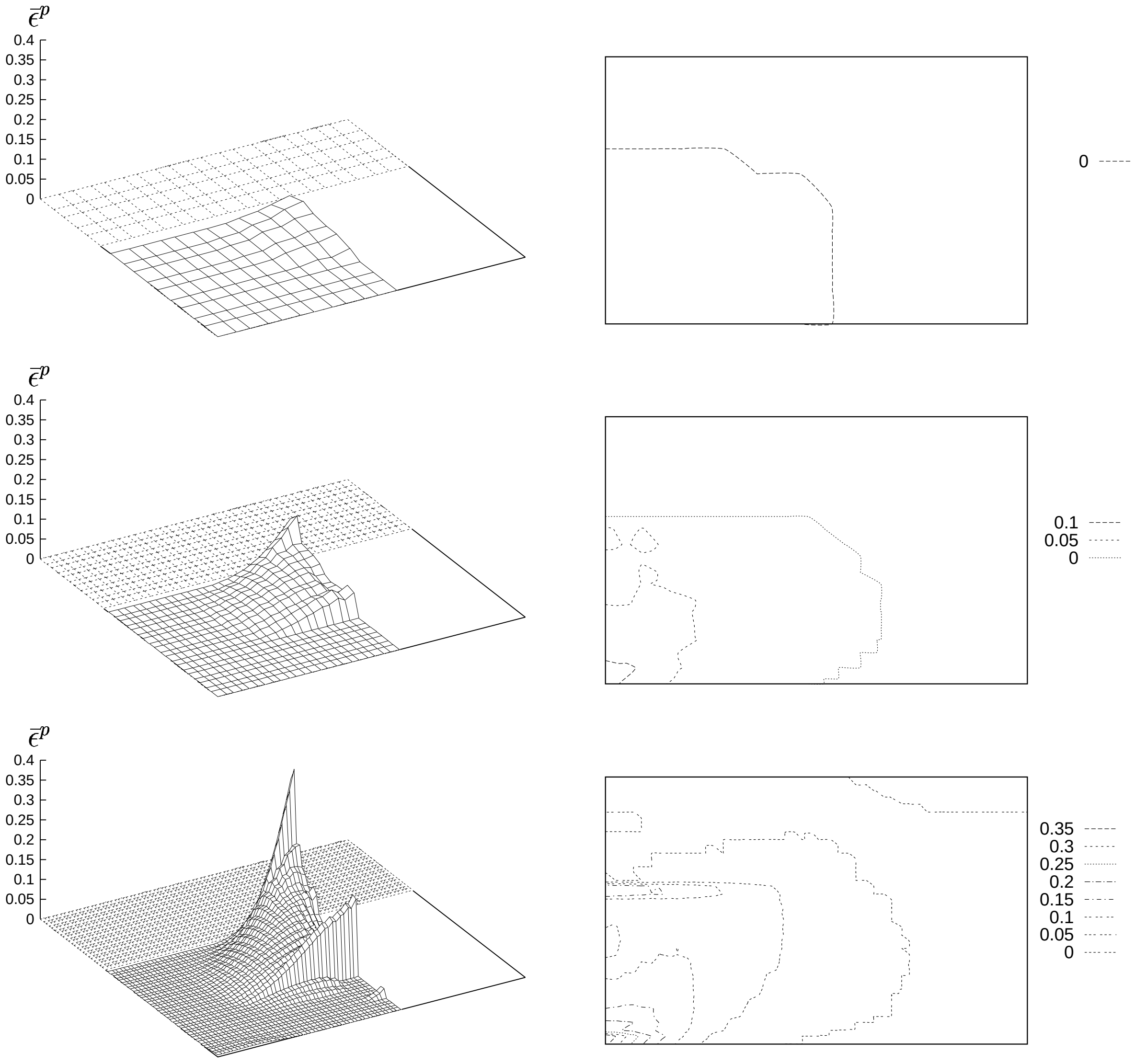

Figure 4.72. Contour plots of effective plastic strain $\bar{\epsilon}^p$ (×100%) for standard solution at end of excavation sequence ($\beta = b = 0.0978$). Base contour plots on the right are of soil portion only (i.e., rock base is ignored).

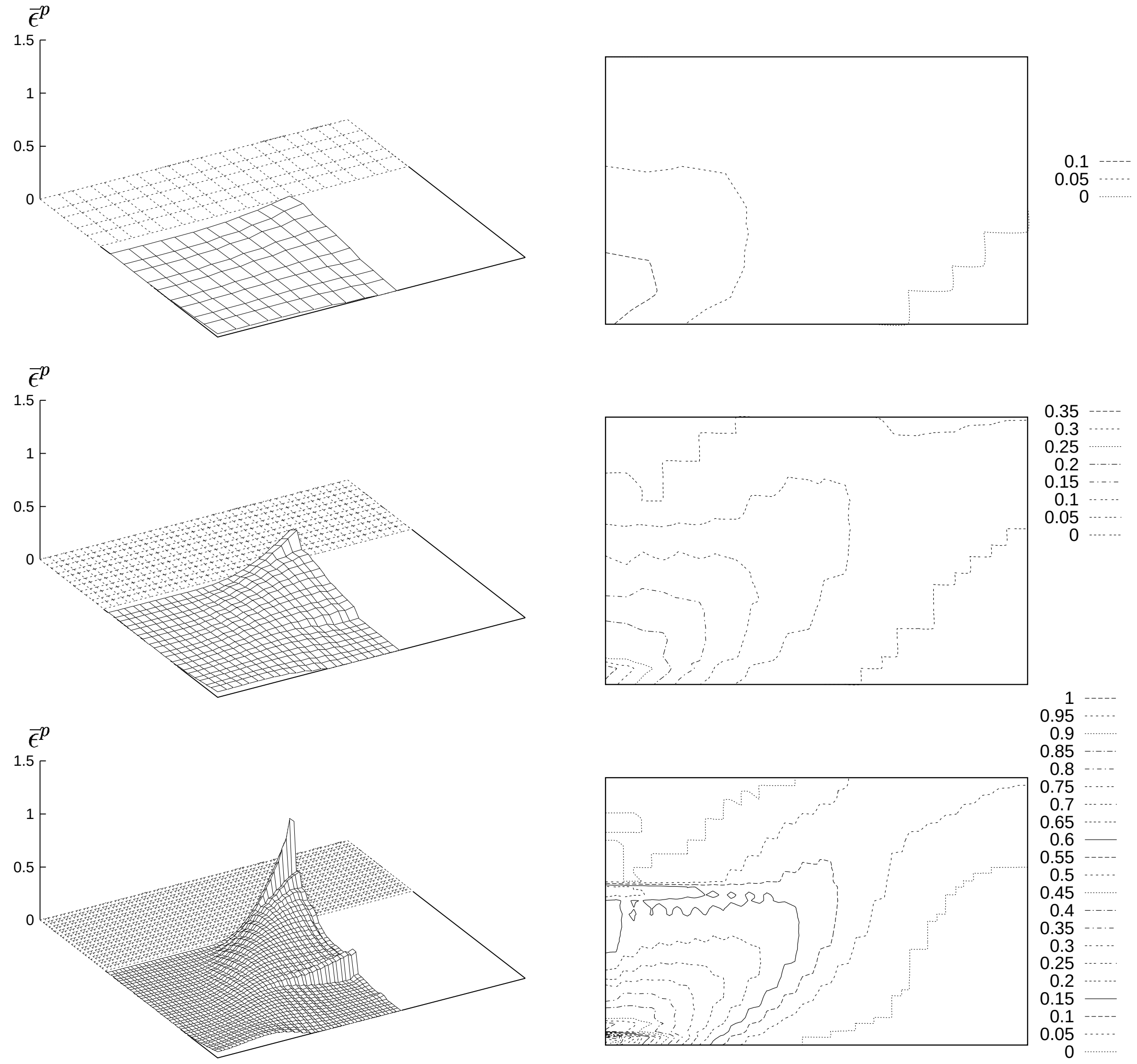

Figure 4.73. Contour plots of effective plastic strain $\bar{\epsilon}^p$ (×100%) for standard solution at end of simulation ($\beta = b = 0.0978$). Base contour plots on the right are of soil portion only (i.e., rock base is ignored).

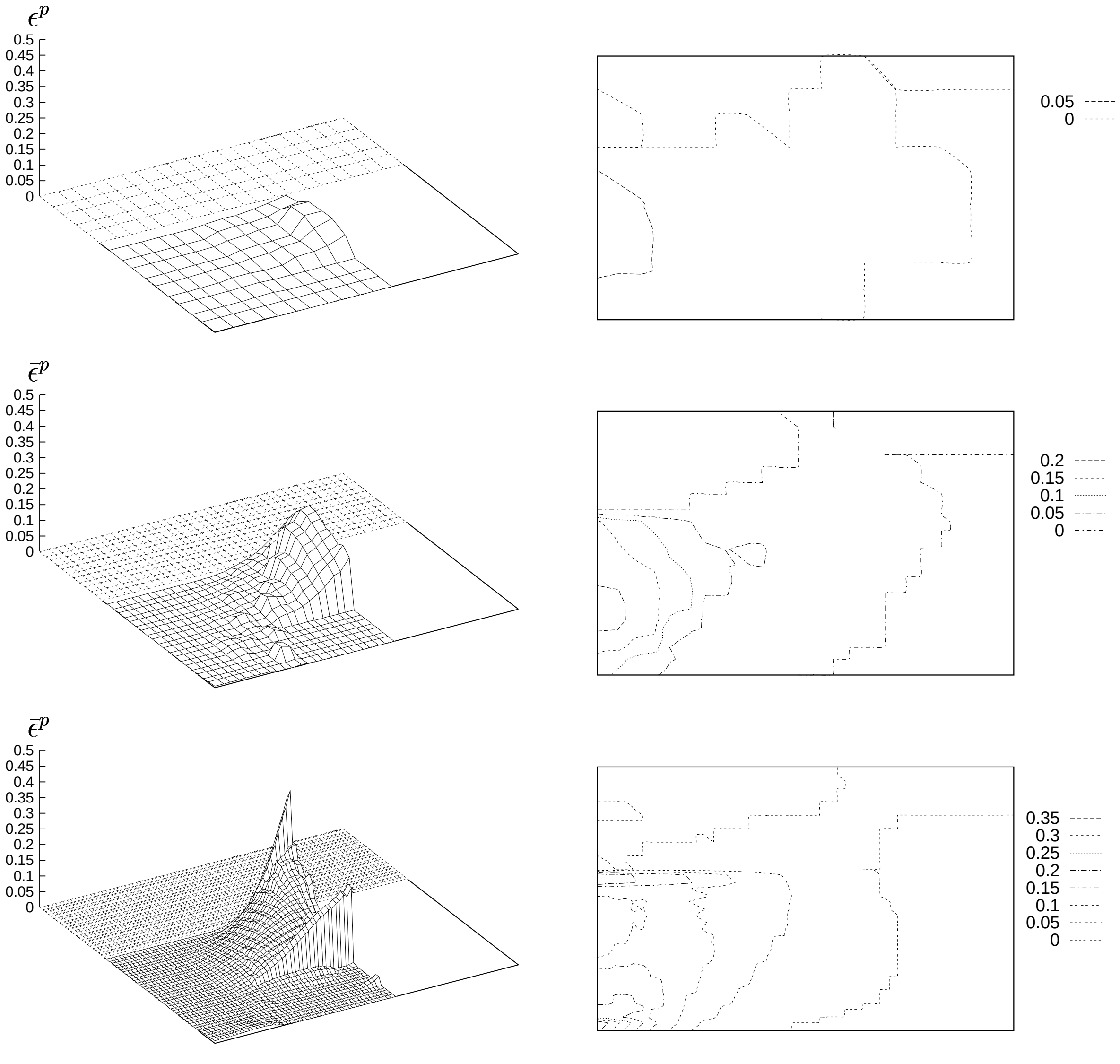

Figure 4.74. Contour plots of effective plastic strain $\bar{\epsilon}^p$ (×100%) for enhanced solution at end of simulation ($\beta = b = 0.0978$). Base contour plots on the right are of soil portion only (i.e., rock base is ignored).

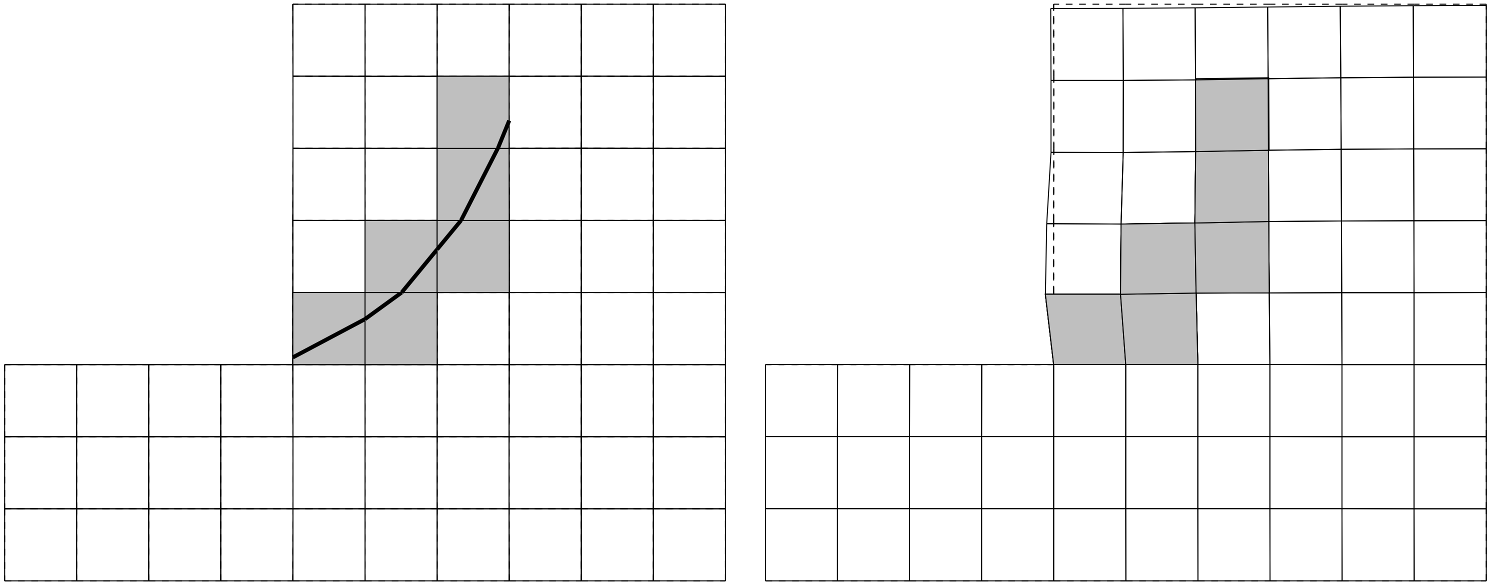

Figure 4.75. Plane strain excavation problem. Slip line at mid simulation just before slip-line fully propagates through 80-element mesh ($\Delta d = 0.025$m in Fig. 4.55). At right, deformed mesh for enhanced solution with associative, dilative plastic flow: $\beta = b = 0.0978$. Localized elements are shaded. Slip line drawn through localized elements.

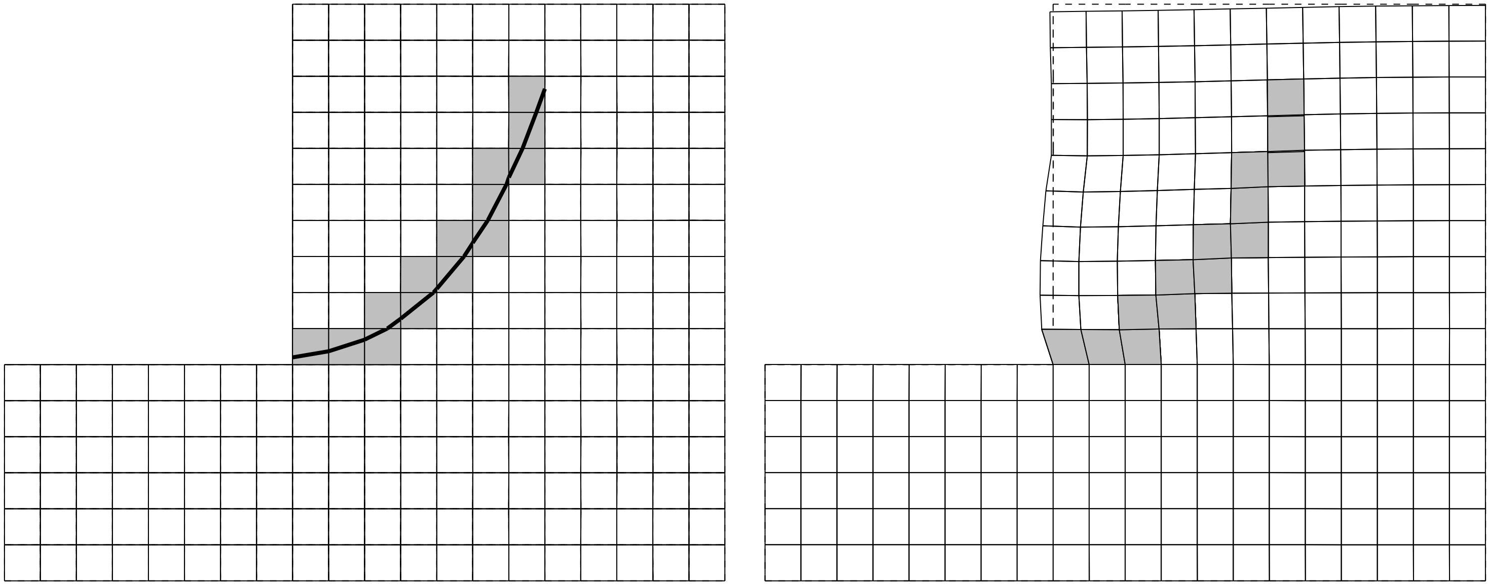

Figure 4.76. Plane strain excavation problem. Slip line at mid simulation just before slip-line fully propagates through 320-element mesh ($\Delta d = 0.019$m in Fig. 4.55). At right, deformed mesh for enhanced solution with associative, dilative plastic flow: $\beta = b = 0.0978$. Localized elements are shaded. Slip line drawn through localized elements.

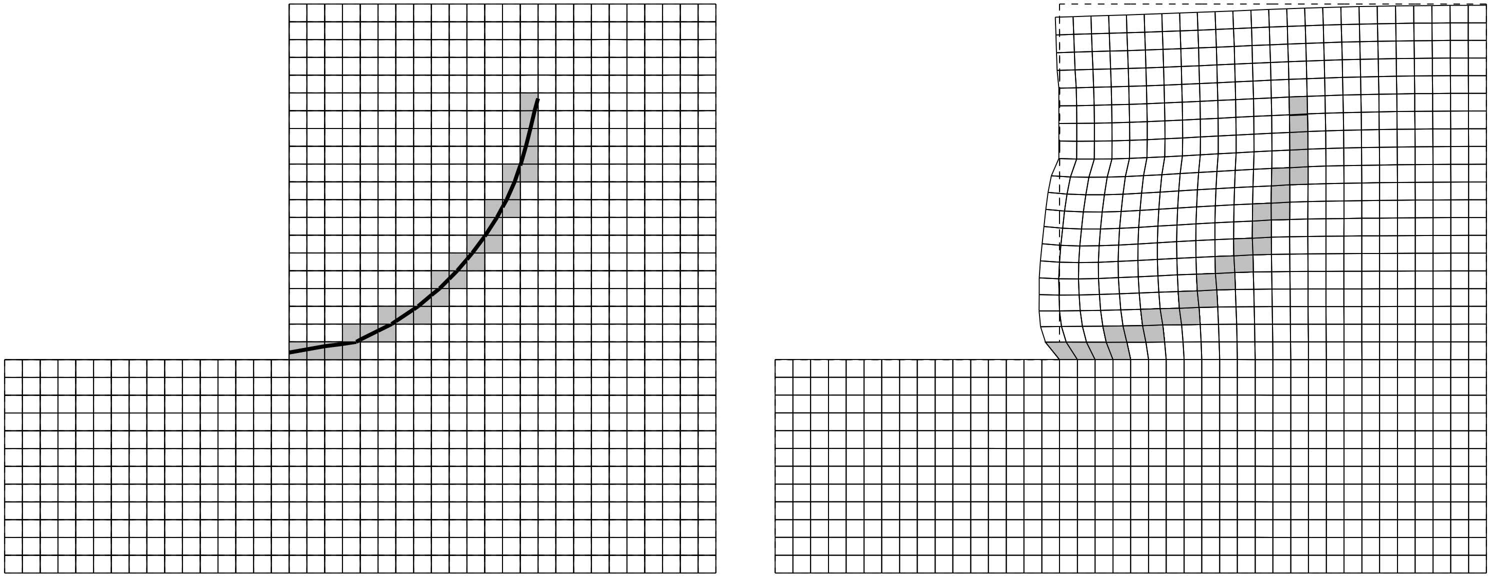

Figure 4.77. Plane strain excavation problem. Slip line at mid simulation just before slip-line fully propagates through 1280-element mesh ($\Delta d = 0.005$m in Fig. 4.55). At right, deformed mesh for enhanced solution with associative, dilative plastic flow: $\beta = b = 0.0978$. Localized elements are shaded. Slip line drawn through localized elements.

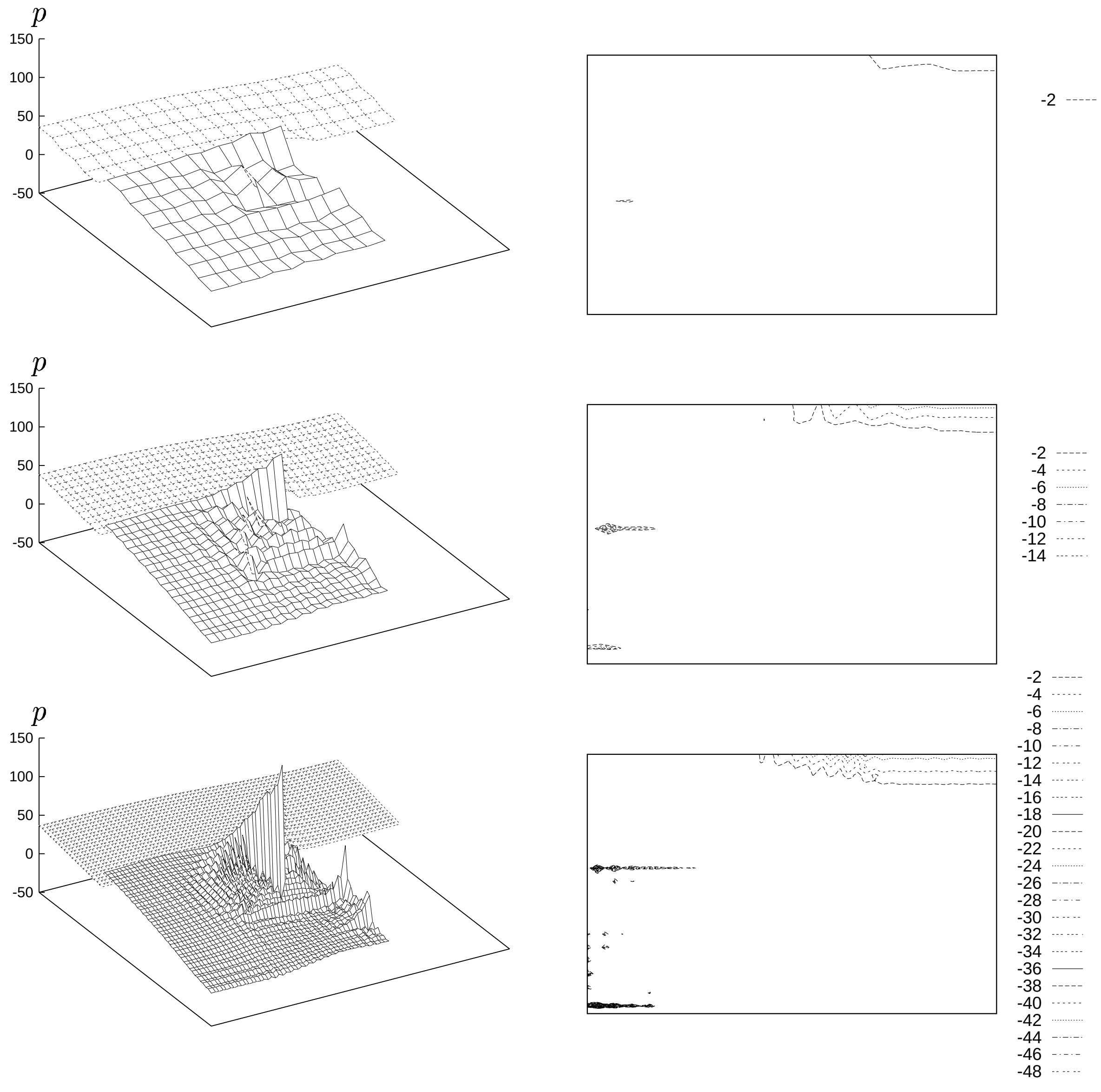

Figure 4.78. Contour plots of mean stress p (kPa) for enhanced solution at partial slip line formation in Figs. 4.75,4.76,4.77 ($\beta = b = 0.0978$). Base contour plots on the right are of soil portion only (i.e., rock base is ignored) and of tension part only ($p < 0$ in these plots).

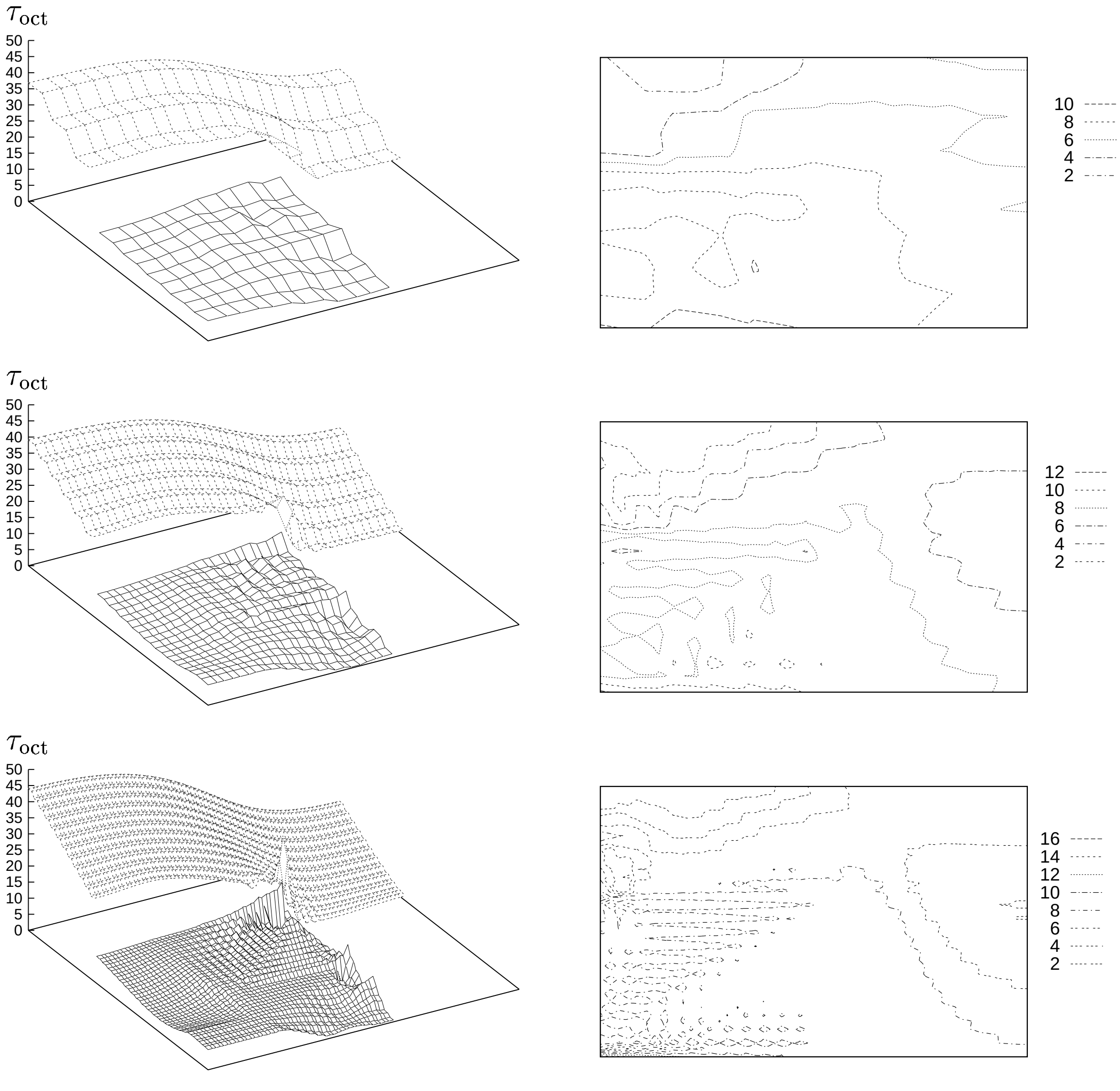

Figure 4.79. Contour plots of octahedral shear stress τ_{oct} (kPa) for enhanced solution at partial slip line formation in Figs. 4.75,4.76,4.77 ($\beta = b = 0.0978$). Base contour plots on the right are of soil portion only (i.e., rock base is ignored).

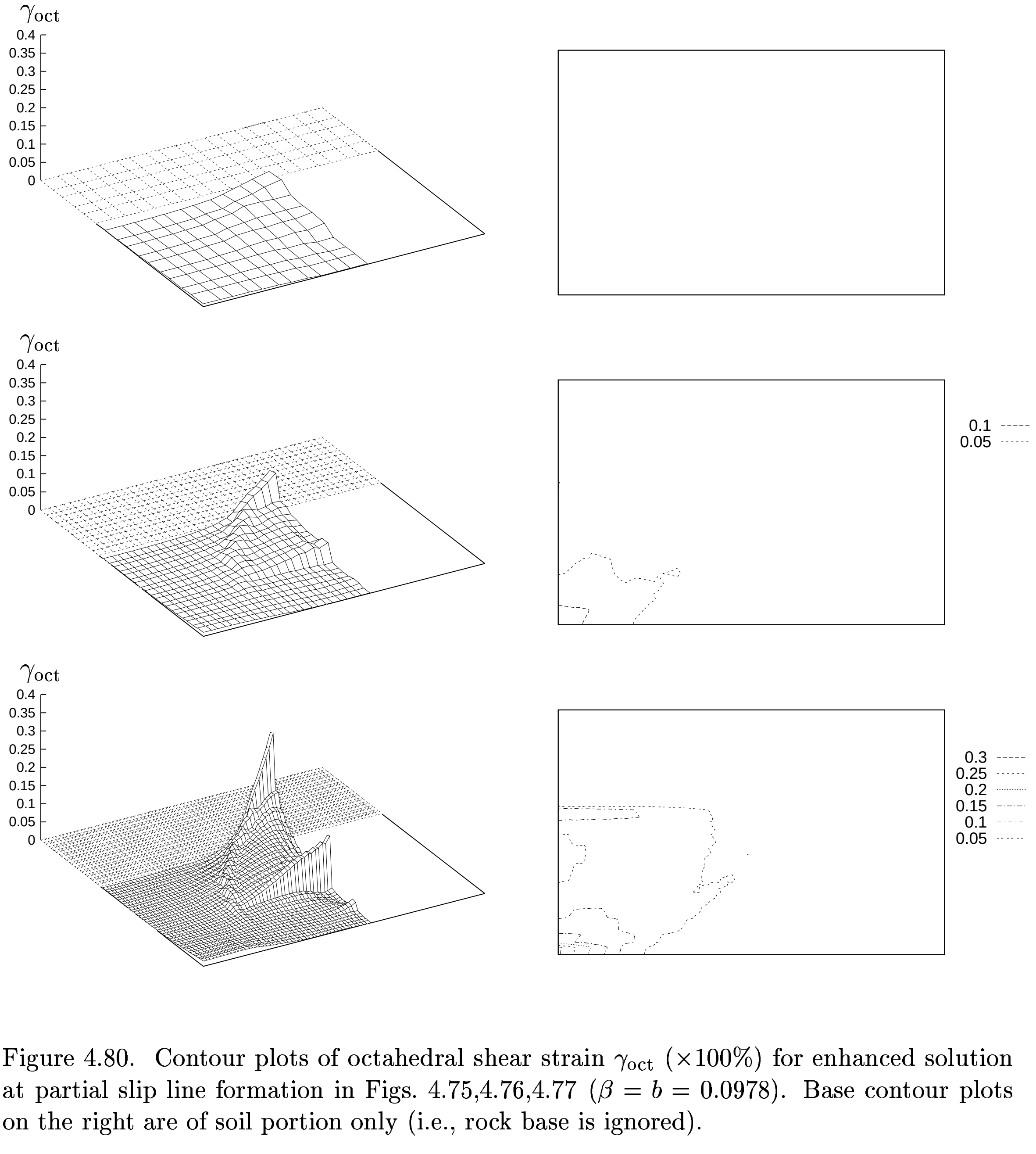

Figure 4.80. Contour plots of octahedral shear strain γ_{oct} (×100%) for enhanced solution at partial slip line formation in Figs. 4.75,4.76,4.77 ($\beta = b = 0.0978$). Base contour plots on the right are of soil portion only (i.e., rock base is ignored).

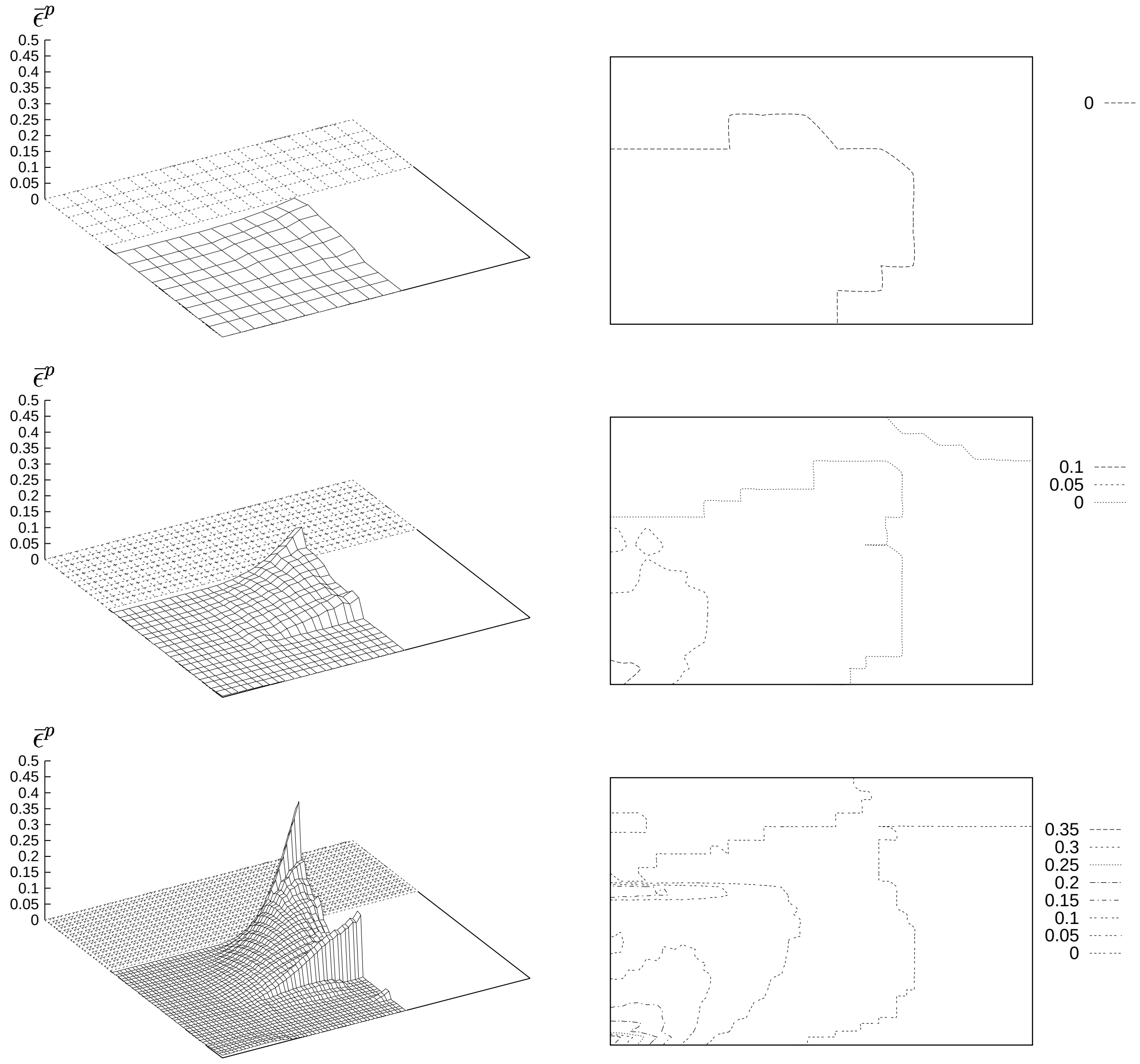

Figure 4.81. Contour plots of effective plastic strain $\bar{\epsilon}^p$ (×100%) for enhanced solution at partial slip line formation in Figs. 4.75,4.76,4.77 ($\beta = b = 0.0978$). Base contour plots on the right are of soil portion only (i.e., rock base is ignored).

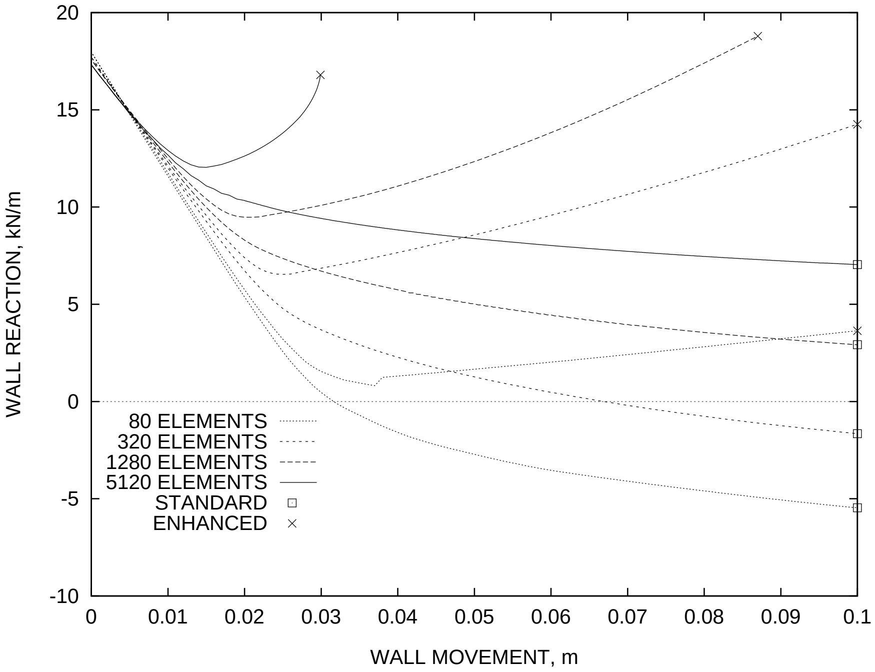

Figure 4.82. Plane strain excavation problem. Load-displacement plots for non-associative, dilative plastic flow: $\beta = 0.1895, b = 0.0978$. $h^{\text{tol}} = 0.001$. Enhanced solution curve for 5120-element mesh (shown in Fig. 4.86) ramps up dramatically.

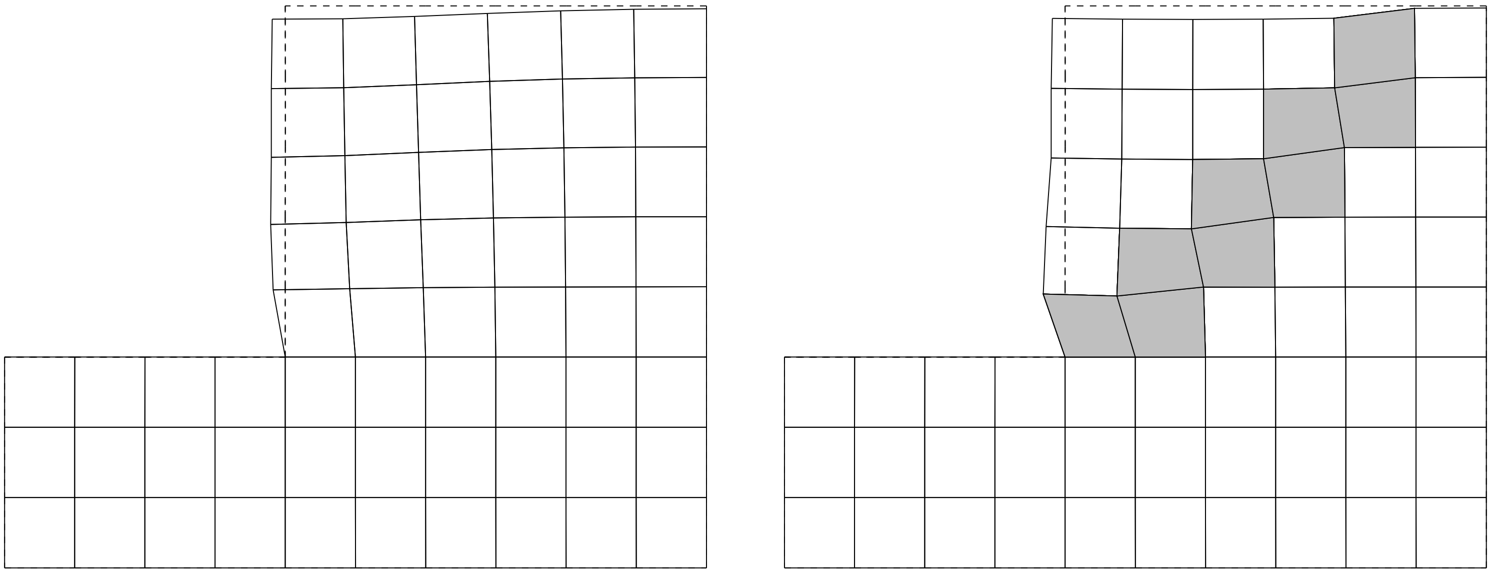

Figure 4.83. Plane strain excavation problem. Deformed meshes for standard and enhanced solutions with non-associative, dilative plastic flow: $\beta = 0.1895, b = 0.0978$. 80 linear quadrilateral elements. Localized elements are shaded.

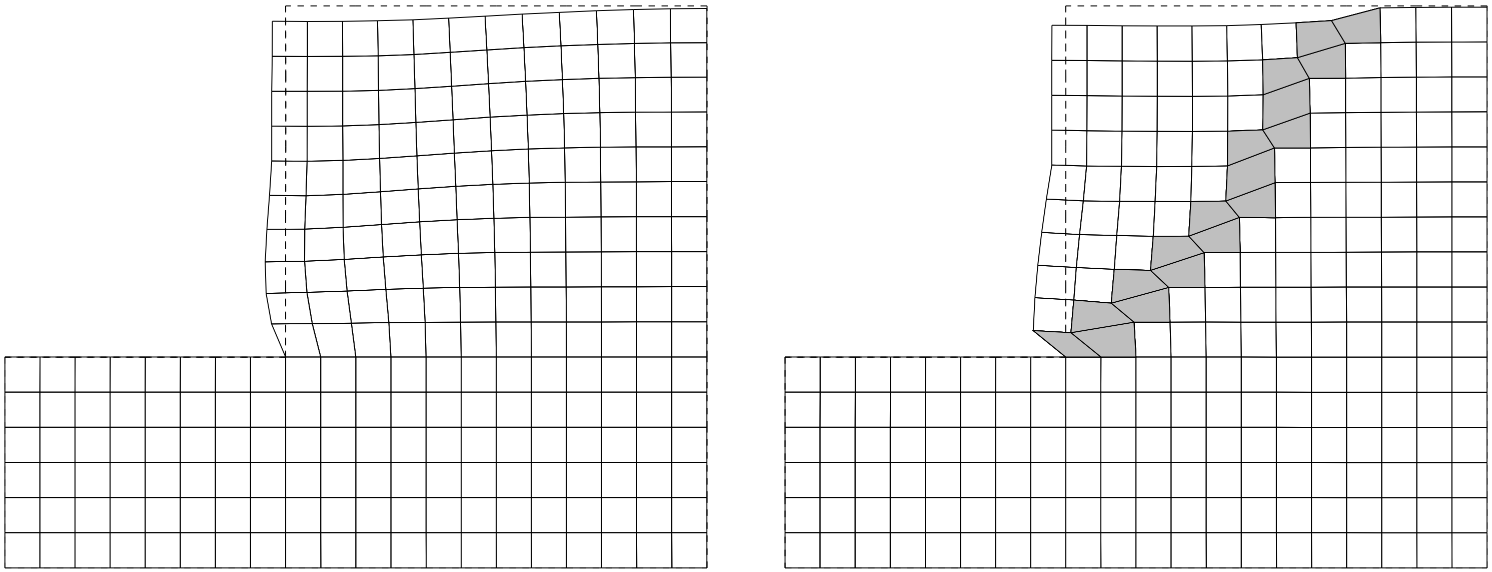

Figure 4.84. Plane strain excavation problem. Deformed meshes for standard and enhanced solutions with non-associative, dilative plastic flow: $\beta = 0.1895, b = 0.0978$. 320 linear quadrilateral elements. Localized elements are shaded.

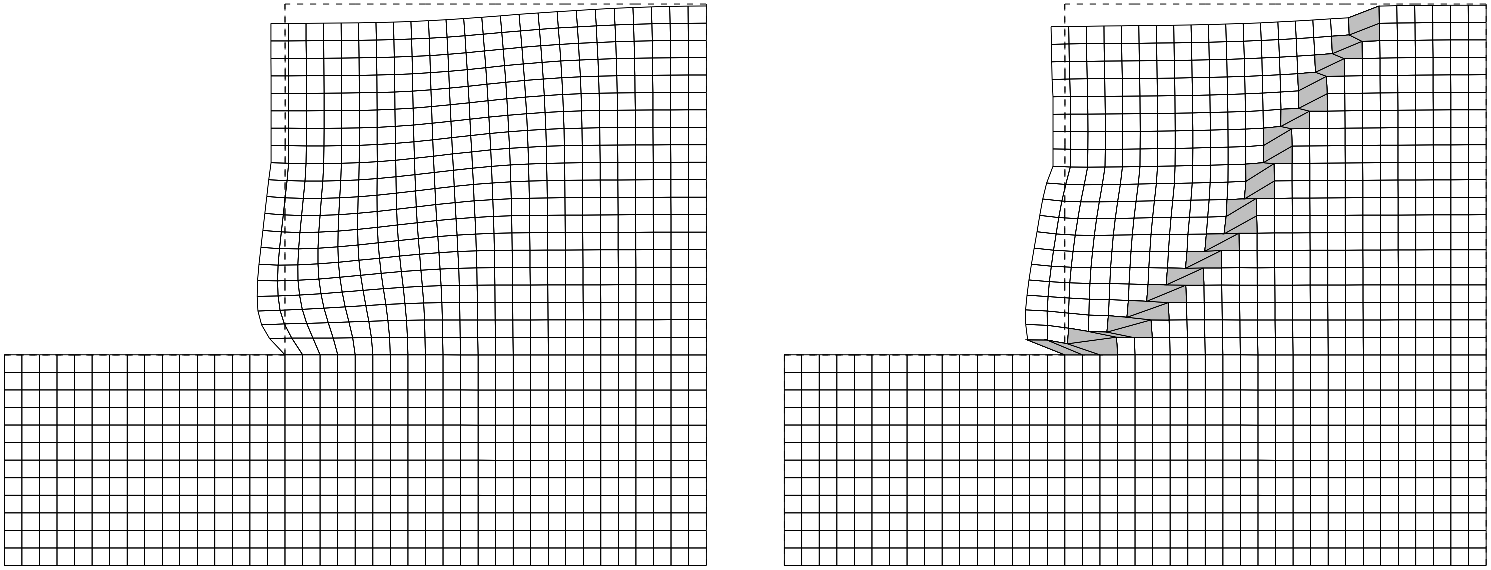

Figure 4.85. Plane strain excavation problem. Deformed meshes for standard and enhanced solutions with non-associative, dilative plastic flow: $\beta = 0.1895, b = 0.0978$. 1280 linear quadrilateral elements. Localized elements are shaded.

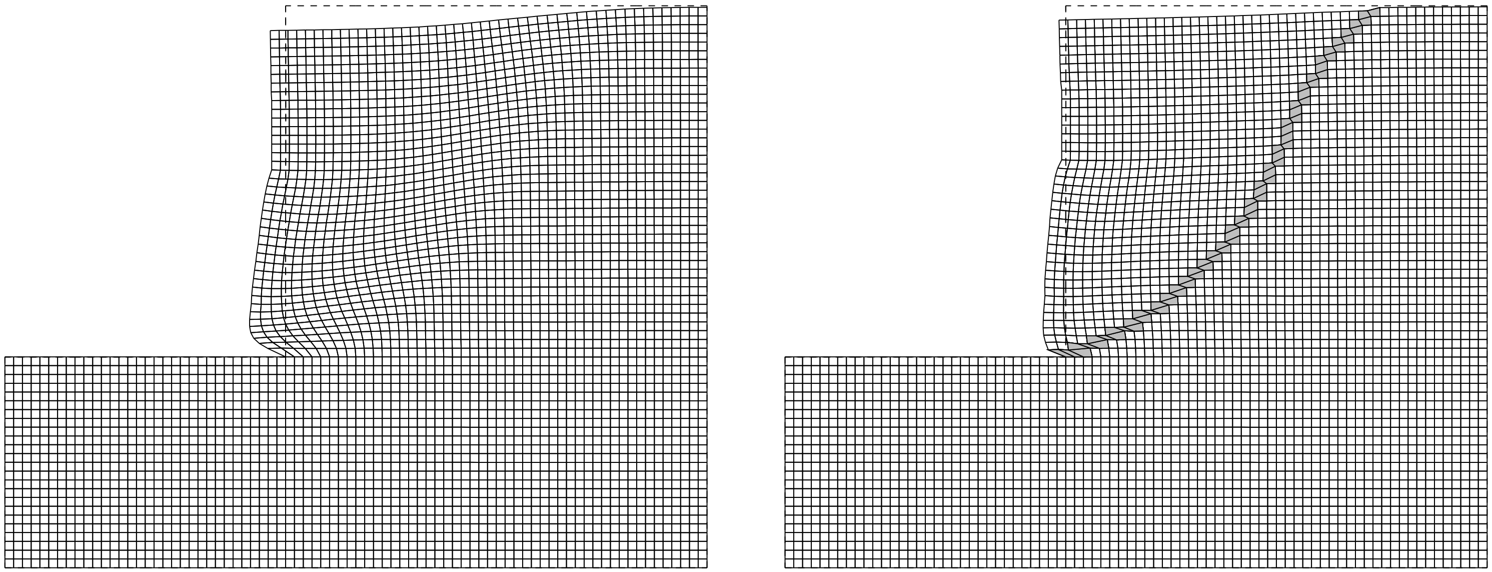

Figure 4.86. Plane strain excavation problem. Deformed meshes for standard and enhanced solutions with non-associative, dilative plastic flow: $\beta = 0.1895, b = 0.0978$. 5120 linear quadrilateral elements. Localized elements are shaded.

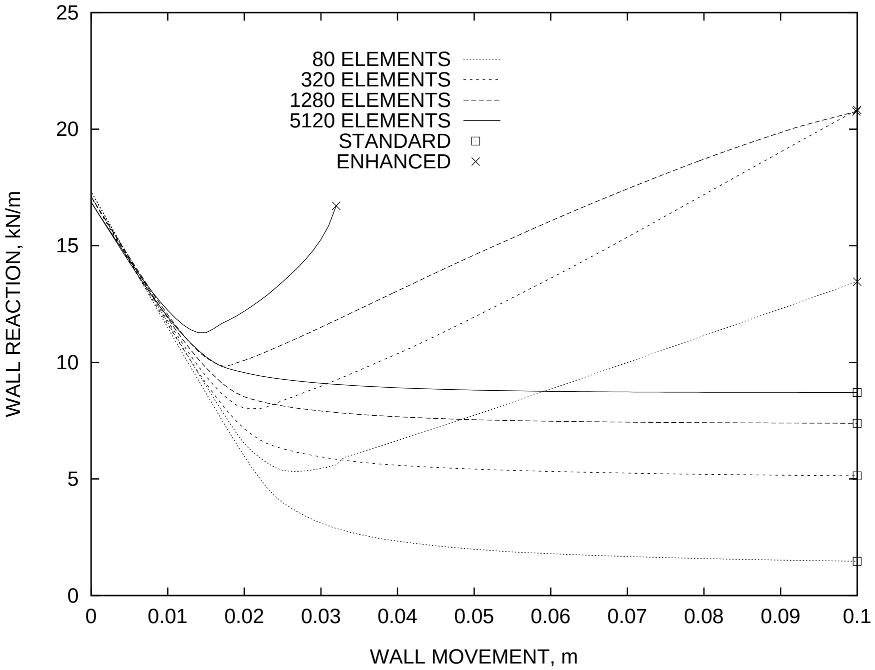

Figure 4.87. Plane strain excavation problem. Load-displacement plots for non-associative, deviatoric plastic flow: $\beta = 0.275, b = 0.0$. $h^{\text{tol}} = 0.001$. Enhanced solution curve for 5120-element mesh (shown in Fig. 4.91) ramps up dramatically.

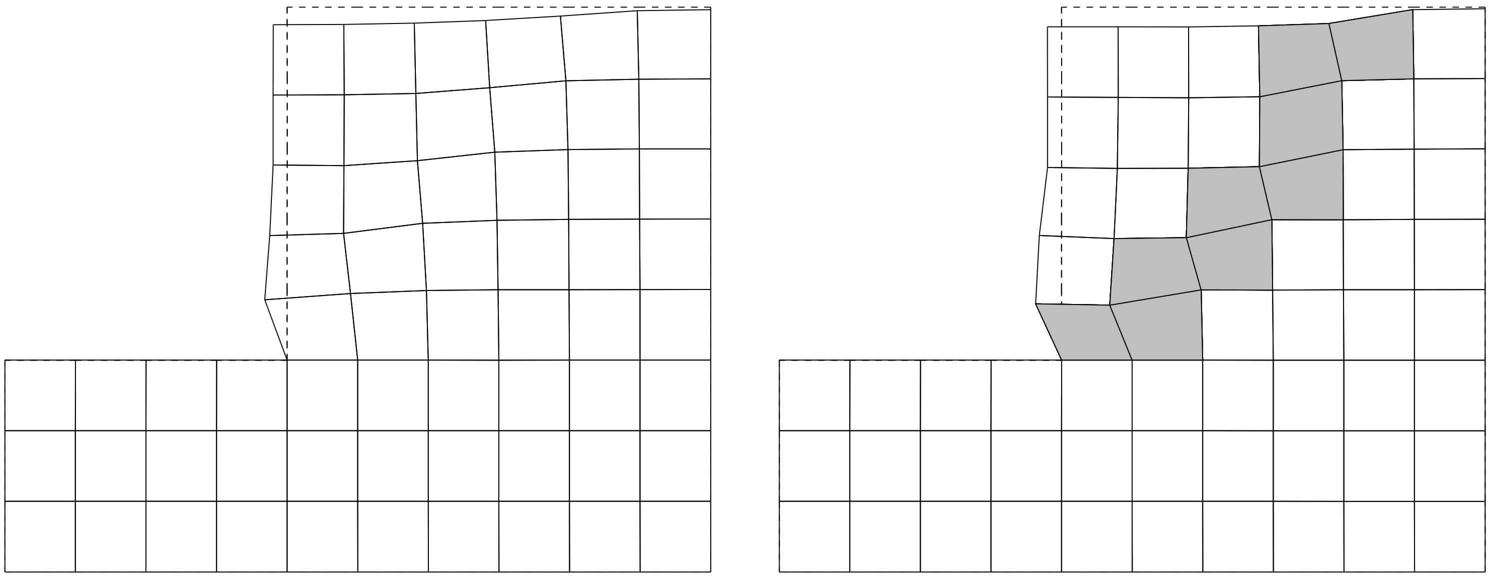

Figure 4.88. Plane strain excavation problem. Deformed meshes for standard and enhanced solutions with non-associative, deviatoric plastic flow: $\beta = 0.275, b = 0.0$. 80 linear quadrilateral elements with $\bar{B}$. Localized elements are shaded.

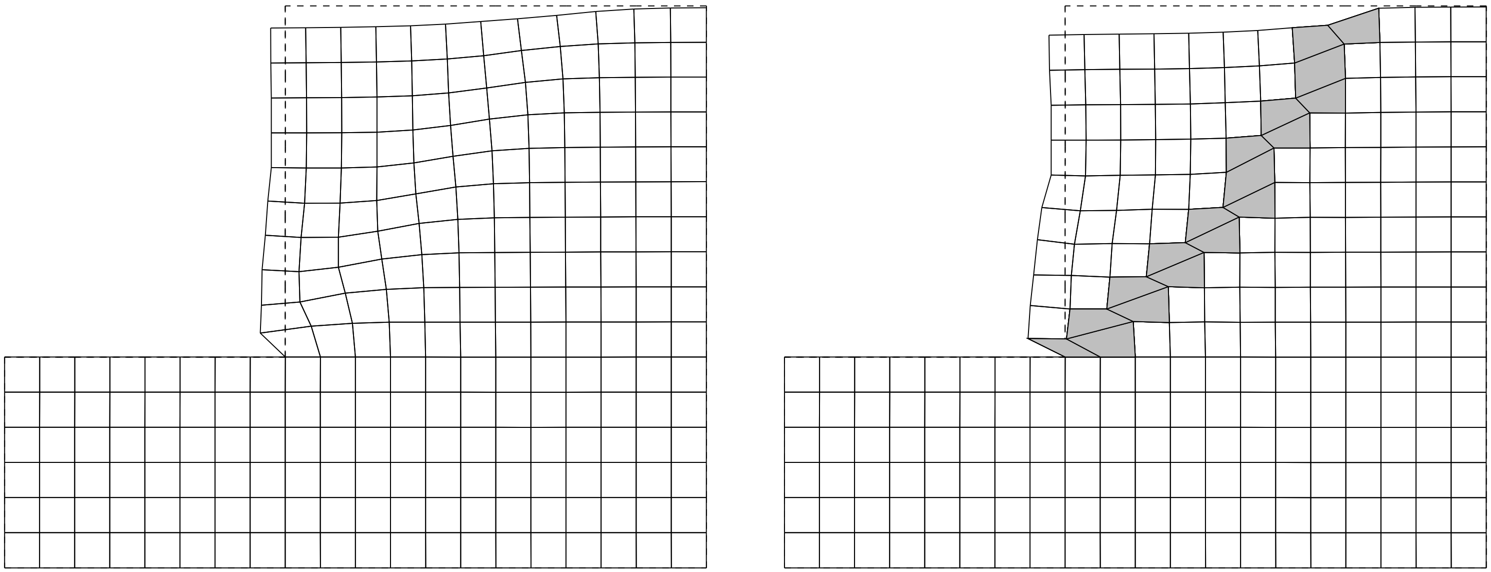

Figure 4.89. Plane strain excavation problem. Deformed meshes for standard and enhanced solutions with non-associative, deviatoric plastic flow: $\beta = 0.275, b = 0.0$. 320 linear quadrilateral elements with $\bar{B}$. Localized elements are shaded.

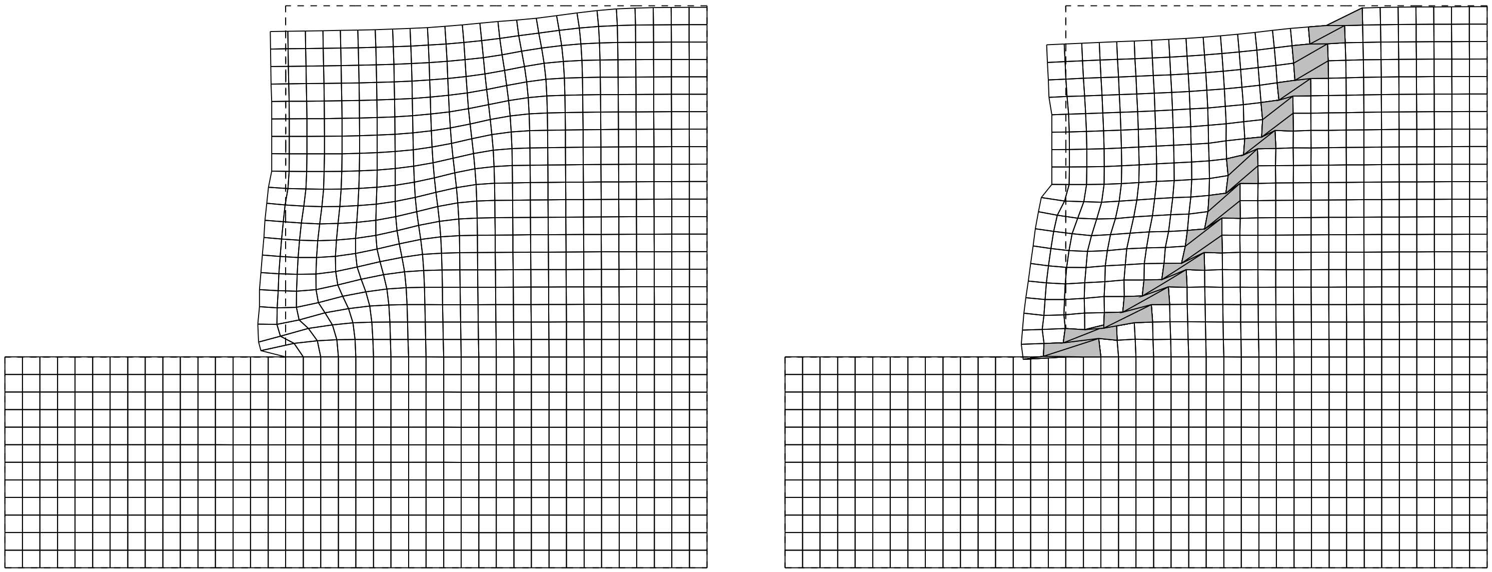

Figure 4.90. Plane strain excavation problem. Deformed meshes for standard and enhanced solutions with non-associative, deviatoric plastic flow: $\beta = 0.275, b = 0.0$. 1280 linear quadrilateral elements with $\bar{B}$. Localized elements are shaded.

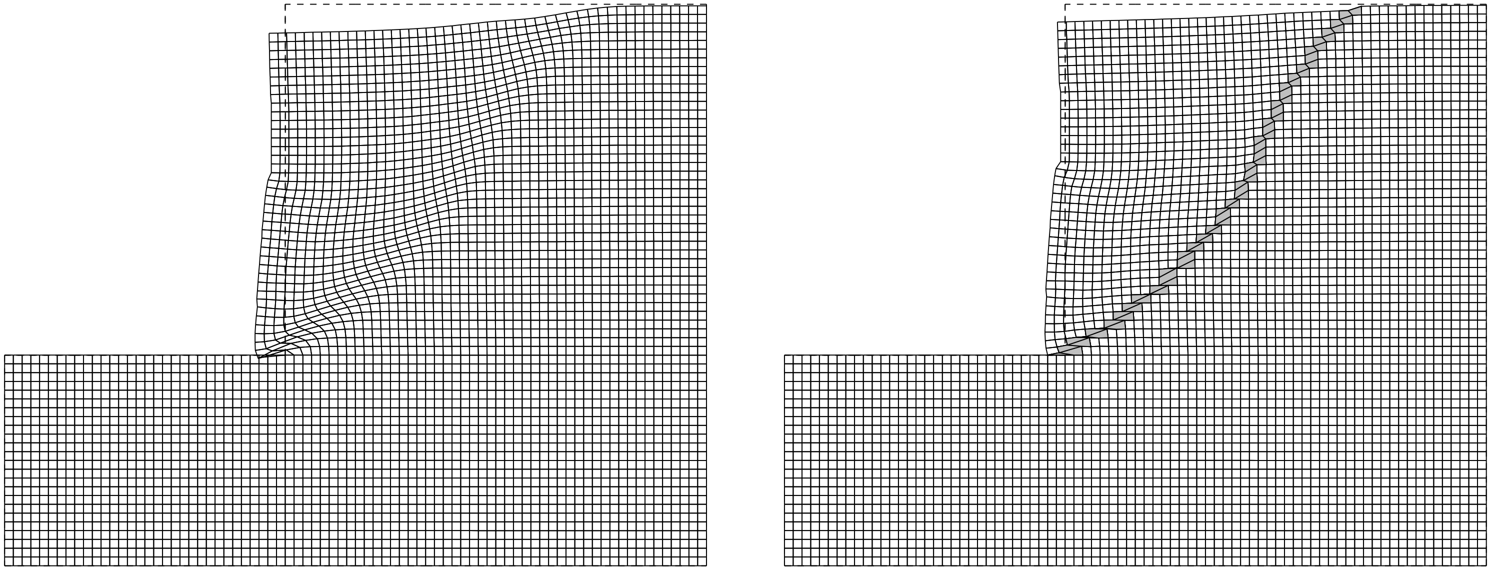

Figure 4.91. Plane strain excavation problem. Deformed meshes for standard and enhanced solutions with non-associative, deviatoric plastic flow: $\beta = 0.275, b = 0.0$. 5120 linear quadrilateral elements with $\bar{B}$. Localized elements are shaded.

4.8 Summary

In this chapter, numerical examples in plane strain demonstrated mesh-independence of finite element solutions for a non-associated, strain-softening Drucker-Prager plasticity model with strong discontinuity. The numerical simulations of plane strain compression experiments on Gosford sandstone and coal demonstrated the ability of the model to approximate the stress level at which onset of localization occurs, failure surface orientation, and post-localization overall 'softening' behavior. Simulations of strain localization developing in classical geotechnical structures like a slope/embankment and top-down sequential excavation were also presented.

Chapter 5

Conclusions and Future Work

A non-associated, rate-independent, strain-softening Drucker-Prager plasticity model was formulated for small deformations and rotations within the context of strong discontinuities. A noteworthy result is that the slip line orientation and localization condition are determined explicity in closed form (i.e., not numerically) and are functions solely of the material dilation constant b. The stress-displacement relation governing the jump displacement evolution is pressure-dependent, as expected. This Drucker-Prager plasticity model was implemented along with an enhanced quadrilateral element within the framework of an assumed enhanced strain method. The enhanced strains and enhanced strain variations are dependent upon the material dilation constant b. The enhanced strain quadrilateral element allows a slip line to cut and isolate one corner node or to cut two element sides, without having to reduce to triangular elements. Numerical simulations in plane strain demonstrated mesh-independence of finite element solutions for the simple model problem of uniform compression, and near mesh-independence for more complex problems such as slope stability and top-down sequential excavation.

The strong discontinuity approach developed by Simo and co-workers, extended in this thesis for geomaterials, provides a model of strain localization which leads to mesh-independent finite element solutions while representing the structural phenomenon of localized deformation directly. The model is predictive to the extent that it can approximate the experimentally observed stress level at which onset of localization is detected, the failure surface orientation, and the post-localization overall 'softening' behavior solely by choosing the moduli E, H', and H_δ as demonstrated for the plane strain Gosford sandstone and coal experiments. Note that the strength parameters $\bar{\alpha}$ and β and material dilation constant b were the same for each confining pressure case in the simulations of these experiments. It is noted, however, that for more complex model problems like slope stability and top-down sequential excavation, enhanced finite element solutions are not completely mesh-independent. In particular, the excavation problem exhibited a ramping-up of the enhanced solution curves for those fine meshes with more S-shaped slip lines than their coarser mesh counterparts.

The model will be extended for three dimensional analysis by implementing an enhanced brick element. For three dimensions, the localization condition and slip-surface orientation are the same as for the 2D problem, except that a numerical eigenvalue problem would need to be solved to determine the directions of the principal stresses. The influence of fluid flow on strain localization may be studied via the strong discontinuity approach. The coupled pore fluid/solid problem would need to be formulated in the context of strong discontinuities. A Drucker-Prager model with strong discontinuity would be formulated in the finite deformation regime in order to account for the possibility of large rotations and displacements occurring in geomaterials such as for the slope stability and excavation problems. Nonlinear slip lines could also be considered to increase the order of interpolation of the jump displacements. This would require an extra strain term to account for the gradient of the displacement jump along the discontinuity surface. Nonlinear strain softening for the Drucker-Prager model in the context of strong discontinuities could be formulated and implemented with relative ease. An arc-length method would allow a load-driven problem to proceed into the softening regime.

References

[1] Achenbach, J.D. *Wave Propagation in Elastic Solids.* Amsterdam: North-Holland Pub. Co., 1973.

[2] Aifantis, E.C. "On the microstructural origin of certain inelastic models," *Journal of Engineering Materials and Technology*, ASME, 106 (1984), 326–330.

[3] Armero, F. & Garikipati, K. "Recent advances in the analysis and numerical simulation of strain localization in inelastic solids," *Proceedings of Computational Plasticity IV*, eds. D.R.J. Owen, E. Oñate, and E. Hinton, CIMNE, Barcelona, Spain, April 1995, 547–561.

[4] Armero, F. & Garikipati, K. "An analysis of strong discontinuities in multiplicative finite strain plasticity and their relation with the numerical simulation of strain localization in solids," *International Journal of Solids and Structures*, 33 (1996), 2863–2885.

[5] Atkinson, J. *An Introduction to the Mechanics of Soils and Foundations through Critical State Soil Mechanics.* New York: McGraw-Hill, 1993.

[6] Aydin, A. & Johnson, A.M. "Analysis of faulting in porous sandstones," *Journal of Structural Geology*, 5 (1983), 19–31.

[7] Bardet, J.P. & Proubet, M. "A numerical investigation of the structure of persistent shear bands in granular media," *Géotechnique*, 41 (1991), 599–613.

[8] Bathe, K.-J. *Finite Element Procedures in Engineering Analysis.* Englewood Cliffs, N.J.: Prentice-Hall Inc., 1982.

[9] Bažant, Z.P., & Lin, F.-B. "Non-local yield limit degradation," *International Journal for Numerical Methods in Engineering*, 26 (1988), 1805–1823.

[10] Belytschko, T., Fish, J., & Engelmann, E. "A finite element with embedded localization zones," *Computer Methods in Applied Mechanics and Engineering*, 70 (1988), 59–89.

[11] Borja, R.I. & Wren, J.R. "Micromechanics of granular media, Part I: Generation of overall constitutive equation for assemblies of circular disks," *Computer Methods in Applied Mechanics and Engineering*, 127 (1995), 13–36.

[12] Borja, R.I. *Finite Element Analysis of Time-Dependent Behavior of Soft Clays*, Ph.D. Thesis, Stanford University, 1984.

[13] Chan, D.H. & Morgenstern, N.R. "Analysis of progressive deformation of the Edmonton Convention Centre excavation," *Canadian Geotechnical Journal*, 24 (1987), 430–440.

[14] Cosserat, E. & Cosserat, F. *Théorie des Corps Déformables*, Paris: Librairie Scientifique A. Hermann et Fils, 1909.

[15] Costin, L.S. "A microcrack model for the deformation and failure of brittle rock," *Journal of Geophysical Research*, 88 (1983), 9485–9492.

[16] Courant, R. & Hilbert, D. *Methods of Mathematical Physics*, Vol. II. New York: Interscience Pub., 1962.

[17] Crisfield, M.A. "A fast incremental/iterative solution procedure that handles 'snap-through'," *Computers and Structures*, 13 (1981), 55–62.

[18] Cundall, P.A., & Strack, O.D.L. "A discrete numerical model for granular assemblies," *Géotechnique*, 29 (1979), 47–65.

[19] Cundall, P.A. "Numerical experiments on localization in frictional materials," *Ingenieur-Archiv*, 59 (1989), 148–159.

[20] de Borst, R. & Sluys, L.J. "Localisation in a Cosserat continuum under static and dynamic loading conditions," *Computer Methods in Applied Mechanics and Engineering*, 90 (1991), 805–827.

[21] de Borst, R. & Pamin, J. "Some novel developments in finite element procedures for gradient-dependent plasticity," *International Journal for Numerical Methods in Engineering*, 39 (1996), 2477–2505.

[22] Drucker, D.C. "A more fundamental approach to plastic stress-strain relations," *Proc. 1st US National Congress in Applied Mechanics*, ASME, 1951. 487–491.

[23] Drucker, D.C., & Prager, W. "Soil mechanics and plastic analysis or limit design," *Quarterly of Applied Mathematics*, 10 (1952), 157–165.

[24] Enger, W.M. (Rear Admiral). *Design Manual: Soil Mechanics, Foundations, and Earth Structures.* NAVFAC DM-7, March 1971.

[25] Finno, R.J., Atmatzidis, D.K., & Perkins, S.B. "Observed performance of a deep excavation in clay," *Journal of Geotechnical Engineering*, ASCE, 115 (1989), 1045–1064.

[26] Finno, R.J., & Nerby, S.M. "Saturated clay response during braced cut construction," *Journal Geotechnical Engineering*, ASCE, 115 (1989), 1065–1084.

[27] Garikipati, K.R. *On Strong Discontinuities in Inelastic Solids and Their Numerical Simulation*, Ph.D. Thesis, Stanford University, 1996.

[28] Garikipati, K.R. & Hughes, T.J.R. "A study of strain localization in a multiple scale framework—the one dimensional problem," *Computer Methods in Applied Mechanics in Engineering*, 159 (1998), 193-222.

[29] Gurtin, M.E. *An Introduction to Continuum Mechanics.* New York: Academic Press, 1981.

[30] Hadamard, J. *Leçons sur la Propagation des Ondes et les Équations de L'Hydrodynamique.* Paris: Librairie Scientifique A. Hermann, 1903.

[31] Hallbauer, D.K., Wagner, H. & Cook, N.G.W. "Some observations concerning the microscopic and mechanical behaviour of quartzite specimens in stiff, triaxial compression tests," *International Journal of Rock Mechanics and Mining Sciences & Geomechanics Abstracts*, 10 (1973), 713–726.

[32] Hill, R. "Acceleration waves in solids," *Journal of the Mechanics and Physics of Solids*, 10 (1962), 1–16.

[33] Hughes, T.J.R. "Generalization of selective integration procedures to anisotropic and nonlinear media," *International Journal for Numerical Methods in Engineering*, 15 (1980), 1413–1418.

[34] Hughes, T.J.R. "Numerical implementation of constitutive models: Rate-independent deviatoric plasticity," *Theoretical Foundations for Large Scale Computations of Nonlinear Material Behavior*, eds. S. Nemat-Nasser, R. Asaro, & G. Hegemier. 29–63. The Netherlands: Martinus Nijhoff Pub., 1984.

[35] Hughes, T.J.R. *The Finite Element Method.* Englewood Cliffs, N.J.: Prentice-Hall, 1987.

[36] Hughes, T.J.R. "Multiscale phenomena: Green's functions, the Dirichlet-to-Neumann formulation, subgrid scale models, bubbles and the origins of stabilized methods," *Computer Methods in Applied Mechanics in Engineering*, 127 (1995), 387–401.

[37] Jaeger, J.C. & Cook, N.G.W. *Fundamentals of Rock Mechanics*, 2nd ed. London: Chapman and Hall, 1976.

[38] Janbu, N. "Stability analysis of slopes with dimensionless parameters," *Harvard University. Harvard Soil Mechanics Series.* Cambridge, MA. 46 (1954) 1–81.

[39] Kachanov, L.M. *Foundations of the Theory of Plasticity.* Amsterdam: North-Holland, 1971.

[40] Kolmogorov, A.N. & Fomin, S.V. *Introductory Real Analysis.* Englewood Cliffs, N.J.: Prentice-Hall, Inc., 1970.

[41] Labuz, J.F., Dai, S.-T., & Papamichos, E. "Plane-strain compression of rock-like materials," *International Journal of Rock Mechanics and Mining Sciences & Geomechanics Abstracts*, 33 (1996), 573–584.

[42] Lambe, T.W. & Whitman, R.V. *Soil Mechanics.* New York: Wiley, 1969.

[43] Larsson, R., Runesson, K., & Ottosen, N.S. "Discontinuous displacement approximation for capturing plastic localization," *International Journal for Numerical Methods in Engineering*, 36 (1993), 2087–2105.

[44] Larsson, R., Runesson, K., & Sture, S. "Embedded localization band in undrained soil based on regularized strong discontinuity—Theory and FE-Analysis," *International Journal of Solids and Structures*, 33 (1996), 3081–3101.

[45] Leroy, Y. & Ortiz, M. "Finite element analysis of strain localization in frictional materials," *International Journal for Numerical Methods in Engineering*, 13 (1989), 53–74.

[46] Loret, B. & Prevost, J.H. "Dynamic strain localization in elasto-(visco)-plastic solids, Part 1. General formulation and one-dimensional examples," *Computer Methods in Applied Mechanics and Engineering*, 83 (1990), 247–273.

[47] Lubliner, J. *Plasticity Theory.* New York: Macmillan, 1990.

[48] Malvern, L.E. *Introduction to the Mechanics of a Continuous Medium*, Englewood Cliffs, N.J.: Prentice-Hall, 1969. p. 242.

[49] Mandel, J. "Conditions de stabilité et postulat de Drucker," *Rheology and Soil Mechanics*, eds. J. Kravtchenko and P.M. Sirieys. 58–68. Berlin: Springer-Verlag, 1966.

[50] Marsden, J.E. & Hughes, T.J.R. *Mathematical Foundations of Elasticity.* Englewood Cliffs, N.J.: Prentice-Hall, 1983. Dover edition, 1994.

[51] Matthies, H., Strang, G., & Christiansen, E. "The saddle point of a differential program," *Energy Methods in Finite Element Analysis*, eds. R. Glowinski, E.Y. Rodin, & O.C. Zienkiewicz. 309–318. New York: Wiley, 1979.

[52] Mindlin, R.D. "Influence of couple-stresses on stress concentrations," *Experimental Mechanics*, 3 (1963), 1–7.

[53] Nacar, A., Needleman, A., & Ortiz, M. "A finite element method for analyzing localization in rate dependent solids at finite strains," *Computer Methods in Applied Mechanics and Engineering*, 73 (1989), 235–258.

[54] Needleman, A. "Material rate dependence and mesh sensitivity in localization problems," *Computer Methods in Applied Mechanics and Engineering*, 67 (1988), 69–85.

[55] Oliver, J. "A consistent characteristic length for smeared cracking models," *International Journal for Numerical Methods in Engineering*, 28 (1989), 461–474.

[56] Ord, A., Vardoulakis, I., & Kajewski, R. "Shear band formation in Gosford sandstone," *International Journal of Rock Mechanics and Mining Sciences & Geomechanics Abstracts*, 28 (1991), 397–409.

[57] Ortiz, M., Leroy, I., & Needleman, A. "A finite element method for localized failure analysis," *Computer Methods in Applied Mechanics and Engineering*, 61 (1987), 189–214.

[58] Owen, D.R.J. & Hinton, E. *Finite Elements in Plasticity: Theory and Practice.* Swansea: Pineridge, 1980.

[59] Palmer, A.C. & Rice, J.R. "The growth of slip surfaces in the progressive failure of over-consolidated clay," *Proceedings. Royal Society of London. Series A. Mathematical and Physical Sciences*, 332 (1973), 527–548.

[60] Perzyna, P. "Fundamental problems in viscoplasticity," *Advances in Applied Mechanics*, Vol. 9, 244–368, 1966.

[61] Petrovskii, I.G. *Lectures on Partial Differential Equations.* New York: Interscience Pub., 1954.

[62] Pietruszczak, S.T., & Mróz, Z. "Finite element analysis of deformation of strain-softening materials," *International Journal for Numerical Methods in Engineering*, 17 (1981), 327–334.

[63] Prevost, J.H. & Höeg, K. "Soil mechanics and plasticity analysis of strain softening," *Géotechnique*, 25 (1975), 279–297.

[64] Prevost, J.H. & Loret, B. "Dynamic strain localization in elasto-(visco)-plastic solids, Part 2. Plane strain examples," *Computer Methods in Applied Mechanics and Engineering*, 83 (1990), 275–294.

[65] RADENKOVIC, D. “Théorèmes limites pour un matériau de Coulomb à dilatation non standardisée,” *Comptes Rendus des Séances de L'Académie des Sciences*, 252 (1961), 4103–4104.

[66] READ, H.E., & HEGEMIER, G.A. “Strain softening of rock, soil, and concrete - A review article,” *Mechanics of Materials*, 3 (1984), 271–294.

[67] REYNOLDS, O. “On the dilatancy of media composed of rigid particles in contact. With experimental illustrations,” *Philosophical Magazine and Journal of Science*, 20 (1885), 469–481.

[68] RICE, J.R. “The initiation and growth of shear bands,” *The Role of Plasticity in Soil Mechanics*, ed. A.C. Palmer. 263–278. 1973.

[69] RICE, J.R. “The localization of plastic deformation,” ed. W.T. Koiter, *Theoretical and Applied Mechanics*, 207–220. North-Holland, 1976.

[70] RIKS, E. “An incremental approach to the solution of snapping and buckling problems,” *International Journal of Solids and Structures*, 15 (1979), 529–551.

[71] ROSCOE, K.H. “The influence of strain in soil mechanics,” 10th Rankine Lecture, *Géotechnique*, 20 (1970), 129–170.

[72] ROYDEN, H.L. *Real Analysis*, 2nd Ed. New York: Macmillan Co., 1968.

[73] RUDNICKI, J.W., & RICE, J.R. “Conditions for the localization of deformation in pressure-sensitive dilatant materials,” *Journal of the Mechanics and Physics of Solids*, 23 (1975), 371–394.

[74] RUDNICKI, J.W. “The inception of faulting in a rock mass with a weakened zone,” *Journal of Geophysical Research*, 82 (1977), 844–854.

[75] RUDNICKI, J.W. “A formulation for studying coupled deformation pore fluid diffusion effects on localization of deformation,” *Symposium on the Mechanics of Ice, Rocks, and Soils*, ASME, ed. S. Nemat-Nasser. 35–44. New York: ASME, 1983.

[76] SANDLER, I.S. & WRIGHT, J.P. “Strain-softening,” *Theoretical Foundations for Large Scale Computations of Nonlinear Material Behavior*, eds. S. Nemat-Nasser, R. Asaro, & G. Hegemier. 285–315. The Netherlands: Martinus Nijhoff Pub., 1984.

[77] SANTARELLI, F.J. & BROWN, E.T. “Failure of three sedimentary rocks in triaxial and hollow cylinder compression tests,” *International Journal of Rock Mechanics and Mining Sciences & Geomechanics Abstracts*, 26 (1989), 401–413.

[78] Simo, J.C. & Taylor, R.L. "Consistent tangent operators for rate-independent elastoplasticity," *Computer Methods in Applied Mechanics and Engineering*, 48 (1985), 101–118.

[79] Simo, J.C. & Rifai, M.S. "A class of mixed assumed strain methods and the method of incompatible modes," *International Journal for Numerical Methods in Engineering.* 29 (1990), 1595–1638.

[80] Simo, J.C., & Hughes, T.J.R. *Computational Inelasticity.* New York: Springer-Verlag, Inc., 1998.

[81] Simo, J.C., & Armero, F. "Geometrically non-linear enhanced strain mixed methods and the method of incompatible modes," *International Journal for Numerical Methods in Engineering*, 33 (1992), 1413–1449.

[82] Simo, J.C., Oliver, J., & Armero, F. "An analysis of strong discontinuities induced by strain- softening in rate-independent inelastic solids," *Computational Mechanics*, 12 (1993), 277–296.

[83] Simo, J.C., & Oliver, J. "A new approach to the analysis and simulation of strain softening in solids," *Fracture and Damage in Quasibrittle Structures*, eds. Z.P. Bažant, Z. Bittnar, M. Jirásek, and J. Mazars. 25–39. London: E&FN Spon, 1994.

[84] Simo, J.C. "Topics on the numerical analysis and simulation of plasticity," *Handbook of Numerical Analysis*, eds. P.G. Ciarlet and J.L. Lions. Vol. III. New York: Elsevier, 1996.

[85] Sluys, L.J., & de Borst, R. "Wave propagation and localization in a rate-dependent cracked medium—Model formulation and one-dimensional examples," *International Journal of Solids and Structures*, 29 (1992), 2945–2958.

[86] Stakgold, I. *Green's Functions and Boundary Value Problems.* 2nd Ed. New York: John Wiley & Sons, Inc., 1998.

[87] Stein, E., Steinmann, P., & Miehe, C. "Instability phenomena in plasticity: Modeling and computation," *Computational Mechanics*, 17 (1995), 74–87.

[88] Strang, G., Matthies, H., & Temam, R. "Mathematical and computational methods in plasticity," *Variational Methods in the Mechanics of Solids*, ed. S. Nemat-Nasser. 20–28. Pergamon Press, 1980.

[89] Suquet, P.-M. "Existence and Regularity of Solutions for Plasticity Problems," *Variational Methods in the Mechanics of Solids*, ed. S. Nemat-Nasser. 304–309. Pergamon Press, 1980.

[90] TAYLOR, R.L., SIMO, J.C., ZIENKIEWICZ, O.C., & CHAN, A.C.H. "The patch test–A condition for assessing FEM convergence," *International Journal for Numerical Methods in Engineering*, 22 (1986), 39–62.

[91] TEMAM, R. & STRANG, G. "Functions of bounded deformation," *Archive for Rational Mechanics and Analysis*, 75 (1980), 7–21.

[92] THOMAS, T.Y. *Plastic Flow and Fracture in Solids.* New York: Academic Press, 1961.

[93] VARDOULAKIS, I., GOLDSCHIEDER, M., & GUDEHUS, G. "Formation of shear bands in sand bodies as a bifurcation problem," *International Journal for Numerical and Analytical Methods in Geomechanics*, 2 (1978), 99–128.

[94] VARDOULAKIS, I. & GOLDSCHIEDER, M. "Biaxial apparatus for testing shear bands in soils," *Soil Mechanics and Foundation Engineering.* 819–824. Rotterdam: A.A. Balkema, 1981.

[95] VERMEER, P.A. & DE BORST, R. "Non-associated plasticity for soils, concrete, and rock," *Heron*, 29 (1984), 3–64.

[96] WAN, R.G., CHAN, D.H., & MORGENSTERN, N. R. "A finite element method for the analysis of shear bands in geomaterials," *Finite Elements in Analysis and Design*, 7 (1990), 129–143.

[97] WASHIZU, K. *Variational Methods in Elasticity and Plasticity.* 3rd Ed. New York: Pergamon Press Inc., 1982.

[98] WAWERSIK, W.R., RUDNICKI, J.W., OLSSON, W.A., HOLCOMB, D.J., & CHAU, K.T. "Localization of deformation in brittle rock: theoretical and laboratory investigations," *Micromechanics of Failure of Quasi-Brittle Materials*, eds. S.P. Shah, S.E. Swartz, and M.L. Wang. 115–124. New York: Elsevier, 1990.

[99] WREN, J.R. & BORJA, R.I. "Micromechanics of granular media, Part II: Overall tangential moduli and localization model for periodic assemblies of circular disks," *Computer Methods in Applied Mechanics and Engineering*, 141 (1997), 221–246.

[100] WU, F.H. & FREUND, L.B. "Deformation trapping due to thermoplastic instability in one-dimensional wave propagation," *Journal of the Mechanics and Physics of Solids*, 32 (1984), 119–132.

[101] YUMLU, M. & OZBAY, M.U. "A study of the behaviour of brittle rocks under plane strain and triaxial loading conditions," *International Journal of Rock Mechanics and Mining Sciences & Geomechanics Abstracts*, 32 (1995), 725–733.

[102] ZIENKIEWICZ, O.C., & HUANG, G.C. "A note on localization phenomena and adaptive finite-element analysis in forming processes," *Communications in Applied Numerical Methods*, 6 (1990), 71–76.

[103] ZIENKIEWICZ, O.C., PASTOR, M., & HUANG, M. "Softening, localisation and adaptive remeshing. Capture of discontinuous solutions," *Computational Mechanics*, 17 (1995), 98–106.

Appendix A

1D Calculation of Dissipation

For clarification of the definition of plastic dissipation as discussed in Section 2.5.2 for the three-dimensional problem, it is helpful to consider a calculation of plastic dissipation in one-dimension, where the plastic dissipation is defined as

$$\mathcal{D} \;:=\; \sigma\dot{\epsilon} \;-\; \dot{\Psi}(\epsilon^{e}, \epsilon^{p})\,. \tag{A.1}$$

Assume a quadratic stored energy function of the form

$$\Psi \;=\; \frac{1}{2}E\epsilon^{e2} \;+\; \frac{1}{2}H\epsilon^{p2} \tag{A.2}$$

where E and H are the constant elastic and plastic moduli, respectively, for linear elasticity and hardening, and $\sigma = E\epsilon^{e}$ via Hooke's Law and $\sigma = \sigma_{Y} + H\epsilon^{p}$ for linear hardening, where σ_{Y} is the yield stress. Thus, the stored energy rate may be expressed as

$$\dot{\Psi} \;=\; \sigma\dot{\epsilon} \;-\; \sigma_{Y}\dot{\epsilon}^{p} \tag{A.3}$$

and the rate of dissipation as

$$\boxed{\mathcal{D} \; = \; \sigma_Y \dot{\epsilon}^p \; > \; 0} \, . \tag{A.4}$$

Four cases are considered to calculate the total dissipation over a given time interval: 1) hardening plasticity with elastic unloading to zero stress, Fig. A.1; 2) perfect plasticity with elastic unloading to zero stress, Fig. A.2; 3) softening plasticity with elastic unloading to zero stress, Fig. A.3; and 4) softening plasticity with softening to zero stress, Fig. A.4. For each case, take the yield stress σ_Y to be the same.

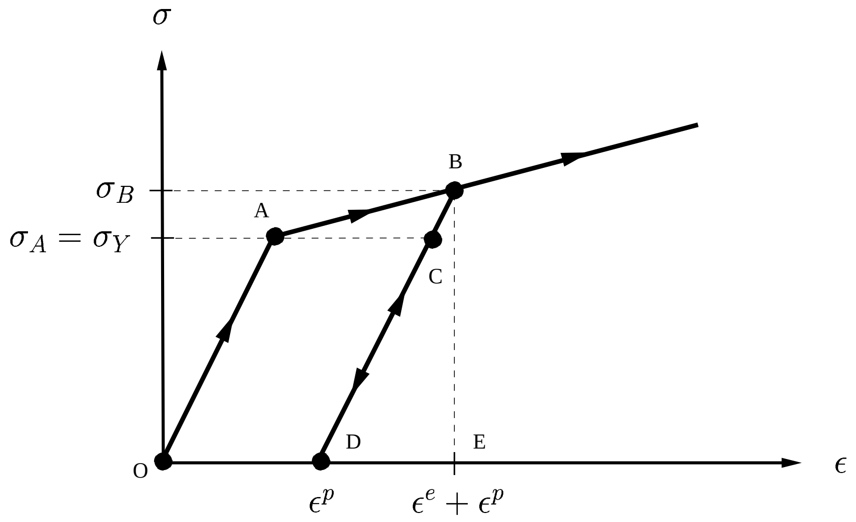

Figure A.1. Case 1. Hardening plasticity with elastic unloading to zero stress. Arrows denote loading path.

For case 1, the following calculates the total dissipation over the loading path OABD:

$$\begin{aligned}
\mathcal{D}_t \;&=\; \int_O^D \mathcal{D}\, dt \;=\; \sigma_Y \int_O^A \dot{\epsilon}^p\, dt \,+\, \sigma_Y \int_A^B \dot{\epsilon}^p\, dt \,+\, \sigma_Y \int_B^D \dot{\epsilon}^p\, dt \\
&=\; \sigma_Y \left[(\epsilon^p_A - \epsilon^p_O) \,+\, (\epsilon^p_B - \epsilon^p_A) \,+\, (\epsilon^p_D - \epsilon^p_B) \right] \\
&=\; \sigma_Y \left[(0 - 0) \,+\, (\epsilon^p - 0) \,+\, (\epsilon^p - \epsilon^p) \right] \\
&=\; \sigma_Y \epsilon^p \, .
\end{aligned} \tag{A.5}$$

It turns out that Eq. (A.5) holds for each case in Figs. A.2, A.3, and A.4. The dissipated energy calculated in Eq. (A.5) is equivalent to Area(OACD), while the internal energy due to plastic hardening is Area(ABC)= $\frac{1}{2}(\sigma_B - \sigma_Y)\epsilon^p = \frac{1}{2}H\epsilon^{p2}$. The internal stored elastic energy in Fig. A.1 may be calculated from Area(DBE)= $\frac{1}{2}\sigma\epsilon^e = \frac{1}{2}E\epsilon^{e2}$, and then the total stored energy is Area(DBE)+Area(ABC)= $\int_O^D \dot{\Psi}\, dt = \Psi_t = \frac{1}{2}E\epsilon^{e2} + \frac{1}{2}H\epsilon^{p2}$. The total energy in the system at the end of loading is $\mathcal{D}_t + \Psi_t$.

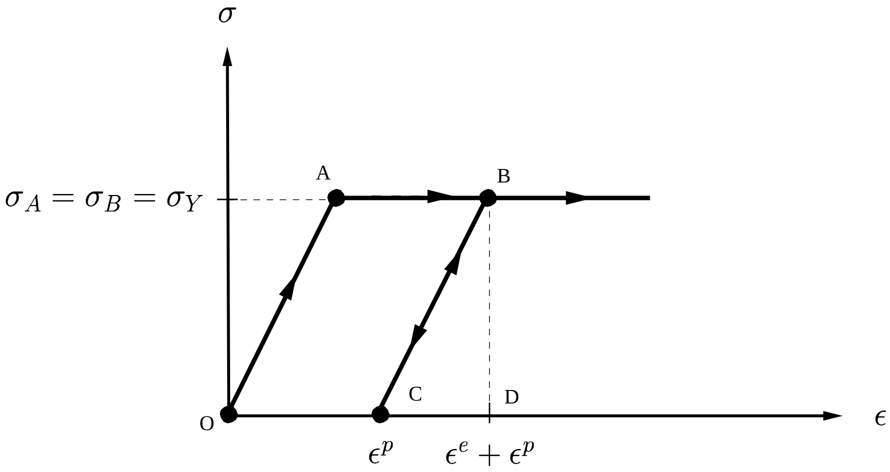

Figure A.2. Case 2. Perfect plasticity with elastic unloading to zero stress. Arrows denote loading path.

For case 2 in Fig. A.2 for perfect plasticity with elastic unloading, there is no internal energy due to plastic hardening/softening. Thus, the total energy in the system at end of loading is calculated as $\mathcal{D}_t + \Psi_t = \sigma_Y\epsilon^p + \frac{1}{2}E\epsilon^{e2}$.

For case 3 in Fig. A.3 for softening plasticity with elastic unloading, the stored energy becomes $\Psi_t = \frac{1}{2}E\epsilon^{e2} - \frac{1}{2}|H|\epsilon^{p2} = \frac{1}{2}\sigma_B\epsilon^e - \frac{1}{2}(\sigma_Y - \sigma_B)\epsilon^p$. Thus, the total energy in the system $\mathcal{D}_t + \Psi_t$ is the Area(OABD).

For case 4 in Fig. A.4 for softening plasticity, the total energy in the system at the end of loading is $\mathcal{D}_t + \Psi_t = \sigma_Y\epsilon^p - \frac{1}{2}|H|\epsilon^{p2} = \frac{1}{2}\sigma_Y\epsilon^p$.

Thus, it is seen that the total dissipation over each loading cycle is calculated from the same equation ($\mathcal{D}_t = \sigma_Y\epsilon^p$), although ϵ^p may vary for each case, while the

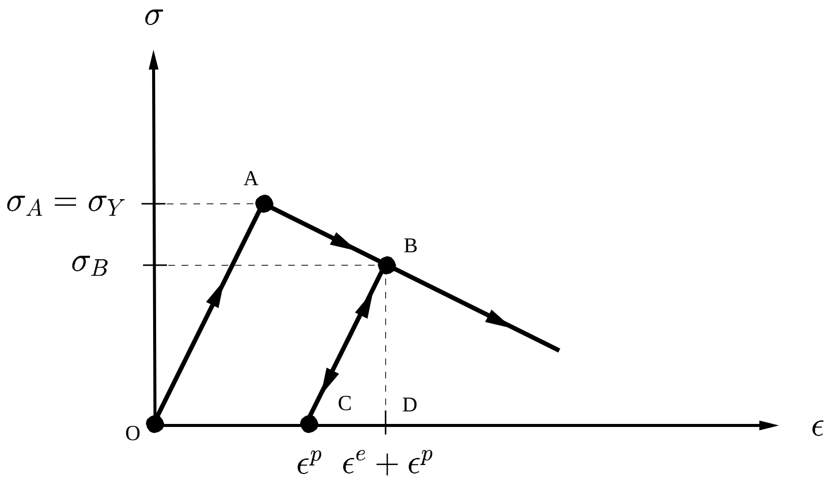

Figure A.3. Case 3. Softening plasticity with elastic unloading to zero stress. Arrows denote loading path.

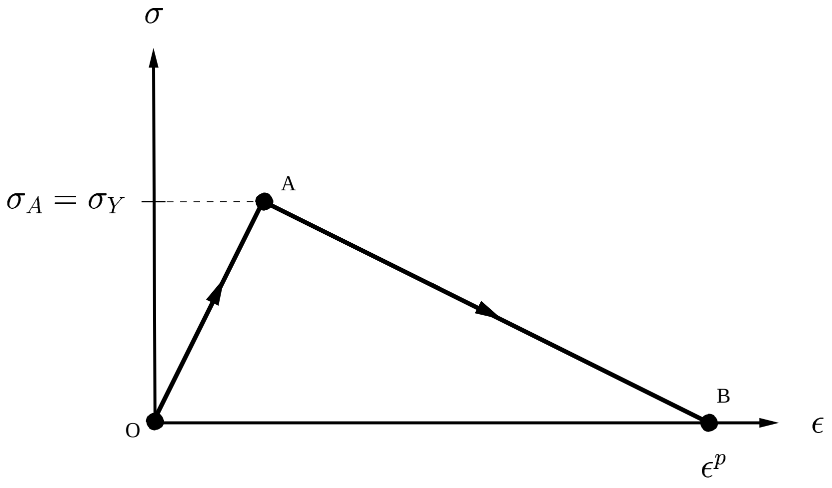

Figure A.4. Case 4. Softening plasticity with softening to zero stress. Arrows denote loading path.

area beneath the loading path—before elastic unloading—represents the total energy in the system, as expected.

Appendix B

Gradient of Discontinuous Displacement Field

A *distribution* needs to be defined before the gradient of a discontinuous displacement field $\boldsymbol{u}(\boldsymbol{x})$ may be derived. This discussion follows from STAKGOLD [86] and GARIKIPATI [27]. Refer also to KOLMOGOROV & FOMIN [40] and ROYDEN [72].

In an unbounded region $\Omega \subset \mathbb{R}^{n_{dim}}$ (see Fig. 2.1 but ignore the boundaries), a *distribution* is a *continuous linear functional* on $C^{\infty}(\Omega)$. To start, a *functional* is defined.

View $\boldsymbol{f}$ as a "rule" which "associates" to each $\boldsymbol{x}$ in $\mathbb{R}^{n_{dim}}$ a function $\boldsymbol{f}$ in $\mathbb{R}^{n_{dim}}$, the value of $\boldsymbol{f}$ at $\boldsymbol{x}$. Now, instead of $\boldsymbol{f}$ at $\boldsymbol{x}$, there is

$$\int_{\Omega} \boldsymbol{f} \cdot \boldsymbol{\phi} \, d\Omega \,, \quad \forall\, \boldsymbol{\phi} \in \mathcal{K} \tag{B.1}$$

where $\mathcal{K}$ is a class of "accessory" functions $\boldsymbol{\phi}$. The choice of class $\mathcal{K}$ is secondary, and the accessory function $\boldsymbol{\phi}$ is just a means to describe $\boldsymbol{f}$. Thus, view $\boldsymbol{f}$ as a *functional* on $\mathcal{K}$. In other words, $\boldsymbol{f}$ "is a rule which associates with each function $\boldsymbol{\phi}$ in $\mathcal{K}$ the real number"

$$\langle \boldsymbol{f}, \boldsymbol{\phi} \rangle \;=\; \int_{\Omega} \boldsymbol{f} \cdot \boldsymbol{\phi} \, d\Omega \tag{B.2}$$

where $\langle \cdot, \cdot \rangle$ is a brief notational form for the *functional* $\boldsymbol{f}$.

Define $\mathcal{K}$ as the class of smooth functions called *test functions.* A *test function* $\boldsymbol{\phi} \in \mathbb{R}^{n_{dim}}$ is a function which is infinitely differentiable on $\mathbb{R}^{n_{dim}}$ and has *compact support* in Ω (i.e. $\boldsymbol{\phi} = \mathbf{0}$ outside Ω). The space of test functions, $C^{\infty}(\Omega)$, is called the "space of infinitely differentiable functions with compact support:"

$$\boldsymbol{\phi} \;\in\; C^{\infty}(\Omega)\,. \tag{B.3}$$

Refer to Stakgold [86] for examples of test functions.

Next, consider the definition of a *linear* functional. The function $\boldsymbol{f}$ is a *linear functional* on $C^{\infty}(\Omega)$ if

$$\langle \boldsymbol{f}\,,\, a_1 \boldsymbol{\phi}_1 \,+\, a_2 \boldsymbol{\phi}_2 \rangle \;=\; a_1 \langle \boldsymbol{f}, \boldsymbol{\phi}_1 \rangle \;+\; a_2 \langle \boldsymbol{f}, \boldsymbol{\phi}_2 \rangle$$

$$\forall\, a_1,\, a_2 \,\in\, \mathbb{R}, \text{ and } \boldsymbol{\phi}_1, \boldsymbol{\phi}_2 \,\in\, C^{\infty}(\Omega)\,. \tag{B.4}$$

Now, consider the definition of a *continuous* linear functional. Given a sequence of test functions $\{\boldsymbol{\phi}_1, ..., \boldsymbol{\phi}_m\}$ that is a *null sequence* in $C^{\infty}(\Omega)$, a linear functional $\boldsymbol{f}$ is said to be *continuous* when the sequence $\langle \boldsymbol{f}, \boldsymbol{\phi}_m \rangle$ approaches zero as m approaches infinity:

$$\lim_{m \to \infty} \langle \boldsymbol{f}, \boldsymbol{\phi}_m \rangle \;=\; \lim_{m \to \infty} \int_{\Omega} \boldsymbol{f} \cdot \boldsymbol{\phi}_m \, d\Omega \;=\; 0\,. \tag{B.5}$$

Equation (B.5) will become clear when a *null sequence* is defined. To define a *null sequence* in $C^{\infty}(\Omega)$, first define a differential operator in three dimensions as

$$D^k \; := \; \frac{\partial^k}{\partial x_1^{k_1} \partial x_2^{k_2} \partial x_3^{k_3}} \quad \text{in } \mathbb{R}^{n_{dim}} \; ; \; k = k_1 + k_2 + k_3 \tag{B.6}$$

for all nonnegative integers k_1, k_2, and k_3. A sequence of test functions $\{\boldsymbol{\phi}_m\}$ is then a *null sequence* in $C^\infty(\Omega)$ if the following two conditions hold:

1. $\boldsymbol{\phi}_m$ has compact support within a bounded region Ω (i.e. $\boldsymbol{\phi}_m = \mathbf{0}$ outside Ω)
2. $\lim_{m\to\infty} D^k \boldsymbol{\phi}_m \; = \; \mathbf{0}$.

Thus, $\{\boldsymbol{\phi}_m\}$ and its derivatives $\left\{D^k \boldsymbol{\phi}_m\right\}$ uniformly approach zero. See STAKGOLD [86] for examples of null sequences. With a null sequence defined, the *continuity* requirement on the linear functional $\boldsymbol{f}$ ($\lim_{m\to\infty}\langle \boldsymbol{f}, \boldsymbol{\phi}_m\rangle = 0$) becomes clear. Therefore, it is now possible to say with confidence that a *distribution* is a *continuous linear functional* on $C^\infty(\Omega)$, and it is possible to define the Heaviside function and Dirac-delta function as distributions.

First, a *regular distribution* should be defined. A distribution is *regular* if the function $\boldsymbol{f}(\boldsymbol{x})$ is *locally integrable* such that the integral vanishes over a set of zero measure (see Theorem 6 and Problem 3a on pages 300, 301 in [40]). As an example of a *regular* distribution, consider the Heaviside function:

$$H_{\mathcal{S}}(\boldsymbol{x}) \; = \; \begin{cases} 1 & \text{if } \boldsymbol{x} \in \Omega_+ \\ 0 & \text{if } \boldsymbol{x} \in \Omega_- \, . \end{cases} \tag{B.7}$$

The Heaviside function is *locally integrable* because of the following result:

$$\lim_{\Omega\to\mathcal{S}} \int_\Omega H_{\mathcal{S}} \boldsymbol{\phi} \, d\Omega \; = \; \lim_{\Omega\to\mathcal{S}} \int_{\Omega_+} \boldsymbol{\phi} \, d\Omega \; = \; \mathbf{0} \tag{B.8}$$

where $\mathcal{S}$ is the discontinuity surface which is a set of zero measure. Thus, the Heaviside function is a *regular distribution.* On the other hand, an example of a *singular* distribution is the Dirac-delta function because it is *not* locally integrable:

$$\lim_{\Omega \to \mathcal{S}} \int_{\Omega} \delta_{\mathcal{S}} \boldsymbol{\phi} \, d\Omega \;=\; \int_{\mathcal{S}} \boldsymbol{\phi} \, d\Gamma \;\neq\; \mathbf{0} \,. \tag{B.9}$$

Note that the Dirac-delta function is a *distribution* because it is a *continuous linear functional* on $C^{\infty}(\Omega)$, and is denoted a singular distribution because it is not locally integrable, as demonstrated in Eq. (B.9). Therefore, in summary, the Dirac-delta function $\delta_{\mathcal{S}}(\boldsymbol{x})$ is a *functional* defined as

$$\langle \delta_{\mathcal{S}}, \boldsymbol{\phi} \rangle \;=\; \int_{\Omega} \delta_{\mathcal{S}} \boldsymbol{\phi} \, d\Omega \,. \tag{B.10}$$

It is *linear* because

$$\langle \delta_{\mathcal{S}} \,,\, a_1 \boldsymbol{\phi}_1 \,+\, a_2 \boldsymbol{\phi}_2 \rangle \;=\; a_1 \, \langle \delta_{\mathcal{S}}, \boldsymbol{\phi}_1 \rangle \;+\; a_2 \, \langle \delta_{\mathcal{S}}, \boldsymbol{\phi}_2 \rangle \tag{B.11}$$

or

$$\int_{\Omega} \delta_{\mathcal{S}} (a_1 \boldsymbol{\phi}_1 \,+\, a_2 \boldsymbol{\phi}_2) \, d\Omega \;=\; a_1 \int_{\Omega} \delta_{\mathcal{S}} \boldsymbol{\phi}_1 d\Omega \;+\; a_2 \int_{\Omega} \delta_{\mathcal{S}} \boldsymbol{\phi}_2 d\Omega \,. \tag{B.12}$$

Finally, the Dirac-delta function $\delta_{\mathcal{S}}(\boldsymbol{x})$ is *continuous* because, given a null sequence in $C^{\infty}(\Omega)$, $\{\boldsymbol{\phi}_m\}$, the following holds

$$\lim_{m \to \infty} \langle \delta_{\mathcal{S}}, \boldsymbol{\phi}_m \rangle \;=\; \lim_{m \to \infty} \int_{\Omega} \delta_{\mathcal{S}} \boldsymbol{\phi}_m \, d\Omega \;=\; \lim_{m \to \infty} \int_{\mathcal{S}} \boldsymbol{\phi}_m \, d\Gamma \;=\; \mathbf{0} \tag{B.13}$$

where, for example,

$$\boldsymbol{\phi}_m \;=\; \frac{1}{m} \boldsymbol{\phi}(\boldsymbol{x}) \,; \quad \boldsymbol{\phi}(\boldsymbol{x}) \;=\; g(\boldsymbol{x}) \boldsymbol{h} \tag{B.14}$$

and

$$g(\boldsymbol{x}) \;=\; \begin{cases} \exp\left(\frac{1}{\boldsymbol{x} \cdot \boldsymbol{x} - R^2}\right) & \text{for } \boldsymbol{x} \in \Omega \\ \quad 0 & \text{for } \boldsymbol{x} \in \partial\Omega \,, \text{ and } \boldsymbol{x} \notin \bar{\Omega} = \Omega \cup \partial\Omega \end{cases} \tag{B.15}$$

where $\boldsymbol{h}$ is a constant vector and $\partial\Omega$ defines a sphere of radius R and origin at $\boldsymbol{x} = \mathbf{0}$.

Now, use this framework of distributional theory to define the gradient of a discontinuous displacement field. Consider the discontinuous function $\boldsymbol{f}(\boldsymbol{x})$ defined as

$$\boldsymbol{f}(\boldsymbol{x}) \;=\; \bar{\boldsymbol{f}}(\boldsymbol{x}) \;+\; [\![\boldsymbol{f}]\!]\; H_{\mathcal{S}}(\boldsymbol{x}) \tag{B.16}$$

where $\bar{\boldsymbol{f}}$ is the continuous part of $\boldsymbol{f}$ and $[\![\boldsymbol{f}]\!]$ is the jump of $\boldsymbol{f}$ across $\mathcal{S}$ and is independent of $\boldsymbol{x}$. With the definition of a singular distribution given above, it is possible to determine $\boldsymbol{\nabla f}$.

Express $\boldsymbol{\nabla f}$ as a functional:

$$\int_\Omega \boldsymbol{\nabla f} \cdot \boldsymbol{\phi}\, d\Omega \;=\; \int_\Omega \boldsymbol{\nabla} \bar{\boldsymbol{f}} \cdot \boldsymbol{\phi}\, d\Omega \;+\; \int_\Omega \left([\![\boldsymbol{f}]\!] \otimes \boldsymbol{\nabla} H_{\mathcal{S}}\right) \cdot \boldsymbol{\phi}\, d\Omega\,. \tag{B.17}$$

Consider the second term of the right hand side of Eq. (B.17). Notice the following result from the chain rule:

$$\boldsymbol{\nabla} H_{\mathcal{S}} \cdot \boldsymbol{\phi} \;=\; \boldsymbol{\nabla} \cdot (H_{\mathcal{S}} \boldsymbol{\phi}) \;-\; H_{\mathcal{S}} \boldsymbol{\nabla} \cdot \boldsymbol{\phi}\,. \tag{B.18}$$

Making use of the Divergence Theorem and the fact that Ω is an open region (i.e. without boundaries), the following holds:

$$\begin{aligned} \int_\Omega [\![\boldsymbol{f}]\!]\, \boldsymbol{\nabla} \cdot (H_{\mathcal{S}} \boldsymbol{\phi})\, d\Omega \;&=\; \int_{\Omega_+} [\![\boldsymbol{f}]\!]\, \boldsymbol{\nabla} \cdot (H_{\mathcal{S}} \boldsymbol{\phi})\, d\Omega \;+\; \int_{\Omega_-} [\![\boldsymbol{f}]\!]\, \boldsymbol{\nabla} \cdot (H_{\mathcal{S}} \boldsymbol{\phi})\, d\Omega \\ &=\; \int_{\mathcal{S}} [\![\boldsymbol{f}]\!]\, H_{\mathcal{S}} \boldsymbol{\phi} \cdot \boldsymbol{n}_-\, d\Gamma \;+\; \int_{\mathcal{S}} [\![\boldsymbol{f}]\!]\, H_{\mathcal{S}} \boldsymbol{\phi} \cdot \boldsymbol{n}_+\, d\Gamma \\ &=\; \mathbf{0} \end{aligned} \tag{B.19}$$

where $\boldsymbol{n}_- \;=\; -\boldsymbol{n}_+$. The second part of the right hand side of Eq. (B.17) then becomes:

$$\begin{aligned}\int_{\Omega} (\llbracket \boldsymbol{f} \rrbracket \otimes \boldsymbol{\nabla} H_{\mathcal{S}}) \cdot \boldsymbol{\phi} \, d\Omega &= -\int_{\Omega} \llbracket \boldsymbol{f} \rrbracket \, \boldsymbol{\nabla} \cdot \boldsymbol{\phi} H_{\mathcal{S}} \, d\Omega \\ &= -\int_{\Omega_{+}} \llbracket \boldsymbol{f} \rrbracket \, \boldsymbol{\nabla} \cdot \boldsymbol{\phi} \, d\Omega \\ &= -\int_{\mathcal{S}} \llbracket \boldsymbol{f} \rrbracket \, \boldsymbol{\phi} \cdot \boldsymbol{n}_{-} \, d\Gamma \\ &= \int_{\mathcal{S}} \llbracket \boldsymbol{f} \rrbracket \, \boldsymbol{\phi} \cdot \boldsymbol{n}_{+} \, d\Gamma \\ &= \int_{\Omega} (\llbracket \boldsymbol{f} \rrbracket \otimes \boldsymbol{n}) \cdot \boldsymbol{\phi} \, \delta_{\mathcal{S}} \, d\Omega \, . \end{aligned} \tag{B.20}$$

The last equation in Eq. (B.20) is reached by the definition of the Dirac-delta function as a distribution. Thus, in total, Eq. (B.17) becomes:

$$\int_{\Omega} \boldsymbol{\nabla} \boldsymbol{f} \cdot \boldsymbol{\phi} \, d\Omega = \int_{\Omega} \boldsymbol{\nabla} \bar{\boldsymbol{f}} \cdot \boldsymbol{\phi} \, d\Omega + \int_{\Omega} (\llbracket \boldsymbol{f} \rrbracket \otimes \boldsymbol{n}) \cdot \boldsymbol{\phi} \delta_{\mathcal{S}} \, d\Omega \, . \tag{B.21}$$

Localizing the integral in Eq. (B.21) (see page 38 of GURTIN [29]), the following expression results for the gradient of a discontinuous function:

$$\int_{\Omega} \left[\boldsymbol{\nabla} \boldsymbol{f} - \boldsymbol{\nabla} \bar{\boldsymbol{f}} - (\llbracket \boldsymbol{f} \rrbracket \otimes \boldsymbol{n}) \, \delta_{\mathcal{S}} \right] \cdot \boldsymbol{\phi} \, d\Omega = \boldsymbol{0} \tag{B.22}$$

and in local form,

$$\boldsymbol{\nabla} \boldsymbol{f} = \boldsymbol{\nabla} \bar{\boldsymbol{f}} + (\llbracket \boldsymbol{f} \rrbracket \otimes \boldsymbol{n}) \, \delta_{\mathcal{S}} \, . \tag{B.23}$$

Therefore, the symmetric gradient of a discontinuous displacement rate results in a singular strain rate:

$$\dot{\boldsymbol{\epsilon}} := \boldsymbol{\nabla}^{s} \dot{\boldsymbol{u}} = \boldsymbol{\nabla}^{s} \dot{\bar{\boldsymbol{u}}} + (\llbracket \dot{\boldsymbol{u}} \rrbracket \otimes \boldsymbol{n})^{s} \, \delta_{\mathcal{S}} \, . \tag{B.24}$$

Throughout this work the Dirac-delta function appearing in the singular part of $\dot{\boldsymbol{\epsilon}}$ must be treated properly in the context of distributional theory.

Appendix C

Determination of Parameters for Drucker-Prager Yield Function

C.1 Review of Mohr-Coulomb Yield Function

Consider the two Mohr's circles at failure which define the classical Mohr-Coulomb failure criterion of soil mechanics (see Lambe & Whitman [42]) via the friction angle $\bar{\phi}$ and cohesion $\bar{c}$ as shown in Fig. C.1.

The two circles represent the state of stress at peak load for a particular soil loaded under compression (i.e. plane strain, true triaxial, or 'triaxial' stress conditions) for two different confining pressures (hence, the noticeable frictional/pressure dependence). The 'cohesion' $\bar{c}$ (actually, just the intercept of the shear stress τ-axis and not the true cohesion) and friction angle $\bar{\phi}$ (not the interparticle friction angle) are defined from a line drawn tangent to the two Mohr's circles (it is preferrable to use more Mohr's circles to define $\bar{c}$ and $\bar{\phi}$, but for the purposes of this discussion, two are sufficient). Choosing one Mohr's circle defined via its major and minor principal stresses, σ_1 and σ_3, respectively, the Mohr-Coulomb failure criterion may be written

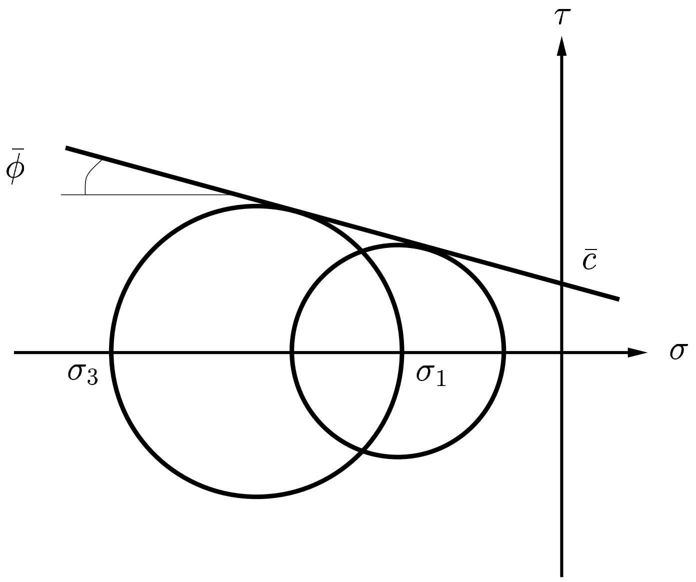

Figure C.1. Mohr-Coulomb failure criterion.

in terms of principal stress and a yield function f as

$$f \;:=\; (\sigma_1 - \sigma_3) \;+\; (\sigma_1 + \sigma_3)\sin\bar{\phi} \;-\; 2\bar{c}\cos\bar{\phi} \;=\; 0\,. \tag{C.1}$$

Equation (C.1) defines one yield plane of a hexagonal yield cone (see figures in [58] and [95]).

C.2 Material Dilation Angle

It has been shown experimentally (see [95]) that an associative flow rule ($\dot{\boldsymbol{\epsilon}}^p = \lambda\partial_{\boldsymbol{\sigma}} f$) overestimates the amount of plastic dilatation, and thus a plastic potential function g, similar to f, is defined as [65], [95]

$$g \;:=\; (\sigma_1 - \sigma_3) \;+\; (\sigma_1 + \sigma_3)\sin\bar{\psi} \;-\; 2\bar{c}\cos\bar{\phi} \;=\; 0 \tag{C.2}$$

where $\bar{\psi}$ is the material dilation angle. The flow rule then becomes

$$\dot{\boldsymbol{\epsilon}}^p = \lambda \partial_{\boldsymbol{\sigma}} g \tag{C.3}$$

or

$$\left\{ \begin{array}{c} \dot{\epsilon}_1^p \\ \dot{\epsilon}_2^p \\ \dot{\epsilon}_3^p \end{array} \right\} = \lambda \left\{ \begin{array}{c} 1 + \sin\bar{\psi} \\ 0 \\ -1 + \sin\bar{\psi} \end{array} \right\} \tag{C.4}$$

where it can be shown that

$$\sin\bar{\psi} = \frac{\dot{\epsilon}_1^p + \dot{\epsilon}_3^p}{\dot{\epsilon}_1^p - \dot{\epsilon}_3^p} \tag{C.5}$$

which is valid for the planar problem [5]. Substituting Eq. (C.5) into Eq. (2.66) and assuming $\dot{\epsilon}_2^p = -\dot{\epsilon}_2^e \approx 0$ for plane strain yields

$$b = \sqrt{\frac{3\sin^2\bar{\psi}}{3 + \sin^2\bar{\psi}}}\,. \tag{C.6}$$

Equation (C.6) is the same as that derived for b in terms of the jump dilation angle ψ because the out-of-plane component of localized plastic flow is zero (i.e. $\dot{\epsilon}_{2,\delta}^p = 0$). Recall that the regularity of stress in Section 2.5.2 requires

$$\dot{\boldsymbol{\epsilon}}_\delta^p = \lambda_\delta \partial_{\boldsymbol{\sigma}} \varphi = \dot{\zeta} (\boldsymbol{m} \otimes \boldsymbol{n})^s \tag{C.7}$$

where $\dot{\boldsymbol{\epsilon}}^p = \dot{\boldsymbol{\epsilon}}_\delta^p \delta_{\mathcal{S}}$. Because $\boldsymbol{m}$ and $\boldsymbol{n}$ lie in the major-minor principal stress plane via the analysis in Sections 2.6.2.1 and E, from Eq. (2.78) it turns out that (using $\dot{\epsilon}_{2,\delta}^p$ here as the intermediate principal localized plastic strain rate instead of $\dot{\epsilon}_{3,\delta}^p$ in Section 2.6.2.1)

$$\dot{\epsilon}_{2,\delta}^p = 0 \tag{C.8}$$

which leads to the equivalence of Eq. (C.6) and Eq. (2.92).

C.3 Parameters for Drucker-Prager Yield Function

The constants $\bar{\alpha}$ and β from Eq. (2.57) may be determined such that the Drucker-Prager yield cone passes through the outer apexes of the Mohr-Coulomb yield surface ($A = -1$ in Eq. (2.61)), and the inner apexes of the Mohr-Coulomb yield surface ($A = 1$ in Eq. (2.61)) [58]. Refer to Fig. C.2 for a view of the yield surfaces on the $\pi-$plane.

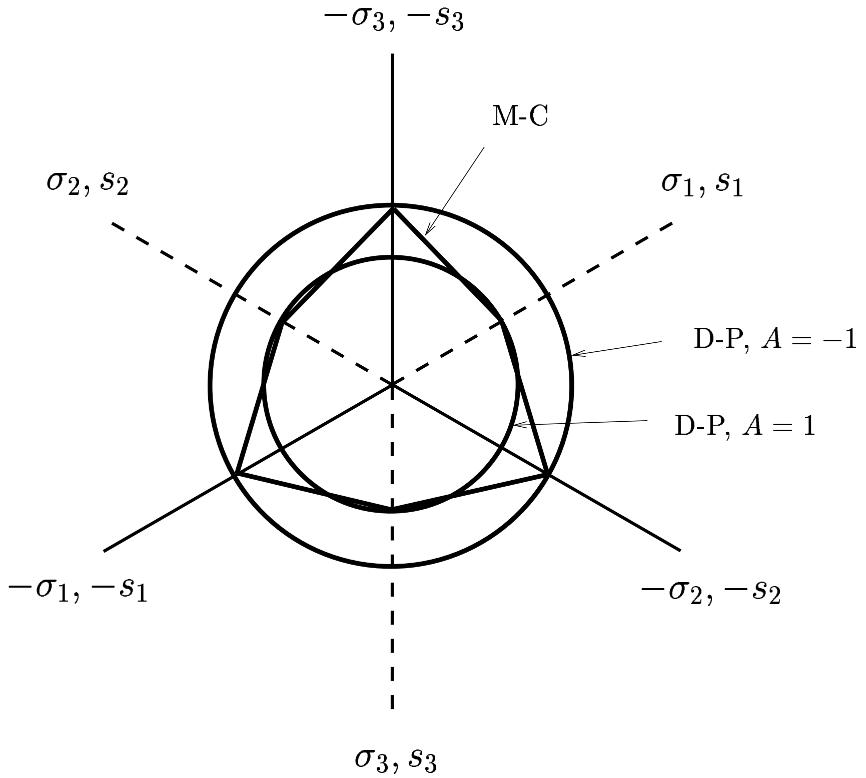

Figure C.2. π-plane showing Mohr-Coulomb (M-C) and Drucker-Prager (D-P) yield surfaces for $\bar{\phi} = 30°$ and a given value of $\bar{c}$.

Notice that for high friction angles ($\bar{\phi} = 30°$ used to create the yield surfaces in Fig. C.2), the Drucker-Prager yield cone with $A = 1$ or $A = -1$ becomes a gross approximation of the Mohr-Coulomb yield surface; thus, a value of A in between -1 and 1 (i.e. $A = 0$) would be more appropriate.

To begin, recall Eq. (C.1)

$$(\sigma_1 - \sigma_3) \, + \, (\sigma_1 + \sigma_3) \sin \bar{\phi} \, - \, 2\bar{c} \cos \bar{\phi} \, = \, 0 \, . \tag{C.9}$$

Solve for σ_1 and σ_3 ($\sigma_3 < \sigma_1 < 0$) as

$$\begin{aligned} \sigma_1 &= \left(\frac{1 - \sin \bar{\phi}}{1 + \sin \bar{\phi}} \right) \sigma_3 \, + \, \frac{2\bar{c} \cos \bar{\phi}}{1 + \sin \bar{\phi}} \\ \sigma_3 &= \left(\frac{1 + \sin \bar{\phi}}{1 - \sin \bar{\phi}} \right) \sigma_1 \, - \, \frac{2\bar{c} \cos \bar{\phi}}{1 - \sin \bar{\phi}} \end{aligned} \tag{C.10}$$

or, with $\boldsymbol{\sigma} = \boldsymbol{s} + p\mathbf{1}$,

$$\begin{aligned} s_1 &= \left(\frac{1 - \sin \bar{\phi}}{1 + \sin \bar{\phi}} \right) s_3 \, - \, \left(\frac{2 \sin \bar{\phi}}{1 + \sin \bar{\phi}} \right) p + \frac{2\bar{c} \cos \bar{\phi}}{1 + \sin \bar{\phi}} \\ s_3 &= \left(\frac{1 + \sin \bar{\phi}}{1 - \sin \bar{\phi}} \right) s_1 \, + \, \left(\frac{2 \sin \bar{\phi}}{1 - \sin \bar{\phi}} \right) p - \frac{2\bar{c} \cos \bar{\phi}}{1 - \sin \bar{\phi}} \, . \end{aligned} \tag{C.11}$$

For an outer apex, $s_1 = s_2 = -s_3/2$ (from tr($\boldsymbol{s}$)=0), and

$$s_3 \, = \, \left(\frac{4 \sin \bar{\phi}}{3 - \sin \bar{\phi}} \right) p - \frac{4\bar{c} \cos \bar{\phi}}{3 - \sin \bar{\phi}} \tag{C.12}$$

and for an inner apex, $s_2 = s_3 = -s_1/2$, and

$$s_1 \, = \, - \left(\frac{4 \sin \bar{\phi}}{3 + \sin \bar{\phi}} \right) p + \frac{4\bar{c} \cos \bar{\phi}}{3 + \sin \bar{\phi}} \, . \tag{C.13}$$

Recall the form of the Drucker-Prager yield cone $\phi(\boldsymbol{\sigma})$ for perfect-plasticity from Eq. (2.57):

$$\sqrt{\frac{3}{2}} \|\boldsymbol{s}\| \, + \, \sqrt{3}(-\bar{\alpha} + \beta p) \, = \, 0 \tag{C.14}$$

which matching for an outer apex ($s_1 = s_2 = -s_3/2$) takes the form

$$\frac{3}{2}|s_3| + \sqrt{3}(-\bar{\alpha} + \beta p) = 0 \tag{C.15}$$

where $|s_3| = -s_3$ since $p < 0$ and $\bar{c} > 0$, and for an inner apex takes the form

$$\frac{3}{2}|s_1| + \sqrt{3}(-\bar{\alpha} + \beta p) = 0 \tag{C.16}$$

where $|s_1| = s_1$. Substituting Eq. (C.12) into Eq. (C.15) yields

$$\bar{\alpha} = \frac{6\bar{c}\cos\bar{\phi}}{\sqrt{3}(3-\sin\bar{\phi})}, \quad \beta = \frac{6\sin\bar{\phi}}{\sqrt{3}(3-\sin\bar{\phi})} \tag{C.17}$$

and substituting Eq. (C.13) into Eq. (C.16) yields

$$\bar{\alpha} = \frac{6\bar{c}\cos\bar{\phi}}{\sqrt{3}(3+\sin\bar{\phi})}, \quad \beta = \frac{6\sin\bar{\phi}}{\sqrt{3}(3+\sin\bar{\phi})} \tag{C.18}$$

which may be expressed in terms of the parameter A as in Eq. (2.61).

Appendix D

Numerical Integration of Constitutive Law, and Derivation of Algorithmic Tangent

Here, the stress rate $\dot{\boldsymbol{\sigma}}$ is numerically integrated according to the standard return mapping algorithm (backward Euler; see HUGHES [34]), and the algorithmic (consistent) elastic-plastic tangent operator $\boldsymbol{C}_{n+1}^{ep(k+1)}$ is derived [78]. The superscript $k+1$ denotes the current iteration within a Newton-Raphson solution algorithm, and the subscript $n+1$ denotes the current time step. The Newton-Raphson solution algorithm will be discussed in Section 3.4.3, and for now the superscript $k+1$ will be dropped. Keep in mind that whereever a subscript $n+1$ appears, a superscript $k+1$ would also be written.

Recall the constitutive relation describing the evolution of the Cauchy stress

$$\dot{\boldsymbol{\sigma}} \;=\; \boldsymbol{c}^{e} : (\dot{\boldsymbol{\epsilon}} \,-\, \dot{\boldsymbol{\epsilon}}^{p})\,. \tag{D.1}$$

Integrating Eq. (D.1) over the time increment $\Delta t = t_{n+1} - t_n$ yields

$$\int_{t_n}^{t_{n+1}} \dot{\boldsymbol{\sigma}}\, dt \;=\; \int_{t_n}^{t_{n+1}} \boldsymbol{c}^e : \dot{\boldsymbol{\epsilon}}\, dt \;-\; \int_{t_n}^{t_{n+1}} \boldsymbol{c}^e : \dot{\boldsymbol{\epsilon}}^p\, dt \tag{D.2}$$

and

$$\boldsymbol{\sigma}_{n+1} \;-\; \boldsymbol{\sigma}_n \;=\; \boldsymbol{c}^e : \Delta\boldsymbol{\epsilon} \;-\; \boldsymbol{c}^e : \int_{t_n}^{t_{n+1}} \lambda \partial_{\boldsymbol{\sigma}} \varphi\, dt \tag{D.3}$$

where $\Delta\boldsymbol{\epsilon} = \boldsymbol{\epsilon}_{n+1} - \boldsymbol{\epsilon}_n$ is the prescribed strain increment for the *strain driven* problem. Because the direction of plastic flow and the plastic consistency parameter vary over the time increment Δt, the integration of the plastic strain rate is approximated by an implicit (backward) Euler integration (HUGHES [34], SIMO & HUGHES [80]) as

$$\boldsymbol{\epsilon}^p_{n+1} - \boldsymbol{\epsilon}^p_n \;\approx\; \tilde{\lambda}(\partial_{\boldsymbol{\sigma}} \varphi)_{n+1} \tag{D.4}$$

and

$$\boldsymbol{c}^e : \int_{t_n}^{t_{n+1}} \lambda \partial_{\boldsymbol{\sigma}} \varphi\, dt \;\approx\; \tilde{\lambda} \boldsymbol{c}^e : (\partial_{\boldsymbol{\sigma}} \varphi)_{n+1} \tag{D.5}$$

where $\tilde{\lambda} \;=\; \Delta t \lambda_{n+1}$. Such an integration is unconditionally stable and first order accurate. Typically, in the implementation of such integration, the trial deviatoric direction of $\boldsymbol{\epsilon}^p_{n+1}$ (i.e. $\hat{\boldsymbol{n}}^{\text{tr}}_{n+1}$ from Eq. (2.63)) is substituted. To show the equivalence of these directions ($\hat{\boldsymbol{n}}^{\text{tr}}_{n+1} = \hat{\boldsymbol{n}}_{n+1}$) in the π-plane, consider the following analysis.

Rewrite the updated stress as

$$\boldsymbol{\sigma}_{n+1} \;=\; \boldsymbol{\sigma}^{\text{tr}}_{n+1} \;-\; \tilde{\lambda} \boldsymbol{c}^e : (\partial_{\boldsymbol{\sigma}} \varphi)_{n+1}\,. \tag{D.6}$$

Decompose the stress into deviatoric and pressure terms as follows

$$\boldsymbol{\sigma}_{n+1} \;=\; \boldsymbol{s}_{n+1} \;+\; p_{n+1}\mathbf{1} \;=\; \|\boldsymbol{s}_{n+1}\| \hat{\boldsymbol{n}}_{n+1} \;+\; p_{n+1}\mathbf{1}\,. \tag{D.7}$$

Equation (D.6) may then be written as

$$\|\boldsymbol{s}_{n+1}\|\hat{\boldsymbol{n}}_{n+1} + p_{n+1}\mathbf{1} = \|\boldsymbol{s}^{\text{tr}}_{n+1}\|\hat{\boldsymbol{n}}^{\text{tr}}_{n+1} + p^{\text{tr}}_{n+1}\mathbf{1} - \tilde{\lambda}\left[2\sqrt{\frac{3}{2}}\bar{\mu}\hat{\boldsymbol{n}}_{n+1} + \sqrt{3}b\bar{K}\mathbf{1}\right] \tag{D.8}$$

or

$$\underbrace{\left(\|\boldsymbol{s}_{n+1}\| + 2\sqrt{\frac{3}{2}}\bar{\mu}\tilde{\lambda}\right)}_{>0}\hat{\boldsymbol{n}}_{n+1} + \underbrace{\left(p_{n+1} - p^{\text{tr}}_{n+1} + \sqrt{3}b\bar{K}\tilde{\lambda}\right)}_{=0}\mathbf{1} = \underbrace{\|\boldsymbol{s}^{\text{tr}}_{n+1}\|}_{>0}\hat{\boldsymbol{n}}^{\text{tr}}_{n+1}\,. \tag{D.9}$$

Since $\hat{\boldsymbol{n}}_{n+1}$ and $\hat{\boldsymbol{n}}^{\text{tr}}_{n+1}$ are orthogonal to $\mathbf{1}$ and the terms before them are positive, the current and trial deviatoric stress directions are equal

$$\hat{\boldsymbol{n}}_{n+1} = \hat{\boldsymbol{n}}^{\text{tr}}_{n+1} \tag{D.10}$$

and

$$\begin{aligned}\|\boldsymbol{s}_{n+1}\| &= \|\boldsymbol{s}^{\text{tr}}_{n+1}\| - 2\sqrt{\frac{3}{2}}\bar{\mu}\tilde{\lambda}\\ p_{n+1} &= p^{\text{tr}}_{n+1} - \sqrt{3}b\bar{K}\tilde{\lambda}\,.\end{aligned} \tag{D.11}$$

Thus, Eq. (D.6) may be rewritten as

$$\boldsymbol{\sigma}_{n+1} = \boldsymbol{\sigma}^{\text{tr}}_{n+1} - \tilde{\lambda}\boldsymbol{c}^{e} : (\partial_{\boldsymbol{\sigma}}\varphi)^{\text{tr}}_{n+1}\,. \tag{D.12}$$

This equation is especially useful for implementation of the stress integration algorithm in a computer code.

To determine the discrete plastic consistency parameter $\tilde{\lambda}$, write out the discrete form of the yield condition at time t_{n+1} as

$$\phi(\boldsymbol{\sigma}_{n+1}, \boldsymbol{\alpha}_{n+1}) = \sqrt{\frac{3}{2}}\|\boldsymbol{s}_{n+1}\| + \sqrt{3}(-\bar{\alpha} + \beta p_{n+1}) + (\sqrt{3}b(\alpha_1)_{n+1} + (\alpha_2)_{n+1}) = 0 \tag{D.13}$$

where

$$\begin{aligned}(\alpha_1)_{n+1} &= (\alpha_1)_n - \sqrt{3}bK'\tilde{\lambda} \\ (\alpha_2)_{n+1} &= (\alpha_2)_n - H'\tilde{\lambda}\,. \end{aligned} \tag{D.14}$$

With $\|\boldsymbol{s}_{n+1}\|$ and p_{n+1} defined in Eq. (D.11), the discrete plastic consistency parameter is solved for as

$$\tilde{\lambda} = \frac{\phi(\boldsymbol{\sigma}^{\mathrm{tr}}_{n+1}, \boldsymbol{\alpha}_n)}{\chi + \mathcal{H}} \tag{D.15}$$

where $\chi = 3(\bar{\mu} + \beta b\bar{K})$ and $\mathcal{H} = 3b^2K' + H'$. Note that if Eq. (D.13) was nonlinear due to nonlinear hardening/softening, it would be solved for $\tilde{\lambda}$ by a local Newton-Raphson iteration scheme (see [80] for details).

To formulate the algorithmic elastic-plastic tangent modulus tensor, the derivative of the updated stress tensor needs to be taken:

$$\begin{aligned}\boldsymbol{C}^{ep}_{n+1} &= \left(\frac{\partial \boldsymbol{\sigma}}{\partial \boldsymbol{\epsilon}}\right)_{n+1} = \frac{\partial}{\partial \boldsymbol{\epsilon}}\left[\boldsymbol{\sigma}^{\mathrm{tr}}_{n+1} - \tilde{\lambda}\left(2\sqrt{\frac{3}{2}}\bar{\mu}\frac{\boldsymbol{s}^{\mathrm{tr}}_{n+1}}{\|\boldsymbol{s}^{\mathrm{tr}}_{n+1}\|} + \sqrt{3}b\bar{K}\mathbf{1}\right)\right] \\ &= c_1\,\mathbf{1}\otimes\mathbf{1} + 2c_2\,\boldsymbol{I} + c_3\,\hat{\boldsymbol{n}}_{n+1}\otimes\hat{\boldsymbol{n}}_{n+1} + c_4\left(b\mathbf{1}\otimes\hat{\boldsymbol{n}}_{n+1} + \beta\hat{\boldsymbol{n}}_{n+1}\otimes\mathbf{1}\right)\end{aligned} \tag{D.16}$$

where

$$\begin{aligned} c_1 &= \bar{\lambda} - \frac{3\beta b\bar{K}^2}{\chi + \mathcal{H}} + \frac{\frac{4}{3}\sqrt{\frac{3}{2}}\bar{\mu}^2\tilde{\lambda}}{\|\boldsymbol{s}^{\mathrm{tr}}_{n+1}\|} \\ c_2 &= \bar{\mu}\left(1 - \frac{2\sqrt{\frac{3}{2}}\bar{\mu}\tilde{\lambda}}{\|\boldsymbol{s}^{\mathrm{tr}}_{n+1}\|}\right) \\ c_3 &= 4\bar{\mu}^2\left(\frac{-3/2}{\chi + \mathcal{H}} + \frac{\sqrt{\frac{3}{2}}\tilde{\lambda}}{\|\boldsymbol{s}^{\mathrm{tr}}_{n+1}\|}\right) \\ c_4 &= \frac{-3\sqrt{2}\bar{K}\bar{\mu}}{\chi + \mathcal{H}}\,. \end{aligned} \tag{D.17}$$

The numerical integration algorithm for the stress at each Gauss point is summarized as follows:

1) compute the trial state by freezing plastic flow and incrementing the total strain:

$$\begin{aligned} \boldsymbol{\sigma}^{\mathrm{tr}}_{n+1} &= \boldsymbol{\sigma}_n + \boldsymbol{c}^e : \Delta\boldsymbol{\epsilon} \\ p^{\mathrm{tr}}_{n+1} &= \frac{1}{3}\mathrm{tr}(\boldsymbol{\sigma}^{\mathrm{tr}}_{n+1}) \\ \boldsymbol{s}^{\mathrm{tr}}_{n+1} &= \boldsymbol{\sigma}^{\mathrm{tr}}_{n+1} - p^{\mathrm{tr}}_{n+1}\mathbf{1} \\ \phi^{\mathrm{tr}}_{n+1} &= \phi(\boldsymbol{\sigma}^{\mathrm{tr}}_{n+1}, \boldsymbol{\alpha}_n) = \sqrt{\frac{3}{2}}\|\boldsymbol{s}^{\mathrm{tr}}_{n+1}\| + \sqrt{3}(-\bar{\alpha} + \beta p^{\mathrm{tr}}_{n+1}) \\ &\quad + (\sqrt{3}b(\alpha_1)_n + (\alpha_2)_n) \end{aligned}$$

2) check for yielding, and if yielding is detected, update stress and stress-like plastic internal variables:

```
IF ($\phi^{\mathrm{tr}}_{n+1} < 0$) THEN
        $\boldsymbol{\sigma}_{n+1} = \boldsymbol{\sigma}^{\mathrm{tr}}_{n+1}$
        $(\alpha_1)_{n+1} = (\alpha_1)_n$
        $(\alpha_2)_{n+1} = (\alpha_2)_n$
        return $\boldsymbol{c}^e$
ELSEIF ($\phi^{\mathrm{tr}}_{n+1} > 0$) THEN
        $\tilde{\lambda} = \dfrac{\phi^{\mathrm{tr}}_{n+1}}{\chi + \mathcal{H}}$
        $\boldsymbol{\sigma}_{n+1} = \boldsymbol{\sigma}^{\mathrm{tr}}_{n+1} - \tilde{\lambda}\left(\sqrt{3}b\bar{K}\mathbf{1} + 2\sqrt{\frac{3}{2}}\bar{\mu}\frac{\boldsymbol{s}^{\mathrm{tr}}_{n+1}}{\|\boldsymbol{s}^{\mathrm{tr}}_{n+1}\|}\right)$
        $(\alpha_1)_{n+1} = (\alpha_1)_n - \sqrt{3}bK'\tilde{\lambda}$
        $(\alpha_2)_{n+1} = (\alpha_2)_n - H'\tilde{\lambda}$
        return $\boldsymbol{C}^{ep}_{n+1}$
ENDIF
```

Appendix E

Localization in Three-Dimensional Stress Space

Consider arbitrary orientations of $\boldsymbol{m}$ and $\boldsymbol{n}$ in principal stress space in Fig. E.1, where $\sigma_2 < \sigma_3 < \sigma_1 < 0$, as in Section 2.6.2.1,

$$\boldsymbol{n} = \left\{ \begin{array}{c} \cos\theta\cos\eta \\ \sin\theta \\ \cos\theta\sin\eta \end{array} \right\} ; \quad \boldsymbol{m} = \left\{ \begin{array}{c} \cos\alpha\cos\beta \\ \sin\alpha \\ \cos\alpha\sin\beta \end{array} \right\} . \tag{E.1}$$

Recall Eq. (2.71):

$$(\boldsymbol{m} \otimes \boldsymbol{n})^s = \Lambda \left(\sqrt{\frac{3}{2}} \hat{\boldsymbol{n}} + \frac{1}{\sqrt{3}} b \mathbf{1} \right) \tag{E.2}$$

and expand to get

$$\left[\begin{array}{ccc} \cos\alpha\cos\beta\cos\theta\cos\eta & \cos\alpha\cos\beta\sin\theta & \cos\alpha\cos\beta\cos\theta\sin\eta \\ \sin\alpha\cos\theta\cos\eta & \sin\alpha\sin\theta & \sin\alpha\cos\theta\sin\eta \\ \cos\alpha\sin\beta\cos\theta\cos\eta & \cos\alpha\sin\beta\sin\theta & \cos\alpha\sin\beta\cos\theta\sin\eta \end{array} \right]^s$$

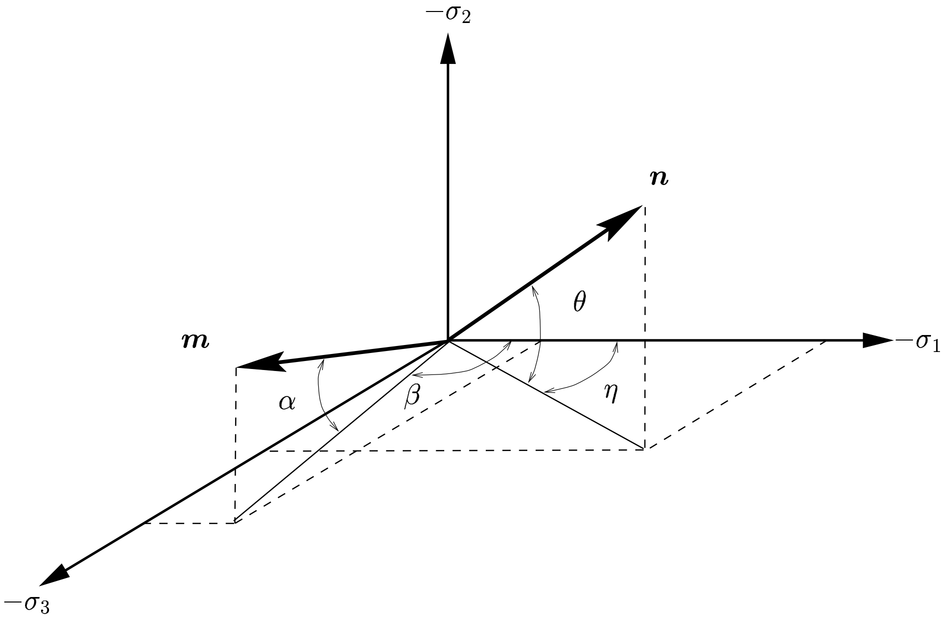

Figure E.1. Orientation of slip vectors in three-dimensions.

$$= \frac{1}{\sqrt{3-b^2}} \begin{bmatrix} \sqrt{\frac{3}{2}}\hat{n}_1 + \frac{1}{\sqrt{3}}b & 0 & 0 \\ 0 & \sqrt{\frac{3}{2}}\hat{n}_2 + \frac{1}{\sqrt{3}}b & 0 \\ 0 & 0 & \sqrt{\frac{3}{2}}\hat{n}_3 + \frac{1}{\sqrt{3}}b \end{bmatrix}. \tag{E.3}$$

In order for $(\boldsymbol{m} \otimes \boldsymbol{n})^s$ to diagonalize, the following three equations must be satisfied

$$\begin{aligned} \cos\alpha\cos\beta\sin\theta + \sin\alpha\cos\theta\cos\eta &= 0 \\ \cos\alpha\cos\beta\cos\theta\sin\eta + \cos\alpha\sin\beta\cos\theta\cos\eta &= 0 \\ \sin\alpha\cos\theta\sin\eta + \cos\alpha\sin\beta\sin\theta &= 0 \end{aligned} \tag{E.4}$$

But there are three equations and four unknown angles; thus, one more equation is needed. Recall that $\boldsymbol{m} \cdot \boldsymbol{n} = \sin\psi$ from Eq. (2.76). Thus, the fourth equation needed to solve for the angles is

$$\boldsymbol{m} \cdot \boldsymbol{n} \;=\; \cos\theta \cos\alpha \cos(\eta - \beta) \;+\; \sin\theta \sin\alpha \;=\; \sin\psi \tag{E.5}$$

We see from Eq. $(\mathrm{E}.4)_1$ that

$$\frac{\tan\alpha}{\tan\theta} \;=\; -\frac{\cos\beta}{\cos\eta}\,. \tag{E.6}$$

Plugging this Eq. (E.6) into Eq. $(\mathrm{E}.4)_3$ produces

$$\beta \;=\; \eta \tag{E.7}$$

which when substituted back into Eq. (E.6) produces

$$\alpha \;=\; -\,\theta\,. \tag{E.8}$$

The vectors $\boldsymbol{m}$ and $\boldsymbol{n}$ now lie in a plane perpendicular to the (σ_1, σ_3) plane. Equation $(\mathrm{E}.4)_2$ then states that

$$\beta \;=\; \begin{cases} 0^\circ & \text{for } (\sigma_1, \sigma_2) \text{ plane} \\ 90^\circ & \text{for } (\sigma_2, \sigma_3) \text{ plane} \end{cases} \tag{E.9}$$

where the (σ_1, σ_3) plane could result if β and η were placed in the (σ_2, σ_3) plane instead of the (σ_1, σ_3) plane to start with (see Fig. E.1). Thus, $\boldsymbol{m}$ and $\boldsymbol{n}$ must lie in one of the principal planes. Finally, Eq. (E.5) produces the orientation of the slip line normal as

$$\theta \;=\; \pm(45^\circ \;-\; \psi/2)\,. \tag{E.10}$$

The localization condition is the same as that derived in Section 2.5.4, where an analysis of the range on the deviator stress ratio h requires that $\boldsymbol{m}$ and $\boldsymbol{n}$ must lie in the major-minor principal stress plane. Thus, it is simply a matter of determining the orientation of the principal stress axes from the eigenvalue problem on the general, three-dimensional stress tensor $\boldsymbol{\sigma}$; for example, refer to BATHE [8] for a variety of numerical solution algorithms for the eigenvalue problem.

Appendix F

Slip-Line Tracing Algorithm

The slip-line tracing algorithm is described in Fig. F.1. There are three cases. For each case the element must have localized according to Eq. (4.1).

The cases are summarized as follows:

1. Element is first to localize. Slip-line is traced through element starting from a given element side location and at an orientation of $\theta = \pm(45^\circ - \psi/2)$ from Eq. (2.81). Whether it is $+(45^\circ - \psi/2)$ or $-(45^\circ - \psi/2)$ will be discussed below.
2. Element is adjacent to a traced element. Slip-line is traced across the element at orientation $\theta = \pm(45^\circ - \psi/2)$ starting at the slip-line intersection of the adjacent traced element.
3. Element is not adjacent to a traced element. Element is not traced.

It is possible to have multiple slip lines. In that case, there is more than one start element, while the tracing algorithm is the same.

To trace a slip-line through an element, the orientation $+(45^\circ - \psi/2)$ or $-(45^\circ - \psi/2)$ must be known. The simple shear case ($\psi = 0^\circ$) shown in Fig. F.2 demonstrates how the angle θ is chosen.

Clearly, the angle $\theta = -45^\circ$ which produces $\boldsymbol{n}^-$ is the correct choice. The following ensures that this correct choice is made for arbitrary element deformations:

```
IF $\left(\sum_{a=1}^{n_{\mathrm{nds}}} \left|\boldsymbol{n}^+ \cdot \boldsymbol{d}^a\right| > \sum_{a=1}^{n_{\mathrm{nds}}} \left|\boldsymbol{n}^- \cdot \boldsymbol{d}^a\right|\right)$ THEN
    $\theta = -(45^\circ - \psi/2)$
ELSE
    $\theta = +(45^\circ - \psi/2)$
ENDIF
```

Thus, according to this algorithm, a slip-line may be traced through a mesh automatically.

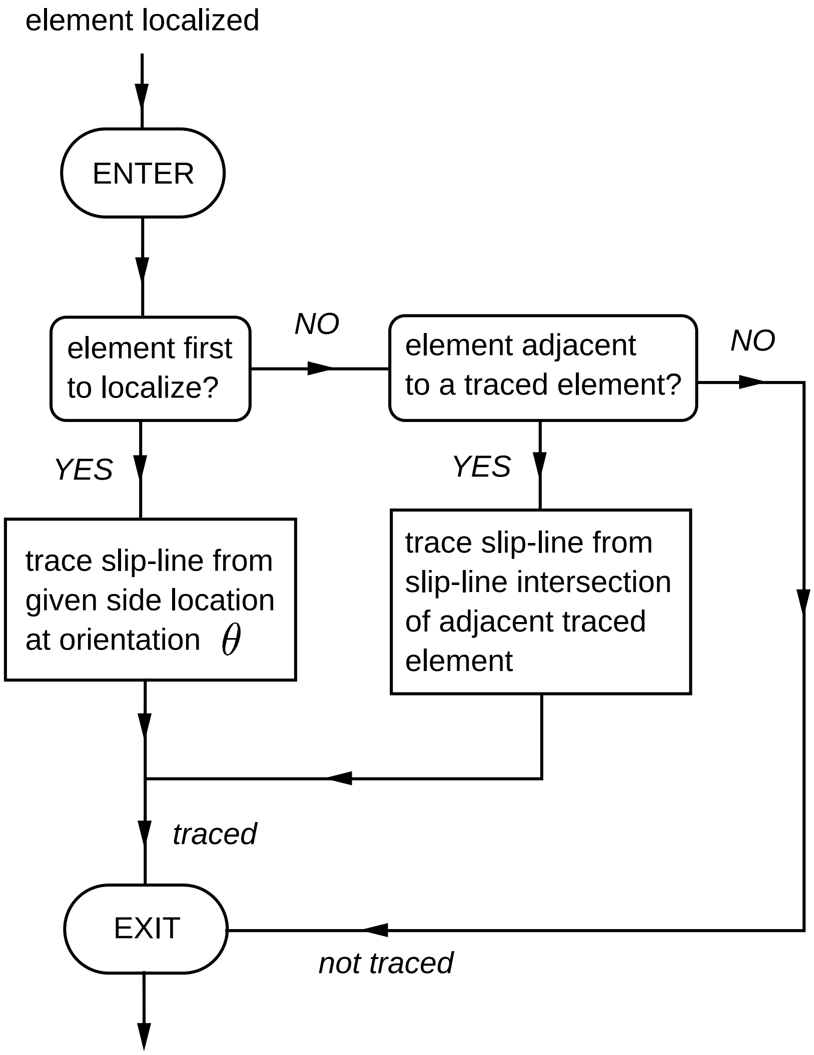

Figure F.1. Flow chart describing slip-line tracing algorithm.

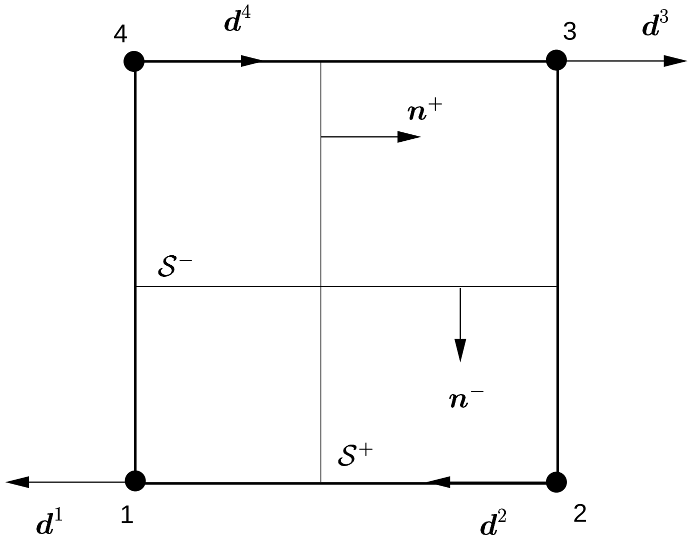

Figure F.2. Description of how to choose slip-line angle $\theta = \pm(45^\circ - \psi/2)$.